

3-YEAR CUMMULATIVE (33-MONTH) ANNUAL REPORT

ONR CONTRACT CONTINUATION OF #N00014-93-0099

Titled

**Correlations Between Micromagnetic, Microstructural and Microchemical  
Properties  
in Ultrathin Epitaxial Magnetic Structures**

and

3-YEAR CUMMULATIVE (33-MONTH) ANNUAL REPORT

ONR AASERT CONTRACT #N00014-95-1-0891

Titled

**Magnetic Microstructure Observed With Electron Holography in STEM**

The Office Of Naval Research

Directed to

Dr. Richard G. Brandt, Electronics Division

Dr. Larry Cooper, Electronics Division

M.R. Scheinfein and G.G. Hembree

Department of Physics and Astronomy

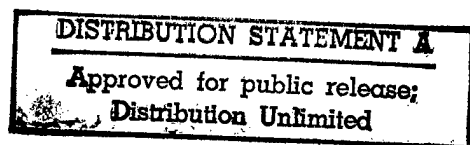
PSF-470 Box 871504

Arizona State University

Tempe, AZ 85287-1504

19980707 155

Submitted : 10 June 1998



## Contents

Title Page .....	1
Contents .....	2
Summary of Selected Research Topics Years 4-6 .....	3
Room-Temperature Dipole-Ferromagnetism In Linear-Self-Assembling Mesoscopic Fe Particle Arrays .....	3
Growth of Self-Organized Mesoscopic Magnetic Structures .....	4
Magnetic Coupling In Self-Organized Narrow-Spaced Fe Nanowire Arrays .....	7
Quantitative Magnetometry Using Electron Holography: Fields Near Magnetic Force Microscope Tips .....	9
Magnetic Nanostructures Produced By Electron Beam Patterning Of Direct Write Transition Metal Fluoride Resists .....	11
Defect Induced Lowering Of Activation Energies At Step Bands In Co/Cu(100) Co on Stepped Cu(100) Surfaces: A Comparison of Experimental Data With Growth Simulations .....	15
Scientific Publications For Years 4-6: January 1996-July 1998 .....	18
Conference Proceedings And Extended Abstracts For Years 4-6: January 1996-July 1998 .....	22
Invited Conference Talks For Years 4-6: January 1996-July 1998 .....	23
Degrees Granted and Students/Post-Docs Supervised For Years 4-6: January 1996-July 1998 .....	23
C.V. For Michael R. Scheinfein .....	24

## Room-Temperature Dipole-Ferromagnetism In Linear-Self-Assembling Mesoscopic Fe Particle Arrays

Magnetic particle systems are ideal for studying interactions and phase transitions [1], and are also of interest for application to high-density magnetic storage devices. Recent experiments in surface and low-dimensional magnetism have focused on the properties of surfaces and small particles in order to explore the structure and dynamics of interactions at small length scales. Advanced synthesis methods for the preparation of transition-metal nanoclusters [2], ordered nanoscale dot-arrays [3], nanostructured magnetic-networks [4], sub-micron [5] and nanometer width wires [6], and random two-dimensional arrays [7] allow new and unusual magnetic phases to be explored. Although the Néel and Brown [8] theories for relaxation in isolated magnetic particles predict relaxation times that are less than microseconds for 6 nm (bulk-anisotropy) diameter Fe particles at room temperature, closely packed mesoscopic linear arrays can be remanent and coercive (ordered) [9]. Long range interactions have been studied by ferromagnetic resonance [10], Mössbauer spectroscopy [9,11], mean field calculations [12] and Monte Carlo simulations [7]. Identifying the mechanism underlying the interactions is facilitated by the preparation of 3d-transition metal islands in and on insulators like SiO<sub>2</sub> [10], MgO [10] and CaF<sub>2</sub> [7], which guarantees that particles do not couple through electronic states in the substrate. Here, we report on the observed and computed magnetic properties in linear self-assembling arrays of nanometer diameter Fe particles. The formation of linear arrays intrinsically breaks the symmetry in the interaction hamiltonian, thereby stabilizing long range order. Self-assembly [6,13] is used to form rows of closely packed ( $2.1 \times 10^{13}/\text{cm}^2$ ) nanometer diameter Fe islands on an amorphous, insulating substrate (SiO). Self-assembly [13] facilitates the fabrication of macroscopic (3 mm x 3mm) arrays, which would take prohibitively long to define using an electron-beam or scanning-tunneling microscope-based lithography [e.g. 3]. The Fe island radius, island density, the width and separation of the linear island arrays can be varied experimentally in the self-assembled growth process for exploring new magnetic phases. Here, we demonstrate how particle diameter in linear magnetic island arrays can be varied to establish a dipole-induced ferromagnetic state above room temperature.

The linear self-assembling arrays of nanometer diameter Fe particles are prepared in UHV ( $2.0 \times 10^{-10}$  mbar). A polished and H<sub>2</sub>O-etched single crystal of NaCl (110) is annealed *in situ*. Regular (nano) grooves result when {100} planes form (facet). This reduces the surface free energy by reducing the area of high-energy (110) planes [13]. The spacing of the grooves is a function of the annealing temperature and time. Ten minutes of annealing at 380°C produce an average trough-to-trough groove spacing of 40 nm. The Fe islands should be randomly oriented and polycrystalline since the goal is to examine the influence of the geometrical particle alignment independent of any intrinsic spin-orbit-induced crystal fields. This is accomplished by coating the NaCl surfaces with an amorphous SiO layer; SiO prevents any epitaxial alignment between the Fe islands and the single crystal NaCl. Fe was deposited from an electron-beam evaporator aligned 70° off the template normal. We show results from three different nominal Fe thicknesses ( $t = 0.3, 0.6, 1.0$  nm) grown at a rate of 0.03 nm/min (normal to the terraces) on a substrate heated to 190°C (thickness as defined in ref. [7]). Fe adatoms agglomerate on SiO in a three-dimensional nucleation and growth mode, where the elevated temperature decreases the nucleation density and liquid-like coalescence is enhanced. The Fe islands are expected to nucleate in the narrow bands exposed to the Fe flux, which here comprise 27% of the ridge-to-ridge distance (10 nm). After Fe deposition, the surface was covered with a 10 nm SiO passivation overlayer.

The magnetic properties of the arrays were measured *ex situ* at room temperature using the longitudinal magneto-optical Kerr effect [14]. Loops were taken along the easy direction, along the wire array, and perpendicular to the wire array, in the hard direction. Kerr loop acquisition times were on the order of seconds to insure that equilibrium magnetization configurations were measured. Hysteresis loops were also computed from Monte Carlo micromagnetics [7] simulations.

Monte Carlo models were used to evaluate the magnetic properties of the linear arrays as a function of particle radius and density [7,15] because the Monte Carlo method rigorously accounts for fluctuations. The model employs an all-orders interparticle interaction hamiltonian [7]. Hysteresis loops are calculated by finding an equilibrium magnetization distribution for an externally applied field value. The magnetization accumulators are reset, the external field value changed, and the previous final magnetization state is preserved as the initial distribution for the next Monte Carlo cycle.

The ordering temperature increases with increasing particle diameter as in the 2-dimensional random array case [7]. Increasing the numbers of lines and changing the particle distribution for alternative random

seeds produce a 10% variation in the remanence. In contrast to the 2-dimensional case, the linear arrays order globally rather than locally. This demonstrates that the linear particle arrays order ferromagnetically due to interparticle magnetostatic dipole fields. This is solely due to the symmetry breaking in the geometric structure of the array. For particles of the appropriate size and proximity, room temperature dipole ferromagnetism can be observed. If only bulk anisotropy were present, the arrays would be superparamagnetic at room temperature. Interface anisotropy, which can be orders of magnitude larger than volume anisotropy in thin film systems, has no preferred in-plane orientation and thus cannot be responsible for the long range order. With typical demagnetization factors of  $\frac{1}{2}$  for cylinders in-plane, the stray fields external to the particles can be as high as 10 kOe, with stray field decay lengths set by the particle diameter. The close proximity of the particles forces neighboring particles to lie in each others (large) stray field resulting in long range order.

- [1] D.C. Mathis, *The Theory of Ferromagnetism II* (Springer-Verlag, Berlin, 1985); H.E. Stanley, *Introduction To Phase Transitions and Critical Phenomena* (Oxford University Press, London, 1971).
- [2] C.P. Gibson, K.J. Putzer, *Science*, **265**, 1338 (1995).
- [3] T. Takeshita, Y. Suzuki, H. Akinaga, W. Mizutani, K. Tanaka, T. Katayama, A. Itoh, *Appl. Phys. Lett.* **68**(21), 3040 (1996); M. Hehn, K. Ounadjela, J.-P. Bucher, F. Rousseaux, D. Decanini, B. Bartenlian, C. Chappert, *Science*, **272**, 1782 (1996); S.Y. Chou, P.R. Krauss, L. Kong, *J. Appl. Phys.* **79**(8), 6101 (1996); R.D. Gomez, M.C. Shih, R.M.H. New, R.F. Pease and R.L. White, *J. Appl. Phys.*, **80**, 342 (1996); S.Gidar, J.Shi, P.F. Hopkins, K.L. Chapman, A.C. Gossard, D.D. Awschalon, A.D. Kent, and S. von Molnar, *Appl. Phys. Lett.*, **69**, 3269 (1996).
- [4] J.A. Barnard, H. Fujiwara, V.R. Inturi, J.D. Jarratt, T.W. Scharf, J.L. Weston, *Appl. Phys. Lett.* **69**(18), 2758 (1996).
- [5] A.O. Adeyeye, G. Lauhoff, J.A.C. Bland, C. Daboo, D.G. Hasko, H. Ahmed, *Appl. Phys. Lett.* **70**(8), 1046 (1997).
- [6] A. Sugawara, S.T. Coyle, G.G. Hembree and M.R. Scheinfein, *Appl. Phys. Lett.*, **70**(8), 1043 (1997).
- [7] M.R. Scheinfein, K.E. Schmidt, K.R. Heim, G.G. Hembree, *Phys. Rev. Lett.* **76**(9), 1541 (1996); K.R. Heim, G.G. Hembree, K.E. Schmidt and M.R. Scheinfein, *Appl. Phys. Lett.* **67**, 2878 (1995).
- [8] L. Neel, *Ann. Geophys.*, **5**, 99 (1949); A. Aharoni, *Introduction To The Theory Of Ferromagnetism* (Oxford Science Publications, Oxford, 1996).
- [9] S. Mørup, *Phys. Rev. Lett.* **72**(20), 3278 (1994); S. Mørup, G. Christiansen, *J. Appl. Phys.* **73**(10), 6955 (1993); S. Mørup, *Hyperfine Int.* **60**, 959 (1990); S. Mørup, P.H. Christensen, B.S. Clausen, *J. Mag. Mag. Mat.* **68**, 160 (1987); S. Mørup, M.B. Madsen, J. Franck, J. Villadsen, C.J.W. Koch, *J. Mag. Mag. Mat.* **40**, 163 (1983).
- [10] W.-N. Wang, Z.-S. Jiang and Y.-W. Du, *J. Appl. Phys.*, **78**, 6679 (1995); S. Matsuo, T. Matsuura, I. Nishida and N. Tanaka, *Jpn. J. Appl.*, **33**, 3907 (1994).
- [11] S. Linderith, L. Balcells, A. Labarta, J. Tejada, P.V. Hendriksen and S.A. Sethi, *J. Magn. Magn. Mater.*, **124**, 269 (1993).
- [12] M. El-Hilo, K. O'Grady and R.W. Chantrell, *J. Magn. Magn. Mater.*, **114**, 295 (1992).
- [13] A. Sugawara, Y. Haga and O. Nittono, *J. Magn. Magn. Mater.*, **156**, 151 (1996).
- [14] Z.J. Yang, M.R. Scheinfein, *J. Appl. Phys.* **74**(11) 6810 (1993).
- [15] N. Metropolis, A.W. Rosenbluth, M.N. Rosenbluth, A.H. Teller, E. Teller, *J. Chem. Phys.* **21**, 1087 (1953).

### Growth of Self-Organized Mesoscopic Magnetic Structures

Mesoscopic magnetic microstructures such as dot and wire arrays are of fundamental interest in the study of coupling and ordering phenomena. From a technological point of view, mesoscopic magnetic structures may produce the future topologies for magnetic storage media. For example, three-dimensional random particle arrays prepared by co-deposition of magnetic and nonmagnetic materials have good high-frequency response and giant magnetoresistance [e.g. 1]. The magnetic properties of these structures depend strongly on the size and spacing of the particles, the concentration of the magnetic element, the growth rate and the substrate temperature [e.g. 2]. Since heterogeneous magnetic particle composites do not have geometrical order, there is no anisotropy in the film plane. However, in-plane anisotropy can be developed by controlling the shape and the spacing of the particles such that the magnetic switching which is characterized by the subtle balance between anisotropy, self-energy, magnetic coupling between particles, and thermal agitation will be well defined.

Specimens with well-defined in-plane anisotropy resulting from specific mesoscopic, geometrical configurations including nanometer size dot and wire arrays have been fabricated by laser-focused atomic deposition [3], electron lithography [4] and local chemical decomposition of metal-organic gas with a scanned probe [5]. Switching mechanisms in these arrays have been studied by magnetic force microscopy [5]. The throughput for producing nanometer size-scale structures with lithographic methods may be low [6], and large areas required for studying macroscopic and collective magnetic properties can be difficult if not impossible to process.



In contrast, our approach is based on self-organization: regular patterns are spontaneously formed in a non-equilibrium system, as in the self-assembling preferential nucleation of hexagonal Co dot arrays on the reconstructed Au(111) surface [7]. We use self-assembly through shadow deposition on patterned templates, *i.e.* the self-masking caused by large-scale surface features. This is a geometrical effect which does not depend strongly on the deposited material. Our method is similar to that proposed by Shinjo [8] who grew a wire array by shadow deposition on a sub-micrometer spaced Si grating that was fabricated by lithography and selective etching. By contrast, we prepare grating templates by self-organization on NaCl non-cleavage ((110) or (111)) planes which become faceted and patterned regularly after thermal annealing [9]. This method allows 10-100 nm spaced, statistically uniform grooves to be formed across centimeter lengths in tens of minutes, though the regularity of the grooves produced by this method is less than that produced lithographically. [10]

We have investigated the relationship between the microstructure and such growth conditions as the annealing temperature of NaCl before deposition, growth temperature and the incident angle of the deposited Fe flux, and the effect on the resultant macroscopic magnetic properties. Three types of the microstructure are described; linear dot arrays, wire arrays, and undulating continuous films. The evolution of the microstructure is explained in terms of nucleation and coalescence kinetics associated with island growth. The magnetization switching processes in these mesostructures which is quite different from those ascribed to flat, continuous Fe films, are also described.

Structures grown on faceted templates include linear arrays of nanometer diameter particles, nanowires with widths of tens of nanometers and lengths of microns or more, and continuous undulating thin films. The type of structure produced depends upon the structure and length scales present in the NaCl template ( $L$ ), the incident angle used to deposit the transition metal ( $q$ ), and the substrate temperature during growth ( $T_g$ ). The NaCl (110) surface sublimates and facets to form (100) and (010) terraces during annealing. The depth of the grooves (peak to trough) is  $\frac{1}{2}$  the distance between peak tops or groove bottoms ( $L$ ). The surface area of the faceted surface is always  $\sqrt{2}$  times larger than the original (110) surface. Experimentally, we kept the annealing time constant (10 minutes) and altered the annealing temperature,  $T_a$  in order to modify the groove spacing ( $L$ ) between 25 nm ( $T_a=380^\circ\text{C}$ ), 40 nm ( $T_a=410^\circ\text{C}$ ), and 90 nm ( $T_a=440^\circ\text{C}$ ).

The area exposed to the incident Fe flux is determined by geometrical shadowing. The exposed terrace is shadowed by the ridge closer to the evaporation source. Since all terraces are oriented  $45^\circ$  from the surface normal, the percentage of the terrace exposed for a given source angle inclination is constant. However, the distance between exposed areas and the width of each patch can be controlled by modifying the substrate annealing temperature  $T_a$ .

Growth temperature is an important parameter used to define microstructure. Fe grows on SiO in a three-dimensional island growth mode. The initial growth is characterized by the competing atomic processes of nucleation, adatom capture and surface diffusion. A detailed numerical analysis of this process has been carried out for the Ag/Gc system. Some of the Fe adatoms diffuse out from the geometrically defined flux region, because an adatom concentration gradient is formed at the mask edge. The nucleation density is expected to be extremely low outside the patch due to low adatom concentration. The grooves can also be preferential nucleation sites. In later stages of growth, coalescence of neighboring islands takes place. When the growth temperature is high, the round shape of the islands is quickly recovered after two or more neighboring islands touch because surface self-diffusion is fast. This might also cause patch broadening: extending the growth front outward from the defined flux regions. Thus, by varying the separation of the flux-exposed regions through geometrical shadowing, and varying the substrate temperature during growth, different nucleation and growth regimes may be exploited in order to fabricate linear dot arrays, nanowires, and thin, undulating films.

The processes driving the formation of the linear arrays are summarized. First, consider the (ideal) growth of a single row of islands along an exposed terrace where the island diameter is approximately equal to the patch width exposed to the deposited Fe flux. The growth scheme to form a single particle width-linear array includes the initial nucleation of closely spaced islands, adatom capture by existing islands, and finally coalescence. In order to grow this type of array, the initial nucleation density must be in a range where the coalesced particles will be well separated. The diffusion length must be long enough to allow adatoms to incorporate into existing islands, yet short enough to forbid adatoms from diffusing across the ridge or groove to the next terrace exposed to Fe flux. For growth at  $T_g=190^\circ\text{C}$ , the nucleation density ( $>2 \times 10^{12}\text{cm}^{-2}$ ) is maximum where the adatom concentration is maximum. When the initial distance between

nuclei ( $< 7$  nm) and the initial island diameter ( $< 2$  nm) is smaller than the width of the area exposed to the Fe flux, several islands nucleate across the exposed area. During later stages of growth with increased island size, neighboring islands come into contact with each other, but at elevated substrate temperatures, surface diffusion rounds off the Fe island surfaces quickly enough to reduce the surface-energy penalty caused when two neighboring islands are touching. After each coalescence event, the center of the new island resulting from the coalescence is near the center of the joined islands. Islands join and form 1-dimensional linear arrays through this process. For a specific range of deposited Fe (e.g.  $t = 1.0$  nm or, when exposed areas would have a uniform film thickness of 1.0 nm for the close-packed face of bcc Fe, (110)), the coalesced Fe island diameter (6.7nm) is roughly as wide as the terrace width and the microstructure approaches a 1-dimensional linear particle array. Linear arrays composed of many particles across an exposed terrace can be fabricated by terminating the growth at lower coverages, thereby preventing island coalescence.

During growth at elevated temperatures ( $T_g=190^\circ\text{C}$ ), adatom diffusion is much faster than at room temperature. Elevated temperature growth produces adatom concentration profiles that become broader at the shadow edge. At elevated temperatures, a small amount of Fe might escape from the flux-exposed zone due to the adatom concentration gradient formed at the shadow edge, and condense at the groove bottom. Experimentally, this effect appears to be negligible since no islands are observed outside of the area exposed to the Fe flux. This observation indicates that when the thickness is small, most adatoms are captured efficiently by pre-existing islands.

By contrast, linear arrays of nanowires can be fabricated using room temperature growth. For slow surface diffusion during room temperature growth, the adatom concentration is almost constant in the patch exposed to Fe flux. As a result, a high density of islands uniformly nucleates in the patch. The initial islands (diameter  $< 2$ nm) are so small that they cannot be clearly resolved by TEM bright-field imaging. Since the profile rapidly drops off at the mask edge, the concentration gradient forces a small amount of Fe to escape from the patch and condense at the groove bottom. As such, extremely thin wires are sometimes observed at the groove bottoms. After the islands (uniformly) cover the patch exposed to the flux, the arriving adatoms are captured by pre-existing (nucleated) islands. The liquid-like coalescence kinetics are slow enough that a network forms (islands fill in) and with increasing coverage, eventually forms a wire, whose cross-section when filled in completely. Wire formation is commonly observed over a wide thickness range for room temperature growth. The wire perimeter boundary fluctuates on a size scale determined by the polycrystalline grain size of the individual, coalesced islands. Thus, growth of better wires with sharper edges will require deposition of fine-grained or amorphous materials.

Wire-broadening occurs during high temperature growth ( $T_g=190^\circ\text{C}$ ) which in the extreme case may lead to bridging between adjacent terraces and the formation of continuous undulating films. With increasing thickness, the wire morphology is completed through a network structure, however, the faster Fe surface self-diffusion causes the wires to broaden. The amount of Fe escaping from the flux-exposed patch increases causing the ultrasmall wires formed at the bottom of the grooves to be thicker than those formed at room temperature. Broadened Fe patches eventually join the wires at the groove bottom causing the other side of the terrace (not the flux exposed terrace) to be partially covered. At higher coverages, the lines join and form continuous films. Naturally, continuous undulating films can also be trivially fabricated through normal incidence evaporation.

- [1] J.Q. Xiao, J.S. Jiang, C.L. Chien, *Phys. Rev. Lett.* **68**(25), 3749 (1992); A.E. Berkowitz, J.R. Mitchell, M.J. Carey, A.P. Young, S. Zhang, F.E. Spada, F.T. Parker, A. Hutten, G. Thomas, *Phys. Rev. Lett.* **68**(25), 3745 (1992); A.E. Berkowitz, J.R. Mitchell, M.J. Carey, A.P. Young, D. Rao, A. Starr, S. Zhang, F.E. Spada, F.T. Parker, A. Hutten, G. Thomas, *J. Appl. Phys.* **73**(10), 5320 (1993); M. El-Hilo, K. O'Grady, *J. Appl. Phys.* **76**(10), 6811 (1994).
- [2] S. Mörup, *Phys. Rev. Lett.* **72**(20), 3278 (1994); S. Mörup, G. Christiansen, *J. Appl. Phys.* **73**(10), 6955 (1993); S. Mörup, *Hyperfine Int.* **60**, 959 (1990); S. Mörup, P.H. Christensen, B.S. Clausen, *J. Mag. Mag. Mat.* **68**, 160 (1987); S. Mörup, M.B. Madsen, J. Franck, J. Villadsen, C.J.W. Koch, *J. Mag. Mag. Mat.* **40**, 163 (1983); W-N. Wang, Z-S. Jiang and Y-W. Du, *J. Appl. Phys.*, **78**, 6679 (1995); S. Matsuo, T. Matsuura, I. Nishida and N. Tanaka, *Jpn. J. Appl. Phys.*, **33**, 3907 (1994).
- [3] R.J. Celotta, R. Gupta, R.E. Scholten and J.J. McClelland, *J. Appl. Phys.*, **79**, 6079 (1996).
- [4] J.F. Smyth, S. Schultz, D.R. Fredkin, D.P. Kern, S.A. Rishton, H. Schmid, M. Cali, and T.R. Koehler, *J. Appl. Phys.*, **69**, 5262 (1991); A.O. Adeyeye, G. Lauhoff, J.A.C. Bland, C. Daboo, D.G. Hasko, H. Ahmed, *Appl. Phys. Lett.* **70**(8), 1046 (1997); R.D. Gomez, M.C. Shih, R.M.H. New, R.F. Pease and R.L. White, *J. Appl. Phys.*, **80**, 342 (1996); S.Y. Chou, P.R. Krauss and L. Kong, *J. Appl. Phys.*, **79**, 6101 (1996).
- [5] S. S. Gidar, J. Shi, P.F. Hopkins, K.L. Campman, A.C. Gossard, D.D. Awschalom, A.D. Kent, and S. von Molnár, *Appl. Phys. Lett.*, **69**, 3269 (1996).

- [6] A. Fernandez, *IEEE-MAG* **32**, 4472 (1996).
- [7] H. Takeshita, Y. Suzuki, H. Akinaga, W. Mizutani, K. Tanaka, T. Katayama, and A. Itoh, *Appl. Phys. Lett.* **68**, 3040 (1996).
- [8] T. Shinjo and T. Ono, *J. Magn. Magn. Meter.*, **156**, 11 (1996).
- [9] A. Sugawara, Y. Haga and O. Nittono, *J. Magn. Magn. Meter.*, **156**, 151 (1996).
- [10] A. Sugawara, S.T. Coyle, G.G. Hembree and M.R. Scheinfein, *Appl. Phys. Lett.*, **70**, 1043 (1997); A. Sugawara and M.R. Scheinfein, *Phys. Rev. Lett.* (submitted).

### Magnetic Coupling In Self-Organized Narrow-Spaced Fe Nanowire Arrays

Fig.1 shows a bright field TEM image of the SiO(10 nm)/Fe wire array(13 nm)/ SiO(20 nm). The wires seen in dark contrast are formed near the ridges of the grating. The average projected width is 30 nm, hence, the real wire width is expected to be 42 nm on facets inclined by 45° from the film normal. The standard deviation of the wire width is 18 nm, approximately 40% of the nominal wire width. Some wires terminate where terraces are perpendicular to steps

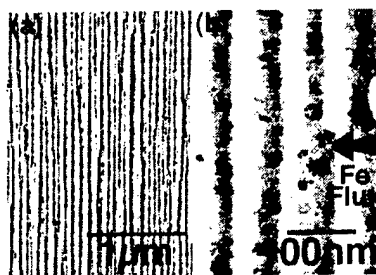


Fig.1 A bright field image of the SiO(10 nm)/Fe wire array(13 nm)/SiO(20 nm) deposited on the stepped NaCl(110). The wire width is 30 nm and the interwire spacing is 90 nm such that the gap between the wires is 60 nm.

accompanied by a miscut from the exact crystal axis. Most of the wires run through the approximately 3  $\mu\text{m}$  field of view shown in Fig. 1a. The average wire length calculated from the termination density is about 10  $\mu\text{m}$ . Though the array looks like a network of straight segments of a few  $\mu\text{m}$  long, low joint density is considered not to affect the magnetic behavior of the array. Since the wire aspect ratio is at least 200, strong shape anisotropy is expected. The corresponding electron diffraction patterns showed typical random polycrystalline features. No specific orientation relationship was observed between neighboring crystal grains.

Fig.2 shows longitudinal MOKE loops of the wire array recorded by applying an external field parallel (solid) and perpendicular (dotted) to the scattering plane, and rotating the specimens in the film plane by  $\theta^\circ$  with respect to the scattering plane. The angular dependence of the hysteresis loops is characteristic of uniaxial Stoner-Wohlfarth coherent rotation [1]. The specimen shows strong in-plane anisotropy when  $\theta=0^\circ$  and the coercivity is approximately 1.8 kOe. When the field is applied perpendicular to the wire, an external field of 3 kOe is not large enough to saturate the magnetization. When  $\theta=45^\circ$ , the switching field is minimum at half of the long-axis coercivity ( $H_c \sim 1.1 \text{ kOe}$ ), and a peak is seen in the magnetization component perpendicular to the wires (indicated by the arrow in Fig. 2). The open-circle loop observed for perpendicular magnetization when  $\theta=80^\circ$  also indicates that the whole wire array switches simultaneously [2]. The long-axis coercivity is still lower than that expected for an infinitely long uniaxial Fe. The coercive field decreases with decreasing wire thickness (e.g.,  $H_c \sim 1.3 \text{ kOe}$  when  $t = 4 \text{ nm}$ ). Domain wall motion is likely not occurring since significant transverse magnetization components are present during switching. Curling and buckling modes are known to effectively reduce the switching field in the case of uniaxial fine particle systems [3], but these processes are not accompanied by the perpendicular magnetization observed in the Kerr loops in Fig. 2.

The extent of the coupling in the wire array was studied using 3-D micromagnetics calculations. The code [4] is capable of calculating three-dimensional magnetization distributions for arbitrary shaped systems composed of ferromagnets, antiferromagnets and metals. The computed

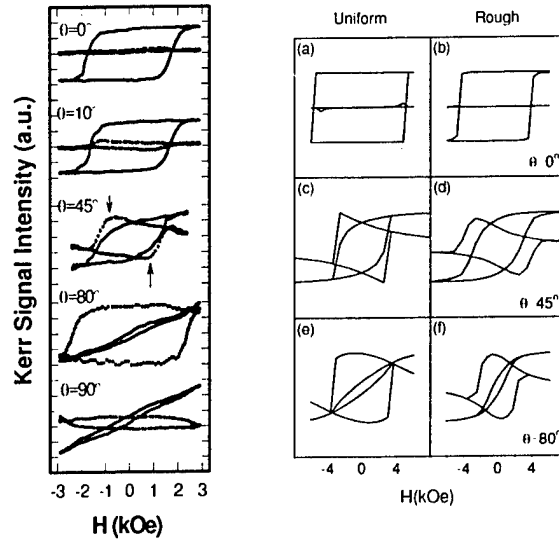


Fig. 2: (left) MOKI hysteresis loops acquired while rotating the specimen in the film plane.  $\theta$  denotes angle between the long-axis of the wire array and the scattering plane with the field applied in plane. Solid and dotted lines are magnetization components parallel and perpendicular to the field, respectively.

Fig. 3: (right) Hysteresis loops obtained from 3-D micromagnetics simulations for perfect (a,c,e) and rough (b,d,f) wire arrays oriented at  $0^\circ, 45^\circ$  and  $80^\circ$  to the field and scattering plane directions.

hysteresis loops shown in Fig.3 use bulk magnetic properties for Fe ( $A = 2.1 \mu\text{erg/cm}$ , and  $M_s = 1714 \text{ emu/cm}^3$ ). No magneto-crystalline anisotropy was included since the orientation of the grains along the wires was random. Periodic boundary conditions were employed for a tiled array of 7 individual wires. Hysteresis loops for perfect (left) and rough (right) wires oriented at  $0^\circ, 45^\circ$  and  $80^\circ$  from the field and Kerr scattering planes also indicate coherent rotation during switching. The broadened  $45^\circ$  loop is the result of pinning at edge defects due to the coarseness of the grid. The coercive field is larger in the computed loops as the result of the rectangular cross section for each individual wire.

The magnetization distribution can be directly examined by electron holography. Fig. 4 shows a reconstructed phase image and accompanying line profile from the wire array at zero field. The Fe nanowire contrast is slightly asymmetric as evidenced by the electrostatic phase shifts arising from the mean inner potential and seen as white in the image. The magnetic contribution to the phase profile manifests itself as the consistent phase increase as each wire is crossed giving rise to the net positive slope. The phase shift expected from each wire is consistent with that expected from an Fe wire with  $390 \text{ nm}^2$  cross section, in agreement the dimensions of the wire. The sign of the magnetic phase shift is the same for each wire indicating that the magnetization within each wire is aligned, i.e. the array is ferromagnetically coupled. This coupling is consistent with the Kerr measurements.

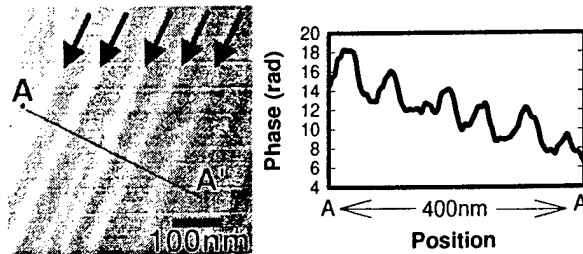


Fig.4: (left) An electron holographic phase image of the wire array reconstructed from an electron hologram, and (right) a line scan across A-A'.

- [1] E.C.Stoner, E.P. Wohlfarth, "A mechanism of magnetic hysteresis in heterogeneous alloys," *Philos. Trans. Roy. Soc. London* A240, p. 599, 1948.
- [2] M. Pruttin, *Thin Ferromagnetic Films* (Butterworths, Washington, 1964).
- [3] D. Craik, *Magnetism, Principles and Applications*, (John Wiley and Sons, Chichester, 1995).

### Quantitative Magnetometry Using Electron Holography: Fields Near Magnetic Force Microscope Tips

In Figs. 1-3, three sets of electron holograms have been reconstructed from three different sputter-coated MFM canilever tips. The nominal radii of the tips are 30 nm. Tip 1 (Fig. 1) and Tip 2 (Fig. 2) were initially magnetized along the axis of the tip while Tip 3 (Fig. 3) was initially magnetized transverse to the tip axis. The full scale widths of these images are 760 nm x 700 nm (Fig. 1a-c), 410 nm x 370 nm (Fig. 2a-c), and 270 nm x 250 nm (Fig. 3a-c). The parameters of the fitting procedure are shown in Table I. Each image is composed of an experimental amplitude image (a), an experimental phase image (b), an experimental phase image with the multipole expansion fit overlayed in the region in proximity to the tip (c), and a magnitude of the magnetic field in proximity to the tip (d). The phase images have been amplified (x4) such that phase contours span  $\pi/2$ .



Fig. 1a. Reconstructed amplitude - Tip 1. 760 nm x 700 nm full scale.

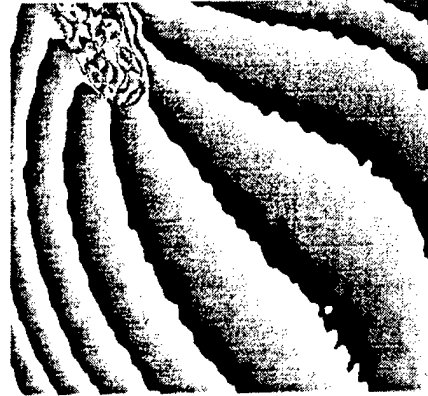


Fig. 1b. Amplified (x4) reconstructed phase - Tip 1.



Fig. 1c. Phase with the fit superimposed - Tip 1.

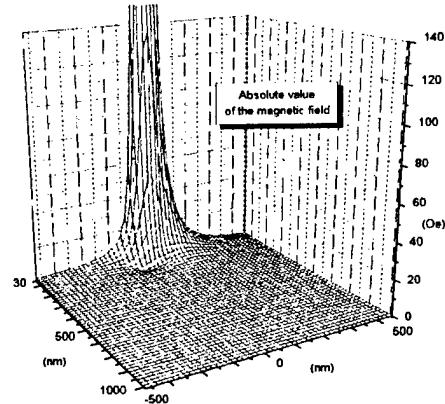


Fig. 1d. Reconstructed magnetic field - Tip 1.

The phase fits of the multipole expansion fields were produced using (6) and (7), and the clear agreement of the fit is evident in the overlays superimposed over the phase data. The reconstructed magnetic fields use only the monopole and dipole terms since the contribution from quadrupole terms (see Table I) were negligible on the distances comparable to the MFM tip radius. The field for the MFM tip shown in Fig. 4 falls from about 620 Oe at (near) the tip surface to 310 Oe 10 nm in front of the tip along the tip axis. The linear terms in the background that are left after a proper centering of the sideband (in Fourier space) result from flux originating from the magnetic material sputtered onto the large conical base supporting the tip. In our implementation, where the sources are separated by about 2 microns at the sample, the upper limit on the residual stray field from the tip base is estimated to be approximately 10 Oe.

The magnetic dipole moments in the plane of the holographic phase images are oriented at  $\theta = 135^\circ$ ,  $167^\circ$ , and  $-160^\circ$  respectively. The tips axes are along at  $\theta = 120^\circ$ ,  $134^\circ$ , and  $115^\circ$  respectively. Thus,

the dipole is oriented nearly along tip 1 ( $15^\circ$  off axis), close to the axis of tip 2 ( $33^\circ$  off axis), and perpendicular to the tip 3 ( $85^\circ$  off axis). This is consistent with the fact that during the magnetization process the tip axis is oriented about  $12^\circ$  away from the magnetic field axis. During magnetization, the physical tip axis is no longer aligned with the magnetic-field axis. Therefore, the measured dipole moment axis is actually quite close to that axis defined during the magnetization process. Some quantitative information about the tip orientation can be extracted from Figs. 1b, 1b, 1b: for the MFM tips with the dipole moment oriented along the tip axis (Fig. 1 and Fig. 1) black-white lines in the tip proximity run along the tip axis, while for the tip with a dipole moment oriented perpendicular to the tip axis (Fig. 3) black-white lines run obliquely to the tip axis.

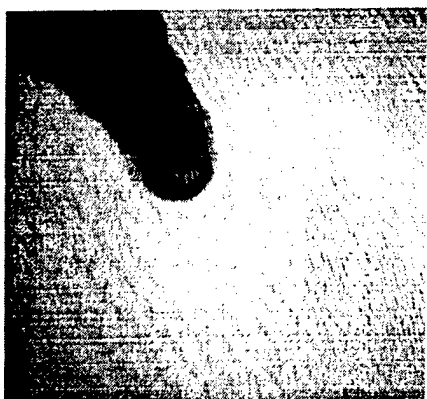


Fig. 2a. Reconstructed amplitude - Tip 2. 410 nm x 370 nm full scale.

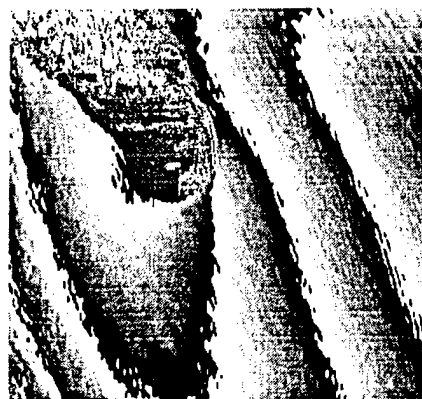


Fig. 2b. Amplified (x4) reconstructed phase - Tip 1



Fig. 2c. Phase with the fit superimposed - Tip 2.

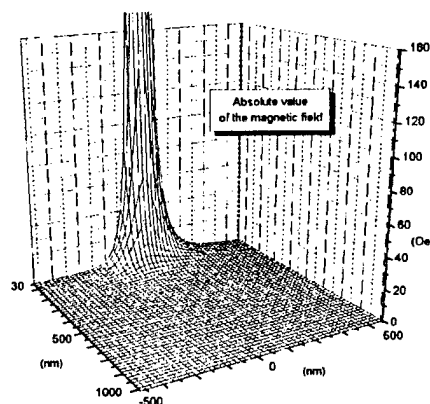


Fig. 2d. Reconstructed magnetic field - Tip 2.

The monopole term contributes mostly on length scales large compared to the tip radius, while dipole and quadrupole terms dominate the magnetic field in the region close to the tip. Fitting the phase in Figures 1b, 2b and 3b without quadrupole terms produces fits almost as good as those with quadrupole terms included, while the fits without monopole and/or dipole terms are completely unsatisfactory. Therefore, we conclude that the magnetic field in the region outside of the tip on the size scale of an MFM tip radius has simple monopole-dipole behavior with quadrupole terms important only in close proximity to the tip. We estimate error in the fit parameters as 4% for the monopole terms, 7% for the dipole terms, and 50% for the quadrupole terms. These errors are primarily due to the presence of the defocused image of the biprism wire producing Fresnel fringes at a distance of a tip radius from the tip surface. Since the coefficients multiply terms with different functional dependence to produce the field, the worst case total error in the magnetic field is approximately 6% at a distance of about 2 radii (about 60 nm) away from the tip. In the typical operating regime, we expect the quadrupole terms to contribute negligibly. We stress that any fields oriented along the direction of the electron beam are not detected, and as such, the error estimates are relevant for only those components of  $\underline{B}$  which are measurable.

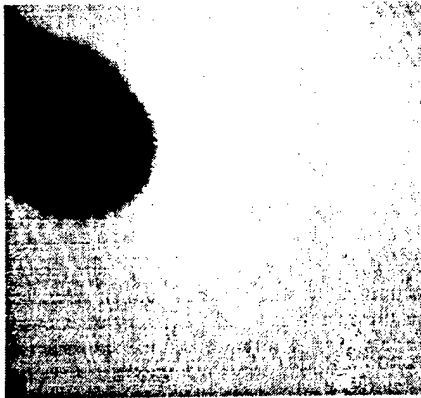


Fig. 3a. Reconstructed amplitude - Tip 3. 270 nm x 250 nm full scale.

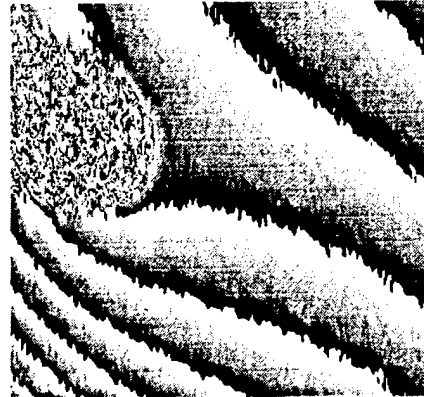


Fig. 3b. Amplified (x4) reconstructed phase - Tip 3.



Fig. 3c. Phase with the fit superimposed - Tip 3.

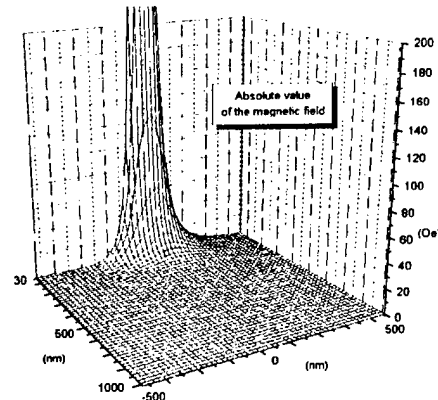


Fig. 3d. Reconstructed magnetic field - Tip 3.

Quantitatively, the fit is reliable enough to be able to reproduce some features seen on Fig. 1b: close to the MFM tip (to the left) a black-white line runs up to the tip surface and then goes down to the right, meaning that magnetic field along the tip axis changes its sign (and therefore is close to zero in that region). Fig. 1d shows the absolute value of the magnetic field and confirms that the fit reproduced that behavior. Although the resolution in this reconstruction is limited by the holographic fringe spacing to about 8 nm, our ultimate spatial resolution is limited to about 2 nm.

#### Magnetic Nanostructures Produced By Electron Beam Patterning Of Direct Write Transition Metal Fluoride Resists

There are several methods that are employed in the manufacture of small magnetic structures. The most common, optical lithography [1], is a well developed technology that has been widely used. Although optical lithography can provide very high throughput, the smallest size that can be created is limited by diffraction to about 0.2  $\mu\text{m}$ . The optical method involves exposure, processing, evaporation and lift-off. Conventional x-ray and electron beam lithography [2-6] increases the resolution of the pattern transfer process to nm length scales, but still requires post processing to remove the resist. The creation of large arrays of small structures can be accomplished through self-organization [7,8]. This method allows for the fast manufacture of nm structures over large (macroscopic) areas. Although self-organization produces a very rich variety of structures, there is little control over individual particle shapes, ordering in arrays and length scales. Self developing resist x-ray and electron beam lithography [9-11] is a compromise among throughput, resolution and chemical reactivity during processing. The method is very flexible for the *in-situ* manufacture of nano-structures yet the throughput is limited by resist sensitivity and serial processing. However, it is ideally suited for the generation of the small structures needed to examine fundamental

magnetic properties at nanometer length scales [7,8]. Na, Li, Mg and Al metal halides self-developing resists [9-11] have been used successfully to prepare nanometer metal structures in an electron microscope. However, there appears to have been no successful attempts at the manufacture of nanometer magnetic structures using direct writing in self-developing resists.

We have tested several transition metal halide compounds for suitability as self-developing resists for the manufacture of magnetic nanostructures. Of the eight transition metal halides tested ( $\text{FeF}_2$ ,  $\text{FeF}_3$ ,  $\text{FeCl}_2$ ,  $\text{FeCl}_3$ ,  $\text{CoF}_2$ ,  $\text{CoF}_3$ ,  $\text{CoCl}_3$  and  $\text{NiF}_2$ ) only  $\text{FeF}_2$  and  $\text{CoF}_2$  are sensitive enough to the electron beam. In this article we report on *in-situ* experiments designed to produce controlled, nanometer sized magnetic structures using  $\text{FeF}_2$  and  $\text{CoF}_2$  electron beam sensitive resists. The resist properties are characterized using electron energy loss spectroscopy.

Both the nanopatterning and nanocharacterization experiments were performed in a Vacuum Generators HB501 Scanning Transmission Electron Microscope. This microscope is equipped with a Gatan<sup>®</sup> Parallel Electron Energy Loss Spectrometer (PEELS) and an EmiSpec Vision<sup>®</sup> computer controlled data acquisition system [16]. Ultimately, this microscope can focus 1 nA of 100 keV electrons into a beam  $\frac{1}{2}$  nm in diameter. Digitized patterns were transferred into the halide films by controlling the 100 keV electron beam with a computer while monitoring the electron dose. The computer controlled National Instruments<sup>®</sup> AT-MIO-16E-2 multichannel digital-to-analog converter can scan the electron beam at rates of up to 400 kHz. Our custom scanning software allows virtually any pattern to be transferred into the resist. Fig. 1 shows a resolution test pattern that has been transferred into the  $\text{CoF}_2$  resist. This high resolution annular dark field (ADF) image shows the  $\text{CoF}_2$  as gray, and the coalesced Co metal as black. A line scan taken across a single Co line at right has a width (FWHM) of approximately 5 nm. This is not the resolution limit of the resist but rather the linewidth selected for this exposure. There are some proximity effects in lines exposed close to one-another. The boxes at the top of Fig. 1 have incomplete exposure of the lines that comprise the left side of each box. This is because the pattern was written from left to right. The exposed right side of the box immediately to the left of a given box decreased the resist sensitivity local to that exposed line. This proximity effect can be seen in the center of the exposed spoke pattern in the wheel at left in Fig. 1, and as roughness in the smallest lines written close together at the top of the array of lines at the bottom of Fig. 1. In all other cases, the lines are continuous, even and clearly resolved.

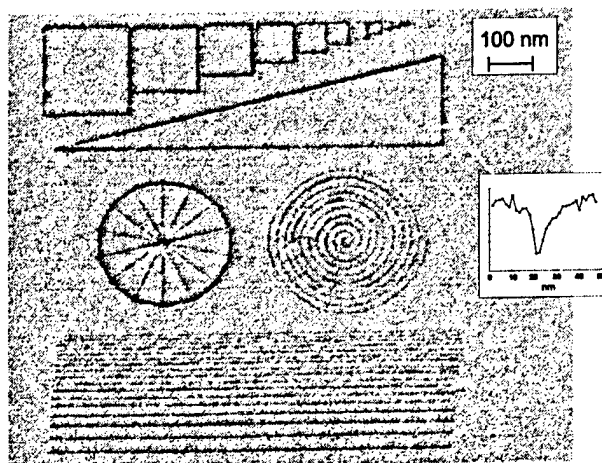
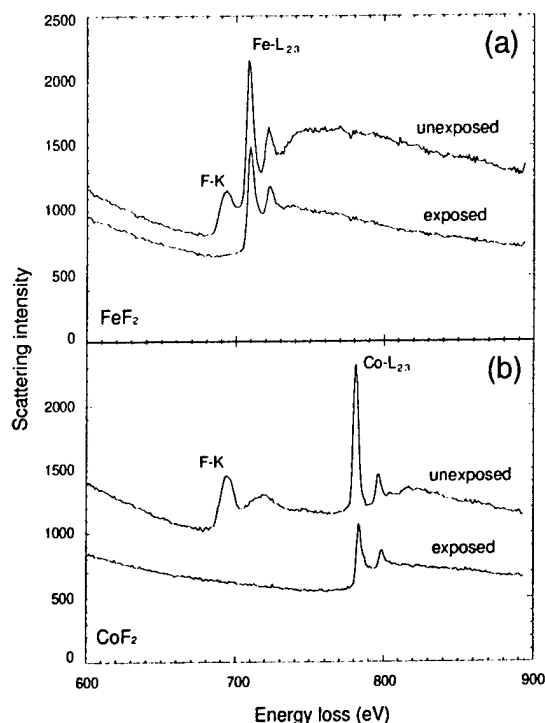


Fig. 1 : High angle annular dark field image of a resolution test pattern transferred into  $\text{CoF}_2$  using 100 keV electrons in STEM. The gray areas are  $\text{CoF}_2$ , the black areas are metallic Co. The resolution here is limited by the scan rather than the resist to about 5 nm. Proximity resist effects can be observed (see text).

The self-development process was qualitatively characterized using bright and dark field imaging, and quantitatively characterized with Electron Energy Loss Spectroscopy (EELS). EELS spectra can provide valuable information in both low loss (0  $\rightarrow$  100 eV) and high or core loss (100  $\rightarrow$  1000 eV) energy loss ranges. The low loss EELS spectra can be used to investigate changes in the electronic properties during irradiation. Changes in the composition of the compound during electron irradiation can be determined by monitoring the core loss excitation spectra (scattering cross section) during the electron exposure process. Figs. 2a (2b) illustrate typical EELS spectra for  $\text{FeF}_2$  ( $\text{CoF}_2$ ) taken from both exposed and



unexposed areas in the energy region surrounding the fluorine K (685 eV) excitation and the Co (779 eV) and Fe (708 eV)  $L_{2,3}$  excitations. It is clear from the spectra shown in Fig. 2 that in the exposed areas fluorine was completely removed, while little iron/cobalt mass loss is observed.



**Fig. 2 :** Electron energy loss spectra in the energy region surrounding the fluorine K-edge (685 eV), the Co (779 eV) and Fe (708 eV)  $L_{2,3}$  excitations for (a) FeF<sub>2</sub> and (b) CoF<sub>2</sub> before and after electron beam irradiation.

We separate the analysis of the self development process in electron beam exposed regions of FeF<sub>2</sub> and CoF<sub>2</sub> into two categories: (a) An electron-beam/resist interaction occurs in exposed areas where F is liberated and the transition metal coalesces. This interaction governs the most basic properties of the resist such as its sensitivity and any thickness dependent effects. (b) In the vicinity of the exposed areas, diffusion of iron/cobalt, redistribution of the halide, and proximity effects due to high angle electron scattering and secondary electron creation reduce the sensitivity of the resist.

The sensitivity of CoF<sub>2</sub> to electron exposure can be measured by monitoring the relative concentrations of Co and F during the irradiation process. Typically, a small region of the sample surface is scanned with the electron beam. The current is monitored as a function of time so that the total electron dose can be established. EELS spectra are accumulated frame by frame as a function of time (dose). One such time series acquired for a 20 nm thick CoF<sub>2</sub> film is shown in Fig. 3. EELS spectra are shown near the F-K and Co- $L_{2,3}$  edges for the five electron doses shown at left. The relative concentration of F can be determined by fitting ( $I = AE^{-f}$ ) the EELS spectra before the edge ( $E < 675$  eV), subtracting this background, and integrating for a fixed energy window under the excitation peak [17]. The relative concentration of F is shown in Fig. 3.

A series of spectra like that shown in Fig. 3 illustrates how the dose response can be extracted from EELS spectra. Using EmiSpec Vision<sup>®</sup> image acquisition and processing software, such EELS spectra can be collected in real time, the background subtracted, and the suitable energy window

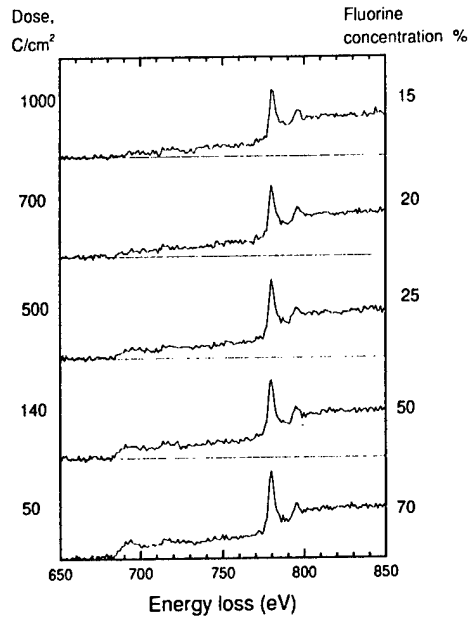


**Fig. 3 :** Dose response EELS spectra in the core excitation region for  $\text{CoF}_2$ . The decrease in the F K-edge intensity near 690 eV energy loss is evident as a function of the dose indicated at left. The relative F concentration is shown at right.

integrated, yielding the elemental concentration as a function of dose. The four dose response curves in Fig. 4 show both the Co and F concentrations as functions of time (dose) for four different exposed areas,  $48 \times 48 \text{ nm}^2$ ,  $70 \times 70 \text{ nm}^2$ ,  $140 \times 140 \text{ nm}^2$  and  $190 \times 190 \text{ nm}^2$  in Figs. 4 a-d respectively. The different size areas were selected in order to explore the dose rate dependence during the exposure process. Each experimental point in Fig. 4 indicated by a solid symbol is extracted from an EELS spectrum similar to those shown in Fig. 3. The time scale in Fig. 4 was normalized to give a constant current of 100 nA on the condenser aperture (corresponding to 140 pA at the specimen) using a series of current measurements, each taken simultaneously with the EELS spectral series. This procedure is required in order to correct for the beam current instabilities which can be as high as 70% over a period of several minutes. Variations in electron beam current (dose) were also monitored by measuring the area under the carbon K-edge excitation peak in each EELS spectrum. Since each transition metal halide film was deposited on a thin amorphous C substrate, this signal should remain constant in time unless carbon builds up on the specimen during exposure. Bright and dark field STEM images and EELS spectra were inspected both before and after each exposure to ensure that no appreciable carbon buildup occurred.

The image shown in Fig. 1 suggests that  $\text{CoF}_2$  resist resolution is not limited by the polycrystallite size. Unlike some other self-developing electron sensitive resists (e.g.  $\text{AlF}_3$ ) [9], the coalescent metal in  $\text{CoF}_2$  and  $\text{FeF}_2$  resists does not seem to form clusters. Rather it is distributed uniformly across exposed areas. However, the proximity effect can limit the resist resolution.  $\text{CoF}_2$  and  $\text{FeF}_2$  may become less sensitive to the electron beam in the vicinity of exposed areas since some transition metal can diffuse out of the locally exposed areas, and cap the resist layers below. EELS spectrum taken from an exposed point (limited by the resist resolution rather than by the electron beam size) shows a somewhat lower concentration of the Fe/Co than a similar spectrum taken from an unexposed area. This loss of the transition metal in extremely small areas supports the explanation that some of the transition metal may spill over onto adjacent areas during exposure.

- [1] W. Van Roy, E. L. Carpi, M. Van Hove, A. Van Esch, R. Bogaerts, J. De Boeck, G. Borghs, J. Magn. Mater., 121, 197 (1993).
- [2] P. R. Krauss and S. Y. Chou, J. Vac. Sci. Technol. B13, 2850, (1995).
- [3] S. McVitie and J. N. Chapman, IEEE MAG-24, 1778, (1988).
- [4] J. F. Smyth, S. Schultz, D. Kern, H. Schmid and Dennis Yea, J. Appl. Phys., 63, 4237, (1988).

- [5] S. J. Hefferman, J. N. Chapman, S. McVitie, J. Magn. Magn. Mater., 95, 76, (1991).
- [6] A. B. Johnston, J. N. Chapman, B. Khanshepour and C. D. W. Wilkinson, J. Phys., 29, 1419, (1996).
- [7] A. Sugawara, T. Coyle, G. G. Hembree and M. R. Scheinfein, Appl. Phys. Lett., 70, 1043, (1997).
- [8] A. Sugawara and M. R. Scheinfein, Phys. Rev. B56, in-press, (1997).
- [9] A. Muray, M. Scheinfein, M. Isaacson, J. Vac. Sci. Technol. B3, 367, (1985).
- [10] Qun Dou, D. W. Lynch, Surf. Sci. 219, 623, (1989).
- [11] Heiji Watanabe, Jun-ichi Fujita, Yukinori Ochiai, Shinji Matsui and Masakazu Ichikawa, Jpn. J. Appl. Phys., 34, 6950, (1995).
- [12] A. Tonamura, Electron Holography (Springer Verlag, Berlin, 1993).
- [13] L. Reimer, Transmission Electron Microscopy (Springer Verlag, Berlin, 1993).
- [14] R. D. Mathis Company, Thin film evaporation source reference (Lebow Co, Gioletta, 1987).
- [15] R. C. Weast (Ed.), CRC Handbook of Chemistry and Physics (CRC Press, Boca Raton, 1980).
- [16] Thanks to scientists at EmiSpec Corporation for help with custom data acquisition and control software.
- [17] R.F. Egerton, Electron Energy Loss Spectroscopy in the Electron Microscope ( Plenum Press, New York, 1986).

### Defect Induced Lowering Of Activation Energies At Step Bands In Co/Cu(100)

Experiments on the growth and magnetic properties of the Co/Cu(100) system often produce disparate results. STM studies of stepped Cu surfaces demonstrate that adatoms and kinks at steps are quite mobile.<sup>1,2</sup> Mobility at steps has also been studied theoretically using the embedded atom method.<sup>3,4</sup> It was suggested<sup>5</sup> that Fe islands which decorate step edges on Cu(111) relax the nearby Cu lattice, and decrease the activation energy for Cu diffusion along steps. This drives the migration of Cu and produces single-layer deep pits in Cu terraces. Large rectangular pits have been observed in Co/Cu(100) systems which have been annealed following room temperature (RT) growth.<sup>6,7</sup> These pits, from which Cu was believed to have migrated and covered the Co surface, typically formed near steps. An experimental study<sup>8</sup> of the growth and magnetic properties of Co/Cu(100) performed in our laboratory produced two characteristic growth morphologies for films grown under apparently identical conditions. The first growth mode is characterized by the formation of islands on terraces with little interaction with steps. The second growth mode is characterized by a lower island density and a high degree of interaction with and restructuring of step edges. Combinations of these two modes have been observed in different films. Kinetic Monte Carlo simulations have been performed for Co growth on Cu(100) in the presence of steps in an attempt to characterize these growth modes and the resulting film morphologies.<sup>9</sup> The first growth mode has been reproduced reasonably well. Enhanced roughening of step edges was observed in simulations, however, the length scale of features was smaller than the experimental results. The large scale etching features and pits characteristic of the second growth mode were not reproduced in the Monte Carlo simulations. This was attributed to the simple model of activation energies for processes at steps.<sup>9</sup> The kinetic Monte Carlo growth simulations of Co on Cu(100) in the presence of step bands described here have been performed in order to characterize the striking morphological growth features found experimentally.

In the simulations, the Cu substrate (template) was discretized into a region 100 by 100 atoms square (along  $\langle 100 \rangle$ , 36x36 nm) and 14 layers deep (2.5 nm) with periodic boundary conditions. The region included one or two trenches with steps oriented along either  $\langle 100 \rangle$  or  $\langle 110 \rangle$ . The trenches, which were intended to simulate step bands, were 7 layers deep. The terrace width of each layer (step down) was four ( $\langle 100 \rangle$ ) or three ( $\langle 110 \rangle$ ) atomic rows. The simulations assumed an Arrhenius-type barrier model,<sup>10</sup> where the transition rate is  $r = R_0 \exp(-\epsilon/kT)$ . Activation energies ( $\epsilon$ ) were set proportional to beginning and ending bond energies according to  $\epsilon = A/(1+|\Delta E|/B) + H(\Delta E)$ . The constant A is the energy barrier for hopping to a state of the same energy, and was set to approximate the experimental activation energy for Co adatom diffusion on Co(100).<sup>11</sup> H is the Heaviside function, T is the substrate temperature, k is Boltzmann's constant, and B is a constant which reduces the barrier somewhat when the final state is more tightly bound than the initial state. A and B were each set to 0.5 eV. The attempt frequency ( $R_0$ ) for the transition rate was  $2 k T/h$ , where h is Plank's constant. The Co-Co bond energy was 0.271 eV/nearest-neighbor (NN) and 0.004 eV/next-NN (NNN).<sup>12</sup> The Cu-Cu bond energy was 0.190 eV/NN and 0.003 eV/NNN.<sup>12</sup> The Co-Cu bond energy was 0.2305 eV/NN and 0.0035 eV/NNN.<sup>9</sup> In order to compare directly with experimental observations, results are presented for one monolayer (ML, 1 ML =  $1.53 \times 10^{15}$  atoms/cm<sup>2</sup>) of Co deposited at 275 K and subsequently annealed at 350 K for 30 seconds.

Experimental results were obtained from Co growth on bulk single crystal Cu(100) samples.<sup>8</sup> Cu substrates were cleaned by repeated Ar<sup>+</sup> ion sputter and anneal (600 C) cycles. Co was grown by electron-

beam evaporation at pressures  $<5 \times 10^{-10}$  mbar. Samples were transferred *in-situ* into an ultrahigh vacuum scanning transmission electron microscope (STEM) for nanometer resolution secondary electron imaging.<sup>13</sup>

In Fig. 1, characteristic samples of high resolution UHV secondary electron micrographs of the first (a) and second (b) growth modes are shown. The  $\langle 100 \rangle$  direction is denoted by the inserted arrow. Gray scale images have been rendered in three dimensions. Both films consist of 0.2 ML of Co grown at 300 K on Cu(100) at 0.15 ML/min. Since restructuring is observed for such small amounts of deposit (Fig. 1(b)), we believe that the relief of strain in the Co film may not be a significant driving force in the early stages of growth. Restructuring takes the form of facets with low energy  $\langle 110 \rangle$  steps, suggesting that the lowering of free energy is the driving force. The large scale faceting and step edge restructuring shown in Fig. 1(b) was not well reproduced by kinetic Monte Carlo simulations in the presence of single atom high steps,<sup>9</sup> although when annealed simulated structures exhibit morphologies remarkably similar to those produced during growth experiments. Experimental and computed morphologies for growth near step bands are shown in Fig. 2. Brighter areas are higher. Simulations are in the left column (Fig. 2(a, c)) and SEM results at right (Fig. 2(b, d)). White arrows inserted into the images denote the  $\langle 100 \rangle$  direction. The simulations include 1.0 ML of Co grown near step bands aligned along  $\langle 100 \rangle$  (Fig. 2(a)) and  $\langle 110 \rangle$  (Fig. 2(c)) followed by a 30 second anneal at 350 K. No differentiation is made between Co and Cu atoms. The SEM results also include growths of 1.0 ML with step bands aligned close to  $\langle 100 \rangle$  (Fig. 2(b)) and  $\langle 110 \rangle$  (Fig. 2(d)), however, without annealing.

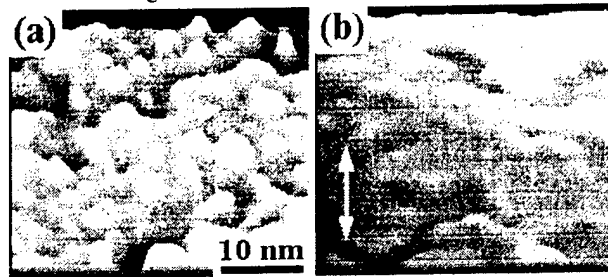


FIG. 1. Secondary electron micrographs of 0.2 ML Co/Cu(100) grown at 300 K, which show examples of the first (a) and the second (b) growth modes described in the text. White arrows denote the  $\langle 100 \rangle$  direction. Gray scale images have been rendered in three dimensions. The scale is the same for both images.

The simulation results (Fig. 2(a, c)) contain large rectangular vacancies from which Cu has migrated. Before annealing these were exposed regions of the Cu substrate. The experimental results (Fig. 2(b, d)) contain similar features, although the length scales are slightly larger. Adjacent to the  $\langle 100 \rangle$  step bands in Fig. 2(a) are long connected vacancy regions with  $\langle 110 \rangle$  facets separated from the step bands by Co islands (see e.g. region around the arrow). These regions are within the adatom random walk distance of the step band. The Co island density during growth was low in this region, leaving exposed Cu after the growth. This Cu was then free to migrate during the anneal. Co which migrated over the step from this denuded region formed islands at the step bands. Regions of similar morphology can be seen in our SEM data along  $\langle 100 \rangle$  step bands. Such a region surrounds the arrow in Fig. 2(b). The large rectangular vacancies in the simulation terraces were formed by incomplete Co coverage, from which Cu migrated during annealing. Similar structures were also observed in the SEM data, as can be seen in the terrace of Fig. 2(d). Inclusions into the  $\langle 110 \rangle$  step bands (Fig. 2(c, d)) are more rectangular than those into  $\langle 100 \rangle$  step bands, and are not separated from the step band by Co islands.

The top level atomic species for the simulations before (left) and after (right) annealing are shown in Fig. 3 for  $\langle 100 \rangle$  (top) and  $\langle 110 \rangle$  (bottom) step bands. Black squares are Co atoms and white squares are Cu atoms. Figure 3(b, d) are the same post-annealing simulation results shown in Fig. 2(a, c). Cu has clearly migrated from exposed areas to cover and/or surround the Co islands. This migration has occurred without invoking a direct exchange process.<sup>14</sup> Very few Co islands are exposed (on top) after the anneal, however, a large number of Co atoms along steps are exposed. The shapes of Co islands are now much less rectangular and closer to those obtained experimentally from the first growth mode. These islands are now surrounded by Cu (i.e. part of a terrace). Interdiffusion has obviously increased dramatically during annealing.

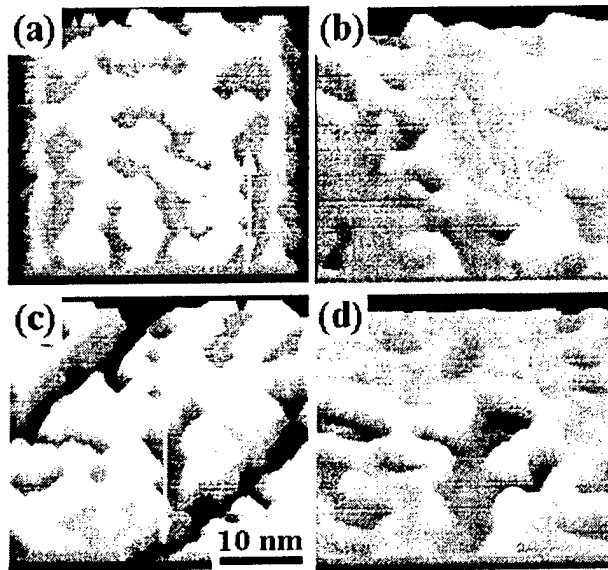


FIG. 2. Simulation results (a, c) and SEM results (b, d) for 1 ML Co/Cu(100) grown at RT near  $\langle 100 \rangle$  (a, b) and  $\langle 110 \rangle$  (c, d) step bands. The simulations were annealed at 350 K for 30 seconds. Bright regions are higher. White arrows denote the  $\langle 100 \rangle$  direction. Gray scale images have been rendered in three dimensions. The scale is the same for all images.

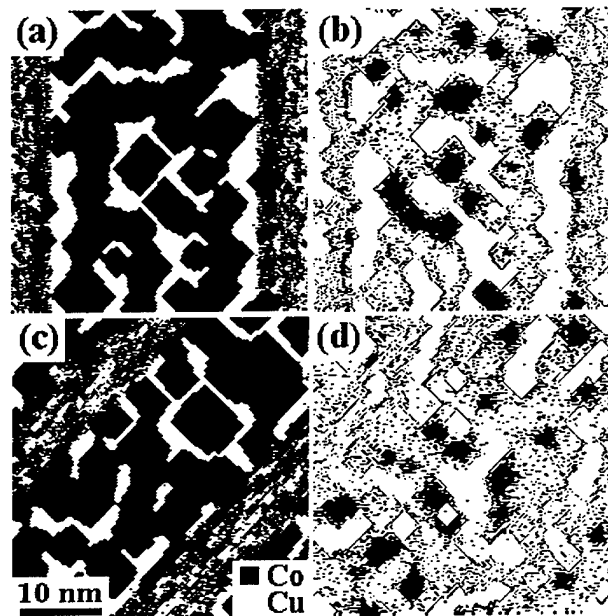


FIG. 3. Simulation results for 1 ML Co/Cu(100) before (a, c) and after (b, d) annealing. The atomic species of the topmost exposed atom is shown. Black squares are Co atoms and white squares are Cu atoms.

The activation energies for processes at steps (bands) may be lower than the simple model predicts. This could cause the discrepancy between the simulations of RT growth and the experimental morphologies. Transition rates in the model are dependent on attempt frequency, temperature, and the parameters A and B. A change in any of these parameters will change the rate at which processes occur. Increasing T, as in our annealing simulations, is equivalent to increasing  $R_0$  or decreasing  $\epsilon$ . The ratios of these parameters, then, affect the growth dynamics as much as their magnitudes. The exposed Cu atoms are apparently close to an activation energy threshold since a small increase in temperature (75 K) dramatically increases their mobility. One possible method to improve the simulations is to change the model for activation energy ( $\epsilon$ ). Lowering  $\epsilon$  for processes whose beginning bond energies are smaller should increase

the rate for processes on atoms with lower coordination, such as at steps. We have chosen not to search the vast parameter space for combinations which produce the experimentally observed morphology. Rather, we have approximated the increased mobility of Cu atoms at defects by annealing. This produced morphologies remarkably similar to those observed in SEM data.

SEM results (not shown) reveal a continuum of combinations of the first and second growth modes. We have been unable to correlate contamination levels with growth mode, although a surfactant-like contaminant effect cannot be ruled out. The range of growth modes could instead be due to variations in defect densities. The width and density of step bands was not constant between different samples used in our growth experiments. Agglomerations of vacancies were evident in some samples, suggesting the presence of a high density of defects that we could not detect. Samples with higher defect densities would exhibit an increased proportion of the second growth mode. Differences in defect density and the resultant changes in activation energies, then, could account for the differences in observed morphology. Lowered activation energies for Cu atoms could be the result of relaxation near defects, or changes in the strain field caused by nearby Co atoms.

- 1 F. Thibaudau and J. Cousty, *Ultramicroscopy* 42-44, 511 (1991).
- 2 M. Giesen, et al., *J. Vac. Sci. Technol. A* 10, 2597 (1992).
- 3 Per Stoltze, *J. Phys. Condens. Matter* 6, 9495 (1994).
- 4 Z.-J. Tian and T. S. Rahman, *Phys. Rev. B* 47, 9751 (1993).
- 5 M. Klaua, et al., *Surf. Sci.* 381, 106 (1997).
- 6 A. K. Schmid, et al., *Phys. Rev. B* 48, 2855 (1993).
- 7 M. Giesen, F. Schmitz, and H. Ibach, *Surf. Sci.* 336, 269 (1995).
- 8 S. T. Coyle, G. G. Hembree, and M. R. Scheinfein, *J. Vac. Sci. Technol. A* 15, 1785 (1997).
- 9 S. T. Coyle, J. L. Blue, and M. R. Scheinfein, *J. Vac. Sci. Technol.* (submitted).
- 10 James L. Blue, to be published.
- 11 M. T. Kief and W. F. Egelhoff Jr., *Phys. Rev. B* 47, 10785 (1992).
- 12 L. Z. Mezey and J. Gibber, *Jpn. J. Appl. Phys.* 21, 1569 (1982).
- 13 K. R. Heim, et al., *J. Appl. Phys.* 74, 7422 (1993).
- 14 For e.g., see P. J. Feibelman, *Surf. Sci.* 299, 426 (1994).

#### Co on Stepped Cu(100) Surfaces: A Comparison of Experimental Data with Growth Simulations.

Co/Cu(100) has become an important system in the study of thin film magnetism. Face centered cubic (fcc) Co has a small lattice mismatch with fcc Cu(100) and will grow pseudomorphically. Cu surfaces vicinal to  $\langle 100 \rangle$  allow Co to be grown with a regularly spaced array of  $\langle 110 \rangle$  steps and  $\langle 100 \rangle$  terraces<sup>1</sup>. Bulk Co and Cu are considered immiscible below  $\sim 900$  K, however, Co and Cu have been reported to form an alloy<sup>2</sup> above  $\sim 450$  K, and interdiffusion during growth above 0 C has been suggested<sup>3</sup>. Co/Cu multilayers exhibit giant magnetoresistance, therefore, understanding the Co/Cu interface is important.

We have performed a study of the growth and magnetic properties of Co/Cu(100) at room temperature (RT)<sup>4</sup> in an attempt to understand how morphology and defects affect film growth and magnetic properties. We described two growth modes: island growth and exchange mediated growth, and reported a continuum of combinations of these two modes in different films. Island growth mode is characterized by the formation of islands on terraces and little interaction with steps, while exchange mediated growth is characterized by little island formation and a high degree of roughening of step edges. A Co adatom moves along a Cu step until it is pinned by a kink, thereby lowering the free energy. Because Co has a higher free energy<sup>5, 6</sup> than Cu, the configurational energy may be lowered when Cu atoms move to surround the Co atom. This results in a restructuring of the step edge resulting in faceting along the lower energy  $\langle 110 \rangle$  directions. Incorporation into a  $\langle 110 \rangle$  step is much more energetically favorable than incorporation into a  $\langle 100 \rangle$  step<sup>4</sup>, and this difference may contribute to the difference between island and exchange growth.

We have performed growth simulations using J. L. Blue's kinetic Monte Carlo simulation program<sup>7</sup> in order to understand the various growth modes encountered during growth experiments. We are also interested in exploring the effects of growth parameters on interdiffusion. Interdiffusion and its affect on magnetic properties at the Co-Cu interface is of central importance in understanding GMR and other

thin-film magnetic properties. We attempt to describe the sharpness and character of the interface, and its dependence on parameters such as growth temperature, growth rate, and terrace width.

Kinetic Monte Carlo simulations of the growth of Co on Cu(100) in the presence of step edges were performed. Prior to deposition the Cu substrate was 100 by 100 atoms (square), 6 layers deep, and included one or two terraces with steps oriented along either  $\langle 100 \rangle$  or  $\langle 110 \rangle$ . Simulations were also performed at intermediate step orientations in 5 degree increments. Deposition of Co was simulated at rates of 0.15 ML/min (slow) and 1.5 ML/min (fast), and for coverages between 0.05 ML and 0.50 ML in increments of 0.05 ML. Initial kink densities of 0 and 0.15 kinks per site along the step edges were selected. Substrate temperature during growth was varied from 275 K to 325 K to investigate the effect of temperature on morphology and interdiffusion for RT deposition. Five different simulations were performed with different random number seeds, and the quantitative measures were averaged.

The shape, size and density of the islands is essentially the same for simulations with the same deposition rate, independent of step orientation. The islands are approximately rectangular with edges along  $\langle 110 \rangle$  directions. Between 30 and 60 percent of the adatoms were captured by terraces, with more being captured during slower growth. Mean island area increases approximately linearly with increasing coverage until approximately 0.4 ML have been deposited, where island capture by steps and the agglomeration of very large islands becomes significant. Island density initially increased, then above 0.15 ML was fairly constant as a function of deposition. Both island density and mean island size were essentially unaffected by initial kink density. Interface width increases approximately linearly with coverage due to the deposition of adatoms and the nucleation of islands. Films grown at 1.5 ML/min have a slightly larger interface width than films grown at 0.15 ML/min due to their higher nucleation density. Interface width is essentially unaffected by initial kink density. Step width of  $\langle 100 \rangle$  and  $\langle 110 \rangle$  steps are approximately the same and are unaffected by growth rate and initial kink density within the statistical uncertainty. The largest increase in step width occurs between 0 and 0.05 ML of Co deposit. A small amount of Co arriving at a step edge apparently induces a significant amount of restructuring, after which further Co deposition causes only incremental restructuring of the step edge. The addition of initial kinks to the steps did not affect the interdiffusion width. Slow growth produced significantly more interdiffusion than fast growth, with the effect being more pronounced on  $\langle 100 \rangle$  steps compared to  $\langle 110 \rangle$  steps.

Simulations were also performed on terraces without Co deposition.  $\langle 100 \rangle$  steps formed  $\langle 110 \rangle$  facets similar to those formed during the Co deposition simulations, however, the step width was approximately half as large for the equivalent amount of simulation time.  $\langle 110 \rangle$  steps formed rectangular inclusions only during simulations that included a nonzero initial kink density. These inclusions were much less deep and wider than those simulated during Co deposition. Co deposition is therefore enhancing the roughening of the step edges.

Monte Carlo growth simulations reproduced many features of the island growth mode observed during growth experiments. The faceting of step edges is reproduced, however, the length scale of the facets is smaller in the simulations than in the growth experiments. During growth experiments step bands tend to form arcs between pinning sites, therefore, perfect  $\langle 100 \rangle$  or  $\langle 110 \rangle$  step edges are not the norm. We do find, however, many small lengths of step edges which are aligned nearly along crystallographic axes. These segments can be compared to simulation results in order to test the efficacy of the simulations. Fig. 1 includes SEM micrographs (left) and simulation results (right) of RT growth of 0.1, 0.2, and 0.4 ML, all at 0.15 ML/min. White arrows in the micrographs denote the  $\langle 100 \rangle$  direction. The step edge parallel to the arrow in Fig. 1(a) shows large scale faceting, on the order of 5-7 nm. Faceting of the step edge in the 0.10 ML simulation (Fig. 1(b)) appears similar although the size of the facets is slightly smaller (2-3 nm). In Fig. 1(d), an island has grown into the step edge in the middle of the right step which produces a feature similar to the facets seen in Fig. 1(c). This could conceivably account for the larger scale faceting observed in the micrographs, however, the islands do not appear to be large enough or rectangular enough to have caused the faceting in either Fig. 1(a) or (c). The irregular shape of the islands in the micrographs is not reproduced by the shape of the islands in the simulations. STM images<sup>9, 11-13</sup> show islands with similar shapes to those in Fig. 1(a, c, e). Relaxation likely occurs at the edge of islands and at steps. This process is omitted in our simulation model. Addition of this process would change the kinetics and might account for the discrepancy in island shapes.

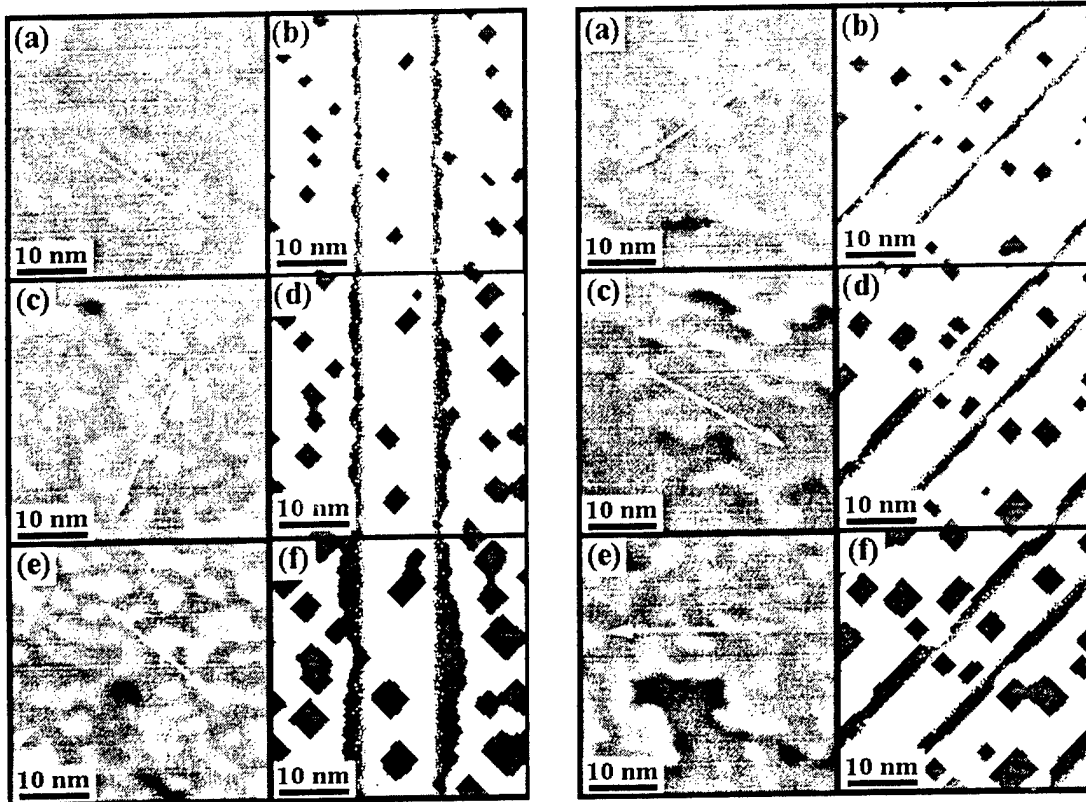


FIG. 1 (Left): Comparison of SEM micrographs with simulation results for 0.1 ML (a, b), 0.2 ML (c, d) and 0.4 ML (e, f) depositions with step edges aligned along  $\langle 100 \rangle$ . Arrows denote  $\langle 100 \rangle$  directions. Growth rate was 0.15 ML/min for all.

FIG. 2 (Right): Comparison of SEM micrographs with simulation results for 0.1 ML (a, b), 0.2 ML (c, d) and 0.35 ML (e, f) depositions with step edges aligned along  $\langle 110 \rangle$ . Arrows denote  $\langle 110 \rangle$  directions. Growth rate was 0.15 ML/min for all.

Fig. 2 includes SEM micrographs (left) and simulation results (right) of growth of 0.1, 0.2, and 0.35 ML, also at 0.15 ML/min. The step edges in the simulations have formed approximately rectangular inclusions, usually in a region with islands close to the step. Areas without these inclusions tend to have a region denuded of islands near the terrace. The missing Co atoms are obviously in the islands near the inclusions. Such a region appears to exist in the vicinity of the arrow in Fig. 2(a), however, the inclusions are much deeper than those in (b). This suggests that an exchange mechanism may be contributing to the restructuring of the step edges. As deposition increases (Fig. 2(c-f)) the size of the inclusions increase, both in the growth and simulation experiments, however, produce some striking step edge morphologies, as seen in Fig. 2(c) and (e). These features were not reproduced in the simulations, except perhaps for higher deposition where island capture by the terrace is evidenced. This observation suggests, again, that some exchange process is at work, or perhaps Cu has migrated from this area, thereby forming the inclusion. Clearly the kinetics at steps are more complicated than the barrier model in our simulation produces. The surface in Fig. 2(c) is an example of the exchange growth mode described previously<sup>4</sup>. Islands are quite rare and step edge restructuring tends to be more pronounced than in surfaces exhibiting the island growth mode. This morphology has not been reproduced in the corresponding simulations.

Interdiffusion is essentially complete by 0.20 ML deposition. Interdiffusion increases with increasing temperature and decreasing growth rate, consistent with more time for atoms to rearrange positions between subsequent adatom arrival. Interdiffusion increased with increasing Co-Cu binding energy. Presumably because these Co-Cu bonds are more difficult to break and thus the rate at which they break decreases. Varying the step orientation from  $\langle 100 \rangle$  to  $\langle 110 \rangle$  in small increments produced a steady decrease in interdiffusion. This result may be important for the magnetism of vicinal (100) surfaces which have regularly spaced  $\langle 110 \rangle$  steps only,<sup>1</sup> and thus would have a minimum amount of interdiffusion for a



given step density. It is clear that the interface between Co and Cu is not sharp on an atomic scale: the width of the interdiffusion region (10-90% concentration) is approximately 0.7-1.5 nm. For growth at 0.15 ML/min there is approximately one interdiffused atom for every two unit cells (~0.7 nm) along the length of an average step. Interdiffusion, therefore, is highly dependent on step density (terrace width).

Island size and density compare favorably with growth results for the island growth mode, and the effects of deposition rate and temperature are consistent with accepted kinetic models. Island shapes are not well reproduced. Many of the features observed in the exchange mediated growth mode suggest an etching of the step rather than a simple restructuring along  $\langle 110 \rangle$  facets. This morphology was duplicated somewhat during annealing simulations. We believe the discrepancy between growth experiments and simulation experiments is due to kinetics. The barrier height model employed in our simulations works well for nucleation and growth of islands, however, the kinetics at steps is more complicated. One or more processes at steps must occur at much different rates than predicted by our model. One possible example is adatom diffusion along a step, which evidence suggests<sup>15</sup> may have a lower activation energy than adatom diffusion across a terrace. The most promising method to improve the simulation results would be to use a complete set of barrier height calculations. This may allow the determination of exactly which processes are responsible for the etching features we observed.

- 1 A. Berger, U. Linke, and H. P. Oepen, Phys. Rev. Lett. 68, 839 (1992).
- 2 M. T. Kief, G. J. Mankey, and R. F. Willis, J. Appl. Phys. 10, 5929 (1991).
- 3 J. Shen, R. Skomski, M. Klaua, et al., Phys. Rev. B 56, 2340 (1997).
- 4 S. T. Coyle, G. G. Hembree, M. R. Scheinfein, J. Vac. Sci. Technol. A 15, 1785 (1997).
- 5 L. Z. Mezey and J. Gibber, Jpn. J. Appl. Phys. 21, 1569 (1982).
- 6 Y. W. Lee, K. C. Russell, and H. I. Aaronson, Scr. Metall. 15, 723 (1981).
- 7 J. L. Blue, to be published.
- 8 M. T. Kief and W. F. Egelhoff Jr., Phys. Rev. B 47, 785 (1992).
- 9 A. K. Schmid, D. Atlan and H. Itoh, et al., Phys. Rev. B 48, 2855 (1993).
- 10 M. Giesen, F. Schmitz, and H. Ibach, Surf. Sci. 336, 69 (1995).
- 11 U. Ramsperger, A. Vaterlaus, and D. Pescia, Phys. Rev. B 53, 1 (1996).
- 12 A. K. Schmid and J. Kirschner, Ultramicroscopy 42, 483 (1992).
- 13 R. Allenspach, A. Bischof, and U. Durig, Surf. Sci. Lett. 381, L573 (1997).
- 14 R. L. Schwoebel, J. Appl. Phys. 40, 614 (1969).
- 15 P. Stoltze, J. Phys. Condens. Matter 6, 495 (1994).

**Scientific Publications For Years 4-6: January 1996-July 1998**

- 18 A Reliable Calibration Method Based on Ion Current Measurement for an Electron Beam Transition Metal Deposition Source, E.T. Bullock, S.T. Coyle, G.G. Hembree, M.R. Scheinfein, Rev. Sci. Instrum. (in press 1998).
- 17 Differential Phase Contrast in TEM, M.R. McCartney, P. Kruit, A.H. Buist, M.R. Scheinfein, Ultramicrosc. **65**, 179-186 (1996).
- 16 Magnetic Ordering in Co Films On Stepped Cu(100) Surfaces, S.T. Coyle, M.R. Scheinfein, J. Appl. Phys. **83**(11) in-press (1998).
- 15 Defect Induced Lowering Of Activation Energies At Step Bands in Co/Cu(100), S.T. Coyle, J.L. Blue, M.R. Scheinfein, Appl. Phys. Lett. **72**(8), 912 (1998)
- 14 Magnetic Coupling In Self-Organized Narrow-Spaced Fe Nanowire Arrays, A. Sugawara, D. Streblechenko, M. McCartney, M.R. Scheinfein, IEEE-Trans. **MAG** in-press (1998).
- 13 Co on Stepped Cu(100) Surfaces: A Comparison of Experimental Data with Monte Carlo Growth Simulations, S.T. Coyle, M.R. Scheinfein, J.L. Blue, J. Vac. Sci. Technol. In-press (1998).
- 12 Magnetic Nanostructures Produced By Electron Beam Patterning Of Direct Write Transition Metal Fluoride Resists, Dmitry Streblechenko and M.R. Scheinfein, J. Vac. Sci. Technol. **16**(3) in-press (1998).
- 11 Self Organized Mesoscopic Magnetic Structures, A. Sugawara, M.R. Scheinfein, J. Appl. Phys. **82**(11) 5662 (1997).
- 10 Room Temperature Dipole Ferromagnetism in Linear, Self-Assembling Mesoscopic Fe Particle Arrays, A. Sugawara, M.R. Scheinfein, Phys. Rev. **B56**(14), R8499 (1997).
- 9 Self-Organized Fe Nanowire Arrays Prepared by Shadow Deposition on NaCl(110) Templates, A. Sugawara, S.T. Coyle, G.G. Hembree, M.R. Scheinfein, Appl. Phys. Lett. **70**(8), 1043 (1997).
- 8 Growth, Morphology and Magnetic Properties of Ultrathin Epitaxial Co Films on Cu(100), S.T. Coyle, G.G. Hembree, M.R. Scheinfein, J. Vac. Sci. Technol. **A15**(3), 1785(1997).
- 7 Quantitative Magnetometry Using Electron Holography: Field Profiles Near Magnetic Force Microscopy Tips, D.G. Streblechenko, M.R. Scheinfein, M. Mankos, K. Babcock, IEEE-Trans. **MAG-32**(5), 4124 (1996).
- 6 Long Range Order in 2-D Arrays of Nanometer-Sized Fe Islands on CaF<sub>2</sub>/Si(111), M.R. Scheinfein, K.E. Schmidt, K.R. Heim, G.G. Hembree, J. Appl. Phys. **79**, 5056 (1996).
- 5 Comment on "Flux Quantization in Magnetic Nanowires Imaged by Electron Holography," Conradin Beeli, Bernard Doudin, Pierre Stadelmann, Phys. Rev. Lett. **75**(25), 4630 (1995). M.R. Scheinfein, D. Streblechenko, M.Mankos, **77**(5), 976 (1996).
- 4 Growth of Nanometer Size Magnetic Particles on CaF<sub>2</sub>(111), Heim, S.T. Coyle, G.G. Hembree, J.A. Venables, M.R. Scheinfein, J. Appl. Phys. **80**(2), 1161 (1996).
- 3 Electron Holography and Lorentz Microscopy of Magnetic Materials, M.Mankos, M.R. Scheinfein, J.M. Cowley, Advances in Imaging and Electron Physics, P.W. Hawkes ed. vol. 98, 323-426 (1996).
- 2 Greatly Defocused Off-Axis STEM Electron Holography, J.M. Cowley, M.Mankos, M.R. Scheinfein, Ultramicrosc. **63**, 133 (1996).
- 1 Long Range Order and Coupling in Two-Dimensional Arrays of Nanometer Size Superparamagnets, M.R. Scheinfein, K.E. Schmidt, K.R. Heim, G.G. Hembree, Phys. Rev. Lett. **76**(9), 1541 (1996).

**Conference Proceedings And Extended Abstracts For Years 4-6: January 1996-July 1998**

- 2 Holography and the STEM, M. Mankos, M.R. Scheinfein, J.M. Cowley, 9th Pfefferkorn Conference, New York, May 1996.
- 1 Quantitative Micromagnetics Using Electron Holography: Field Profiles Near Magnetic Force Microscope Tips, IEEE-Intermag-96 Digest, p. BE-1. Seattle, WA 9-12 April 1996.

**Invited Conference Talks For Years 4-6: January 1996-July 1998**

- 6 The Micromagnetics of MRAM Structures, American Physical Society, March 1999.
- 5 Quantitative Micromagnetics : Electron Holography Small Particles and MFM Tips, Topical MFM Workshop, San Francisco, CA, 10-11 January 1998.
- 4 Quantitative Micromagnetics : Electron Holography (A Tutorial) , Tutorial Session, 7<sup>th</sup> Joint Intermag-MMM 98, San Francisco, CA, 6-9 January 1998.
- 3 Quantitative Micromagnetics : Electron Holography of Thin Films, Superlattices and Small Particles, 7<sup>th</sup> Joint Intermag-MMM 98, San Francisco, CA, 6-9 January 1998.
- 2 Quantitative Micromagnetics Using Electron Holography: Field Profiles Near Magnetic Force Microscope Tips, IEEE-Intermag 96. Seattle, WA 9-12 April 1996.
- 1 Quantitative Micromagnetics : Electron Holography of Thin Films, Superlattices and Small Particles, American Physical Society, St. Louis, MO, 16-19 March 1996.

**Invited Seminars And Colloquia For Years 4-6: January 1996-July 1998**

- 5 Quantitative Micromagnetics, Seagate Magnetics, Minneapolis, MN 03 October 1997.
- 4 Quantitative Micromagnetics, IBM Almaden Research Laboratory, Almaden, CA 31 October 1996.
- 3 Quantitative Micromagnetics Using Electron Holography, Jet Propulsion Laboratory, Cal. Tech., Pasadena, CA 21 October 1996.
- 2 Quantitative Micromagnetics Using Electron Holography: Field Profiles Near Magnetic Force Microscope Tips, Motorola Corporate Research Laboratory 15 April 1996.
- 1 Two-Dimensional Long-Range Coupling : Enhanced Superparamagnetism in Two-Dimensional Arrays of Nanometer Sized Fe Islands, Michigan Tech. University, 6 May 1996.

**Degrees Granted and Students/Post-Docs Supervised For Years 4-6: January 1996-July 1998**

<u>Status</u>	<u>Name</u>	<u>Graduation Date</u>	<u>Current Employment</u>
Post Doc	Akira Sugawara	March 1996	JAIST, Ishikawa, Japan
PhD	Steve Coyle	May 1997	ETEC Systems, Hayward, Ca
PhD Student	Eugene Bullock	Expected December 1999	
PhD Student	Dmitry Streblechenko	Expected August 1999	

## C.V. For MICHAEL R. SCHEINFELD

**Citizenship:** United States

**Birth Date:** March 24, 1958

**Education:**

- Ph. D. (1985) Applied and Engineering Physics,  
Cornell University, Ithaca, NY.
- M.S. (1982) Applied and Engineering Physics,  
Cornell University, Ithaca, NY.
- B.S. (1980) Electrical Engineering and Computer Science,  
MIT, Cambridge, MA.

**Professional Activities:**

American Physical Society, Materials Research Society, American Vacuum Society, IEEE, Microscopy Society of America.

**Experience:**

- 8/96 - Present Professor, Department of Physics and Astronomy, Arizona State University, Tempe, AZ
- 07/91 - 8/96 Associate Professor, Department of Physics and Astronomy, Arizona State University, Tempe, AZ.  
Tenure granted April 1995.
- 10/90 - 07/91 Associate Research Scientist, Center for Solid State Science, Arizona State University, Tempe, AZ.
- 08/87 - 09/90 Staff Physicist, Electron Physics Group, National Institute of Standards and Technology,  
Gaithersburg, MD.
- 01/86 - 05/87 Associate Research Scientist, University of Arizona, Tucson, AZ.
- 05/85 - 12/85 Post-Doc/Research Associate, University of Arizona, Tucson, AZ.
- 09/80 - 05/85 Graduate Research Assistant, Cornell University, Ithaca, NY.

## SCIENTIFIC PUBLICATIONS

- 104 High Resolution X-Ray Photoemission Electron Microscopy at the Advanced Light Source, T. Stammler, S. Anders, H.A. Padmore, J. Stohr, M. Scheinfein, H. Ade, Proceeding of the Materials Research Society, (submitted 1998).
- 103 A Reliable Calibration Method Based on Ion Current Measurement for an Electron Beam Transition Metal Deposition Source, E.T. Bullock, S.T. Coyle, G.G. Hembree, M.R. Scheinfein, Rev. Sci. Instrum. (in press 1998).
- 102 Differential Phase Contrast in TEM, M.R. McCartney, P. Kruit, A.H. Buist, M.R. Scheinfein, Ultramicroscopy. 65, 179-186 (1996).
- 101 Magnetic Ordering in Co Films On Stepped Cu(100) Surfaces, S.T. Coyle, M.R. Scheinfein, J. Appl. Phys. 83(11) in-press (1998).
- 100 Defect Induced Lowering Of Activation Energies At Step Bands in Co/Cu(100), S.T. Coyle, J.L. Blue, M.R. Scheinfein, Appl. Phys. Lett. 72(8), 912 (1998)
- 99 Magnetic Coupling In Self-Organized Narrow-Spaced Fe Nanowire Arrays, A. Sugawara, D. Streblechenko, M. McCartney, M.R. Scheinfein, IEEE-Trans. MAG in-press (1998).

- 98 Co on Stepped Cu(100) Surfaces: A Comparison of Experimental Data with Monte Carlo Growth Simulations, S.T. Coyle, M.R. Scheinfein, J.L. Blue, J. Vac. Sci. Technol. In-press (1998).
- 97 Magnetic Nanostructures Produced By Electron Beam Patterning Of Direct Write Transition Metal Fluoride Resists, Dmitry Streblechenko and M.R. Scheinfein, J. Vac. Sci. Technol. **16**(3) in-press (1998).
- 96 Design of a High-Resolution X-Ray Photo-Emission Electron Microscope (X-PEEM) For ALS Beamline 7.3.1.1, S. Anders, M.R. Scheinfein, LBL-Internal Rpt # LSBL-366 (1997).
- 95 Self Organized Mesoscopic Magnetic Structures, A. Sugawara, M.R. Scheinfein, J. Appl. Phys. **82**(11) 5662 (1997).
- 94 Room Temperature Dipole Ferromagnetism in Linear, Self-Assembling Mesoscopic Fe Particle Arrays, A. Sugawara, M.R. Scheinfein, Phys. Rev. **B56**(14), R8499 (1997).
- 93 A Transmission X-Ray Microscope Based on Secondary-Electron Imaging, R.N. Watts, S.D. Liang, Z.H. Levine, T.B. Lucatorto, F. Polack, M.R. Scheinfein, Rev. Sci. Instrum. **68**(9), 3463 (1997).
- 92 Self-Organized Fe Nanowire Arrays Prepared by Shadow Deposition on NaCl(110) Templates, A. Sugawara, S.T. Coyle, G.G. Hembree, M.R. Scheinfein, Appl. Phys. Lett. **70**(8), 1043 (1997).
- 91 Growth, Morphology and Magnetic Properties of Ultrathin Epitaxial Co Films on Cu(100), S.T. Coyle, G.G. Hembree, M.R. Scheinfein, J. Vac. Sci. Technol. **A15**(3), 1785(1997).
- 90 Electron Holography in the Transmission Microscope, M. Mankos, M.R. Scheinfein, J.M. Cowley, Proceedings of the Pfeifferkorn Conference, SEM International (in press 1996).
- 89 Quantitative Magnetometry Using Electron Holography: Field Profiles Near Magnetic Force Microscopy Tips, D.G. Streblechenko, M.R. Scheinfein, M. Mankos, K. Babcock, IEEE-Trans. **MAG-32**(5), 4124 (1996).
- 88 Long Range Order in 2-D Arrays of Nanometer-Sized Fe Islands on CaF<sub>2</sub>/Si(111), M.R. Scheinfein, K.E. Schmidt, K.R. Heim, G.G. Hembree, J. Appl. Phys. **79**, 5056 (1996).
- 87 Comment on "Flux Quantization in Magnetic Nanowires Imaged by Electron Holography," Conradin Beeli, Bernard Doudin, Pierre Stadelmann, Phys. Rev. Lett. **75**(25), 4630 (1995). M.R. Scheinfein, D. Streblechenko, M.Mankos, **77**(5), 976 (1996).
- 86 Growth of Nanometer Size Magnetic Particles on CaF<sub>2</sub>(111), Heim, S.T. Coyle, G.G. Hembree, J.A. Venables, M.R. Scheinfein, J. Appl. Phys. **80**(2), 1161 (1996).
- 85 Electron Holography and Lorentz Microscopy of Magnetic Materials, M.Mankos, M.R. Scheinfein, J.M. Cowley, Advances in Imaging and Electron Physics, P.W. Hawkes ed. vol. 98, 323-426 (1996).
- 84 Greatly Defocused Off-Axis STEM Electron Holography, J.M. Cowley, M.Mankos, M.R. Scheinfein, Ultramicrosc. **63**, 133 (1996).
- 83 Long Range Order and Coupling in Two-Dimensional Arrays of Nanometer Size Superparamagnets, M.R. Scheinfein, K.E. Schmidt, K.R. Heim, G.G. Hembree, Phys. Rev. Lett. **76**(9), 1541 (1996).
- 82 Two-Dimensional Long-Range Coupling : Enhanced Superparamagnetism in Two-Dimensional Arrays of Nanometer Sized Fe Islands, M.R. Scheinfein, K.E. Schmidt, K.R. Heim, G.G. Hembree, Appl. Phys. Lett. **67**(19), 2878 (1995).
- 81 Interfacial Roughness Effects on Giant Magnetoresistance and Interlayer Coupling in Co/Cu Superlattices, Z.J. Yang and M.R. Scheinfein, Phys. Rev. **B52**(6), 4263 (1995).
- 80 An Alternative Approach For Magneto-Optic Calculations Involving Layered Media, K.R. Heim, M.R. Scheinfein, J. Mag. Mag. Mat. **154**, 141 (1996).
- 79 Scanning Electron Microscopy With Polarization Analysis (SEMPA), J. Unguris, M.R. Scheinfein, M.H. Kelley, A. Gavrin, R.J. Celotta, D.T. Pierce, in *Handbook of Electron Microscopy Volume II*, edited by S. Amelinckx, D. Van Dyck, J.F. Van Landuyt, G. Van Tendeloo, (VCH Verlagsgesellschaft mbH, Weinheim, 1997), Chapter V.2, pp 735.

- 78 Absolute Magnetometry Using Electron Holography: Magnetic Superlattices and Small Particles, Marian Mankos, J.M. Cowley, M.R. Scheinfein, Material Research Society Bulletin, October 95', 45, (1995).
- 77 Quantitative Micromagnetics: Electron Holography of Magnetic Thin Films and Multilayers, Marian Mankos, M.R. Scheinfein, J.M. Cowley, IEEE Trans. MAG-32(5), 4150 (1996).
- 76 90° Domains and Coupling in Co/Cu Giant Magnetoresistance Superlattices, Z.J. Yang, M.R. Scheinfein, IEEE Trans. MAG-31(6), 3921 (1995).
- 75 Nanomagnetometry: Electron Holography of Small Particles, M. Mankos, J.M. Cowley, M.R. Scheinfein, IEEE Trans. MAG-31(6), 3796 (1995).
- 74 Quantitative Micromagnetics at High Spatial Resolution Using Electron Holography (Review Article), M. Mankos, J.M. Cowley, M.R. Scheinfein, phys. stat. sol.(a), 154, 469 (1996).
- 73 Electron Holography of P-N Junctions, M.R. McCartney, B. Frost, R. Hull, M.R. Scheinfein, D.J. Smith, E. Voelkl, in *Electron Holography*, Delta Series, eds. A. Tonomura, L. Allanrd, G. Pozzi, D. Joy, Y. Ono, Elsevier Science BV, 189-198, (1995).
- 72 STEM Holography of Magnetic Materials, M. Mankos, P. de Haan, V. Kambersky, G. Matteucci, M.R. McCartney, Z.J. Yang, M.R. Scheinfein, J.M. Cowley, in *Electron Holography*, Delta Series, eds. A. Tonomura, L. Allanrd, G. Pozzi, D. Joy, Y. Ono, Elsevier Science BV, 329-341, (1995).
- 71 Magnetoresistance, M.R. Scheinfein, in *Macmillan Encyclopedia of Physics*, Macmillan Press, New York, pp. 926-927 (1996).
- 70 90° Domains in Co/Cu Giant Magnetoresistance Superlattice, Z.J. Yang, M.R. Scheinfein, Appl. Phys. Lett. 66(2), 236 (1995).
- 69 A Low Cost Preamplifier for Fast Pulses from Microchannel Plates, S.T. Coyle, G.G. Hembree, M.R. Scheinfein, Rev. Sci. Instrum. 66(7), 4000 (1995).
- 68 Absolute Magnetometry of Thin Cobalt Films and Co/Cu Multilayer Structures at Nanometer Spatial Resolution, Marian. Mankos, Z.J. Yang, M.R. Scheinfein, J.M. Cowley, IEEE-Trans. MAG 30(6), 4497 (1994).
- 67 Far Out-of-Focus Electron Holography in a Dedicated FEG STEM, M. Mankos, A.A. Higgs, M.R. Scheinfein, J.M. Cowley, Ultramicrosc. 58, 87 (1995).
- 66 A Picosecond Electron Gun For Surface Analysis, M. Aeschlimann, E. Hull, C.A. Schmuttenmaer, J. Cao, L.G. Jahn, Y. Gao, H.E. Elsayed-Ali, D.A. Mantell, M.R. Scheinfein, Rev. Sci. Instrum. 66(2), 1000 (1995).
- 65 Evaluation of CoCrTaPt Alloy For Longitudinal Magnetic Recording, Y. Cheng, M. Sedighi, I. Lam, R. Gardener, Z.J. Yang, M.R. Scheinfein, J. Appl. Phys. 75(10), 6138 (1994).
- 64 Absolute Magnetometry At Nanometer Spatial Resolution : STEM Holography Of Thin Cobalt Films, M. Mankos, M.R. Scheinfein, J.M. Cowley, J. Appl. Phys. 75(11) 7418 (1994).
- 63 Ultra High Vacuum Scanning Electron Microscopy Characterization of the Growth of Fe on CaF<sub>2</sub>/Si(111): Selective Nucleation on Electron-Beam Modified Surfaces, K.R. Heim, G.G. Hembree, M.R. Scheinfein, J. Appl. Phys. 76(12), 8105 (1994).
- 62 Structural and Magnetic Properties of Epitaxially Grown fcc Fe/Cu(100) and Fe/CaF<sub>2</sub>/Si(111), M.R. Scheinfein, S.D. Healy, K.R. Heim, Z.J. Yang, J.S. Drucker, G.G. Hembree, Proc. Mat. Res. Soc. vol. 332, *Determining Nanoscale Properties of Materials by Microscopy and Spectroscopy*, eds. M. Isaacson, M. Sarikaya, K. Wickramasinghe, 473 (1994).
- 61 Surface Magnetization Processes Investigated by the Combined Surface Magneto-Optical Kerr Effects in fcc Fe/Cu(100) Thin Films, Z.J. Yang, S.D. Healy, K.R. Heim, J.S. Drucker, G.G. Hembree, M.R. Scheinfein, J. Appl. Phys. 75(10), 5589 (1994).
- 60 The Initial Phases of Epitaxy of fcc Fe/Cu(100): Supersurface and Subsurface Island Formation, S.D. Healy, K.R. Heim, Z.J. Yang, J.S. Drucker, G.G. Hembree, M.R. Scheinfein, J. Appl. Phys. 75(10), 5592 (1994).

- 59 Combined Three-Axis Surface Magneto-Optical Kerr Effects in the Study of Surface and Ultrathin Film Magnetism, Z.J. Yang, M.R. Scheinfein, J. Appl. Phys. 74(11) 6810 (1993).
- 58 Correlations Between Ultrathin Film Microstructure and Magnetic Properties in Epitaxial Films of fcc Fe/Cu(100), K.R. Heim, S.D. Healy, Z.J. Yang, J.S. Drucker, G.G. Hembree, M.R. Scheinfein, J. Appl. Phys. 74(12), 7422 (1993).
- 57 Field Induced Metastable States in Ultrathin Films of fcc Fe/Cu(100), G.G. Hembree, J.S. Drucker, S. Healy, K. Heim, Z. Yang, M.R. Scheinfein, Appl. Phys. Lett. 64(8), 1036 (1993).
- 56 Time Aberrations of Uniform Fields: An Improved Reflectron Mass Spectrometer for an Atom Probe Field Ion Microscope, M.R. Scheinfein, D.N. Seidman, Rev. Sci. Instrum., 64(11), 3126 (1993).
- 55 Scanning Transmission Electron Microscopy of Thin Magnetic Films, M. Mankos, J.M. Cowley, R.V. Chamberlin, M.R. Scheinfein, M.B. Stearns, IEEE Trans. MAG-30(2), 720 (1994).
- 54 Micromagnetic Structure of Domains in Co/Pt Multilayers - Part A: Investigations of Wall Structure, R. Ploessl, J.N. Chapman, M.R. Scheinfein, J.L. Blue, M. Mansuripur, H. Hoffman, J. Appl. Phys. 74(12), 7431 (1993).
- 53 Electron Coincidence Spectroscopy Study of Secondary and Auger Electron Generation Mechanisms, J.S. Drucker, M.R. Scheinfein, J.Y. Liu, J.K. Weiss, J. Appl. Phys. 74(12), 7329 (1993).
- 52 Brightness Measurements of nanometer Sized Field Emission Electron Sources, W. Qian, M.R. Scheinfein, J.C.H. Spence, J. Appl. Phys. 73(11), 7041 (1993).
- 51 The Origins Of High Spatial Resolution Secondary Electron Microscopy, M.R. Scheinfein, J.S. Drucker, J.K. Weiss, J. Lui, G.G. Hembree, J.M. Cowley, Materials Research Society Symposium, Materials Research Society, 295, 253 (1993).
- 50 Secondary Electron Generation Studied by Momentum Resolved Electron Coincidence Spectroscopy, J.S. Drucker, M.R. Scheinfein, Phys. Rev. B47(23), 15973 (1993).
- 49 Electron Optical Properties of Nanometer Field Emission Electron Sources, W. Qian, M.R. Scheinfein, J.C.H. Spence, Appl. Phys. Lett. 62(3), 315 (1993).
- 48 Aberrations of Subnanometer Field Emission Electron Sources, M.R. Scheinfein, W. Qian, J.C.H. Spence, J. Appl. Phys. 73(5), 2057 (1993).
- 47 Secondary Electron Production Pathways By Fast Incident Electrons, M.R. Scheinfein, J.S. Drucker, Phys. Rev. B47(7), 4068 (1993).
- 46 Correlations of Modulation Noise with Magnetic Microstructure, Transition Parameter and RMS Transition Variation For CoCrTa and CoNi Thin Film Media, M.R. Kahn, B. Marchon, D. Speliotis, M. Scheinfein, J. Mag. Mat. 120, 310 (1993).
- 45 Magnetic Force Microscopy Utilizing an Ultra-Sensitive Vertical Cantilever Geometry, A. DiCarlo, M.R. Scheinfein, R.V. Chamberlin, Appl. Phys. Lett. 61(17), 2108 (1992).
- 44 Slow Magnetic Relaxation in Iron, R.V. Chamberlin, M.R. Scheinfein, Science 260, 1098 (1993).
- 43 Slow Relaxation in Magnetic Materials, R.V. Chamberlin, M.R. Scheinfein, Ultramicrosc. 47, 408 (1992).
- 42 Magnetic Force Microscope Utilizing An Ultra-Small Spring Constant Vertically Cantilevered Tip, A. DiCarlo, M.R. Scheinfein, R.V. Chamberlin, Ultramicrosc. 47, 383 (1992).
- 41 Spin-Polarized Photoemission Spectroscopy of Magnetic Surfaces Using Undulator Radiation, P.D. Johnson, S.L. Hulbert, R. Klaffky, N.B. Brookes, A. Clarke, B. Sinkovic, N.V. Smith, R. Celotta, M.H. Kelley, D.T. Pierce, M.R. Scheinfein, B.J. Wacławski, M.R. Howells, Rev. Sci. Instr. 63(3), 1902 (1992).
- 40 Micromagnetics of Surface Segregations Regions in Domains Written in TbFeCo Alloys, M.R. Scheinfein, J.L. Blue and M. Aeschlimann, IEEE Trans. on Magnetism, MAG-27(6), 5124 (1991).
- 39 Decreased Computation Time for Magnetostatic Self-Energy Using Multipoles, J.L. Blue and M.R. Scheinfein, IEEE Trans. on Magnetism MAG-27(6), 4778 (1991).

- 38 Laser Focusing of Atoms: A Particle Optics Approach, J.J. McClelland, M.R. Scheinfein, J. Opt. Soc. Am. B8(9), 1974 (1991).
- 37 Micromagnetic Calculations of 180° Surface Domain Walls, M.R. Scheinfein and J.L. Blue, J. Appl. Phys. 69(11), 7740 (1991).
- 36 Correlations of Modulation Noise with Anisotropy, Magnetic Microstructure and Intergranular Interactions for CoCrTa and CoNi Thin Film Media, M.R. Kahn, S.Y. Lee, S.L. Duan, J.L. Pressesky, N. Heiman, M.R. Scheinfein, J. Appl. Phys. 69(8) 4745 (1991).
- 35 SEMPA Measurements of Magnetic Microstructure in Ultrathin Films, J. Unguris, M.W. Hart, M.R. Scheinfein, R.J. Celotta, D.T. Pierce, J. Appl. Phys. 69(8) 6096 (1991).
- 34 Micromagnetic Calculations of 180° Surface Domain Wall Magnetization Profiles With Comparisons to Measurements, J.L. Blue, M.R. Scheinfein, J. Appl. Phys. 68(12) 6504 (1990).
- 33 180° Surface Domain Wall Magnetization Profiles: Comparisons Between SEMPA Measurements, MO Kerr Measurements and Micromagnetic Models, M.R. Scheinfein, P.J. Ryan, J. Unguris, D.T. Pierce, R.J. Celotta, Appl. Phys. Lett. 57(17), 1817 (1990).
- 32 Magnetic Imaging Via Scanning Electron Microscopy With Polarization Analysis, R.J. Celotta, M.R. Scheinfein, J. Unguris, D.T. Pierce, NATO ASI Advanced Study Institute on the Science and Technology of Nanostructured Magnetic Materials, Eds. G.C. Hadjipaniysi, G.A. Prinz (Plenum Press, New York, 1991), pp. 335-338.
- 31 Micromagnetics of 180 Degree Domain Walls at Surfaces, M.R. Scheinfein, J. Unguris, J.L. Blue, K.J. Coakley, D.T. Pierce, R.J. Celotta, P.J. Ryan, Phys. Rev. B43(4), 3395 (1991).
- 30 Scanning Electron Microscopy With Polarization Analysis (SEMPA) Studies of Domains, Domain Walls and Magnetic Singularities at Surfaces and in Thin Films, M.R. Scheinfein, J. Unguris, M. Aeschlimann, D.T. Pierce and R.J. Celotta, J. Mag. Mag. Mat., 93, 109 (1991).
- 29 Correlations Between Magnetic Microstructure and Noise Spectra for CoNi and CoCrTa Thin Film Media, M.R. Kahn, S.Y. Lee, J.L. Pressesky, D. Williams, R.D. Fisher, N. Heiman, M.R. Scheinfein, J. Unguris, D.T. Pierce and R.J. Celotta, IEEE Trans. MAG-26(5), 2715 (1990).
- 28 Magnetic Field Modulated Written Bits in TbFeCo Thin Films: TEM Lorentz and SEMPA Studies, M. Aeschlimann, M. Scheinfein, J. Unguris, F.J. Greidanus, S. Klahn, J. Appl. Phys. 68(9), 4710 (1990).
- 27 Scanning Electron Microscopy With Polarization Analysis Studies of Magnetic Microstructure, J. Unguris, M.R. Scheinfein, R.J. Celotta and D.T. Pierce, Chemistry and Physics of Solid Surfaces VII, eds. R. Vaneslow and R. Howe, (Springer-Verlag, Berlin, 239, 1990).
- 26 High Spatial Resolution Quantitative Micromagnetics, M.R. Scheinfein, J. Unguris, D.T. Pierce and R.J. Celotta, J. Appl. Phys. 67(9), 5932 (1990).
- 25 The Magnetic Microstructure of the (0001) Surface of hcp Cobalt, J. Unguris, M.R. Scheinfein, R.J. Celotta and D.T. Pierce, Appl. Phys. Lett. 55(24), 2553 (1989).
- 24 Scanning Electron Microscopy With Polarization Analysis (SEMPA), M. R. Scheinfein, M. H. Kelley, J. Unguris, D. T. Pierce, R. J. Celotta, Rev. Sci. Instrum. 61(10), 2501 (1990).
- 23 Scanning Electron Microscopy With Polarization Analysis (SEMPA) Studies Of Surface Magnetic Microstructure, M.W. Hart, M.R. Scheinfein, J. Unguris, D.T. Pierce and R.J. Celotta, Proceedings of the Symposium on Magnetic Materials, Processes and Devices, eds. L.T. Romankiw and D.A. Herman Jr., (The Electrochemical Society, Inc. 1990), p. 111.
- 22 The Influence of the Surface on Magnetic Domain Wall Microstructure, M. R. Scheinfein, J. Unguris, R. J. Celotta, D. T. Pierce, Phys. Rev. Lett. 63(6), 668 (1989).
- 21 Magnetic Microstructure of Thin Films and Surfaces: Exploiting Spin-Polarized Electrons in the SEM and STM, D. T. Pierce, M. R. Scheinfein, J. Unguris, R. J. Celotta, Materials Research Society Symposium Proceedings, Materials Research Society Vol. 151, 49 (1989).



- 20 Surface Magnetic Microstructure, M. R. Scheinfein, J. Unguris, R. J. Celotta, D. T. Pierce, Magnetic Properties of Low Dimensional Systems, eds. L. Falicov and J.L. Moran-Lopez, (Springer-Verlag Proceedings in Physics - 50, Berlin, 1990), p. 1.
- 19 Vector Imaging of Magnetic Microstructure, M. H. Kelley, J. Unguris, M. R. Scheinfein, D. T. Pierce, R. J. Celotta, Microbeam Analysis - 1989, P. E. Russell ed. 392 (San Fransisco Press, San Fransisco, CA 1989).
- 18 Scanning Electron Microscopy with Polarization Analysis Studies of Ni-Fe Magnetic Memory Elements, J. Unguris, M. R. Scheinfein, R. J. Celotta, D. T. Pierce, IEEE Trans. On Magnetism MAG-25(9), 4204 (1989).
- 17 Second Order Transfer Matrices of an Inhomogeneous Field Wien Filter Including Spin Precession, M. Scheinfein, Optik 82(3), 99 (1989).
- 16 Definition of Ultimate Attainable Spatial Resolution, M. R. Scheinfein, Ultramicro. 28, 359 (1989).
- 15 Use of Thorium as a Target in Electron Spin Analyzers, J. J. McClelland, M. R. Scheinfein, D. T. Pierce, Rev. Sci. Instrum. 60(4), 683 (1989).
- 14 Improved Low-Energy Diffuse Scattering Electron-Spin Polarization Analyzer, M. R. Scheinfein, D. T. Pierce, J. Unguris, J. J. McClelland, R. J. Celotta, M. M. Kelley, Review of Scientific Instruments 60(1), 1 (1989).
- 13 Electrical Characteristics of Single Buried Microstrip Lines in the TEM Approximation, J. L. Prince, R. Senthinathan, O. A. Palusinski, M. R. Scheinfein, IEEE Trans. On Comps. Hyb. Man. Tech. CHMT-11(3), 279 (1988).
- 12 Methods of Calculation Of Electrical Parameters For Electronic Packaging Applications, M. Scheinfein and O. Palusinski, Transactions Of The Society For Computer Simulation, Vol. 4(3), 187 (1987).
- 11 Characteristics of Coupled Buried Microstrip Lines by Modeling and Simulation, R. Senthinathan, J. L. Prince, M. Scheinfein, IEEE Transactions on Components, Hybrids and Manufacturing Technology, CHMT-10, 604 (1987).
- 10 Electron Energy Loss Spectroscopy At High Spatial Resolution Using The Low Loss Spectrum, M. Scheinfein, Scanning Microscopy Supplement I: Physical Aspects Of Microscopic Characterization of Materials, eds. J. Kirschner, K. Murata and J. Venables, 161 (1987).
- 9 Electrical Performance Of High Speed Interconnect Systems, M. Scheinfein, J. Prince, O. Palusinski and L. C. Liao, IEEE Transactions on Components, Hybrids and Manufacturing Technology, CHMT-10, 303 (1987).
- 8 Multiobjective Optimization Techniques For Design Of Electrostatic Charged Particle Lenses, M. Scheinfein and A. Galantai, Optik 74(4), 154 (1986).
- 7 High Performance Two Electrode Electron Gun Lenses: Beyond The Butler Gun, M. Scheinfein, Ultramicro. 19, 225 (1986).
- 6 Electronic And Chemical Analysis Of Fluoride Interface Structures At Subnanometer Spatial Resolution, M. Scheinfein and M. Isaacson, J. Vac. Sci. Technol. B4(1), 326 (1986).
- 5 Electronic And Chemical Analysis Of A Metal-Insulator Interface Utilizing Transmission Electron Energy Loss Spectroscopy At 5 Å Spatial Resolution, M. Scheinfein and M. Isaacson, Materials Research Society Symposium Proceedings, Materials Research Society, Vol. 41, 343 (1985).
- 4 Electron Energy Loss Spectroscopy Across A Metal-Insulator Interface At Sub-nanometer Spatial Resolution, M. Scheinfein, A. Muray and M. Isaacson, Ultramicro. 16, 233 (1985).
- 3 Radiolysis And Resolution Limits Of Halide Inorganic Resists, A. Muray, M. Scheinfein, I. Adesida and M. Isaacson, J. Vac. Sci. Technol. B3(1), 367 (1985).
- 2 Design And Performance Of Second Order Corrected Spectrometers For Use With The Scanning Transmission Electron Microscope, M. Scheinfein and M. Isaacson, Scanning Elec. Microsc. 1984/IV, 1681 (1984).
- 1 A High Performance Electron Energy Loss Spectrometer For Use With Dedicated STEM, M. Isaacson and M. Scheinfein, J. Vac. Sci. Technol. B1(4), 1338 (1983).

# **CONFERENCE PROCEEDINGS AND EXTENDED ABSTRACTS : SCIENTIFIC PUBLICATIONS**

- 37 Holography and the STEM, M. Mankos, M.R. Scheinfein, J.M. Cowley, 9th Pfefferkorn Conference, New York, May 1996.
- 36 Quantitative Micromagnetics Using Electron Holography: Field Profiles Near Magnetic Force Microscope Tips, IEEE-Intermag-96 Digest, p. BE-1. Seattle, WA 9-12 April 1996.
- 35 Part of the article (39-40 and Fig. 6) in "Micromagnetic Microscopy and Modeling," E. Dan Dahlberg, J-G. Zhu, Physics Today, April, 34-40 (1995).
- 34 Differential Phase Contrast in TEM For Magnetic Microstructure Observation, P. Kruit, A.H. Buist, M.R. McCartney, M.R. Scheinfein, Proceedings of Microscopy and Microanalysis Society 1995, G. W. Bailey, M.H. Ellisman, R.A. Hennigan, N.I. Zaluzec, Eds.,(Jones and Begell, New York, NY,1995) p. 606.
- 33 Quantitative Micromagnetics: Electron Holography of Magnetic Thin Films and Multilayers, Marian Mankos, M.R. Scheinfein, J.M. Cowley Intermag-95 Digest, San Antonio, Texas, 19 April 1995.
- 32 Nanomagnetometry: Electron Holography of Small Particles, M. Mankos, J.M. Cowley, M.R. Scheinfein, IEEE Intermag-95 Digest, Intermag-95, 18-21 April, 1995, San Antonio, TX.
- 31 90° Coupling in Co/Cu Giant Magnetoresistance Superlattices, Z.J. Yang, M.R. Scheinfein, IEEE Intermag-95 Digest, Intermag-95, 18-21 April, 1995, San Antonio, TX.
- 30 Holography of P-N Junction, M.R. McCartney, R. Hull, J.C. Bean, E. Voelkl, B. Frost, M.R. Scheinfein, D.J.Smith, Proc. of the International Workshop on Electron Holography, Oak Ridge National Laboratory, 28-31 August 1994, p. 9.3 (1994).
- 29 STEM Holography: Quantitative Characterization of Magnetic Microstructure at Nanometer Spatial Resolution, M. Mankos, M.R. Scheinfein, J.M. Cowley, Proc. of the International Workshop on Electron Holography, Oak Ridge National Laboratory, 28-31 August 1994, p. 8.3 (1994).
- 28 Low-Voltage Nanometer-Size Field Emission Sources, W. Qian, M.R. Scheinfein, J.C.H. Spence, Proceedings of the Microbeam Analysis Society (MAS), Ed. John Friel, New Orleans, LA July 31-August 5,1994, p. 129-130 (1994).
- 27 STEM Holography of Small Metal Particles, M. Mankos, G. Matteucci, M.R. Scheinfein, J.M. Cowley, Proceedings of ICEM-13, Paris, France, 17-22 July 1994, p. 1179.
- 26 Quantitative Investigations of Magnetic Microstructure: Electron Holography in a Scanning Transmission Electron Microscope, M. Mankos, Z.J. Yang, M.R. Scheinfein, J.M. Cowley, Proceedings of ICEM-13, Paris, France, 17-22 July 1994, p. 317.
- 25 SIMS Input Lens, R.L. Gerlach, M.R. Scheinfein, G.A. Crow, M. Utlaut, C. Bickford, Proceedings of the International Journal of Optical Engineering, SPIE vol. 2024, 149 (1993).
- 24 Characterization of Magnetic Microstructure at High Spatial Resolution, M.R. Scheinfein, Proceedings of the 51<sup>st</sup> Annual Microscopy Society Of America (MSA), G. W. Bailey, Ed.,(San Francisco Press, San Francisco, CA 1993) p. 5.
- 23 Brightness Measurements of Nanometer Sized Field Emission Tips, M.R. Scheinfein, W. Qian, J.C.H. Spence, Proceedings of the 51<sup>st</sup> Annual Microscopy Society Of America (MSA), G. W. Bailey, Ed.,(San Francisco Press, San Francisco, CA 1993) p. 632.
- 22 The Origins of High Spatial Resolution Secondary Electron Microscopy, M.R. Scheinfein, J.S. Drucker, J.K. Weiss, Proceedings of the 51<sup>st</sup> Annual Microscopy Society Of America (MSA), G. W. Bailey, Ed.,(San Francisco Press, San Francisco, CA 1993) p. 766.
- 21 STEM of Order and Dynamics in Novel Magnetic Materials, M. Mankos, J.M. Cowley, R.V. Chamberlin, M.R. Scheinfein, J.D. Ayers, Proceedings of the 1<sup>st</sup> Annual Microscopy Society Of America (MSA), G. W. Bailey, Ed.,(San Francisco Press, San Francisco, CA 1993) p. 1026.

- 20 Magnetic Force and Force Gradient Microscopy Utilizing An Ultra-Sensitive Vertical Cantilever Geometry, A. DiCarlo, M.R. Scheinfein, R.V. Chamberlin, Scanning Probe Microscopies II, ed. C. Williams, Proceedings SPIE-1855, 187 (1993).
- 19 Micromagnetic Calculations of 180 Degree Surface Domain Wall Magnetization Profiles With Comparison To Measurements, J.L. Blue and M.R. Scheinfein, NISTIR 90-4427, Applied and Computational Mathematics Division, Center For Computing and Applied Mathematics, NIST, September 1990.
- 18 Laser Focusing of Atoms: A Particle Optics Approach, J.J. McClelland, M.R. Scheinfein, Proceedings of the 12<sup>th</sup> International Conference on Atomic Physics, Ann Arbor, MI, 29 July 1990, ICAP-12, p. 312.
- 17 Surface Magnetic Microstructural Analysis Using Scanning Electron Microscopy With Polarization Analysis, M.R. Scheinfein, J. Unguris, D.T. Pierce, R.J. Celotta, Proceedings of the 49<sup>th</sup> Annual Electron Microscopy Society Of America (EMSA) and the XII<sup>th</sup> International Conference on Electron Microscopy, G. W. Bailey, Ed., (San Francisco Press, San Francisco, CA 1990) p. 216.
- 16 Correlations Between Magnetic Microstructure and Noise Spectra for CoNi and CoCrTa Thin Film Media, M.R. Kahn, S.Y. Lee, J.L. Pressesky, R.D. Fisher, N. Heiman, M.R. Scheinfein, J. Unguris, D.T. Pierce and R.J. Celotta, Proceeding of INTERMAG-1990, Brighton, U. K., IEEE ITERMAG-90 Digest, HB-08 (1990).
- 15 Increased Sherman Function In Electron Spin Analyzers Using A Bulk Thorium Target, J. J. McClelland, M. R. Scheinfein, D. T. Pierce, Proceedings of the XVI International Conference on the Physics of Electronic and Atomic Collisions - ICPEAC XVI, 26 July 1989, New York, New York, p. 805.
- 14 Scanning Electron Microscopy with Polarization Analysis Studies of Ni-Fe Magnetic Memory Elements, J. Unguris, M. R. Scheinfein, R. J. Celotta, D. T. Pierce, Proceeding of INTERMAG-1989, Washington D. C., IEEE ITERMAG-89 Digest, KB-06 (1989).
- 13 Definition of Ultimate Attainable Spatial Resolution (Rapporteur), M. R. Scheinfein, Proceedings of the Aussois Workshop on Electron Beam Induced High Spatial Resolution Spectroscopies, 28 February 1988, Aussios, France, 500 (1988).
- 12 Scanning Electron Microscopy With Polarization Analysis (SEMPA): High Spatial Resolution Magnetic Imaging Status Report, M. R. Scheinfein, J. Unguris, D. T. Pierce, R. J. Celotta, Proceedings of the Aussois Workshop on Electron Beam Induced High Spatial Resolution Spectroscopies, 28 February 1988, Aussios, France, 116 (1988).
- 11 University of Arizona Tools for Electrical Design of Packaging Structures, O. Palusinski, J. Prince and M. Scheinfein, Proceedings of NEPCON West-1988, 126 (1988).
- 10 Electrical Optimization of Integrated Circuit Packages, J. Prince, O. Palusinski, J. C. Liao and M. Scheinfein, Proceedings of the AIME Annual Meeting, (1988).
- 9 VLSI Packaging Design Methodology Considerations, J. Prince, Z. Staszak, M. Scheinfein, O. Palusinski, Proceedings of the 4<sup>th</sup> International Work-shop on the Physics of Semiconductor Devices, Madras, India, 115 (1987).
- 8 Development of Computer Aids For Packaging Electrical Design, J. Prince, R. Jones, O. Palusinski, J. C. Liao and M. Scheinfein, Proceeding of the 7<sup>th</sup> International Electronics Packaging Society Conference (IEPS-1987), 932 (1987).
- 7 Characteristics Of Coupled, Buried Microstrip Lines By Modeling And Simulation, R. Senthinathan, J. Prince and M. Scheinfein, Proceedings of the 37<sup>th</sup> Electronics Components Conference (ECC-1987), 363 (1987).
- 6 Electrical Performance Of Integrated Circuit Packages: Three Dimensional Structures, M. Scheinfein and J. Prince, Proceedings of the 37<sup>th</sup> IEE Electronics Components Conference (ECC-1987), 377 (1987).
- 5 Electrical Characteristics Of Buried Microstrip In The TEM Approximation, J. Prince, M. Scheinfein, R. Senthinathan and O. Palusinski, Proceedings of the 6<sup>th</sup> Annual International Electronic Packaging Conference (IEPS-1986), Nov. 17-19, 1986, San Diego, CA. (International Electronics Packaging Society, Inc., Wheaton, IL), 424 (1986).

- 4 Electrical Performance Of High Speed Interconnect Systems, M. Scheinfein, J. Prince, O. Palusinski and L. C. Liao, Proceedings of the IEEE International Electronics Manufacturing And Technology Symposium (IEMT-1986), San Francisco, CA., Sept. 21-23, 23 (1986).
- 3 Electron Energy Loss Spectroscopy At 5 Å Spatial Resolution, M. Isaacson and M. Scheinfein, Proceedings of the 43rd Annual Electron Microscopy Society Of America (EMSA), G. W. Bailey, Ed., 396 (San Francisco Press, San Francisco, CA, 1985).
- 2 Surface Plasmons: A Sensitive Diagnostic Tool For Characterizing Interfaces, M. Scheinfein, Proceedings of the 43rd Annual Electron Microscopy Society Of America (EMSA), G. W. Bailey, Ed., 254 (San Francisco Press, San Francisco, CA 1985).
- 1 Nanometer Structure Fabrication Using Electron Beam Lithography, M. Isaacson, A. Muray, M. Scheinfein, I. Adesida and E. Kratschmer, Proceedings Of The International Symposium Of Nanometer Structure Electronics (Osaka, April 1984), Ohmsha Ltd. Tokyo, Japan, 58 (1985).

#### **PEDAGOGICAL PUBLICATIONS**

- 2 Physics 114 Laboratory Manual, M.R. Scheinfein, Kendall-Hunt Publishing Company, (1993). ISBN-0-8403-8815-2
- 1 Physics 113 Laboratory Manual, M.R. Scheinfein, Kendall-Hunt Publishing Company, (1993). ISBN-0-8403-8811-X.

(Both manuals had three printings before they were rewritten.)

#### **INVITED CONFERENCE TALKS**

- 19 Quantitative Micromagnetics : Electron Holography Small Particles and MFM Tips, Topical MFM Workshop, San Francisco, CA, 10-11 January 1998.
- 18 Quantitative Micromagnetics : Electron Holography (A Tutorial) , Tutorial Session, 7<sup>th</sup> Joint Intermag-MMM 98, San Francisco, CA, 6-9 January 1998.
- 17 Quantitative Micromagnetics : Electron Holography of Thin Films, Superlattices and Small Particles, 7<sup>th</sup> Joint Intermag-MMM 98, San Francisco, CA, 6-9 January 1998.
- 16 Quantitative Micromagnetics Using Electron Holography: Field Profiles Near Magnetic Force Microscope Tips, IEEE-Intermag 96. Seattle, WA 9-12 April 1996.
- 15 Quantitative Micromagnetics : Electron Holography of Thin Films, Superlattices and Small Particles, American Physical Society, St. Louis, MO, 16-19 March 1996.
- 14 Two-Dimensional Long-Range Coupling : Enhanced Superparamagnetism in Two-Dimensional Arrays of Nanometer Sized Fe Islands, Magnetism and Magnetic Materials Meeting, Philadelphia, PA, 6-9 November 1995.
- 13 Quantitative Micromagnetics : Electron Holography of Thin Films, Superlattices and Small Particles, American Vacuum Society, Minneapolis, MN, 16-19 October 1995.
- 12 Long Range Exchange Coupling in Two Dimensional Arrays of Nanometer Sized Fe Islands on CaF<sub>2</sub>/Si(111), ARPA/ONR/NRL Workshop on Magnetic Materials, Arlington, VA, 16-18 May 1995.
- 11 Characterization of Magnetic Microstructure at High Spatial Resolution, Materials Research Society Meeting, Boston, MA, 29 November 1993.
- 10 Characterization of Magnetic Microstructure at High Spatial Resolution, Presidential Symposium,, 51<sup>st</sup> Annual Microscopy Society Of America (MSA) Meeting, Cincinnati OH, 1 August 1993.
- 9 Nanometer Lateral Spatial Resolution Characterization of the Growth of Fe on CaF<sub>2</sub>/Si(111): Selective Nucleation on Electron-Beam Modified Surfaces, Topical ONR Conference on Low Dimensional Magnetism, Albuquerque, NM, 24 June 1994.

- 8 Nanometer Sized Field Emission Cathodes, Field Emission Electron Microscopy Workshop, Oak Ridge National Laboratory, 24 September 1993.
- 7 Origin of High Resolution Secondary Electron Scattering, Materials Research Society, Boston, MA, 2 December 1992.
- 6 Scanning Electron Microscopy With Polarization Analysis (SEMPA) Studies of Domains, Domain Walls and Magnetic Singularities at Surfaces and in Thin Films, European Materials Research Society Meeting, Strasbourg, France, May 29, 1990.
- 5 Scanning Electron Microscopy With Polarization Analysis of Surface Magnetic Microstructure, Magnetics and Magnetic Materials Meeting, Boston, MA, December 1, 1989.
- 4 Surface Magnetic Microstructure, Second Int. Workshop on the Magnetic Properties of Low Dimensional Systems, San Luis Potosi, Mexico, 22 May 1989.
- 3 Considerations For Ultimate Attainable Spatial Resolution in Microanalysis, Joint U.S./ France Workshop on Electron Beam Induced Spectroscopies at High Spatial Resolution, Aussios, France, March 1988.
- 2 Scanning Electron Microscopy with Polarization Analysis (SEMPA), Joint U.S./ France Workshop on Electron Beam Induced Spectroscopies at High Spatial Resolution, Aussios, France, March 1988.
- 1 Electron Energy Loss Spectroscopy At High Spatial Resolution Using The Low Loss Spectrum, 5<sup>th</sup> Pfefferkorn Conference, Brueggen, W. Germany, October 1986.

#### INVITED SEMINARS AND COLLOQUIA

- 21 Quantitative Micromagnetics, Seagate Magnetics, Minneapolis, MN 03 October 1997.
- 20 Quantitative Micromagnetics, IBM Almaden Research Laboratory, Almaden, CA 31 October 1996.
- 19 Quantitative Micromagnetics Using Electron Holography, Jet Propulsion Laboratory, Cal. Tech., Pasadena, CA 21 October 1996.
- 18 Quantitative Micromagnetics Using Electron Holography: Field Profiles Near Magnetic Force Microscope Tips, Motorola Corporate Research Laboratory 15 April 1996.
- 17 Two-Dimensional Long-Range Coupling : Enhanced Superparamagnetism in Two-Dimensional Arrays of Nanometer Sized Fe Islands, Michigan Tech. University, 6 May 1996.
- 16 Nanomagnetometry Using Electron Interferometry : Electron Holography In STEM, Center for Magnetic Recording, University of California at San Diego, 15 November 1994.
- 15 Characterization of Magnetic Microstructure at High Spatial Resolution, Argonne National Laboratory, Symposium, 20 April 1994.
- 14 Electron Spectroscopy In A Scanning Transmission Electron Microscope : More Than Pretty Pictures, Colloquium, Arizona State University Department of Physics and Astronomy, 18 November 1993.
- 13 The Origins of High Spatial Resolution Secondary Electron Microscopy, 51<sup>st</sup> Annual Microscopy Society Of America (MSA) Meeting, Cincinnati OH, 1 August 1993.
- 12 Surface and Thin Film Magnetism, Physics Department Symposium, Arizona State University, Tempe, AZ, 13 February 1992.
- 11 Scanning Electron Microscopy With Polarization Analysis of Surface Magnetic Microstructure, Physics Department Symposium, Arizona State University, Tempe, AZ, 15 January 1991.
- 10 Scanning Electron Microscopy With Polarization Analysis of Surface Magnetic Microstructure, Center For Solid State Science Symp., Arizona State University, Tempe, AZ, 19 November 1990.
- 9 Scanning Electron Microscopy With Polarization Analysis of Surface Magnetic Microstructure, Symposium, Arizona State University, Tempe, AZ, 5 July 1990.

- 8 Electron Energy Loss Spectroscopy at Subnanometer Spatial Resolution in the Scanning Transmission Electron Microscope, Symposium, Materials Science Department, Northwestern University, Evanston, IL, April 11, 1990.
- 7 Scanning Electron Microscopy With Polarization Analysis of Surface Magnetic Micro-structure, Symposium, Physical Electronics, Perkin Elmer, Eden Prairie, MN, April 6, 1990.
- 6 Scanning Electron Microscopy With Polarization Analysis of Surface Magnetic Microstructure, Symposium, Materials Science Department, Northwestern University, Evanston, IL, April 2, 1990.
- 5 Scanning Electron Microscopy With Polarization Analysis of Surface Magnetic Microstructure, Symposium, Physics Department, McMaster University, Hamilton, Ontario, Canada, March 28, 1990.
- 4 Scanning Electron Microscopy With Polarization Analysis of Surface Magnetic Microstructure, Symposium, Physics Department, Simon Fraser University, Burnaby, British Columbia, Canada, December 8, 1989.
- 3 Scanning Electron Microscopy With Polarization Analysis of Surface Magnetic Microstructure, Symposium, Physics Department, Rensselaer Polytechnic Institute, Troy, NY, November 1, 1989.
- 2 Scanning Electron Microscopy With Polarization Analysis of Surface Magnetic Microstructure, Symposium, Kodak Research Labs, Rochester, NY, July 17, 1989.
- 1 Particle Optics of Scanning Electron Microscopy With Polarization Analysis, Symposium, Applied Physics Department, Cornell University, Ithaca, NY, June 9, 1989.

#### **CONTRIBUTED TALKS**

(This list does not include talks by my students or colleagues on which I am a coinvestigator, only those that I delivered)

- 19 Magnetic Coupling In Self-Organized Narrow-Spaced Fe Nanowire Arrays, A.VS Meeting 1997, San Jose, CA 20 October 1997.
- 18 Brightness Measurements of Nanometer Sized Field Emission Tips, 51<sup>st</sup> Annual Microscopy Society Of America (MSA) Meeting, Cincinnati OH, 1 August 1993.
- 17 Emission Cathodes : Nanometer Diameter Field Emission Electron Sources, J.M. Cowley Symposium, Scottsdale AZ, 7 January 1993.
- 16 Micromagnetics of Surface Segregations Regions in Domains Written in TbFeCo Alloys, M.R. Scheinfein, Magnetism-Magnetic Materials/Intermag Conference, Pittsburg, PA, 1 June 1991.
- 15 Micromagnetics of Surface Segregations Regions in Domains Written in TbFeCo Alloys, M.R. Scheinfein, 2<sup>nd</sup> International Conf. on Magneto-Optical Materials, Tucson, AZ, 1 February 1991.
- 14 Observation of the Surface Domain Structure of an hcp (0001) Co Crystal, 1989 American Physical Society Meeting, St. Louis, Mo, March 1989.
- 13 Electrical Performance Of Integrated Circuit Packages: Three Dimensional Structures, 37<sup>th</sup> IEE Electronics Components Conference, Boston, MA, May 1987.
- 12 Field Simulation, Particle Optics and Electron Energy Loss Spectroscopy at High Spatial Resolution, Symposium at Dartmouth College, Hanover, NH, March 1987.
- 11 Field Simulation, Particle Optics and Electron Energy Loss Spectroscopy at High Spatial Resolution, Spectral Sciences, Burlington, MA, March, 1987.
- 10 Particle Optics and Electron Energy Loss Spectroscopy At High Spatial Resolution, NBS, Gaithersburg, MD., December 1987.
- 9 Electrical Performance Of High Speed Interconnect Systems, IEEE International Electronics Manufacturing And Technology Symposium (IEMT-1986), San Francisco, CA., Sept. 21, 1986.
- 8 Electron Energy Loss Spectroscopy At 5 Å Spatial Resolution, 43<sup>rd</sup> Annual Electron Microscopy Society Of America (EMSA) Meeting, Louisville, KY, August 3, 1985.

- 7 Surface Plasmons: A Sensitive Diagnostic Tool For Characterizing Interfaces, M. Scheinfein, 43rd Annual Electron Microscopy Society Of America (EMSA) Meeting, Louisville, KY, August 3, 1985.
- 6 Electron Energy Loss Spectroscopy Across A Metal-Insulator Interface At Sub-nanometer Spatial Resolution, Symposium, Physics Department, Arizona State University, July 1985.
- 5 Electronic And Chemical Analysis Of Fluoride Interface Structures At Sub-nanometer Spatial Resolution, Electron, Ion and Photon Beam Conference, Portland, OR, May 1985.
- 4 Transmission Electron Energy Loss Spectroscopy In STEM: Electronic And Chemical Analysis Of Interface Structures At 5 Å Spatial Resolution, American Physical Society (APS), March 1985.
- 3 Electronic And Chemical Analysis Of A Metal-Insulator Interface Utilizing Transmission Electron Energy Loss Spectroscopy At 5 Å Spatial Resolution, Materials Research Society Meeting, Boston, MA, November 1984.
- 2 Design And Performance Of Second Order Corrected Spectrometers For Use With The Scanning Transmission Electron Microscope, Scanning Electron Microscopy Conference, Philadelphia, PA, May 1984.
- 1 A High Performance Electron Energy Loss Spectrometer For Use With Dedicated STEM, Electron, Ion and Photon Beam Conference, Los Angeles, CA., June 1983.

#### **GRANT ACTIVITY**

##### **Current :**

continuation to "Correlations Between Micromagnetic, Microstructural and Microchemical Properties in Ultrathin Epitaxial Magnetic Structures," M.R. Scheinfein, G.G. Hembree. Office of Naval Research, Physics Division. \$375,537. Duration 33 months. Start date, 1 January 1996. N00014-93-1-0099.

"Magnetic Microstructure Observed With Electron Holography in STEM," M.R. Scheinfein. The Tri-Services AASERT Program. \$115,440. Duration 36 months. Start Date 1 June 1995. N00014-95-1-0891.

"Magnetic Memory Elements," M.R. Scheinfein. IBM Almaden Research Center. \$231,711. Duration 60 months. Start date, 1 January 1996. (Awarded by DARPA, subcontract incomplete).

"Dynamics of Mesoscopic Structures in Magnetic Materials," R.V. Chamberlin, M.R. Scheinfein, Division of Materials Research, National Science Foundation. \$332,770. Duration 36 months. Start Date 1 July 1997.

"Proposal to Develop X-Ray/Electron Optical Devices: A High Resolution Photo-Electron Electron Microscope", M.R. Scheinfein, T. Lucatorto, Collaborative Research Grants of the National Institute of Standards and Technology, US Department of Commerce. \$38,500. Duration 36 months. Start date, October 1, 1997. NIST-.

##### **Pending:**

"BiContinuous Functional Nanostructures," Karl Sieradzki and Michael Scheinfein, National Science Foundation. \$657,889. Duration 36 months. Proposed start date, 1 July 1998.

##### **Recently Completed :**

" Proposal to Develop the Nanodetector: A High Resolution Photo-Electron Electron Microscope", M.R. Scheinfein, R. Watts, T. Lucatorto, F. Pollack, Collaborative Research Grants of the National Institute of Standards and Technology, US Department of Commerce. \$85,242. Duration 36 months. Start date, October 1, 1993. NIST-70NANB4H1532.

"Correlations Between Micromagnetic, Microstructural and Microchemical Properties in Ultrathin Epitaxial Magnetic Structures," M.R. Scheinfein, J.S. Drucker, G.G. Hembree. Office of Naval Research, Physics Division. \$510,280. Duration 36 months. Start date, January 1, 1993. N00014-93-1-0099.

"A Low Energy Electron Microscope," J.D. Dow, E. Bauer, G.G. Hembree, W.E. Packard, M.R. Scheinfein, O.F. Sankey, D.J. Smith, J.C.H. Spence, I.S.T. Tsong, J.A. Venables. Instrumentation for Materials Research Division of the National Science Foundation. \$577,500. Duration 24 months. Start date, July 1, 1991. DMR-91-12021.

"Development of New Point Sources for Ions and Electrons," J.C.H. Spence and M.R. Scheinfein. Instrumentation for Materials Research Division of the National Science Foundation. \$210,599. Duration 18 months. Start date, October 1, 1991. DMR-91-12550.

# Self-organized Fe nanowire arrays prepared by shadow deposition on NaCl(110) templates

Akira Sugawara,<sup>a)</sup> T. Coyle, G. G. Hembree, and M. R. Scheinfein<sup>b)</sup>  
Department of Physics and Astronomy, Arizona State University, Tempe, Arizona 85287-1504

(Received 29 October 1996; accepted for publication 17 December 1996)

Iron nanowire arrays have been grown by shadow deposition on a self-organized grating template produced by annealing the sodium chloride (110) surface. The typical wire size as measured using transmission electron microscopy is  $45\text{ nm} \times 13\text{ nm} \times 10\text{ }\mu\text{m}$ . The typical wire array period is 90 nm. The magnetic properties were dominated by a strong in-plane shape anisotropy. The hysteresis loops examined by magneto-optical Kerr effect measurements indicated coherent switching, even though the individual wires were isolated from one another. © 1997 American Institute of Physics.  
[S0003-6951(97)03908-9]

Nanostructured magnetic systems are of interest from a fundamental point of view because excitations can be probed in a mesoscopic system with well-characterized interaction energies. High-density magnetic recording motivates much of the applied research in systems composed of small magnetic structures. The magnetic properties of nanostructures depend upon their shape, size, and spatial distribution. In one-dimensional laterally structured films, e.g., nanowire arrays, we expect easy-axis hysteresis loops with large remanence and coercivity, accompanied by strong in-plane anisotropy.<sup>1,2</sup> In two-dimensional dot arrays, where the magnetic coupling and the domain structure are modified by such laterally structured systems, magnetization reversal of single domain particles has been studied extensively for application to high-density recording<sup>3-5</sup> and to determine its effect on the magnetoresistance.<sup>1,2,6-8</sup>

Attempts have been made to fabricate laterally structured magnetic dot and wire arrays by electron-beam lithography,<sup>1-4</sup> the step-edge method,<sup>9</sup> laser-focused atomic deposition,<sup>10</sup> and electrodeposition.<sup>8</sup> Electron-beam lithography, the most popular method, has been used successfully to fabricate wires as narrow as 15 nm,<sup>3</sup> however, the throughput is so slow that processing the large areas required for magnetic data storage media is quite difficult. Another approach is needed for large-area fabrication of nanostructures with high throughput.

One possible solution is application of self-organization phenomena which have been used in the nanofabrication of semiconductors and polymers in recent years. For example, Takeshita *et al.*<sup>5</sup> have reported that Co islands preferentially nucleate at elbow sites of the herringbone pattern on the reconstructed Au surface, forming nanometer-diameter dots 2 monolayers thick arranged in a triangular lattice. This microstructure disappears with increasing film thickness due to coalescence, limiting the self-organized structures to small volumes. We are interested in thicker mesoscopic structures which produce the large output signals required for digital storage technologies.

We report here on the growth of Fe nanowire arrays prepared by shadow deposition. Shadow growth has been

proposed for wire deposition on a Si grating prepared by electron-beam lithography and selective etching.<sup>6</sup> In this study we use grating templates produced by self-organization. Regular grooves in NaCl(110) as small as 10 nm in both width and depth have been produced previously by Sugawara, Haga, and Nittono.<sup>11</sup> In this study, typical linewidths are about 100 nm. The width of the grooves is a function of the annealing temperature and time.<sup>12</sup> When a NaCl(110) surface plane is annealed in vacuum, the surface becomes faceted with (100) and (010) planes in order to minimize the surface energy. Periodic macrosteps parallel to [001] are formed as schematically shown in Fig. 1. This is a thermal process, hence, we can fabricate uniform nanoscaled grooves quickly even in the ultrahigh vacuum (UHV) ambient. When Fe is deposited on these templates at a low angle of incidence ( $65^\circ$  from the template normal in this study), approximately 60% of (100) terraces are exposed to Fe flux, and Fe wires are formed only near the edge of the ridges (Fig. 1).

Sample preparation was performed in UHV ( $3 \times 10^{-8}$  Pa). The NaCl(110) substrate was etched by water for a few seconds before being loaded into the UHV chamber, where it was etched thermally at  $440^\circ\text{C}$  for 10 min to produce a clean faceted surface. Amorphous SiO was deposited as a passivation layer. This 20-nm-thick film insured a disordered template for the randomly oriented polycrystalline Fe film. The Fe was deposited from a collimated electron-beam source aligned  $65^\circ$  from the template normal. The deposition rate was 0.15 nm/min, and the nominal Fe wire thickness was 13 nm. Finally, a 10-nm-thick SiO passivation layer was deposited on top of the nanowire array to prevent oxidation during

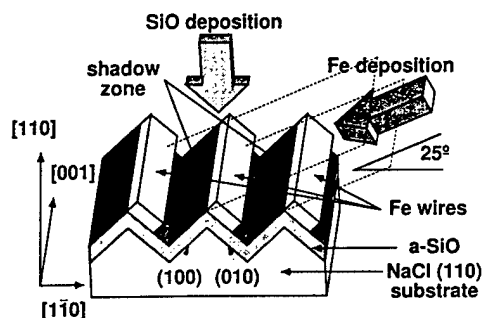


FIG. 1. Surface topography of the substrate surface and deposition geometry.

<sup>a)</sup>On leave from the Dept. of Metallurgical Engineering, Tokyo Institute of Technology, Tokyo, Japan.

<sup>b)</sup>Electronic mail: michael.scheinfein@asu.edu



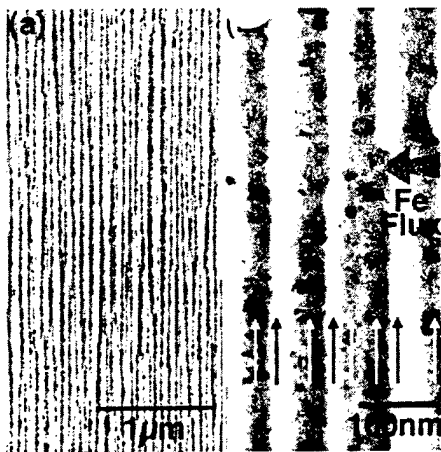


FIG. 2. Bright field TEM images of the SiO (10 nm)/Fe wire array (13 nm)/SiO (20 nm) deposited on the stepped NaCl(110) substrate: (a) A low-magnification image and (b) a high magnification image. Thick lines due to shadow depositions (white arrows) are indicated. An array of ultrafine particles that nucleate in the bottom of the groove remains there after the formation of the wires (black arrows). The diameter of the ultrafine particles in the groove bottom is several nm.

subsequent *ex situ* analysis. The Fe wire array, embedded in the SiO layer, was floated off the NaCl substrate in water. Oxidation caused by this step was negligible. No iron oxide phase was detectable by electron diffraction during the microstructural analysis of the film in a Topcon EM-002B transmission electron microscope (TEM). Microstructural features, such as wire widths, lengths, and separations, were evaluated quantitatively by image analysis.

Figure 2 shows bright field TEM images of a nanowire array. The Fe wires seen in dark contrast run along the macrosteps of the substrate. We confirmed that this microstructure is uniform over the entire 3-mm-diam specimen area of the TEM grid. A corresponding electron-diffraction pattern showed that these wires are polycrystalline Fe with no texture orientation. Therefore, we expect that we can neglect the contribution of magnetocrystalline anisotropy to the magnetic properties. The average periodicity of wires is 90 nm, and their average width (projected) is 30 nm. The average length is estimated to be 10  $\mu\text{m}$ . An aspect ratio larger than 100 has been achieved. However, nanowires smaller than 10 nm in width tend to be discontinuous with shorter segments. This observation suggests that the smallest possible width of wires grown by shadow deposition is determined by the initial nucleation density of Fe islands and coalescence kinetics. The initial nucleation density of Fe islands on SiO is high in the area exposed to flux due to the high local adatom concentration. With increasing thickness, grain growth is caused by the coalescence of islands. Surface diffusion at the neck where two large islands touch is not fast enough to cause reorientation at room temperature, so the wires are composed of several grains in the short axis direction, as seen in Fig. 2(b). The surface roughness of these wires is associated with the grain size controlled by the coalescence kinetics. In Fig. 2(b) the flux comes from the right-hand side, judging from shadows formed around three-dimensional obstacles on the substrate. We can also see very thin wires are formed on the right-hand (deposition) side of each wide wire. These thin wires are considered to be formed at the bottom of the

grooves, i.e., clustering of Fe atoms by macrosteps. The detail of the microstructural evolution will be presented elsewhere.<sup>12</sup>

The fluctuation of the wire width, separation, and length may arise from local imperfections on the surface. The standard deviation of wire widths was 18 nm, approximately 20% of the average width. This results from both the fluctuation in crystallite size and the depth variation of the grooves. The average width is 48% of the periodicity, and is larger than the percentage of area (35%) exposed to Fe flux expected from the geometry shown in Fig. 1. Since the film was grown at room temperature, broadening of the wire width is not caused by long-range surface diffusion. This kind of broadening seems to take place where neighboring macrosteps are so close that narrow grooves are formed. In this case Fe fills up the grooves so easily that neighboring wires touch each other. This increases the coverage of the wires with respect to the surface area.

Hysteresis loops were measured *ex situ* by the magneto-optical Kerr effect (MOKE) at an incident angle of 45°. Since both SiO and NaCl are transparent at optical frequencies (He-Ne laser at 632.8 nm), the MOKE signal was relatively weak. We utilized a phase-sensitive detection scheme, and results are presented for the detection of the first harmonic (2F mode) which gave stronger signals than the fundamental (1F mode). To examine the switching process, longitudinal MOKE loops were recorded for magnetic fields positioned at various angles relative to the nanowire axis. This was accomplished by applying a longitudinal field and rotating the sample in the film plane while keeping the detection optics fixed.

The film shown in Fig. 2 (characteristic of many examined in this study) had strong in-plane magnetic anisotropy, as expected from the observed microstructure. When the field is applied along the macrosteps, a longitudinal loop shows easy-axis behavior with high coercivity about 2 kOe (Fig. 3). When the field is applied perpendicular to the steps, the loops show hard-axis behavior. The magnetization did not saturate for external fields of 3 kOe due to large demagnetization field along the short axis of the wire array. We should note that the real hard axis is considered to be perpendicular to the thin Fe slabs, i.e., out of the film plane by 45°. However, we could not measure this magnetization component by MOKE, because there was no strong reflection in that direction, indicating that the wires themselves are not planar but rather cylindrical. This agrees with results of contrast analysis of Fig. 2(b). The longitudinal loops measured with the applied field oriented between the easy and hard axes gives information on the magnetization rotation process. The two columns of loops shown in Fig. 3 are for the magnetization along [left-hand side (lhs)] and perpendicular [right-hand side (rhs)] to the steps for the field angle with the wire direction as specified. The peaks when  $\theta=45^\circ$  (rhs) and the large open-circle loop for perpendicular magnetization when  $\theta=80^\circ$  are also characteristic of coherent rotation.<sup>13</sup> These results suggest that the magnetization process is not dominated by domain wall motion. The collapsed loop for  $\theta=90^\circ$  results from the limited applied field strength. Even though we cannot ascertain that the switching proceeds through coherent rotation, it is clear that the whole

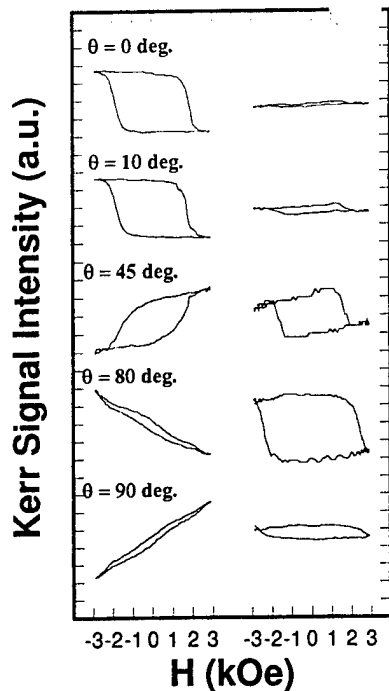


FIG. 3. Hysteresis loops measured by MOKE rotating the specimen in the film plane.  $\theta$  denotes angle between the macrostep direction and the scattering plane with the field applied in plane. The loops on the left-hand side (right-hand side) are magnetization components parallel (perpendicular) to the applied magnetic field.

wire array switches simultaneously. This result is interesting in that the magnetization switching process seems to be present across the film array even though individual lines are not coupled. Either each wire has nearly the same coercivity, and hence each wire individually switches coherently in unison with all others, or all the wires are magnetostatically linked, and hence switch as a single film.

The main advantage of self-organized growth is that it is a simple procedure with high throughput. In contrast to lift-off type lithography, the self-organized pattern formation can

be completed without breaking vacuum. There are many other choices of ionic crystals to be used as templates. We have obtained preliminary results from other types of microstructure such as dot array and continuous films having undulating surface topography.<sup>12</sup> In addition, similar surface macrosteps are reported for other insulating materials such as  $\text{LiNbAlO}_3$  (Ref. 14) and as-deposited  $\text{CaF}_2$  on  $\text{Si}(110)$ .<sup>15</sup> Application of shadow deposition on self-organized templates may show promise for the fabrication of on-chip micromagnetic devices.

The authors would like to acknowledge stimulating discussions with Professor J. Venables. A.S. is supported by a 1995–1997 JSPS postdoctoral fellowship for research abroad. This work is partially supported by ONR under Grant No. N00014-93-1-0099. The microscopy was performed at the NSF supported CHREM at ASU, Grant No. DMR-91-15680.

- <sup>1</sup> S. J. Blundell, M. J. Baird, J. A. C. Bland, M. Gester, H. Ahmed, and H. P. Hughes, *J. Appl. Phys.* **75**, 5249 (1994).
- <sup>2</sup> M. Kume, A. Meda, T. Tamura, and K. Kuroki, *J. Appl. Phys.* **79**, 6402 (1996).
- <sup>3</sup> S. Y. Chou, P. R. Krauss, and L. Kong, *J. Appl. Phys.* **79**, 6101 (1996).
- <sup>4</sup> R. D. Gomez, M. C. Shih, R. M. H. New, R. F. W. Pease, and R. L. White, *J. Appl. Phys.* **80**, 342 (1996).
- <sup>5</sup> H. Takeshita, Y. Suzuki, H. Akinaga, W. Mizutani, K. Tanaka, T. Katayama, and A. Itoh, *Appl. Phys. Lett.* **68**, 3040 (1996).
- <sup>6</sup> T. Shinjo and T. Ono, *J. Magn. Magn. Mater.* **156**, 11 (1996).
- <sup>7</sup> K. Hong and N. Giordano, *J. Magn. Magn. Mater.* **151**, 396 (1995).
- <sup>8</sup> B. Voegeli, A. Blondel, B. Doudin, and J.-Ph. Ansermet, *J. Magn. Magn. Mater.* **151**, 388 (1995).
- <sup>9</sup> K. Hong and N. Giordano, *J. Magn. Magn. Mater.* **151**, 396 (1995).
- <sup>10</sup> R. J. Celotta, R. Guota, R. R. Scholten, and J. J. McClelland, *J. Appl. Phys.* **79**, 6079 (1996).
- <sup>11</sup> A. Sugawara, Y. Haga, and O. Nittono, *J. Magn. Magn. Mater.* **156**, 151 (1996).
- <sup>12</sup> A. Sugawara, M. R. Scheinfein, and G. G. Hembree (unpublished).
- <sup>13</sup> M. Prutton, *Thin Ferromagnetic Films* (Butterworths, Washington, 1964).
- <sup>14</sup> Z. L. Wang and A. J. Shapiro, *Mater. Res. Soc. Symp. Proc.* **355**, 175 (1995).
- <sup>15</sup> L. J. Schowalter and R. W. Fartahuer, *CRC Crit. Rev. Solid State Mater. Sci.* **15**, 367 (1989).

# Growth, morphology, and magnetic properties of ultrathin epitaxial Co films on Cu(100)

S. T. Coyle, G. G. Hembree, and M. R. Scheinfein<sup>a)</sup>

Department of Physics and Astronomy, Arizona State University, Tempe, Arizona 85287-1504

(Received 27 September 1996; accepted 23 December 1996)

The room temperature growth and morphology of epitaxial Co films on Cu(100) were studied from the initial nucleation of islands through thicknesses of several monolayers using *in situ* nanometer resolution ultrahigh vacuum scanning electron microscopy, Auger electron spectroscopy, and the surface magneto-optic Kerr effect. The films became ferromagnetic at room temperature at  $\sim 1.7$  ML (1 ML =  $1.53 \times 10^{15}$  atoms/cm<sup>2</sup>). Roughening structures, seen as large inclusions into step bands and terrace pits from which Cu may have migrated, were observed. Minimization of surface energy along step edges is offered as a possible explanation for the observed morphology at the beginning stages of the formation of these structures. A second Co magnetic phase was detected in many films with out-of-plane remanence and a coercivity 5–10 times the in-plane value.

© 1997 American Vacuum Society. [S0734-2101(97)02703-6]

## I. INTRODUCTION

Research in thin film magnetism has grown remarkably in recent years due in part to the possibility of studying two-dimensional (2D) magnetism and novel phases of materials. Although the Mermin and Wagner theorem<sup>1</sup> precludes the possibility of long range order for a 2D Heisenberg ferromagnet, the existence of intrinsic magnetic surface anisotropy has allowed for the fabrication of 2D ferromagnetic films. Co/Cu(100) has become a model system for investigating the properties of these films. Bulk Co at room temperature (RT) has a hexagonal close packed structure, however face-centered-cubic (fcc) Co has a small lattice mismatch (1.9%) with Cu(100), and thus initially grows pseudomorphically, thereby matching the fcc structure of the substrate. Although bulk Co and Cu are considered immiscible below  $\sim 900$  K, Co and Cu have been reported to form an alloy above  $\sim 450$  K.<sup>2</sup> The application of Co/Cu multilayers to giant magnetoresistance devices is imminent, therefore the study of the Co/Cu interface is important.

A great deal of theoretical and experimental work has been done on the fcc Co/Cu(100) system, and the results have been quite varied. Curie temperature<sup>3–6</sup> increases with film thickness and coercivity increases steeply just after the ferromagnetic transition.<sup>7</sup> Anisotropy is in plane along  $\langle 110 \rangle$ .<sup>3,8,9</sup> The onset of ferromagnetism at RT has been found to be between 1 and 2 monolayer (ML) coverage (1 ML =  $1.53 \times 10^{15}$  atoms/cm<sup>2</sup>).<sup>3,4,8,10–12</sup> Both layer-by-layer<sup>3,4,6</sup> and bilayer<sup>14,15</sup> growth have been reported. A Cu capping layer and perpendicular anisotropy after annealing<sup>16,17</sup> have been reported, as well as coercivity dependent on capping layer thickness,<sup>12,13</sup> peaking at about 1 ML. Co grown on vicinal Cu substrates has a uniaxial in-plane anisotropy along  $\langle 110 \rangle$  step directions.<sup>18</sup> Much of the variability of these results has been attributed to inconsistent film preparation conditions and contaminants.<sup>19</sup> It is important, therefore, to understand how morphology and defects

affect film growth and magnetic properties. In this article, we describe Co films grown under seemingly identical conditions on Cu(100) which resulted in very different film morphologies. Our experimental apparatus allows us to acquire nanometer-resolution secondary-electron images of these films, as well as to probe their macroscopic magnetic properties. Our goal is to find correlations between the evolution of film structure during growth and magnetic properties.

## II. EXPERIMENTAL APPARATUS AND PROCEDURES

Our sample preparation and characterization facility, which has been described in detail elsewhere,<sup>20</sup> consists of a modified Vacuum Generators HB 501S ultrahigh vacuum (UHV) scanning transmission electron microscope (STEM) with attached sample preparation and characterization chamber. The microscope and preparation chamber are baked for 36 h at 170 °C, producing base pressures better than  $5 \times 10^{-11}$  mbar. Samples are grown and characterized using standard surface science techniques, transferred *in situ* to the surface magneto-optic Kerr effect (SMOKE) chamber for magnetic characterization, then transferred *in situ* to the microscope for nanometer lateral resolution secondary electron (SE) imaging.

Single crystal Cu(100) samples 3 mm in diameter were mechanically polished and electropolished. The samples were cleaned by repeated Ar<sup>+</sup> ion sputtering and annealing cycles. Each cycle consisted of 1 h of sputtering at 30 °C, 3 h of sputtering at 330 °C, and 15 min of annealing at 600 °C. Sputtering was done at a 45° incident angle, using  $\sim 200$  nA of 600 eV Ar<sup>+</sup> ions at a pressure of  $\sim 8 \times 10^{-7}$  mbar. Sample cleanliness was confirmed using Auger spectroscopy and SE imaging. Nanometer-resolution SE imaging allowed detection of contamination at the 0.02 at. % level,<sup>20</sup> well below the detection threshold of our broad beam analysis cylindrical mirror analyzer ( $\sim 1$  at. %). Oxide typically has a higher secondary electron yield and hence appears very bright in SE images, whereas carbon contami-

<sup>a)</sup>Electronic mail: Michael.Scheinfein@asu.edu

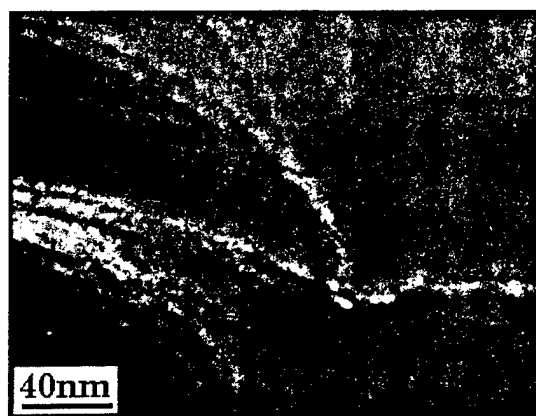


FIG. 1. SE micrograph of typical Cu(100) substrate prior to Co deposition.

nation turns an image dark upon continued electron irradiation. Clean samples showed broad terraces separated by bunched step bands which were pinned by copper oxide islands (Fig. 1). Cobalt films were grown by electron-beam evaporation at about 0.15 ML/min. Pressure during evaporation was typically  $<5 \times 10^{-10}$  mbar. Growth rates were calibrated using Auger spectroscopy.<sup>20</sup> Statistical analysis of thickness measurements yields an uncertainty of  $\pm 10\%$  below 1 ML and  $\pm 0.15$  ML above 1 ML.

Longitudinal and polar hysteresis loops were recorded by scattering light of a 632.8 nm intensity-stabilized He-Ne laser from the sample at a  $45^\circ$  angle of incidence. This geometry allows both polar and longitudinal Kerr measurements to be made by changing only the *ex situ* magnet. Analysis of the hysteresis loops is somewhat complicated by the presence of both polar and longitudinal components in polar loops, due to the  $45^\circ$  angle of incidence.<sup>21</sup> After SMOKE analysis the samples were transferred to the electron microscope for SE imaging. Images were collected digitally and analyzed using our own software program<sup>22</sup> which allowed for measurement of particle and coverage statistics as well as characterizing particle shapes using a variety of methods including Fourier descriptors. The experimental images shown are representative samples of different surfaces. These images are characteristic of the entire surface for each experiment and have been selected from four surveys of ten images each across each sample surface. These representative samples were selected from 40 individual experiments.

### III. GROWTH

From the beginning stages of film growth, many different structures were observed. Some films grew via island nucleation on terraces with little interaction with steps while other films grew with very little island formation and a high degree of step roughening. Figure 2 includes representative SE micrographs from three different fcc Co/Cu(100) films, grown at RT at a rate of 0.15 ML/min. These images will be used to illustrate different growth processes on a typical Cu(100) surface as shown in Fig. 1 (prior to Co deposition). The bright lines are bunched step bands which are pinned by copper oxide islands (brightest spot). The dark spot in the top

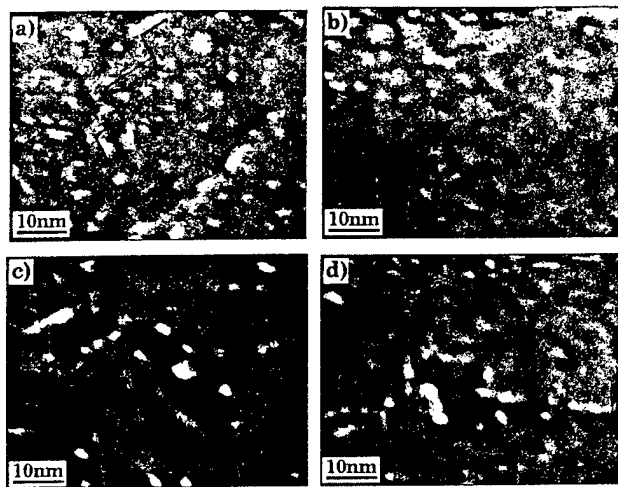


FIG. 2. SE micrographs of Co/Cu(100) films grown at RT at  $\sim 0.15$  ML/min for the following coverages: (a) 0.1 ML, (b) 0.4 ML, (c) 0.3 ML, and (d) 0.3 ML. The arrow and black line in (a) highlight a roughened step edge.

right corner is a vacancy island (inclusion) typical of these substrates. In secondary electron images, dark regions can result from lower secondary yield areas (composition) or pits where the pit edges screen the detector and hence limit detection yield. In this case, compositional variation (contamination) is unlikely since no contaminants were detected by Auger spectroscopy and the regions are impervious to beam damage. The density of the vacancy islands varied greatly between substrates (from  $<20/\mu\text{m}^2$  to  $10^3/\mu\text{m}^2$ ) and, to a lesser degree, between different areas of any particular sample. The vacancy islands do not appear to serve as nucleation sites during film growth, however they may serve as sources for Cu migration onto the surface during later stages of growth since they often persist through several monolayers of growth.

In Figs. 2(a) and 2(b), sequential growths of 0.2 and 0.4 ML of Co are shown. Co islands are clearly visible on the terraces. A monatomic step is visible on the left side of Fig. 2(a), while a three-step step band is visible on the right side of Fig. 2(a), running diagonally across the image. The two dark spots in Fig. 2(a) are vacancy islands in the substrate. By 0.4 ML coverage, Fig. 2(b), it can be seen that the Co islands are beginning to coalesce. By contrast, Fig. 2(c) shows a micrograph of a 0.3 ML film grown under identical conditions (pressure  $<3 \times 10^{-10}$  mbar, temperature measured by thermocouple between 20 and  $30^\circ\text{C}$ ) on a different substrate. There is very little island formation and a great deal of roughening of steps. There is also the formation of large meandering vacancy islands on the terraces. We will refer to this mode as step edge mediated growth. The top third of the micrograph shows a bunched step band with many kinks. The kinks make some of the step edges seem nonorthogonal. The roughened step edges align mostly along crystallographic axes  $\langle 110 \rangle$ . Islands have nucleated preferentially along the up side of step edges. This may be indicative of an Ehrlich-Schwoebel barrier.<sup>23</sup> A 0.3 ML film on an-

TABLE I. Island statistics for three sequential growths of Co/Cu(100).

Coverage (ML)	Coverage (% surface area)	Island density (islands/nm <sup>2</sup> )	Average island area (nm <sup>2</sup> )
0.1	12	0.0222	4.8
0.2	21	0.0287	5.6
0.4	35	0.0204	10.4

other substrate is shown in Fig. 2(d). This film exhibits both island growth and extensive reordering of step edges, i.e., is a combination of the island growth and step edge mediated growth modes. The bare Cu(100) surfaces of the films shown in Fig. 2, when imaged in a scanning electron microscope (SEM) prior to deposition, appeared similar to that shown in Fig. 1.

We have investigated many films grown on several different substrates and found a continuum of combinations of the island growth and step edge mediated growth modes. We have attempted to correlate the growth mode to the following factors without success: C and O contamination as measured by broad beam Auger electron spectroscopy (AES), average terrace width, density of vacancy islands in the substrate, growth temperature between 300 and 360 K, average step band width and percentage of the surface covered by step bands. The most obvious explanation would be that the terrace width is greater than the adatom diffusion length for island growth and significantly less than the diffusion length for step edge mediated growth. The three films in Fig. 2, however, have nearly the same average terrace width and were all grown at  $\sim 300$  K. Analysis of other images of the film shown in Fig. 2(c) indicated that single height steps between step bands may be common. This would make the actual terrace width less than that of the other films shown in Fig. 2, and perhaps less than the average random walk distance between nucleation sites.

We have analyzed images from the film shown in Figs. 2(a) and 2(b) for coverages of 0.1, 0.2, and 0.4 ML, and assembled the data in Table I. Column one is the coverage in ML as determined by AES. Column two is the percent of the surface covered by islands, which is fairly consistent with the coverage in ML. In the 0.4 ML film we begin to see a measurable amount of second layer coverage ( $\sim 0.003$  ML). Column three is the island density. The decrease in island density from 0.2 to 0.4 ML is indicative of coalescence. Column four is the average island area. The island size distribution of the 0.1 and 0.2 ML films, which have a single peak, are typical of island nucleation.<sup>24</sup> The island size distribution of the 0.4 ML film has a major peak followed by a minor one.

The formation of rectangular pits from small pinholes in Co/Cu(100) after annealing has been reported by Schmid *et al.*<sup>16</sup> They concluded that Cu migrated from these pits to form a capping layer. Similar pinholes were reported by Giesen *et al.*<sup>17</sup> for room temperature growth of Co/Cu(1 1 17). They found that the size of these pinholes increased and the density decreased upon annealing. They also found a dramatic roughening of step edges at the beginning stages of

film growth. Terraces on their vicinal surfaces are aligned along  $\langle 110 \rangle$ , and roughening took the form of steps oriented perpendicular to the original step direction. Giesen *et al.* calculated the change in surface energy for the formation of a pit. Initially the surface energy increases significantly with the size of the pit, then decreases beyond a critical size. Because of this they question why the pits form at all. They then calculated the elastic energy stored in the film due to misfit strain and the change in energy due to strain relief by formation of a pit. For thicker films they find significantly more elastic energy than surface energy stored in the pits. They concluded that the relief of misfit strain is the driving force behind the enlargement of pits upon annealing.

We find similar pits in our films without annealing, and they appear to form differently. Early stages of such pits can be seen in Figs. 2(c) and 2(d). After continued Co growth these pits will appear similar [see, e.g., Fig. 4(b)] to those described separately by Schmid and Giesen. We believe that surface energy may be a significant component in pit formation along steps, at least in the early stages of growth. The pits along step bands in our experiments seem to form from the reorientation of randomly oriented steps along mainly  $\langle 110 \rangle$  directions rather than the spontaneous formation of rectangular pits. Step bands often follow curves between pinning sites, thus the step edges have a high density of kinks. When a Co adatom adheres to a step edge it is probably free to move along the step<sup>25</sup> until it encounters another Co atom or adheres to a kink site. Once one or more Co atoms are trapped, the surface energy may be lowered if Cu atoms move to surround the Co atom. This produces a reordering of the step in the region surrounding the Co atoms. The new step faces will prefer to be  $\langle 110 \rangle$ , since this has the lowest surface energy (see below). If such sites are arranged randomly along a step one can imagine a step forming a jagged edge such as that indicated by the arrow and the jagged dark line inserted in Fig. 2(a). Pits on terraces where island growth occurs appear to form due to incomplete Co coverage, and their growth likely proceeds, as described by Giesen *et al.*<sup>17</sup> Pits on terraces where step edge mediated growth occurs seem to form due to the exchange process described above.

We have estimated the change in free energy for the rearrangement of atoms in the vicinity of a Co step adatom. The free energy of a collection of atoms is found from

$$\bar{\gamma}_{\text{tot}} = n_{\text{Co}} \bar{\gamma}_{\text{Co}} + n_{\text{Cu}} \bar{\gamma}_{\text{Cu}} + n_{\text{Co-Cu}} \bar{\gamma}_{\text{Co-Cu}},$$

where  $n_{\text{Co}}$  and  $n_{\text{Cu}}$  are the number of dangling Co and Cu bonds,  $\bar{\gamma}_{\text{Co}}$  and  $\bar{\gamma}_{\text{Cu}}$  are the surface free energies per bond,  $n_{\text{Co-Cu}}$  is the number of Co-Cu nearest-neighbor bonds, and  $\bar{\gamma}_{\text{Co-Cu}}$  is the interfacial free energy per bond. Here we have considered only nearest-neighbor bonds. We used  $\gamma_{\text{Co}} = 1.1$  eV per atom,<sup>26</sup>  $\gamma_{\text{Cu}} = 0.77$  eV per atom,<sup>26</sup> and  $\gamma_{\text{Co-Cu}} = 0.063$  eV per atom<sup>27</sup> and divided by four to find the energy per bond ( $\bar{\gamma}$ ). Including strain in this calculation changes the result negligibly and never changed the sign of the calculated energy. The strain contribution was therefore omitted. The free energy per unit cell of a  $\langle 110 \rangle$  step is only

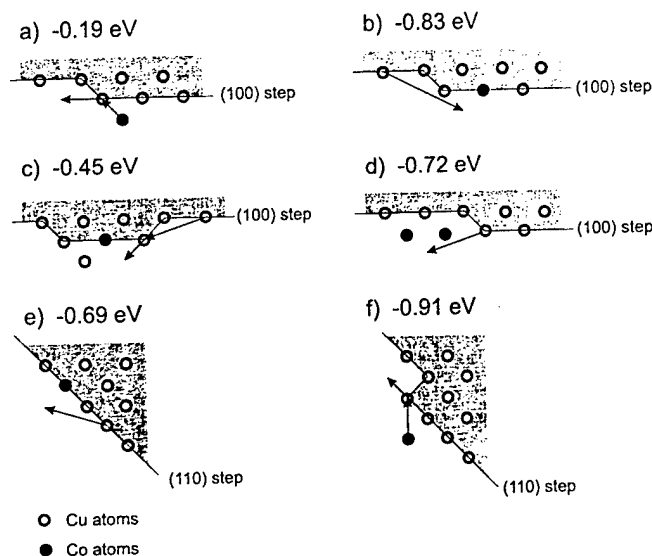


FIG. 3. Examples of morphological changes near a Co adatom (solid circle) near Cu (open circle) steps and kinks on Cu(100) and the associated change in surface free energy. Arrows denote the movement of atoms, lines denote step edges, and shaded regions denote terraces above steps.

slightly lower than that of a 100 step ( $1.88 \text{ eV}/a_0$  vs  $1.90 \text{ eV}/a_0$ ). There is, however, a significant difference in the free energy per atomic site ( $1.33 \text{ eV}/\text{site}$  vs  $1.90 \text{ eV}/\text{site}$ ), where the atomic site refers to the atom at the step edge and its nearest neighbors in the plane below, which may also have a different number of dangling bonds. Thus a rearrangement of the same number of atoms from a  $\langle 100 \rangle$  step into a  $\langle 110 \rangle$  step will reduce the free energy.

In Fig. 3 we show a few examples of how altering step edge morphology results in lowering the free energy of Cu step atoms near Co adatoms. Open circles are Cu atoms, solid circles are Co atoms, solid lines are step edges, and shaded regions denote terraces above steps. Arrows indicate the movement of individual atoms, and the calculated change in surface free energy is listed in eV. These energies are significant when compared to an estimated activation energy for Co adatom diffusion across a Cu(100) terrace of  $0.4\text{--}0.5 \text{ eV}$ . To our knowledge this activation energy has not been reported in the literature, however we consider it reasonable to assume it is close to the energies for Cu/Cu(100) of  $0.40 \text{ eV}$  (Ref. 28) and Co/Co(100) of  $0.49 \text{ eV}$ .<sup>19</sup> The change in surface energy is  $-0.75 \text{ eV}$  for Co dimer nucleation on terraces.

From the examples in Fig. 3 we can see how surface energetics may play a role in step edge restructuring for  $\langle 100 \rangle$  steps [Figs. 3(a)–3(d)] and  $\langle 110 \rangle$  oriented steps [Figs. 3(e) and 3(f)]. Surface energy is lowered significantly as a Co adatom moves along a step and is then incorporated into the step at a kink site, as in Figs. 3(a) and 3(f). Once a Co atom is incorporated into a step the energy may be lowered further by Cu atoms surrounding it, as in Figs. 3(b)–3(e). For a step initially along  $\langle 100 \rangle$ , this restructuring creates short segments of  $\langle 110 \rangle$  step edges, as in Figs. 3(b)–3(d). Cu atoms further along the step may continue to rearrange in order

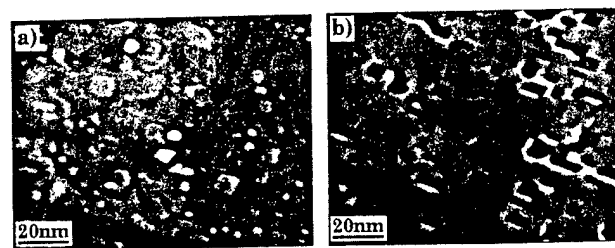


FIG. 4. (a) An 11.6 ML Co/Cu(100) film illustrating the island growth mode. (b) A 2.30 ML Co/Cu(100) film illustrating the step edge mediated growth mode.

to lengthen these  $\langle 110 \rangle$  segments, thus lowering the energy even more. Multiple Co incorporation sites along a  $\langle 100 \rangle$  step edge may then create a jagged shape such as that seen in Fig. 2(a). For a step initially along  $\langle 110 \rangle$ , the restructuring will be slightly different. Step edges will still want to be along  $\langle 110 \rangle$ , therefore more rearrangement of Cu atoms will be necessary in order to surround the Co atoms and maintain  $\langle 110 \rangle$  steps. An example of this can be seen in Fig. 2(d), where the original step edge direction and the direction of the restructured step are principally along  $\langle 110 \rangle$ . This difference between a step initially along  $\langle 100 \rangle$  and  $\langle 110 \rangle$  may be responsible for the island and step edge mediated growth modes. Incorporation into a step is much more energetically favorable at a  $\langle 110 \rangle$  kink site, Fig. 3(f), than at a  $\langle 100 \rangle$  kink site, Fig. 3(a). If a step is initially along  $\langle 110 \rangle$  and the terrace width is relatively narrow, the step edge growth mode may dominate. If a step is initially along  $\langle 100 \rangle$ , then fewer Co atoms will be incorporated into the step, and the island growth mode may dominate. For highly curved steps and intermediate orientations a combination of the two growth modes will be present.

For higher coverages the island growth mode proceeds as simultaneous multilayer growth. By about 0.8 ML coverage, a second layer typically covers about 10% of the first layer. The first layer is almost completely filled in by about 2 ML coverage, except for the pits described earlier, which vary in size and density between different films. Three layers are easily distinguished for subsequent coverages, with the top layer oscillating between about 1% and about 50% coverage. An example is shown in Fig. 4(a). In this 11.6 ML film, three layers are clearly seen. The top layer covers about 10% of the surface, the next layer about 50%, and the lower layer about 40%. The dark bands are believed to be misfit dislocations along  $\langle 110 \rangle$ .

When the step edge mediated growth mode is dominant, higher coverages of films grow somewhat differently. The etching features in the steps begin to form rectangular shapes, then eventually become separate rectangular pits. As growth continues, these pits slowly fill in. An example of such a film is shown in Fig. 4(b), which is the film shown in Fig. 2(c) after another 2 ML of Co has been deposited (2.3 ML total). Most of the pits in this film were probably formed at steps, some of which were in step bands and some of which were single height steps in the middle of terraces. The recorded intensity contrast in this micrograph can be separated

rated into three levels: the brightest (topmost) which occupies ~50% of the surface area, the middle which occupies ~40% of the surface area, and the pits which occupy ~10%. Since the pits (bare substrate) occupy 10% of the surface area, two layers of coverage would require 1.8 ML of growth. Another 0.5 ML of growth would then cover ~50% of the surface. This is consistent with 2.3 ML total coverage. We have analyzed many such micrographs with similar results, indicating that growth occurs by incomplete single layers rather than bilayers. The average pit size for this micrograph is  $9.8 \pm 6.9 \text{ nm}^2$ , and the pit density is  $7 \times 10^3/\mu\text{m}^2$ . We cannot determine whether the topmost layer consists of Cu or Co.

The growth mechanisms of these films are clearly quite complicated. We have identified two growth modes that appear to contribute to the morphology: island growth and step edge mediated growth. We have shown how surface energy considerations may be used to help explain the beginning stages of these growth modes, and how step orientation may cause one mode to be dominant. In later stages, we expect some combination of surface and strain energies to be responsible for the observed morphology.

#### IV. MAGNETIC PROPERTIES

Co/Cu(100) films grown in this study became ferromagnetic at RT at about 1.7 ML, regardless of the growth mode. For films exhibiting nearly pure island growth, this corresponded to complete coverage of the first layer. Zero field susceptibility in the paramagnetic regime and remanence in the ferromagnetic regime generally increase with coverage. In many of our films we detected a second magnetic phase with out-of-plane remanence and a coercivity 5–10 times larger than the in-plane value. There appears to be a correlation between out-of-plane remanence and terrace width. We did not detect out-of-plane remanence in any films with >100 nm terrace width, and out-of-plane remanence appeared to be more likely to occur for very narrow terraces (<50 nm).

We consider four possible causes for the out-of-plane remanence. One possibility is that {111} surfaces are created by {110} steps bunched completely together. This could happen in the walls of the pits, or along step bands. The {111} surface atoms have biaxial in-plane anisotropy<sup>29</sup> oriented along {110} directions, thus their easy axis could be aligned at 45° from the sample normal. For the sample in Fig. 4(b), ~5% of the area could be composed of such surfaces. A second possible cause is due to the growth process described earlier. If a large number of Co atoms are surrounded by Cu atoms at steps, then an alloy could be formed. Evidence for perpendicular remanence has been reported for Co–Cu alloys,<sup>2</sup> however the authors did not report a larger polar coercivity. The third possibility is that of a Cu capping layer, which also has been shown to produce perpendicular remanence.<sup>8</sup> Different coercivities could be the result of changes in Cu overlayer thickness.<sup>12</sup> Other groups<sup>16,17</sup> report Cu overlayers forming upon annealing, concurrent with the formation and growth of pits, through which they believe the

Cu is migrating. Since pits form in our surfaces during growth at RT, it is possible that Cu is also migrating to the surface through these pits.

The fourth possibility is due to the uniaxial anisotropy of atoms along the bottom of a {110} step (denoted “step corner” by Chuang *et al.*<sup>29</sup>). The easy axis is canted 45° from the sample normal and aligned along the step direction.<sup>29</sup> The magnetization of these atoms may couple to neighboring atoms, creating an out-of-plane component in the affected atoms. We have performed one-dimensional (1D) micromagnetic calculations which indicate that this may be a significant effect for regions magnetized parallel to the step direction. Continued work in this area is in progress and will be published at a later date.<sup>30</sup>

We have examined the RT macroscopic magnetic properties of Co/Cu(100) films grown at RT, as well as the associated film morphology. We find that films which exhibit the island growth mode become ferromagnetic when the first Co layer is essentially complete. Films which exhibit a combination of the island and step edge mediated growth modes become ferromagnetic at the same coverage (~1.7 ML), however this does not correspond to complete coverage of the first Co layer. We have detected out-of-plane remanence in many films, and offered several possible explanations for its existence.

#### ACKNOWLEDGMENTS

The authors would like to thank Akira Sugawara for useful discussions and Dmitry Streblechenko for his image processing program. This work is supported by the Office of Naval Research under Grant No. N00014-93-1-0099.

<sup>1</sup>N. D. Mermin and H. Wagner, *Phys. Rev. Lett.* **17**, 1133 (1966).

<sup>2</sup>M. T. Kief, G. J. Mankey, and R. F. Willis, *J. Appl. Phys.* **70**, 5929 (1991).

<sup>3</sup>C. M. Schneider, P. Bressler, P. Schuster, J. Kirschner, J. J. de Miguel, and R. Miranda, *Phys. Rev. Lett.* **64**, 1059 (1990).

<sup>4</sup>G. J. Mankey, M. T. Kief, and R. F. Willis, *J. Vac. Sci. Technol. A* **9**, 1595 (1991).

<sup>5</sup>F. Huang, M. T. Kief, and G. J. Mankey, *Phys. Rev. B* **49**, 3962 (1994).

<sup>6</sup>J. J. De Miguel, A. Cebollada, J. M. Gallego, S. Ferrer, R. Miranda, C. M. Schneider, P. Bressler, J. Garbe, K. Bethke, and J. Kirschner, *Surf. Sci.* **211**, 732 (1989).

<sup>7</sup>F. O. Schumann and J. A. C. Bland, *J. Appl. Phys.* **73**, 5945 (1993).

<sup>8</sup>P. Krams, F. Lauks, R. L. Stamps, B. Hillebrands, and G. Guntherodt, *Phys. Rev. Lett.* **69**, 3674 (1992).

<sup>9</sup>D. Kerkmann, D. Pescia, and R. Allenspach, *Phys. Rev. Lett.* **68**, (1992).

<sup>10</sup>T. Beier, H. Jahrreiss, and D. Pescia, *Phys. Rev. Lett.* **61**, 1875 (1988).

<sup>11</sup>D. Kerkmann, *Appl. Phys. A* **49**, 523 (1989).

<sup>12</sup>F. O. Schumann, M. E. Buckley, and J. A. C. Bland, *J. Appl. Phys.* **76**, 6093 (1994).

<sup>13</sup>B. N. Engel, M. H. Wiedmann, R. A. Van Leeuwen, and C. M. Falco, *Phys. Rev. B* **48**, 9894 (1993).

<sup>14</sup>H. Li and B. P. Tonner, *Surf. Sci.* **237**, 141 (1990).

<sup>15</sup>S. Ferrer, E. Vlieg, and I. K. Robinson, *Surf. Sci. Lett.* **250**, L363 (1991).

<sup>16</sup>A. K. Schmid, D. Atlan, H. Itoh, B. Heinrich, T. Ichinokawa, and J. Kirschner, *Phys. Rev. B* **48**, 2855 (1993).

<sup>17</sup>M. Giesen, F. Schmitz, and H. Ibach, *Surf. Sci.* **336**, 269 (1995).

<sup>18</sup>A. Berger, U. Linke, and H. P. Oepen, *Phys. Rev. Lett.* **68**, 839 (1992).

<sup>19</sup>M. T. Kief and W. F. Egelhoff, Jr., *Phys. Rev. B* **47**, 10 785 (1992).

<sup>20</sup>K. R. Heim, S. D. Healy, Z. J. Yang, J. S. Drucker, G. G. Hembree, and M. R. Scheinfein, *J. Appl. Phys.* **74**, 7422 (1993).

<sup>21</sup>Z. J. Yang and M. R. Scheinfein, *J. Appl. Phys.* **74**, 6810 (1993).

<sup>22</sup>D. Streblechenko (private communication).

- <sup>23</sup>G. Ehrlich and F. Hudda, *J. Chem. Phys.* **44**, 1039 (1966).
- <sup>24</sup>J. A. Venables, G. D. T. Spiller, and M. Hanbucken, *Rep. Prog. Phys.* **47**, 399 (1984).
- <sup>25</sup>There is evidence that the diffusion barrier for motion along a step is lower than the barrier for diffusion across a terrace. See, for example, P. Stoltze, *J. Phys. Condens. Matter* **6**, 9495 (1994) and references therein.
- <sup>26</sup>L. Z. Mezey and J. Giber, *Jpn. J. Appl. Phys.* **21**, 1569 (1982).
- <sup>27</sup>Y. W. Lee, K. C. Russell, and H. I. Aaronson, *Scr. Metall.* **15**, 723 (1981).
- <sup>28</sup>J. J. Miguel, *Surf. Sci.* **189/190**, 1062 (1987).
- <sup>29</sup>D. S. Chuang, C. A. Ballentine, and R. C. O'Handley, *Phys. Rev. B* **49**, 15 084 (1994).
- <sup>30</sup>S. T. Coyle, G. G. Hembree, and M. R. Schein, *J. Vac. Sci. Technol. A*, these proceedings.



# Room-temperature dipole ferromagnetism in linear-self-assembling mesoscopic Fe particle arrays

Akira Sugawara\* and M. R. Scheinfein

Department of Physics and Astronomy, Arizona State University, Tempe, Arizona 85287-1504

(Received 15 May 1997)

Quasi-one-dimensional, nanometer-diameter Fe particle arrays have been prepared by self-organized shadow growth on regularly faceted NaCl (110) surfaces. A room-temperature dipole-ferromagnetic phase was observed for linear arrays of Fe particles with radii larger than 2.5 nm. Surface magneto-optic Kerr magnetization curves indicate easy-axis alignment along the rows of particles. Remanence and coercivity were strong functions of particle diameter and linear island density. Experimental results are compared with Monte Carlo micromagnetics calculations, which, with no free parameters, reproduce the experimental observations. [S0163-1829(97)50438-3]

Magnetic particle systems are ideal for studying interactions and phase transitions,<sup>1</sup> and are also of interest for application to high-density magnetic storage devices. Recent experiments in surface and low-dimensional magnetism have focused on the properties of surfaces and small particles in order to explore the structure and dynamics of interactions at small length scales. Advanced synthesis methods for the preparation of transition-metal nanoclusters,<sup>2</sup> ordered nanoscale dot-arrays,<sup>3</sup> nanostructured magnetic-networks,<sup>4</sup> submicron<sup>5</sup> and nanometer width wires,<sup>6</sup> and random two-dimensional arrays<sup>7</sup> allow new and unusual magnetic phases to be explored. Although the Néel and Brown<sup>8</sup> theories for relaxation in isolated magnetic particles predict relaxation times that are less than microseconds for 6-nm- (bulk-anisotropy) diameter Fe particles at room temperature, closely packed mesoscopic linear arrays can be remanent and coercive (ordered).<sup>9</sup> Long-range interactions have been studied by ferromagnetic resonance,<sup>10</sup> Mössbauer spectroscopy,<sup>9,11</sup> mean field calculations<sup>12</sup> and Monte Carlo simulations.<sup>7</sup> Identifying the mechanism underlying the interactions is facilitated by the preparation of 3d-transition metal islands in and on insulators like SiO<sub>2</sub> (Ref. 10), MgO (Ref. 10), and CaF<sub>2</sub> (Ref. 7), which guarantees that particles do not couple through electronic states in the substrate. Here, we report on the observed and computed magnetic properties in linear self-assembling arrays of nanometer-diameter Fe particles. The formation of linear arrays intrinsically breaks the symmetry in the interaction Hamiltonian, thereby stabilizing long-range order. Self-assembly<sup>6,13</sup> is used to form rows of closely packed ( $2.1 \times 10^{12}/\text{cm}^2$ ) nanometer-diameter Fe islands on an amorphous, insulating substrate (SiO). Self-assembly<sup>13</sup> facilitates the fabrication of macroscopic (3 mm $\times$ 3 mm) arrays, which would take prohibitively long to define using an electron-beam or scanning-tunneling microscope-based lithography (e.g., Ref. 3). The Fe island radius, island density, the width and separation of the linear island arrays can be varied experimentally in the self-assembled growth process for exploring new magnetic phases. Here, we demonstrate how particle diameter in linear magnetic island arrays can be varied to establish a dipole-induced ferromagnetic state above room temperature.

The linear self-assembling arrays of nanometer-diameter Fe particles are prepared in UHV ( $2.0 \times 10^{-10}$  mbar). A

schematic depicting the deposition process is shown in Fig. 1. A polished and H<sub>2</sub>O-etched single crystal of NaCl (110) is annealed *in situ*. Regular (nano) grooves result when {100} planes form (facet). This reduces the surface free energy by reducing the area of high-energy (110) planes.<sup>13</sup> The spacing of the grooves is a function of the annealing temperature and time. Ten minutes of annealing at 380 °C produce an average trough-to-trough groove spacing of 40 nm. The Fe islands should be randomly oriented and polycrystalline since the goal is to examine the influence of the geometrical particle alignment independent of any intrinsic spin-orbit-induced crystal fields. This is accomplished by coating the NaCl surfaces with an amorphous SiO layer; SiO prevents any epitaxial alignment between the Fe islands and the single crystal NaCl. Fe was deposited from an electron-beam evaporator aligned 70° off the template normal. We show results from three different nominal Fe thicknesses ( $t=0.3, 0.6, 1.0$  nm) grown at a rate of 0.03 nm/min (normal to the terraces) on a substrate heated to 190 °C (thickness as defined in Ref. 7). Fe adatoms agglomerate on SiO in a three-dimensional nucleation and growth mode, where the elevated temperature decreases the nucleation density and liquidlike coalescence is enhanced. The Fe islands are expected to nucleate in the narrow bands exposed to the Fe flux, which here comprise 27% of the ridge-to-ridge distance (10 nm). After Fe deposition, the surface was covered with a 10-nm SiO passivation overlayer.

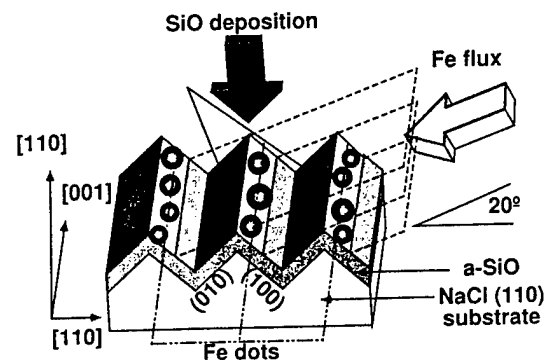


FIG. 1. Schematic depiction of the preparation of self-assembling nanometer-diameter arrays of Fe islands (see text).

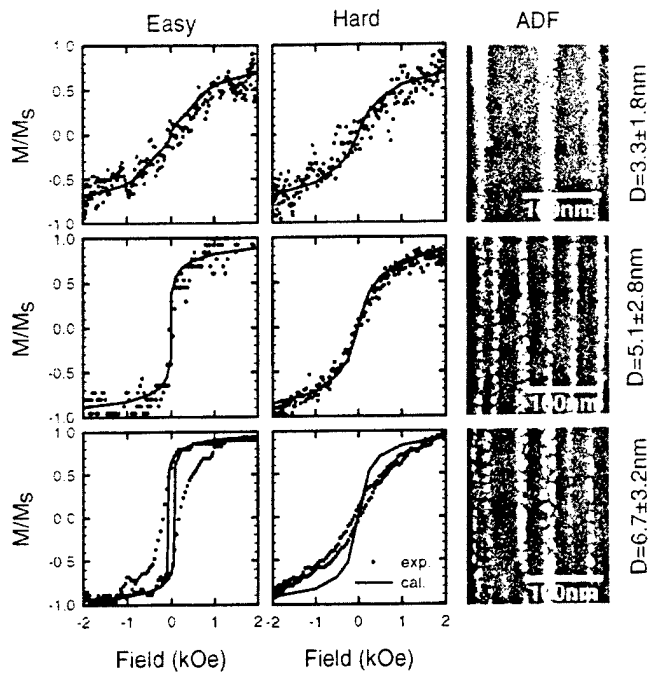


FIG. 2. Magnetic and structural properties of linear arrays of Fe particles of nominal diameter  $D = 3.3$  nm (top row),  $5.1$  nm (middle row), and  $6.7$  nm (bottom row). SMOKE hysteresis loops taken along the easy direction, along the wire (left most column), and perpendicular to the wire, the hard direction, (center column) are shown with solid symbols. The Monte Carlo micromagnetics simulated hysteresis loops are plotted with solid lines. ADF-STEM images of each linear array are shown (right most column) for each nominal particle size.

The microstructure in the linear arrays was examined using conventional transmission electron microscopy, TEM (Topcon EM-002B) and high resolution annular dark-field scanning transmission electron microscopy, ADF-STEM (VG HB-501). Results are given in Fig. 2. The column of images on the right-hand side displays ADF-STEM images of ultrafine particle arrays, with the different (nominal) island diameters indicated. The separated and distinct islands are seen in bright contrast and are aligned parallel to the nanogrooves. Electron diffraction patterns, formed from irradiating large numbers of Fe islands, showed that these islands were randomly oriented polycrystalline bcc Fe. No iron oxide phases were detected. Particles along the lines are clearly separated, and the large interline distance is clearly visible. Typically, lines of particles have a length of  $1\text{--}10\text{ }\mu\text{m}$ ; the aspect ratio is about 100:1. The intermediate contrast between particles results from fluctuations in the SiO underlayer and overlayer thicknesses, and is not related to the Fe. No particle-to-particle crystalline orientation, and no interparticle lattice fringes (bridges) were detected in HRTEM images (not shown). Particle size statistics were obtained by image analysis of several  $200\times 200\text{ nm}^2$  areas for each film. The particle size statistics are summarized in Table I.

The microstructural evolution driving the formation of the linear arrays is dominated by the high Fe island nucleation density ( $>2\times 10^{12}\text{ cm}^{-2}$ ) in areas exposed to the Fe flux. The initial distance between nuclei ( $<7\text{ nm}$ ), and the initial island diameter ( $<2\text{ nm}$ ) is smaller than the width of the

TABLE I. Average particle diameter (mean diameter of island-size distribution), island density and interparticle spacing for the Fe particle arrays grown at  $190\text{ }^\circ\text{C}$ . The nucleation density is normalized to the area exposed to Fe flux, i.e., the array wire width.

Thickness (nm)	Diameter (nm)	Density ( $\text{nm}^{-2}$ )	Spacing (nm)
0.3	$3.3\pm 1.8$	0.0216	6.8
0.6	$5.1\pm 2.8$	0.0136	8.6
1.0	$6.7\pm 3.2$	0.0118	9.2

area exposed to the Fe flux. Several islands can nucleate across the area exposed to the Fe flux. A small amount of Fe might escape from the flux zone due to the adatom concentration gradient formed at the shadow edge. However, this effect appears to be negligible since most adatoms are effectively captured by pre-existing islands. At later stages of growth at  $190\text{ }^\circ\text{C}$  substrate temperatures, liquidlike coalescence of smaller islands keeps the Fe island perimeters circular (ADF images in Fig. 2). Elevated substrate temperatures round the Fe island surface quickly enough to reduce the surface-energy penalty caused by two neighboring islands that are touching. In contrast, at room temperature, thin wire arrays are formed<sup>6</sup> at an early stage because of slow Fe self-diffusion on the surface. Since the Fe island diameter is on the same order as the terrace width in  $D = 6.7\text{ nm}$  case, the microstructure approaches a one-dimensional linear particle array.

The magnetic properties of the arrays were measured *ex situ* at room temperature using the longitudinal magneto-optical Kerr effect (SMOKE).<sup>14</sup> In Fig. 2, results are shown for linear arrays of Fe particles of nominal diameter  $D = 3.3\text{ nm}$  (top row),  $5.1\text{ nm}$  (middle row), and  $6.7\text{ nm}$  (bottom row). Experimental SMOKE hysteresis loops are shown with solid symbols. Loops were taken along the easy direction, along the wire array (left most column), and perpendicular to the wire array, in the hard direction (center column). Kerr loop acquisition times were on the order of seconds to ensure that equilibrium magnetization configurations were measured. The computed hysteresis loops from Monte Carlo micromagnetics<sup>7</sup> simulations are plotted with solid lines.

Monte Carlo models were used to evaluate the magnetic properties of the linear arrays as a function of particle radius and density<sup>7,15</sup> because the Monte Carlo method rigorously accounts for fluctuations. Simulations used periodic boundary conditions, and between 200 and 400 islands randomly arranged into 3 to 5 wires. The model employs an all-orders interparticle interaction Hamiltonian.<sup>7</sup> As input, the model uses the bulk saturation magnetization value, an adjustable externally applied field and the experimental-size distribution of Fe islands given in Table I. The average island diameter is the mean diameter of the island-size distribution. The variation in the island diameter is the standard deviation of the Gaussian fit to the island-size distribution. The slightly irregular experimental island shapes are approximated by cylinders. The cylindrical approximation is justified because there is no orientational order in the films (except the lines) and the intrainland demagnetization fields due to random individual island orientation averages out over the entire film surface. Hysteresis loops are calculated by finding an equi-

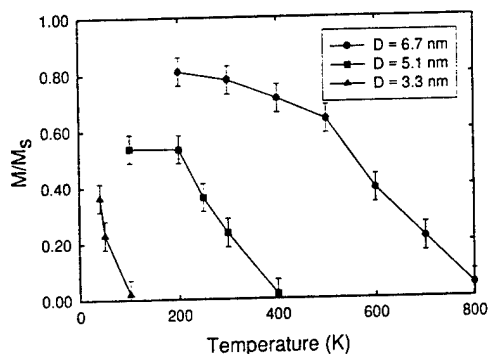


FIG. 3. Order parameter ( $M_{\text{along wire}}/M_s$ ) as a function of temperature and nominal Fe island diameter computed from Monte Carlo micromagnetics.

librium magnetization distribution for an externally applied field value. The magnetization accumulators are reset, the external field value changed, and the previous final magnetization state is preserved as the initial distribution for the next Monte Carlo cycle.

Figure 3 shows the computed normalized magnetization as a function of temperature for the three distributions of islands given in Table I and shown in Fig. 2. The ordering temperature increases with increasing particle diameter as in the two-dimensional random array case.<sup>7</sup> Increasing the number of lines and changing the particle distribution for alternative random seeds produce a 10% variation in the remanence, as indicated by the error bars in Fig. 3. In contrast to the two-dimensional case, the linear arrays order globally rather than locally. This demonstrates that the linear particle arrays order ferromagnetically due to interparticle magnetostatic dipole fields. This is solely due to the symmetry breaking in the geometric structure of the array. For particles of the appropriate size and proximity, room temperature dipole ferromagnetism can be observed. If only bulk anisotropy were present, the arrays would be superparamagnetic at room temperature. Interface anisotropy, which can be orders of magnitude larger than volume anisotropy in thin film systems, has no preferred in-plane orientation and thus cannot be responsible for the long-range order. With typical demag-

netization factors of  $\frac{1}{2}$  for cylinders in-plane, the stray fields external to the particles can be as high as 10 kOe, with stray field decay lengths set by the particle diameter. The close proximity of the particles forces neighboring particles to lie in each others (large) stray field resulting in long-range order.

A transition to a room temperature, remnant and coercive ferromagnetic state is observed with increasing island diameter (Fig. 2). The easy axis hysteresis loop for  $D = 5.1$  nm shows an abrupt jump in both the experimental ( $H_c < 5$  Oe, our experimental resolution limit) and computed ( $H_c < 1$  Oe) loops. Figure 3 shows that this array is just at the transition to its ordered state at room temperature. The larger islands,  $D = 6.7$  nm, show easy axis remanence and coercivity in both measured and computed hysteresis loops. The predictive value of the model with no free parameters is evident in Fig. 2. Dipole ferromagnetically ordered films have an easy axis along the wire since the shape anisotropy in that direction is small. Since the particles have no preferential crystallographic orientation in the film plane, magnetocrystalline anisotropy is also negligible. Therefore, the anisotropy that orders the array is ascribed to the strong magnetic interaction between self-aligned particles.

We have fabricated mesoscopic linear arrays of Fe particles whose size and spacing allow them to couple through the interparticle magnetostatic field and order ferromagnetically, even at room temperature. The experimentally determined magnetic properties of these arrays were compared to those predicted by a Monte Carlo micromagnetics simulation with no free parameters. The computation predicts global ordering at room temperature through dipole fields, and the computed hysteresis loops accurately reproduce the results of the experiment.

We are indebted to G. Hembree and S. Coyle for technical support and valuable discussions. We have also benefited from valuable discussions with K. Schmidt and J. Venables. This work was supported by the Office of Naval Research under Grant No. N00014-93-1-0099. The microscopy was performed at the Center for High Resolution Electron Microscopy at Arizona State University. A.S. was supported by JSPS.

\*Present address: JAIST, 1-1 Asahi-dai, Tatsunokuchi, Ishikawa, 923-12, Japan.

<sup>1</sup>D. C. Mathis, *The Theory of Ferromagnetism II* (Springer-Verlag, Berlin, 1985); H. E. Stanley, *Introduction To Phase Transitions and Critical Phenomena* (Oxford University Press, London, 1971).

<sup>2</sup>C. P. Gibson and K. J. Putzer, *Science* **265**, 1338 (1995).

<sup>3</sup>T. Takeshita, Y. Suzuki, H. Akinaga, W. Mizutani, K. Tanaka, T. Katayama, and A. Itoh, *Appl. Phys. Lett.* **68**, 3040 (1996); M. Hehn, K. Ounadjela, J.-P. Bucher, F. Rousseaux, D. Decanini, B. Bartenlian, and C. Chappert, *Science* **272**, 1782 (1996); S. Y. Chou, P. R. Krauss, and L. Kong, *J. Appl. Phys.* **79**, 6101 (1996); R. D. Gomez, M. C. Shih, R. M. H. New, R. F. Pease, and R. L. White, *ibid.* **80**, 342 (1996); S. Gidar, J. Shi, P. F. Hopkins, K. L. Chapman, A. C. Gossard, D. D. Awschalon, A. D. Kent, and S. von Molnár, *Appl. Phys. Lett.* **69**, 3269 (1996).

<sup>4</sup>J. A. Barnard, H. Fujiwara, V. R. Inturi, J. D. Jarratt, T. W. Scharf, and J. L. Weston, *Appl. Phys. Lett.* **69**, 2758 (1996).

<sup>5</sup>A. O. Adeyeye, G. Lauhoff, J. A. C. Bland, C. Daboo, D. G. Hasko, and H. Ahmed, *Appl. Phys. Lett.* **70**, 1046 (1997).

<sup>6</sup>A. Sugawara, S. T. Coyle, G. G. Hembree, and M. R. Scheinfein, *Appl. Phys. Lett.* **70**, 1043 (1997).

<sup>7</sup>M. R. Scheinfein, K. E. Schmidt, K. R. Heim, and G. G. Hembree, *Phys. Rev. Lett.* **76**, 1541 (1996); K. R. Heim, G. G. Hembree, K. E. Schmidt, and M. R. Scheinfein, *Appl. Phys. Lett.* **67**, 2878 (1995).

<sup>8</sup>L. Néel, *Ann. Geophys.* **5**, 99 (1949); A. Aharoni, *Introduction To The Theory Of Ferromagnetism* (Oxford Science, Oxford, 1996).

<sup>9</sup>S. Mørup, *Phys. Rev. Lett.* **72**, 3278 (1994); S. Mørup and G. Christiansen, *J. Appl. Phys.* **73**, 6955 (1993); S. Mørup, *Hyperfine Interact.* **60**, 959 (1990); S. Mørup, P. H. Christensen, and B. S. Clausen, *J. Magn. Magn. Mater.* **68**, 160 (1987); S. Mørup, M. B. Madsen, J. Franck, J. Villadsen, and C. J. W. Koch, *ibid.* **40**, 163 (1983).

<sup>10</sup>W.-N. Wang, Z.-S. Jiang, and Y.-W. Du, *J. Appl. Phys.* **78**, 6679

- (1995); S. Matsuo, T. Matsuura, I. Nishida, and N. Tanaka, Jpn. J. Appl. Phys., Part 1 **33**, 3907 (1994).
- <sup>11</sup>S. Linderith, L. Balcells, A. Labarta, J. Tejada, P. V. Hendriksen, and S. A. Sethi, J. Magn. Magn. Mater. **124**, 269 (1993).
- <sup>12</sup>M. El-Hilo, K. O'Grady, and R. W. Chantrell, J. Magn. Magn. Mater. **114**, 295 (1992).
- <sup>13</sup>A. Sugawara, Y. Haga, and O. Nittono, J. Magn. Magn. Mater. **156**, 151 (1996).
- <sup>14</sup>Z. J. Yang and M. R. Scheinfein, J. Appl. Phys. **74**, 6810 (1993).
- <sup>15</sup>N. Metropolis, A. W. Rosenbluth, M. N. Rosenbluth, A. H. Teller, and E. Teller, J. Chem. Phys. **21**, 1087 (1953).

# Self-organized mesoscopic magnetic structures

Akira Sugawara,<sup>a)</sup> G. G. Hembree, and M. R. Scheinfein<sup>b)</sup>

Department of Physics and Astronomy, Arizona State University, PSF-470, Box 871504, Tempe, Arizona 85287-1504

(Received 23 June 1997; accepted for publication 5 September 1997)

Three types of mesoscopic magnetic microstructure have been formed using self-organization: linear arrays of nanometer diameter islands, nanometer width lines, and undulating, continuous films. These structures were produced by annealing NaCl (110) and (111) surfaces *in situ* to produce patterned templates with 10–100 nm periodicity. Growth parameters such as groove spacing, substrate temperature and total deposit thickness can be varied in order to define specific mesoscopic magnetic structures. The microstructural evolution during growth is discussed in the context of nucleation and coalescence kinetics. The resulting magnetic properties are described, and their connection to the underlying microstructure elucidated. © 1997 American Institute of Physics. [S0021-8979(97)08323-0]

## I. INTRODUCTION

Mesoscopic magnetic microstructures such as dot and wire arrays are of fundamental interest in the study of coupling and ordering phenomena. From a technological point of view, mesoscopic magnetic structures may produce the future topologies for magnetic storage media. For example, three-dimensional random particle arrays prepared by co-deposition of magnetic and nonmagnetic materials have good high-frequency response and giant magnetoresistance (e.g., Ref. 1). The magnetic properties of these structures depend strongly on the size and spacing of the particles, the concentration of the magnetic element, the growth rate and the substrate temperature (e.g., Ref. 2). Since heterogeneous magnetic particle composites do not have geometrical order, there is no anisotropy in the film plane. However, in-plane anisotropy can be developed by controlling the shape and the spacing of the particles such that the magnetic switching which is characterized by the subtle balance between anisotropy, self-energy, magnetic coupling between particles, and thermal agitation will be well defined.

Specimens with well-defined in-plane anisotropy resulting from specific mesoscopic, geometrical configurations including nanometer size dot and wire arrays have been fabricated by laser-focused atomic deposition,<sup>3</sup> electron lithography<sup>4</sup> and local chemical decomposition of metal-organic gas with a scanned probe.<sup>5</sup> Switching mechanisms in these arrays have been studied by magnetic force microscopy.<sup>5</sup> The throughput for producing nanometer size-scale structures with lithographic methods may be low,<sup>6</sup> and the large areas required for studying macroscopic and collective magnetic properties can be difficult if not impossible to process.

In contrast, our approach is based on self-organization: regular patterns are spontaneously formed in a nonequilibrium system, as in the self-assembling preferential nucleation of hexagonal Co dot arrays on the reconstructed Au(111)

surface.<sup>7</sup> We use self-assembly through shadow deposition on patterned templates, i.e., the self-masking caused by large-scale surface features. This is a geometrical effect which does not depend strongly on the deposited material. Our method is similar to that proposed by Shinjo<sup>8</sup> who grew a wire array by shadow deposition on a sub-micrometer spaced Si grating that was fabricated by lithography and selective etching. By contrast, we prepare grating templates by self-organization on NaCl noncleavage [(110) or (111)] planes which become faceted and patterned regularly after thermal annealing.<sup>9</sup> This method allows 10–100 nm spaced, statistically uniform grooves to be formed across centimeter lengths in tens of minutes, although the regularity of the grooves produced by this method is less than that produced lithographically.<sup>10</sup>

We have investigated the relationship between the microstructure and such growth conditions as the annealing temperature of NaCl before deposition, growth temperature and the incident angle of the deposited Fe flux, and the effect on the resultant macroscopic magnetic properties. Three types of the microstructure are described; linear dot arrays, wire arrays, and undulating continuous films. The evolution of the microstructure is explained in terms of nucleation and coalescence kinetics associated with island growth. The magnetization switching processes in these mesostructures which is quite different from those ascribed to flat, continuous Fe films, are also described.

## II. EXPERIMENTAL PROCEDURE

Optical-grade (111) and (110) polished NaCl single crystals (miscut angle  $<3^\circ$ ) were used as substrates.<sup>11</sup> These substrates were etched in de-ionized water for several seconds to remove surface contamination prior to loading into an ultrahigh vacuum growth chamber (base pressure  $\sim 3 \times 10^{-8}$  Pa) equipped with Fe electron-beam and SiO thermal evaporation sources. Annealing these substrates *in situ* produces ordered templates. The annealed (110) oriented substrates form long, straight in-plane macrosteps along [001] as shown in Fig. 1(a). The (100) and (010) terraces which result from the thermal annealing process are tilted by  $45^\circ$  with respect to the surface normal. When Fe is deposited at an

<sup>a)</sup>Present address: Schools of Materials Science, Japan Advanced Institute of Science and Technology, Asahi-dai 1-1, Tatsunokuchi, Ishikawa 923-12, Japan.

<sup>b)</sup>Electronic mail: michael.scheinfein@asu.edu

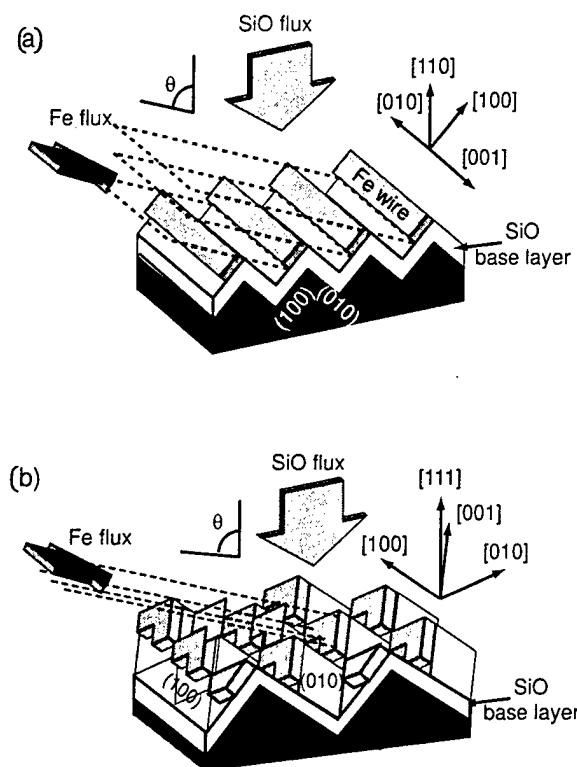


FIG. 1. Schematic deposition geometry on (a) (110) and (b) (111) templates. The NaCl surface becomes faceted by {100} planes, and long and straight macrosteps run parallel to <100> directions.

angle  $\theta$  with respect to the surface normal  $[1\bar{1}0]$  direction, terraces exposed to the flux nucleate islands which can coalesce and form rectangular wires. When (111) oriented NaCl crystals are annealed, three crystallographically equivalent out-of-plane <100> steps appear as shown in Fig. 1(b). Each {100} facet is tilted by  $54.7^\circ$  from the template normal. The region exposed to the Fe flux is chevron-hat shaped. The step/chevron separation is determined by the annealing temperature and time. Annealing the NaCl at  $350\text{--}450^\circ\text{C}$  for 10–15 min produces step separations between 10 and 100 nm. A 10–15 nm SiO passivation layer was deposited directly on both types of stepped NaCl surfaces (normal incidence deposition) since the NaCl substrates must be removed prior to characterization using electron microscopy. The surface topography of the nano-scale stepped NaCl surface is well preserved even after the SiO coating, however, the smooth surface masks the single atomic steps on the NaCl, which might serve as preferential nucleation sites. This also prevents the Fe from establishing an epitaxial relationship with the single crystal substrates which is important in island coupling (strength) studies.

Fe was deposited from an electron-beam evaporation source at a rate between 0.03 and 0.20 nm/min. We denote the thickness,  $t$ , to be that nominal thickness on an exposed terrace in the direction normal to that terrace, e.g.,  $45^\circ$  off of the (macroscopic) template normal for annealed (110) substrates. The substrate holder could be rotated with respect to the Fe flux direction so that the incident angle of the flux,  $\theta$ , could be varied from  $0^\circ$  (normal) to  $80^\circ$  (Fig. 1). This rota-

tion allowed for a systematic change of the patch (terrace) width exposed to the Fe flux. The substrate holder could also be translated with respect to the source. A masked substrate was used such that three different thickness films could be grown during a single experiment. After Fe deposition, a 10–15 nm SiO capping layer was deposited to prevent oxidation upon removal from ultrahigh vacuum (UHV). Thus, the magnetically active Fe layer was embedded in a SiO matrix.

Hysteresis loops were recorded *ex situ* using the longitudinal magneto-optical Kerr effect (MOKE).<sup>12</sup> Since both SiO and NaCl are transparent at the He–Ne laser wavelength, and the Fe films were extremely thin, the Kerr intensity was very small. The  $2F$  (first harmonic of the photoelastic modulator) mode<sup>12</sup> was employed in order to obtain as high a signal-to-noise ratio as possible. Both the sample and the magnet could be rotated with respect to the optical scattering plane to examine the magnetization components parallel and perpendicular to the field, and along and perpendicular to the macrostep (groove) direction.

The microstructure was examined using conventional transmission electron microscopy [(TEM); Topcon EM-002B] and high resolution annular dark-field scanning transmission electron microscopy [(ADF-STEM), VG HB-501]. Specimens were fixed to 200-mesh Cu grids by floating the films off of the NaCl substrates in de-ionized water. ADF-STEM was required when the Fe particles were smaller than a few nanometers in diameter, and the Z contrast from the bright field images obtained by TEM was masked by background intensity from the SiO layers. The sizes of individual particles and wires were quantitatively measured using image analysis software.

### III. GROWTH MODES ON FACETED TEMPLATES

Structures grown on faceted templates include linear arrays of nanometer diameter particles, nanowires with widths of tens of nanometers and lengths of microns or more, and continuous undulating thin films. The type of structure produced depends upon the structure and length scales present in the NaCl template ( $L$ ), the incident angle used to deposit the transition metal ( $\theta$ ), and the substrate temperature during growth ( $T_g$ ). The NaCl (110) surface sublimates and facets to form (100) and (010) terraces during annealing. The depth of the grooves (peak to trough) is  $\frac{1}{2}$  the distance between peak tops or groove bottoms ( $L$ ). The surface area of the faceted surface is always  $\sqrt{2}$  times larger than the original (110) surface. Experimentally, we kept the annealing time constant (10 min) and altered the annealing temperature,  $T_a$ , in order to modify the groove spacing ( $L$ ) between 25 nm ( $T_a=380^\circ\text{C}$ ), 40 nm ( $T_a=410^\circ\text{C}$ ), and 90 nm ( $T_a=440^\circ\text{C}$ ).

The area exposed to the incident Fe flux is determined by geometrical shadowing as depicted in Fig. 1(a). The exposed terrace is shadowed by the ridge closer to the evaporation source. Since all terraces are oriented  $45^\circ$  from the surface normal, the percentage of the terrace exposed for a given source angle inclination is constant. However, the distance between exposed areas and the width of each patch can

be controlled by modifying the substrate annealing temperature  $T_a$ .

Growth temperature is an important parameter used to define microstructure. Fe grows on SiO in a three-dimensional island growth mode. The initial growth is characterized by the competing atomic processes of nucleation, adatom capture and surface diffusion. A detailed numerical analysis of this process has been carried out for the Ag/Ge system.<sup>13</sup> Some of the Fe adatoms diffuse out from the geometrically defined flux region, because an adatom concentration gradient is formed at the mask edge. The nucleation density is expected to be extremely low outside the patch due to low adatom concentration. The grooves can also be preferential nucleation sites. In later stages of growth, coalescence of neighboring islands takes place. When the growth temperature is high, the round shape of the islands is quickly recovered after two or more neighboring islands touch because surface self-diffusion is fast. This might also cause patch broadening: extending the growth front outward from the defined flux regions. Thus, by varying the separation of the flux-exposed regions through geometrical shadowing, and varying the substrate temperature during growth, different nucleation and growth regimes may be exploited in order to fabricate linear dot arrays, nanowires, and thin, undulating films.

The processes driving the formation of the linear arrays are summarized for high temperature ( $T_g = 190^\circ\text{C}$ ) and room temperature growth in Figs. 2 and 3, respectively. First, consider the (ideal) growth of a single row of islands along an exposed terrace where the island diameter is approximately equal to the patch width exposed to the deposited Fe flux [Fig. 2(a)]. The growth scheme to form a single particle width-linear array includes the initial nucleation of closely spaced islands (solid outline), adatom capture by existing islands (dotted outline), and finally coalescence (filled). In order to grow this type of array, the initial nucleation density must be in a range where the coalesced particles will be well separated. The diffusion length must be long enough to allow adatoms to incorporate into existing islands, yet short enough to forbid adatoms from diffusing across the ridge or groove to the next terrace exposed to Fe flux. For growth at  $T_g = 190^\circ\text{C}$ , the nucleation density ( $> 2 \times 10^{12} \text{ cm}^{-2}$ ) is maximum where the adatom concentration is maximum [i.e., at the patch center in Fig. 2(a)]. When the initial distance between nuclei ( $< 7 \text{ nm}$ ) and the initial island diameter ( $< 2 \text{ nm}$ ) is smaller than the width of the area exposed to the Fe flux [outlined islands in Fig. 2(a)], several islands nucleate across the exposed area. During later stages of growth with increased island size, neighboring islands come into contact with each other, but at elevated substrate temperatures, surface diffusion rounds off the Fe island surfaces quickly enough to reduce the surface-energy penalty caused when two neighboring islands are touching. After each coalescence event, the center of the new island resulting from the coalescence is near the center of the joined islands. Islands join and form one-dimensional linear arrays through this process. For a specific range of deposited Fe [e.g.,  $t = 1.0 \text{ nm}$  or, when exposed areas would have a uniform film thickness of  $1.0 \text{ nm}$  for the close-packed face of bcc Fe, (110)], the coalesced Fe

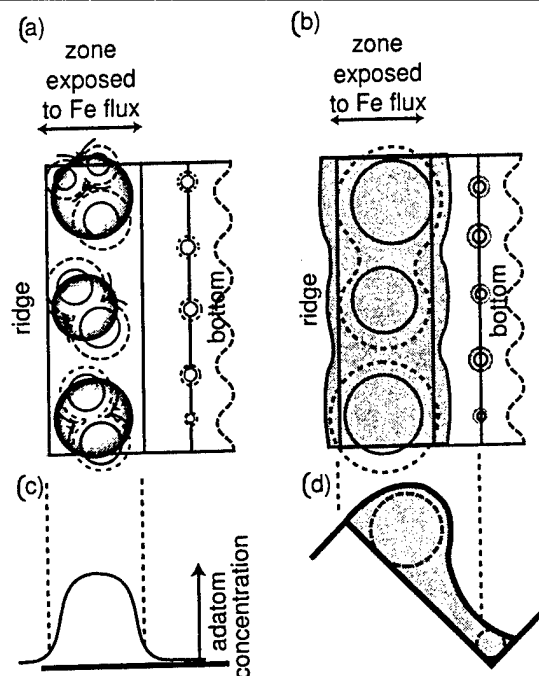


FIG. 2. Schematic evolution process of wire array at high temperature. Because of high diffusivity of Fe, the initial nucleation density is low and the coalescence kinetics are fast: (a) The initial island nucleation (solid outlined), growth (dashed outlined) and coalescence (solid). (b) At higher coverages, the islands form a continuous network and the wire broadens. (c) Concentration profile across the island array during the initial stages of growth shown in (a). The wire cross section for the structure shown in (b) after more material is deposited. A solid cross-section (asymmetric) is shown.

island diameter ( $6.7 \text{ nm}$ ) is roughly as wide as the terrace width and the microstructure approaches a one-dimensional linear particle array. Linear arrays composed of many particles across an exposed terrace can be fabricated by terminating the growth at lower coverages, thereby preventing island coalescence.

During growth at elevated temperatures ( $T_g = 190^\circ\text{C}$ ), adatom diffusion is much faster than at room temperature. Elevated temperature growth produces adatom concentration profiles that become broader at the shadow edge. This is schematically depicted in Fig. 2(c) directly beneath the island profiles in Fig. 2(a). At elevated temperatures, a small amount of Fe might escape from the flux-exposed zone due to the adatom concentration gradient formed at the shadow edge, and condense at the groove bottom. Experimentally, this effect appears to be negligible since no islands are observed outside of the area exposed to the Fe flux. This observation indicates that when the thickness is small, most adatoms are captured efficiently by pre-existing islands.

By contrast, linear arrays of nanowires can be fabricated using room temperature growth as illustrated in Fig. 3(a). For slow surface diffusion during room temperature growth, the adatom concentration is almost constant in the patch exposed to Fe flux. As a result, a high density of islands uniformly nucleates in the patch [Fig. 3(a)]. The initial islands (diameter  $< 2 \text{ nm}$ ) are so small that they cannot be clearly resolved by TEM bright-field imaging. Since the profile rapidly drops

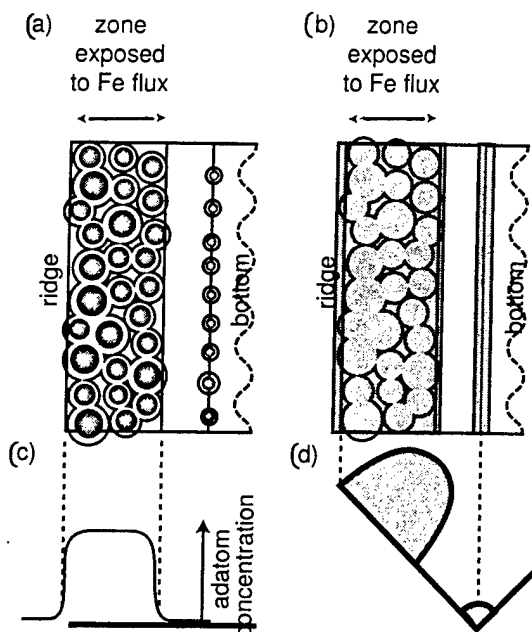


FIG. 3. Schematic evolution process of wire array at room temperature. Because of low diffusivity of Fe, the initial nucleation density is high and the coalescence kinetics are slow. (a) The initial island nucleation (solid outlined), and growth (solid). (b) At higher coverages, the islands form a continuous network. (c) Concentration profile across the island array during the initial stages of growth shown in (a). The wire cross section for the structure shown in (b). The ultrasmall wire seen in the groove sometimes results from adatom escape from the wire and nucleation in the groove.

off at the mask edge [Fig. 3(c)], the concentration gradient forces a small amount of Fe to escape from the patch and condense at the groove bottom. As such, extremely thin wires are sometimes observed at the groove bottoms. After the islands (uniformly) cover the patch exposed to the flux, the arriving adatoms are captured by pre-existing (nucleated) islands. The liquidlike coalescence kinetics are slow enough that a network forms (islands fill in) and with increasing coverage, eventually forms a wire [Fig. 3(d)], whose cross-section when filled in completely is depicted schematically in Fig. 3(d). Wire formation is commonly observed over a wide thickness range for room temperature growth. The wire perimeter boundary fluctuates on a size scale determined by the polycrystalline grain size of the individual, coalesced islands. Thus, growth of better wires with sharper edges will require deposition of fine-grained or amorphous materials.

Wire-broadening occurs during high temperature growth ( $T_g = 190^\circ\text{C}$ ) which in the extreme case may lead to bridging between adjacent terraces and the formation of continuous undulating films. The wire broadening mechanism at high growth temperatures ( $T_g > 150^\circ\text{C}$ ) is summarized in Fig. 2(b). With increasing thickness, the wire morphology is completed through a network structure as described above and seen in Fig. 2(b), however, the faster Fe surface self-diffusion causes the wires to broaden. The amount of Fe escaping from the flux-exposed patch increases causing the ultrasmall wires formed at the bottom of the grooves to be thicker than those formed at room temperature. Broadened Fe patches eventually join the wires at the groove bottom

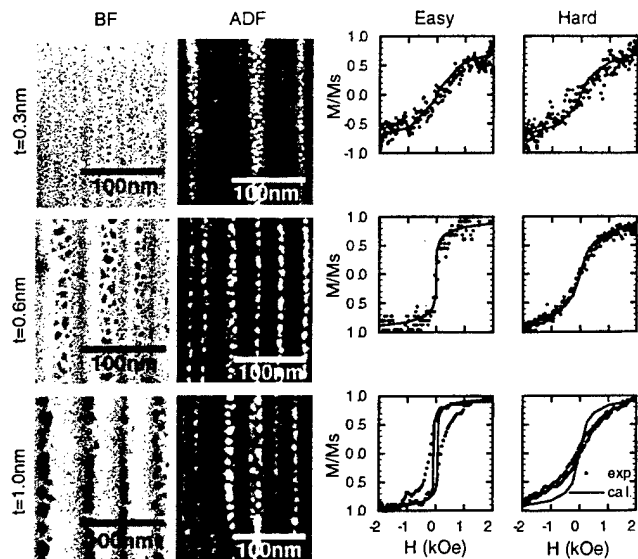


FIG. 4. Bright-field and annular dark field images and corresponding MOKE loops of one-dimensional dot arrays grown on a (110) template at  $190^\circ\text{C}$ . Linear array structures become completed with increasing Fe thickness. The MOKE loops show anisotropic behavior even though the particles are not touching. The solid lines are calculated magnetization curves from a Monte Carlo micromagnetics calculation.

causing the other side of the terrace (not the flux exposed terrace) to be partially covered. At higher coverages, the lines join and form continuous films. Naturally, continuous undulating films can also be trivially fabricated through normal incidence evaporation.

## IV. EXPERIMENTAL RESULTS

### A. Linear dot arrays

Although the Néel and Brown<sup>14</sup> theories for relaxation in isolated magnetic particles predict relaxation times that are less than microseconds for 6 nm (bulk-anisotropy) diameter Fe particles at room temperature, closely packed mesoscopic linear arrays can be remanent and coercive (ordered), since the long-range fields stabilize moments and extend relaxation times.<sup>2</sup> Such long-range interactions have been studied by ferromagnetic resonance,<sup>15</sup> Mössbauer spectroscopy,<sup>2,16</sup> mean field calculations and Monte Carlo simulations.<sup>17</sup> Isolating the coupling mechanism is facilitated by the preparation of 3d transition metal islands in and on insulators like  $\text{SiO}_2$ ,<sup>15</sup>  $\text{MgO}$ ,<sup>11</sup> and  $\text{CaF}_2$ .<sup>17</sup> This guarantees that the particles do not couple through electronic states in the substrate. Here, we show results on the observed and computed magnetic properties in linear self-assembling arrays of nanometer diameter Fe particles. The formation of linear arrays intrinsically breaks the symmetry in the interaction Hamiltonian, thereby stabilizing long-range magnetic order.

Fe grows on the  $\text{SiO}_2$  base layer in a three-dimensional nucleation and growth mode. During shadow deposition, most Fe islands are localized in the patches exposed to the flux. As shown in Fig. 2, linear dot arrays are formed during the initial stage of high temperature ( $T_g = 190^\circ\text{C}$ ) growth on (110) substrates with  $\theta = 70^\circ$ . Figure 4 shows bright field (BF) images (first column), annular dark field (ADF) images



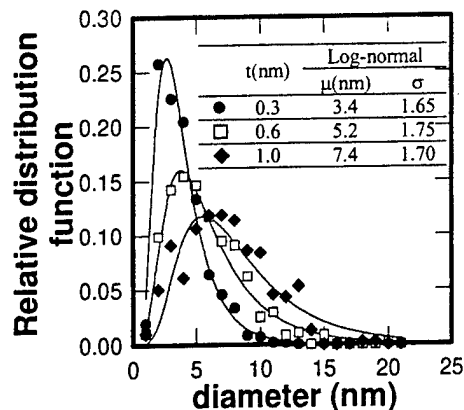


FIG. 5. Size distribution of islands. The experimental results are well fitted by log-normal distribution (solid lines). Median ( $\mu$ ) and geometrical standard deviation ( $\sigma$ ) is summarized in a table (inset).

(second column), easy axis (third column), and hard axis (fourth column) MOKE hysteresis loops of the dot arrays grown at 190 °C for three different nominal Fe deposition thicknesses: 0.3 nm (first row), 0.6 nm (second row) and 1.0 nm (third row). The spacing of the grooves is  $40 \pm 12$  nm. When  $\theta = 70^\circ$ , 28% of the whole surface is expected to be covered by Fe. The projected patch width is  $11 \pm 3$  nm. Each island is isolated within a patch and no correlation in crystal orientation exists between islands. The island size increases and the density decreases with increasing total thickness. This behavior is indicative of liquidlike coalescence where a rounded island shape is quickly recovered. Figure 5 shows the island size distribution obtained from quantitative image analysis of the ADF images. The probability density functions are well fit by a log-normal distribution, as is commonly observed in liquidlike coalescence growth systems.<sup>18</sup> However, the measured geometrical standard deviation obtained here, 1.7, is larger than that observed in normal two-dimensional random particle systems prepared either by evaporation<sup>18</sup> or sputtering.<sup>19</sup> This broadening of the distribution may result from the crossover from a two-dimensional to a one-dimensional coalescence system, which is not accounted for in mean-field kinetic coalescence theory.<sup>20</sup>

The MOKE loops in Fig. 4 show easy-axis behavior when the magnetic field is applied parallel to the arrays, even though each particle is isolated. Experimental MOKE hysteresis loops are shown with solid symbols. Loops were taken along the easy direction, along the wire array (third column), and perpendicular to the wire array, along the hard direction (fourth column). The acquisition time for each loop was on the order of seconds. The computed hysteresis loops from Monte Carlo micromagnetics<sup>10,17</sup> simulations are plotted with solid lines. Immediately evident is the strong asymmetry in the hysteresis loops acquired along and perpendicular to the island-wire direction. The random structure and orientation of the individual particles, the lack of any crystallographic orientation between the particles themselves or between the particles and the substrate, the lack of any interface anisotropy (except in a direction normal to the sur-

face) suggests that the ordering along the island-wire is due to long-range interactions through the purely geometric ordering of the island array.

A Monte Carlo micromagnetic model was used to calculate the magnetic properties of the linear arrays as a function of particle radius and density in order to test for dipole-field induced ordering. One of the main advantages of Monte Carlo is that fluctuations are rigorously included. Simulations used periodic boundary conditions, and between 200 and 400 islands randomly arranged into 3–5 wires. The model employs an all-orders interparticle interaction Hamiltonian.<sup>17</sup> As input, the model uses the bulk saturation magnetization value, an adjustable externally applied field and the experimentally measured size distribution of Fe islands. The slightly irregular experimental island shapes are approximated by cylinders. Hysteresis loops are calculated by finding an equilibrium magnetization distribution for an externally applied field value. The magnetization accumulators are reset, the external field value changed, and the previous final magnetization state is preserved as the initial distribution for the next Monte Carlo cycle. These computed results indicate that the magnetic moment of each island is influenced by the strong interaction field produced by surrounding particles. The room temperature magnetic phase changes from superparamagnetic to ferromagnetic with increasing particle size.<sup>10</sup>

The easy axis hysteresis loop for  $t = 0.6$  nm film shows an abrupt jump in both the experimental ( $H_c < 5$  Oe, our experimental resolution limit) and computed ( $H_c < 1$  Oe) loops. The larger islands in the  $t = 1.0$ -nm-thick film show easy axis remanence and coercivity in both measured and computed hysteresis loops. Dipole ferromagnetically ordered films have an easy axis along the wire since the shape anisotropy in that direction is small. Since the particles have no preferential crystallographic orientation in the film plane, magnetocrystalline anisotropy is also negligible. Therefore, the anisotropy that orders the array is ascribed to the strong magnetic interaction between self-aligned particles. Since the magnetic-coupling field energy of the islands scales with the island volume, the size dependent remanence is ascribed to temperature stabilization of the magnetization of a particle in the stray field of the surrounding particles.

Another candidate structure for forming ordered ferromagnetic particle arrays uses the faceting of NaCl (111) as the shadow growth template as illustrated in Fig. 6. Figures 6(a) and 6(b) show bright field images of an Fe dot array ( $t = 3$  nm) formed on a (111) template. The typical patch-to-patch separation is on the order of 100 nm. This distance is geometrically determined by the faceting of the template caused by the thermal etching process, and is independent of nucleation and coalescence kinetics. The equilibrium spacing between islands would normally be  $N^{-1/2}$  (where  $N$  is the island density) on unfaceted surfaces. Two types of Fe patches, chevron-hat shaped, and parallelogram shaped are observed. The shapes of these two structures can be explained by examining the fluctuations in the peak positions of the etched NaCl(111) surface both in the in- and out-of-plane direction as illustrated in Fig. 6(c) for the projection shadow mask. The array is neither hexagonal or even regu-

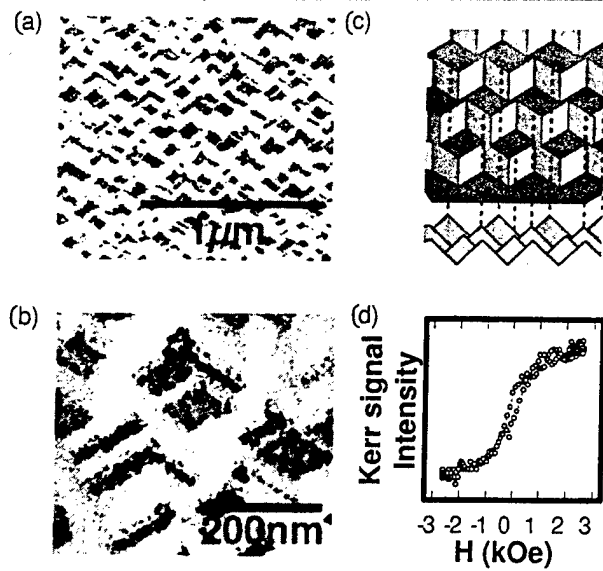


FIG. 6. Dot array formed on a (111) template. (a) Low-magnification TEM image showing both chevron-hat and rectangular shaped patches. (b) High-magnification TEM image of individual dots. (c) Disordered steps of two types can be observed. (d) MOKE loop.

lar, and as a result of high temperature growth ( $T_g = 190^\circ\text{C}$ ), each chevron patch is composed of several independent islands [Fig. 6(b)]. This film did not show strong in-plane magnetic anisotropy as evidenced by the MOKE loop in Fig. 6(d), but did have remanence and coercivity. The magnetic interaction between patches is weak due to their large separation, and the shape of the individual patches is not strongly anisotropic on average.

## B. Wire arrays

With increasing Fe coverage at room temperature, the space between the islands in the structure shown in Fig. 4 fills in, and wire arrays are formed. Figure 7 shows bright-field TEM images of wire arrays deposited onto an annealed (110) grating template at room temperature with  $\theta = 65^\circ$ . The Fe wires seen in dark contrast run along the macrosteps of the substrate as shown in Fig. 7(a). We confirmed that this microstructure is uniform over the entire 3-mm-diam specimen area of the TEM grid. A corresponding electron diffraction pattern (not shown here) and a bright field image [Fig. 7(b)] showed that these wires are polycrystalline Fe with no texture orientation. Therefore, we can neglect the contribution of magnetocrystalline anisotropy to the magnetic properties. The average periodicity of these wires is 90 nm, and their average width (projected) is 30 nm. Both the separation and the width have a broad size distribution due to the inhomogeneous thermal etching during annealing. Furthermore, ultrasmall discontinuous wires ( $<10$  nm in width) intermittently lie at the NaCl groove bottoms between neighboring thick wires. The presence of these ultrasmall wires indicates that a small amount of Fe can escape from the patch and condense at the groove bottom even at room temperature. The aspect ratio of the wires is closely related to the resultant magnetic anisotropy. We estimated the wire length from a foreshortened TEM micrograph [Fig. 7(d)] that illustrates the

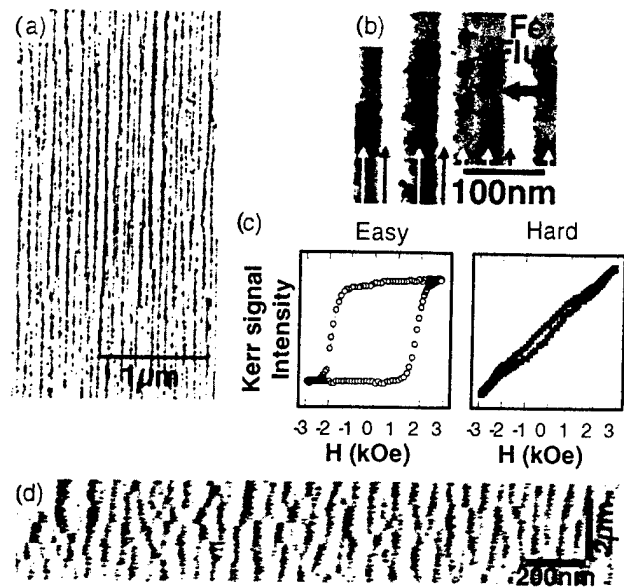


FIG. 7. Typical wire structure of Fe ( $t = 13$  nm) and corresponding MOKE loops. (a) Low-magnification BF image showing that the wire array is uniform over large area. (b) High-magnification BF image showing where the ultrathin wire is formed at the bottom of the grooves. (c) Easy- (left) and hard-axis (right) MOKE loops. (d) Foreshortened BF image illustrating how the wires form a network structure on a large scale.

long-range imperfection of the wires. The wires are terminated where the terraces perpendicular to the steps [e.g., (100)] are accompanied by a miscut from the exact crystal axis. The average wire length calculated from the termination density is about  $10\ \mu\text{m}$ . Therefore, the aspect ratio is about 200. The demagnetization factor of a magnetic cylinder with this aspect ratio is on the order of  $10^{-4}$ , so strong shape anisotropy is expected. Figure 7(c) show easy- and hard-axis MOKE loops for the wire array. Evident is the very strong in-plane anisotropy. The coercivity of the easy-axis loops is typically 2 kOe. Since the diffraction patterns from the arrays indicate that the arrays are indeed polycrystalline, this anisotropy is ascribed to shape anisotropy.

Even though the wire width is determined geometrically by the step spacing and flux inclination angle, arbitrarily small wires could not be obtained on closely spaced grooves. Figures 8(a) and 8(b) show two different thickness films [(a)  $t = 5$  nm and (b)  $t = 14$  nm] grown at room temperature on closely-spaced ( $L = 27$  nm) grooves produced at  $T_a = 380^\circ\text{C}$ . The grooves are easily filled by a small amount of deposited Fe to form an undulating, continuous film. Even in thin regions, the fluctuations in the wire width ( $\sim$  grain size) have the same size scale as the exposed patch width, hence no wires are clearly defined. The magnetic structure of these films is essentially the same as the continuous and undulating films. Figures 8(c) and 8(d) show the same two thickness films as Figs. 8(a) and 8(b) grown on a template with wide-spaced ( $L = 87$  nm) grooves produced at  $T_a = 440^\circ\text{C}$ . The wire width is similar for both films (different thickness) on the broadly spaced grooves. This width is largely independent of Fe coverage at room temperature, consistent with short diffusion lengths and high nucleation densities discussed above.

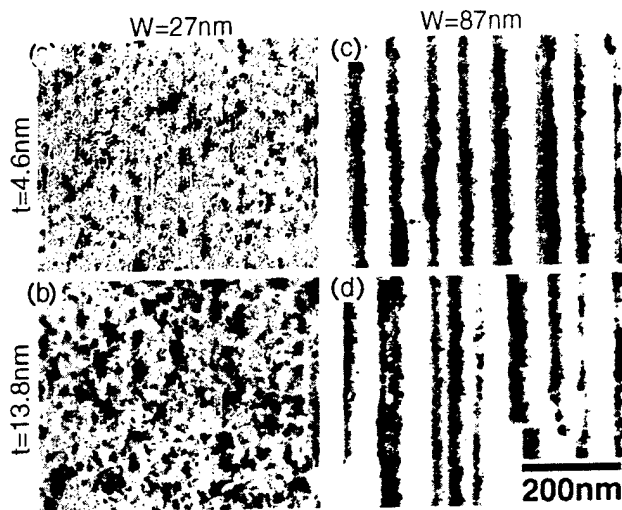


FIG. 8. Microstructure formed on grooves of different spacings at room temperature. In Fe films of nominal thickness (a)  $t=5$  nm and (b)  $t=14$  nm grown on narrowly spaced ( $L=27$  nm) templates, the grooves are filled quickly by small amounts of Fe. The wire morphology remains constant during growth when the Fe thickness is between (c)  $t=5$  nm and (d)  $t=14$  nm for films grown on widely spaced templates,  $L=87$  nm.

In contrast to the wire morphology produced with room temperature growth, wire-broadening was observed for high temperature growth ( $T_g=190^\circ\text{C}$ ). Figure 9(a) shows a thin film ( $t=4$  nm) grown on a wide-spaced ( $L=87$  nm) grating. At this temperature, the transition thickness from a discontinuous to a continuous film increases because compact shapes are quickly recovered after coalescence. Since this thickness is not large enough to form a continuous wire, a network still remains. The width of the patch exposed to the Fe flux is a few times larger than the spacing of the particles, so that one-dimensional linear arrays are not formed. The hysteresis loops for the film in Fig. 9(a) (adjacent to it) show a coercivity smaller than 1 kOe. Figure 9(b) shows a bright field TEM image of 13-nm-thick film. At this thickness, the

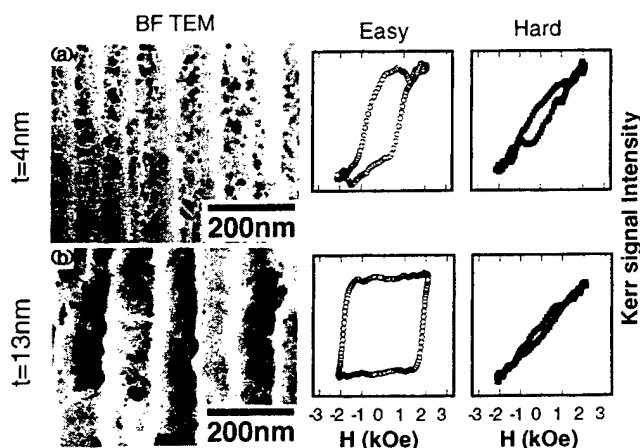


FIG. 9. Wire structure grown on widely spaced ( $L=87$  nm) grooves at elevated temperatures ( $T_g=190^\circ\text{C}$ ). (a) The network structure observed in Fe ( $t=4$  nm) film. The corresponding coercivity is smaller than in the case of a continuous wire array. (b) A broadened continuous wire array ( $t=13$  nm). The wire edges expand past the groove edges, and reach the next facets. The TEM contrast suggests that the wire cross-section is asymmetric.

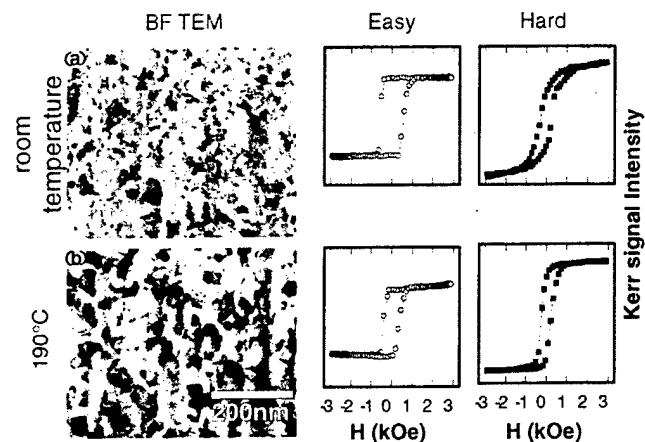


FIG. 10. BF images of undulating continuous films ( $t=9$  nm) grown at (a)  $T_g=\text{room temperature}$  and (b)  $T_g=190^\circ\text{C}$ . The Kerr loops show easy-axis behavior when the field is applied parallel to the grooves, though the in-plane projected microstructures are isotropic.

islands grow together, and wires are formed. The wire width is larger than half of ridge-to-ridge distance, and the wire cross-section is asymmetric. This observation suggests that the wire edge diffused outward and joined the thin wires at the groove bottom. The corresponding MOKE loops [adjacent to Fig. 9(b)] show anisotropic magnetic properties and an easy-axis coercivity larger than 2 kOe.

### C. Undulating continuous films

When Fe is deposited onto the substrate at normal incidence ( $\theta=0^\circ$ ), continuous films having an undulating surface topography are formed. Such undulating films are expected to have different magnetic coupling and domain structure than flat films of the same thickness. Figures 10(a) and 10(b) show bright-field TEM images of such films grown at room temperature and  $190^\circ\text{C}$ , respectively, along with the corresponding MOKE loops. The films are polycrystalline and continuous, and each grain has an isotropic shape.

The MOKE loops show that the easy-axis is parallel to the macrosteps even though there is no anisotropic grain structure. The coercivities are 400–600 Oe, much larger than that typically found in flat Fe films (smaller than a few tens of Oe). This large coercivity is not due to strain since the large coercivity persists in the film grown at  $190^\circ\text{C}$ , in which the strain is expected to be at least partially relaxed. We examined the magnetization component parallel and perpendicular to the magnetic field by rotating both the magnet and the sample. The results suggested that the switching is done by coherent rotation of the magnetization in the film plane. This behavior is quite different from flat films, in which the switching is caused by domain wall motion. This suggests that the magnetic coupling associated with the surface undulation becomes important. The details of the magnetic switching will be discussed elsewhere.

## V. CONCLUSIONS

Fe was deposited onto annealed NaCl (110) and (111) substrates at various Fe flux incident angles. Three kinds of microstructure, i.e., dot arrays, wire arrays, and undulating continuous films, were obtained, and they showed strong in-plane magnetic anisotropy. For room temperature growth, Fe condensed in the zone exposed to the flux, such that wire arrays are typically observed. This growth mode is associated with low adatom mobility on the surface. In the high temperature growth regime, linear dot arrays were observed in the initial growth, because liquidlike coalescence was activated by high adatom mobility.

The nanometer-scale microstructures obtained in this study are statistically uniform over an entire square centimeter. This type of self-organization can be applied to the fabrication of magnetic devices since the method employs only a simple geometrical shadow effect that does not strongly depend on material combinations. The dot size and separation depends strongly on the growth temperature. Since the nucleation density decreases and coalescence is activated at higher growth temperatures, an array composed of even larger islands is expected to form on large periodicity gratings. Due to NaCl sublimation at high temperatures, the growth temperature cannot exceed 300 °C. Similar surface faceting can be expected for materials having anisotropic surface energy. More regular and stable macrostep structures have been found on other materials such as CaF<sub>2</sub> on Si(110),<sup>21</sup> annealed Al<sub>2</sub>O<sub>3</sub>,<sup>22</sup> LiNbO<sub>3</sub>,<sup>23</sup> and Si(311).<sup>24</sup> These materials are the next candidates for self-organization templates.

## ACKNOWLEDGMENTS

The authors are indebted to S. Coyle for technical support and valuable discussions and to Dmitry Streblechenko for providing the custom image processing software. We have also benefitted from valuable discussions with K. Schmidt and J. Venables. We would like to acknowledge P. Crozier for taking the ADF images in Fig. 4. This work is supported by the Office of Naval Research under Grant No. N00014-93-1-0099. The microscopy was performed at the Center for High Resolution Electron Microscopy at Arizona State University. A.S. is supported by a JSPS postdoctoral fellowship for research abroad.

<sup>1</sup> J. Q. Xiao, J. S. Jiang, and C. L. Chien, *Phys. Rev. Lett.* **68**, 3749 (1992); A. E. Berkowitz, J. R. Mitchell, M. J. Carey, A. P. Young, S. Zhang, F. E.

- Spada, F. T. Parker, A. Hutten, and G. Thomas, *ibid.* **68**, 3745 (1992); A. E. Berkowitz, J. R. Mitchell, M. J. Carey, A. P. Young, D. Rao, A. Starr, S. Zhang, F. E. Spada, F. T. Parker, A. Hutten, and G. Thomas, *J. Appl. Phys.* **73**, 5320 (1993); M. El-Hilo and K. O'Grady, *ibid.* **76**, 6811 (1994).
- <sup>2</sup> S. Mörup, *Phys. Rev. Lett.* **72**, 3278 (1994); S. Mörup and G. Christiansen, *J. Appl. Phys.* **73**, 6955 (1993); S. Mörup, *Hyperfine Interact.* **60**, 959 (1990); S. Mörup, P. H. Christensen, and B. S. Clausen, *J. Magn. Magn. Mater.* **68**, 160 (1987); S. Mörup, M. B. Madsen, J. Franck, J. Villadsen, and C. J. W. Koch, *ibid.* **40**, 163 (1983); W.-N. Wang, Z.-S. Jiang, and Y.-W. Du, *J. Appl. Phys.* **78**, 6679 (1995); S. Matsuo, T. Matsuura, I. Nishida, and N. Tanaka, *Jpn. J. Appl. Phys., Part 1* **33**, 3907 (1994).
- <sup>3</sup> R. J. Celotta, R. Gupta, R. E. Scholten, and J. J. McClelland, *J. Appl. Phys.* **79**, 6079 (1996).
- <sup>4</sup> J. F. Smyth, S. Schultz, D. R. Fredkin, D. P. Kern, S. A. Rishton, H. Schmid, M. Cali, and T. R. Koehler, *J. Appl. Phys.* **69**, 5262 (1991); A. O. Adeyeye, G. Lauhoff, J. A. C. Bland, C. Daboo, D. G. Hasko, and H. Ahmed, *Appl. Phys. Lett.* **70**, 1046 (1997); R. D. Gomez, M. C. Shih, R. M. H. New, R. F. Pease, and R. L. White, *J. Appl. Phys.* **80**, 342 (1996); S. Y. Chou, P. R. Krauss, and L. Kong, *ibid.* **79**, 6101 (1996).
- <sup>5</sup> S. S. Gidar, J. Shi, P. F. Hopkins, K. L. Campman, A. C. Gossard, D. D. Awschalom, A. D. Kent, and S. von Molnár, *Appl. Phys. Lett.* **69**, 3269 (1996).
- <sup>6</sup> A. Fernandez, *Proc. IEEE MAG32*, 4472 (1996).
- <sup>7</sup> H. Takeshita, Y. Suzuki, H. Akinaga, W. Mizutani, K. Tanaka, T. Katayama, and A. Itoh, *Appl. Phys. Lett.* **68**, 3040 (1996).
- <sup>8</sup> T. Shinjo and T. Ono, *J. Magn. Magn. Mater.* **156**, 11 (1996).
- <sup>9</sup> A. Sugawara, Y. Haga, and O. Nittono, *J. Magn. Magn. Mater.* **156**, 151 (1996).
- <sup>10</sup> A. Sugawara, S. T. Coyle, G. G. Hembree, and M. R. Scheinfein, *Appl. Phys. Lett.* **70**, 1043 (1997); A. Sugawara and M. R. Scheinfein, *Phys. Rev. B* (to be published).
- <sup>11</sup> The NaCl samples were purchased from Bicon, Inc.
- <sup>12</sup> Z. J. Yang and M. R. Scheinfein, *J. Appl. Phys.* **74**, 6810 (1993).
- <sup>13</sup> J. A. Venables, F. L. Metcalfe, and A. Sugawara, *Surf. Sci.* **371**, 420 (1997).
- <sup>14</sup> L. Néel, *Ann. Geophys. (C.N.R.S.)* **5**, 99 (1949); A. Aharoni, *Introduction To The Theory of Ferromagnetism* (Oxford Science, Oxford, 1996).
- <sup>15</sup> W.-N. Wang, Z.-S. Jiang, and Y.-W. Du, *J. Appl. Phys.* **78**, 6679 (1995); S. Matsuo, T. Matsuura, I. Nishida, and N. Tanaka, *Jpn. J. Appl. Phys., Part 1* **33**, 3907 (1994).
- <sup>16</sup> S. Linderith, L. Balcells, A. Labarta, J. Tejada, P. V. Hendriksen, and S. A. Sethi, *J. Magn. Magn. Mater.* **124**, 269 (1993).
- <sup>17</sup> M. R. Scheinfein, K. E. Schmidt, K. R. Heim, and G. G. Hembree, *Phys. Rev. Lett.* **76**, 1541 (1996); K. R. Heim, G. G. Hembree, K. E. Schmidt, and M. R. Scheinfein, *Appl. Phys. Lett.* **67**, 2878 (1995).
- <sup>18</sup> C. G. Granqvist and R. A. Buhrman, *J. Appl. Phys.* **47**, 2200 (1976).
- <sup>19</sup> A. Sugawara, Y. Nakamura, and O. Nittono, *J. Cryst. Growth* **99**, 583 (1990).
- <sup>20</sup> See, e.g., D. Kashchiev, *Surf. Sci.* **86**, 14 (1979).
- <sup>21</sup> L. Schowalter and F. W. Fathauer, *Crit. Rev. Solid State Mater. Sci.* **15**, 367 (1989).
- <sup>22</sup> J. R. Heffelfinger, M. W. Bench, and C. B. Carter, *Surf. Sci.* **343**, L1161 (1995).
- <sup>23</sup> W.-N. Wang, Z.-S. Jiang, and Y.-W. Du, *J. Appl. Phys.* **78**, 6679 (1995).
- <sup>24</sup> S. Song, M. Yoon, S. G. J. Mochrie, G. B. Stephenson, and S. T. Milner, *Surf. Sci.* **372**, 37 (1997).

# Defect induced lowering of activation energies at step bands in Co/Cu(100)

S. T. Coyle and M. R. Scheinfein<sup>a)</sup>

*Department of Physics and Astronomy, Arizona State University, Tempe, Arizona 85287*

James L. Blue

*National Institute of Standards and Technology, Gaithersburg, Maryland 20899*

(Received 13 October 1997; accepted for publication 18 December 1997)

Complex topological features such as rectangular voids and step inclusions that were seen in secondary electron micrographs of Co films grown on Cu(100) at room temperature were reproduced in Monte Carlo simulations in the presence of step bands. Lowered activation energies at defects such as steps, kinks, and vacancies enhance step edge restructuring during growth and upon annealing. This results in features such as faceted step edges, rectangular pits, incorporation of Co into terraces, surface alloying, and surface segregation. Simulated growth structures are directly compared with those observed in an ultrahigh vacuum scanning transmission electron microscope.

© 1998 American Institute of Physics. [S0003-6951(98)02208-6]

Experiments on the growth and magnetic properties of the Co/Cu(100) system often produce disparate results. Scanning tunneling microscope studies of stepped Cu surfaces demonstrate that adatoms and kinks at steps are quite mobile.<sup>1,2</sup> Mobility at steps has also been studied theoretically using the embedded atom method.<sup>3,4</sup> It was suggested<sup>5</sup> that Fe islands which decorate step edges on Cu(111) relax the nearby Cu lattice, and decrease the activation energy for Cu diffusion along steps. This drives the migration of Cu and produces single-layer deep pits in Cu terraces. Large rectangular pits have been observed in Co/Cu(100) systems, which have been annealed following room-temperature (RT) growth.<sup>6,7</sup> These pits, from which Cu was believed to have migrated and covered the Co surface, typically formed near steps. An experimental study<sup>8</sup> of the growth and magnetic properties of Co/Cu(100) performed in our laboratory characterized different growth morphologies for films grown under apparently identical conditions. The first growth mode is characterized by the formation of islands on terraces with little interaction with steps. The second growth mode is characterized by a lower island density and a high degree of interaction with and restructuring of step edges. Combinations of these two modes have been observed in different films. Kinetic Monte Carlo simulations were performed<sup>9</sup> for Co growth on Cu(100) in the presence of single-height steps in an attempt to characterize these growth modes and the resulting film morphologies. The first growth mode has been reproduced reasonably well. Enhanced roughening of step edges was observed in simulations, however, the roughness length scales were smaller than in the experimental results. The large-scale etching features and pits characteristic of the second growth mode were not reproduced in Monte Carlo simulations in the presence of single-height steps at room temperature. The kinetic Monte Carlo growth simulations described here have incorporated step bands as opposed to single-height steps as well as postdeposition annealing in order to simulate decreased energy barrier heights at step edges. Other features of the model, such as nearest-neighbor

(NN) and next-nearest-neighbor (NNN) coupling and the barrier model on a rigid lattice, are the same in both sets of simulations.

In these simulations, the face-centered-cubic Cu substrate (template) was discretized into a region 100 by 100 atoms square (along  $\langle 100 \rangle$ ,  $36 \times 36$  nm) and 14 layers deep (2.5 nm) with periodic boundary conditions. The region included one or two trenches with steps oriented along either  $\langle 100 \rangle$  or  $\langle 110 \rangle$ . The trenches, which were intended to approximate step bands, were seven layers deep. The terrace width of each layer (step down) was four ( $\langle 100 \rangle$ ) or three ( $\langle 110 \rangle$ ) atomic rows. The simulations assumed a rigid lattice with an Arrhenius-type barrier model,<sup>10</sup> where the transition rate is  $r = R_0 \exp(-\epsilon/k_B T)$ . Activation energies ( $\epsilon$ ) were set proportional to beginning and ending bond energies according to  $\epsilon = A/(1 + |\Delta E|/B) + H(\Delta E)$ . The constant  $A$  is the energy barrier for hopping to a state of the same energy, and was set to approximate the experimental activation energy for Co adatom diffusion on Co(100).<sup>11</sup>  $H$  is the Heaviside function,  $T$  is the substrate temperature,  $k_B$  is Boltzmann's constant, and  $B$  is a constant which reduces the barrier somewhat when the final state is more tightly bound than the initial state.  $A$  and  $B$  were each set to 0.5 eV. The attempt frequency ( $R_0$ ) for the transition rate sets the time scale for the entire simulation and was  $2k_B T/h$ , where  $h$  is Planck's constant. The Co-Co bond energy was 0.271 eV/NN and 0.004 eV/NNN.<sup>12</sup> The Cu-Cu bond energy was 0.190 eV/NN and 0.003 eV/NNN.<sup>12</sup> The Co-Cu bond energy was 0.2305 eV/NN and 0.0035 eV/NNN.<sup>9</sup> The simulations did not include nonuniform lattice effects such as relaxation or strain. Strain can be an important driving force for finite-sized structures.<sup>7</sup> In order to compare directly with experimental observations, results are presented for one monolayer (ML) ( $1 \text{ ML} = 1.53 \times 10^{15} \text{ atoms/cm}^2$ ) of Co deposited<sup>10</sup> at random sites at 275 K and subsequently annealed at 350 K for 30 s. Structures were stable well before the 30 s anneal was complete.

Experimental results were obtained from Co growth on bulk single-crystal Cu(100) samples.<sup>8</sup> Cu substrates were cleaned by repeated Ar<sup>+</sup> ion sputter and anneal (600 °C)

<sup>a)</sup>Electronic mail: Michael.Scheinfein@asu.edu

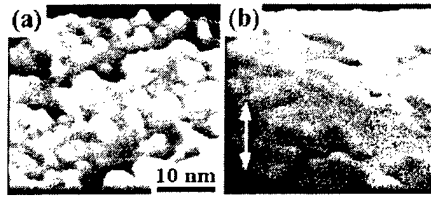


FIG. 1. Secondary electron micrographs of 0.2 ML Co/Cu(100) grown at 300 K, which show examples of the first (a) and the second (b) growth modes. White arrows denote the  $\langle 100 \rangle$  direction. Gray scale images have been rendered in three dimensions. The scale is the same for both images.

cycles. Co was grown at room temperature by electron-beam evaporation at pressures  $< 5 \times 10^{-10}$  mbar. Samples were transferred *in situ* into an ultrahigh vacuum (UHV) scanning electron microscope (SEM) for nanometer resolution secondary electron (SE) imaging.<sup>13</sup>

In Fig. 1, characteristic samples of high-resolution UHV SE micrographs of the first (a) and second (b) growth modes are shown. The  $\langle 100 \rangle$  direction is denoted by the inserted arrow. Gray scale images have been rendered in three dimensions. Both films consist of 0.2 ML of Co grown at 300 K on Cu(100) at 0.15 ML/min. Since restructuring is observed for such small amounts of deposit [Fig. 1(b)], we believe that the relief of strain in the Co film may not be a significant driving force in the early stages of growth. Restructuring takes the form of facets with low-energy  $\langle 110 \rangle$  steps, suggesting that the lowering of free energy is the driving force. The large-scale faceting and step edge restructuring shown in Fig. 1(b) was not well reproduced by kinetic Monte Carlo simulations in the presence of single atom high steps,<sup>9</sup> although simulated structures with step bands, which were annealed, exhibited morphologies remarkably similar to those produced during growth experiments. Experimental and computed morphologies for growth near step bands are shown in Fig. 2. Brighter areas are higher. Simulations are in the left column [Figs. 2(a), and 2(c)] and SEM results at right [Figs. 2(b) and 2(d)]. White arrows inserted into the images denote the  $\langle 100 \rangle$  direction. The simulations include 1.0 ML of Co grown near step bands aligned along  $\langle 100 \rangle$  [Fig. 2(a)] and  $\langle 110 \rangle$  [Fig. 2(c)] followed by a 30 s anneal at 350 K. No differentiation is made between Co and Cu atoms. The SEM results also include growths of 1.0 ML with step bands

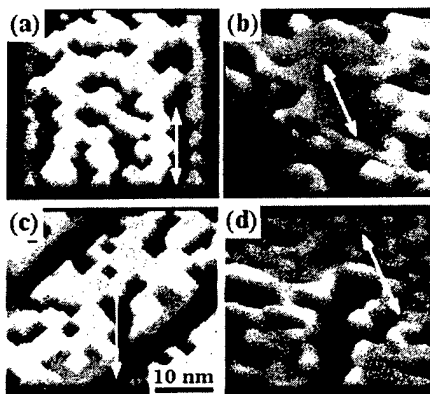


FIG. 2. Simulation results (a,c) and SEM results (b,d) for 1 ML Co/Cu(100) grown at RT near  $\langle 100 \rangle$  (a,b) and  $\langle 110 \rangle$  (c,d) step bands. The simulations were annealed at 350 K for 30 s. Bright regions are higher. White arrows denote the  $\langle 100 \rangle$  direction. Gray scale images have been rendered in three dimensions. The scale is the same for all images.

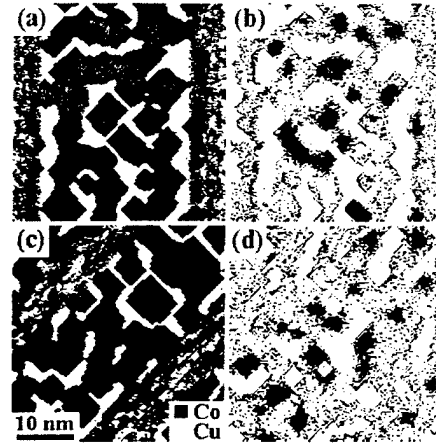


FIG. 3. Simulation results for 1 ML Co/Cu(100) before (a,c) and after (b,d) annealing. The atomic species of the topmost exposed atom is shown. Black squares are Co atoms and white squares are Cu atoms.

aligned close to  $\langle 100 \rangle$  [Fig. 2(b)] and  $\langle 110 \rangle$  [Fig. 2(d)], however, without annealing.

The simulation results [Figs. 2(a) and 2(c)] contain large rectangular vacancies from which Cu has migrated. Before annealing these were exposed regions of the Cu substrate. The experimental results [Figs. 2(b) and 2(d)] contain similar features, although the length scales are slightly larger. Adjacent to the  $\langle 100 \rangle$  step bands in Fig. 2(a) are long connected vacancy regions with  $\langle 110 \rangle$  facets separated from the step bands by Co islands (see, e.g., the region around the arrow). These regions are within the adatom random walk distance of the step band. The Co island density during growth was low in this region, leaving exposed Cu after the growth. This Cu was then free to migrate during the anneal. Co which migrated over the step from this denuded region formed islands at the step bands. Regions of similar morphology can be seen in SEM data along  $\langle 100 \rangle$  step bands. Such a region surrounds the arrow in Fig. 2(b). The large rectangular vacancies in the simulation terraces were formed by incomplete Co coverage, from which Cu migrated during annealing. Similar structures were also observed in the SEM data, as can be seen in the terrace of Fig. 2(d). Inclusions into the  $\langle 110 \rangle$  step bands [Figs. 2(c) and 2(d)] are more rectangular than those into  $\langle 100 \rangle$  step bands, and are not separated from the step band by Co islands.

The top level atomic species for the simulations before (left) and after (right) annealing are shown in Fig. 3 for  $\langle 100 \rangle$  (top) and  $\langle 110 \rangle$  (bottom) step bands. Black squares are Co atoms and white squares are Cu atoms. Figures 3(b) and 3(d) are the same postannealing simulation results shown in Figs. 2(a) and 2(c). Cu has clearly migrated from exposed areas to cover and/or surround the Co islands. This migration has occurred without invoking a direct exchange process.<sup>14</sup> Very few Co islands are exposed (on top) after the anneal, however, a large number of Co atoms along steps are exposed. The shapes of Co islands are now much less rectangular and closer to those obtained experimentally from the first growth mode. These islands are now surrounded by Cu (i.e., part of a terrace). Interdiffusion has obviously increased dramatically during annealing.

Simulations of deposition at higher temperatures<sup>9</sup> did not reproduce the experimental morphologies, while simulations

of deposition at 275 K followed by 350 K anneal did. This suggests that the ratios of activation energies for different processes were inaccurate. The activation energies for processes at steps (bands) may be lower than the simple model predicts. This could cause the discrepancy between the simulations of RT growth and the experimental morphologies. Transition rates in the model are dependent on attempt frequency, temperature, and the parameters  $A$  and  $B$ . A change in any of these parameters will change the rate at which processes occur. Increasing  $T$ , as in our annealing simulations, is equivalent to increasing  $R_0$ , or decreasing  $\epsilon$ . The ratios of these parameters, then, affect the growth dynamics as much as their magnitudes. The exposed Cu atoms are apparently close to an activation energy threshold since a small increase in temperature (75 K) dramatically increases their mobility. One possible method to improve the simulations is to change the model for activation energy ( $\epsilon$ ). Lowering  $\epsilon$  for processes whose beginning bond energies are smaller should increase the rate for processes on atoms with lower coordination, such as at steps. We have chosen not to search the vast parameter space for combinations which produce the experimentally observed morphology. Rather, we have approximated the increased mobility of Cu atoms at defects by annealing. This produced morphologies remarkably similar to those observed in SEM data.

SEM results (not shown) reveal a continuum of combinations of the first and second growth modes. We have been unable to correlate contamination levels with growth mode, although a surfactantlike contaminant effect cannot be ruled out. The range of growth modes could instead be due to variations in defect densities. The width and density of step bands was not constant between different samples used in

our growth experiments. Agglomerations of vacancies were evident in some samples, suggesting the presence of a high density of defects that we could not detect. Samples with higher defect densities would exhibit an increased proportion of the second growth mode. Differences in defect density and the resultant changes in activation energies, then, could account for the differences in observed morphology. Lowered activation energies for Cu atoms could be the result of relaxation near defects, or changes in the strain field caused by nearby Co atoms.

The authors would like to thank Dr. G. G. Hembree for collaboration in the experimental work. This work is supported by ONR under Grant No. N00014-93-1-0099.

<sup>1</sup>F. Thibaudau and J. Cousty, *Ultramicroscopy* **42-44**, 511 (1991).

<sup>2</sup>M. Giesen, J. Frohn, M. Poensgen, J. F. Wold, and H. Ibach, *J. Vac. Sci. Technol. A* **10**, 2597 (1992).

<sup>3</sup>Per Stoltze, *J. Phys.: Condens. Matter* **6**, 9495 (1994).

<sup>4</sup>Z.-J. Tian and T. S. Rahman, *Phys. Rev. B* **47**, 9751 (1993).

<sup>5</sup>M. Klaua, H. Hoche, H. Jenniches, J. Barthel, and J. Kirschner, *Surf. Sci.* **381**, 106 (1997).

<sup>6</sup>A. K. Schmid, D. Atlan, H. Itoh, B. Heinrich, T. Ichinokawa, and J. Kirschner, *Phys. Rev. B* **48**, 2855 (1993).

<sup>7</sup>M. Giesen, F. Schmitz, and H. Ibach, *Surf. Sci.* **336**, 269 (1995).

<sup>8</sup>S. T. Coyle, G. G. Hembree, and M. R. Scheinfein, *J. Vac. Sci. Technol. A* **15**, 1785 (1997).

<sup>9</sup>S. T. Coyle, J. L. Blue, and M. R. Scheinfein, *J. Vac. Sci. Technol. A* (in press).

<sup>10</sup>J. L. Blue, The random deposition rate is set by the time scale of the transition,  $t = 2k_B T/h$  (to be published).

<sup>11</sup>M. T. Kief and W. F. Egelhoff, Jr., *Phys. Rev. B* **47**, 10785 (1992).

<sup>12</sup>L. Z. Mezey and J. Giber, *Jpn. J. Appl. Phys., Part 1* **21**, 1569 (1982).

<sup>13</sup>K. R. Heim, S. D. Healy, Z. J. Yang, J. S. Drucker, G. G. Hembree, and M. R. Scheinfein, *J. Appl. Phys.* **74**, 7422 (1993).

<sup>14</sup>P. J. Feibelman, *Surf. Sci.* **299**, 426 (1994).



BY: okc REV: aortiz@jupiter/first/CLS\_journals/GRP\_jap/JOB\_mmmjun98/DIV\_379811mmmo  
◆379811mmmo  
ALINK:

JOURNAL OF APPLIED PHYSICS

VOLUME 83, NUMBER 11

1 JUNE 1998

## Magnetic ordering in Co films on stepped Cu(100) surfaces

S. T. Coyle and M. R. Scheinfein

Dept. of Physics and Astronomy, PSF 470 Box 871504, Arizona State University, Tempe, Arizona 85287

Ultrathin films of Co were grown on Cu(100) and characterized by nanometer resolution secondary electron microscopy, Auger electron spectroscopy, and the surface magneto-optic Kerr effect. An unexpected out-of-plane remanence was detected in many films. The anisotropy of atoms near defects along the Co/vacuum interface calculated via the Néel model indicates that atoms at the bottom corner of a step edge are canted out-of-plane. Full three-dimensional micromagnetics simulations which incorporate site specific anisotropy (including step edges, kinks, and voids) have been performed. Simulations with unidirectional arrays of [110] steps, such as vicinal surfaces, do not exhibit out-of-plane remanence. Simulations with facets consisting of connected [110] and [110] steps exhibit out-of-plane remanence of 0.03. This is lower than the experimental value of 0.11. © 1998 American Institute of Physics. [S0021-8979(98)37911-6]

### I. INTRODUCTION

Magnetic surface anisotropies play a key role in determining the magnetic properties of thin films and multilayers.<sup>1</sup> Recently the anisotropy of steps has been found to be important in understanding the magnetic behavior of some systems.<sup>2-4</sup> Since the roughness of the Co/Cu interface plays a key role in determining GMR properties,<sup>5</sup> characterizing the Co/Cu interface including the effect of defects is important. Ultrathin films of Co were grown on Cu(100) in order to study the morphology and the resulting magnetic properties at early stages of growth. The films were characterized by nanometer resolution secondary electron microscopy, Auger electron spectroscopy, and the surface magneto-optic Kerr effect (SMOKE).<sup>6</sup> An unexpected out-of-plane remanence was detected in many films.

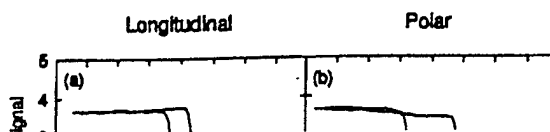
The cause of this out-of-plane component of the magnetization could be related to film morphology at the early stages of growth. One possible mechanism which may produce out-of-plane magnetization is defect related anisotropy on imperfect surfaces. The anisotropy of atoms near defects along the Co/vacuum interface has been calculated. Atoms along the bottom corner of a {110} step which have strong uniaxial anisotropy canted out-of-plane, may couple to the spins of nearby atoms. A significant out-of-plane component to the magnetization may occur for some critical density of these sites. This short article will address the feasibility of this mechanism for the origin of the perpendicular component to the observed magnetization.

Co grown on substrates with high defect densities resulted in dramatic faceting of step edges and the creation of rectangular pits.<sup>6</sup> The anisotropy of atoms of low coordina-

### II. EXPERIMENTAL RESULTS

Morphological characterization with concurrent magnetization measurements was obtained from Co grown on bulk single crystal Cu(100) samples.<sup>6</sup> Cu substrates were cleaned by repeated Ar<sup>+</sup> ion sputter and anneal (600 C) cycles. Co was grown by electron-beam evaporation at rates between 0.05 ML/min and 0.2 ML/min at pressures  $< 5 \times 10^{-10}$  mbar (1 ML =  $1.53 \times 10^{15}$  atoms/cm<sup>2</sup>). Samples were transferred *in situ* into the SMOKE chamber for magnetic characterization, then transferred *in situ* into an ultrahigh vacuum scanning transmission electron microscope for nanometer resolution secondary electron (SE) imaging.<sup>7</sup> SE micrographs revealed complex growth morphologies which varied between different films. Many films contained high densities of steps, kinks, and facets.

room Co/Cu(100) films in this study became ferromagnetic at a low temperature at about 1.7 ML. Zero field susceptibility in the paramagnetic regime and remanence in the ferromagnetic regime generally increased with coverage. In many films a second magnetic phase was detected with out-of-plane remanence and a coercivity 5–10 times the in-plane value which increased with Co coverage. Figure 1 contains such Kerr hysteresis loops taken in the longitudinal [Fig. 1(a)] and polar [Fig. 1(b)] geometries<sup>7</sup> from a 2 ML thick film. As a result of the 45° incident scattering angle, polar signals were five times stronger than the longitudinal signals.<sup>8</sup> The out-of-plane component of the magnetization in the film in Fig. 1 is therefore ~0.11.





rectangular pits. The anisotropy of atomic orientation created by this morphology may significantly affect the magnetization of the film, and may also affect the GMR properties of multilayers. To evaluate the equilibrium magnetic microstructure in such films, and to determine if the anisotropy at sites with low symmetry may be responsible for the observed out-of-plane remanence, full three-dimensional micromagnetics simulations were performed incorporating the calculated site specific anisotropies.

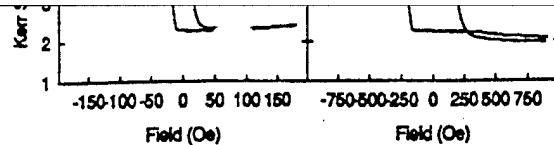


FIG. 1. Kerr hysteresis loops from a sample exhibiting out-of-plane remanence. Part (a) was taken in the longitudinal geometry and (b) was taken in the polar geometry. The Kerr signal is given in arbitrary units, and the scales in (a) and (b) are the same.

### III. MICROMAGNETICS SIMULATIONS

The anisotropy of face centered cubic atoms has been calculated for reduced symmetry structures such as steps and kinks following the Néel model of anisotropy,<sup>9</sup> and including the effects of strain.<sup>10</sup> In agreement with Chuang *et al.*,<sup>11</sup> the anisotropy of atoms along the bottom corner of a step edge (step corner) was found to be uniaxial and canted out-of-plane, while the anisotropy of atoms along the top corner of a step (step edge) was uniaxial in-plane along the step direction. The anisotropy of bulk atoms and surface atoms was biaxial in-plane along  $\langle 110 \rangle$ . The anisotropy of kink edge atoms was biaxial in-plane along  $\langle 110 \rangle$  and that of kink corner atoms was uniaxial in-plane along the kink direction. A summary of these results is given in Table I, and a schematic of a Co surface identifying individual sites is presented in Fig. 2. Strain due to the misfit of face-centered-cubic (fcc) Co and fcc Cu has been included in all anisotropy calculations except when noted.

The anisotropy terms (Table I) proportional to  $\cos^2 \theta$  extract a high penalty for magnetization out of the plane. Of the remaining terms, those proportional to  $L(r_0)$  are larger by a factor of  $10^2$  than terms containing  $e_0$  or  $Q(r)$ . The step corner, kink-in corner and kink-out corner sites hold promise for out-of-plane magnetization due to the term proportional to  $\sin \theta \cos \theta$ . The step corner has an energy minimum which is out-of-plane, while the kink-in corner and kink-out corner sites have energy minima which are in-plane.

These atomic, site specific anisotropy energies have been incorporated into micromagnetics simulations<sup>12</sup> of Co on stepped Cu(100). The simulation searches for solutions to the Landau-Lifshitz-Gilbert equation. The following energies were included: exchange energy, site-specific anisotropy energy, magnetostatic self-energy, and external magnetostatic field energy. The saturation magnetization, exchange stiffness, gyromagnetic frequency gamma, and damping con-

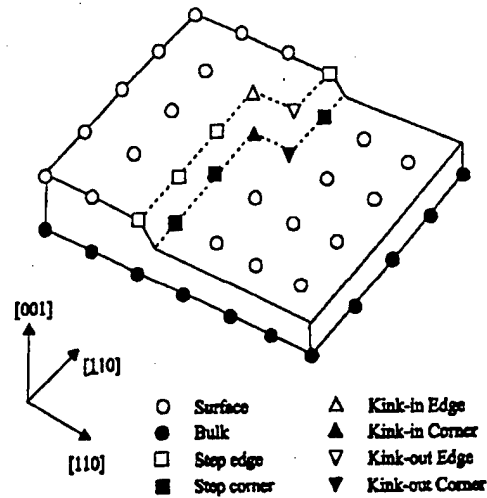


FIG. 2. Schematic representation of atomic sites in the vicinity of a kinked  $\langle 110 \rangle$  step. The anisotropy of these sites is given in Table I.

stant alpha were set to the bulk values for Co. This is a continuum model which has been discretized at atomic length scales.

The micromagnetic structure of two monolayer (ML) films has been simulated where the top layer consists of a terrace one half the width of the bottom layer. The two step edges in the top layer were aligned along  $[1\bar{1}0]$  or  $[100]$ . In some simulations kinks were inserted into the step edges at regular intervals and the terrace widths were varied. The simulations used periodic boundary conditions in both in-plane directions. The system was discretized into cells with sides of length  $a_0/\sqrt{2}$  on a simple cubic lattice, where  $a_0$  is 0.361 nm. This insured that the volume of the region with

TABLE I. Anisotropy energies for fcc (100) sites described in the text and shown schematically in Fig. 2. Derivations of anisotropy energy and the value of the constants have been given in Ref. 9. Note  $r$ ,  $\theta$ , and  $\phi$  have been defined in the usual way. The step direction is  $[1\bar{1}0]$ . For  $[110]$  steps, change  $\phi$  to  $\phi + \pi/2$ .

Site/constant	Anisotropy energy
Bulk unstrained ( $E_{bu}$ )	$Q(r)/4(\sin^2 2\theta + \sin^2 2\phi \sin^2 \theta)$
Bulk strained	$(-6e_0L(r_0) - e_0\partial L/\partial r r_0)\cos^2 \theta + E_{bu}$
Surface	$(-1/2L(r_0) - 3e_0L(r_0) - e_0\partial L/\partial r r_0)\cos^2 \theta + E_{bu}$
Step edge	$(-1/4L(r_0) - 3e_0L(r_0) - 3/4e_0\partial L/\partial r r_0)\cos^2 \theta$ $+ (-1/2L(r_0) - 1/2e_0\partial L/\partial r r_0)\sin^2 \theta \sin \phi \cos \phi + E_{bu}$
Step corner	$(-1/4L(r_0) - 9/2e_0L(r_0) - e_0\partial L/\partial r r_0)\cos^2 \theta$ $- 1/2L(r_0)\sin \theta \cos \theta (\sin \phi + \cos \phi) + E_{bu}$
Kink-in edge	$(-1/2L(r_0) - 3e_0L(r_0) - e_0\partial L/\partial r r_0)\cos^2 \theta + E_{bu}$

Kink-in edge	$(-3e_0L(r_0) - 1/2e_0\partial L/\partial r r_0)\cos^2\theta + E_{\text{vu}}$
Kink-out edge	$(-1/4L(r_0) - 1/2e_0L(r_0) - e_0\partial L/\partial r r_0)\cos^2\theta$
Kink-in corner	$+(-1/4L(r_0) - 1/2e_0L(r_0))\sin^2\theta\cos^2\varphi$
	$-1/2L(r_0)\sin\theta\cos\theta\cos\varphi + E_{\text{vu}}$
Kink-out corner	$(-1/4L(r_0) - 1/2e_0L(r_0) - e_0\partial L/\partial r r_0)\cos^2\theta$
	$+ (1/4L(r_0) + 1/2e_0L(r_0))\sin^2\theta\cos^2\varphi$
	$-1/2L(r_0)\sin\theta\cos\theta\cos\varphi + E_{\text{vu}}$
$Q(r_0)$	$-1.2 \times 10^6 \text{ erg/cm}^2$
$L(r_0)$	$-1.5 \times 10^4 \text{ erg/cm}^2$
$\partial L/\partial r r_0$	$5.5 \times 10^4 \text{ erg/cm}^2$
$e_0$	0.019

step anisotropy matched the volume occupied by a step oriented along  $\langle 110 \rangle$ . The system was allowed to relax with no applied field in order to determine the equilibrium magnetization distribution in the film.

No significant out-of-plane ( $\langle M_z \rangle > 0.01$ ) component of the magnetization was present in the equilibrium magnetization distribution. The spins of the step corner atoms were expected to couple to the spins in the terraces and perhaps cause them to be somewhat canted out-of-plane. This did not occur as a result of the balance between the anisotropy energies of neighboring atoms and the exchange energy which couples them. The out-of-plane anisotropy of the step corner site occurs via the term proportional to  $\cos \theta (\sin \theta \sin \varphi + \sin \theta \cos \varphi)$  [i.e.,  $m_z(m_x + m_y)$ ]. The minimum energy occurs when  $-m_z = m_x + m_y$ . This equals zero for  $\varphi = 3\pi/4$  ( $[1\bar{1}0]$ ), which is the uniaxial anisotropy axis for the step edge site. Although the anisotropy energy of the step edge and step corner sites are about equal, the coupling via exchange to nearby surface and bulk sites (biaxial  $\langle 110 \rangle$ ) ensures that the step edge site is dominant. For any initial condition on the magnetization the final minimized energy configuration has the spins aligned along the step direction, and the out-of-plane component vanishes with  $(\sin \varphi + \cos \varphi)$ .

The magnetization configuration is somewhat different for faceted steps and square islands. At the corner joining a  $[110]$  step to a  $[1\bar{1}0]$  step, the magnetization of each step will be forced away from  $\langle 110 \rangle$  by the field due to the other step, resulting in a nonzero out-of-plane component. If the density of facets is large enough or the size of islands small enough a significant out-of-plane remanence will exist. This configuration has been simulated via a square island ( $3 \text{ nm} \times 3 \text{ nm}$ ) on a  $5 \text{ nm} \times 5 \text{ nm}$  square layer with periodic boundary conditions. The length of the sides of the island was chosen to approximate the length of facets observed in films which exhibited out-of-plane remanence. The out-of-plane component of the calculated average equilibrium magnetization was  $\sim 0.03$ . This was significantly less than the results from Kerr loops shown in Fig. 1.

#### IV. CONCLUSION

It is apparent from these micromagnetics simulations that the anisotropy of step atoms can not be responsible for

the out-of-plane remanence we observed experimentally. For surfaces with a high density of  $\langle 110 \rangle$  facets, this anisotropy may be a contributing factor. This micromagnetics result from semi-infinite parallel  $\langle 110 \rangle$  steps agrees with the experimental results from Co deposits on vicinal  $\text{Cu}/\langle 111 \rangle$  surfaces.<sup>4</sup> The anisotropy switches to biaxial in-plane at increased temperatures.<sup>13</sup> This may be due to Cu atoms decorating the step edges,<sup>14</sup> or to restructuring of the step edges with rectangular protrusions perpendicular to the original step.<sup>15</sup> In the latter case, micromagnetics simulations reported here predict a small ( $\sim 3\%$ ) out-of-plane component to the magnetization.

#### ACKNOWLEDGMENTS

The authors would like to acknowledge Dr. G. G. Hembree for collaboration in the experimental work. This work is supported by ONR under Grant No. N00014-93-1-0099.

- <sup>1</sup>U. Gradmann, J. Magn. Magn. Mater. 54/57, 733 (1986).
- <sup>2</sup>M. E. Buckley, F. O. Shumann, and J. A. C. Bland, J. Phys. 8, L147 (1996).
- <sup>3</sup>M. Albrecht, T. Furubayashi, M. Przybylski, J. Korecki, and U. Gradmann, J. Magn. Magn. Mater. 113, 207 (1992).
- <sup>4</sup>A. Berger, U. Linke, and H. P. Oepen, Phys. Rev. Lett. 68, 839 (1992).
- <sup>5</sup>W. F. Egelhoff, Jr., P. J. Chen, R. D. K. Misra, T. Ha, Y. Kadmon, C. J. Powell, M. D. Stiles, R. D. McMichael, C.-L. Lin, J. M. Sivertsen, and J. H. Judy, J. Appl. Phys. 79, 282 (1996).
- <sup>6</sup>S. T. Coyle, G. G. Hembree, and M. R. Scheinfein, J. Vac. Sci. Technol. A 15, 1785 (1997); S. T. Coyle, J. L. Blue, and M. R. Scheinfein, J. Vac. Sci. Technol. A (in press); S. T. Coyle and M. R. Scheinfein, Appl. Phys. Lett. (in press).
- <sup>7</sup>K. R. Heim, S. D. Healy, Z. J. Yang, J. S. Drucker, G. G. Hembree, and M. R. Scheinfein, J. Appl. Phys. 74, 7422 (1993).
- <sup>8</sup>Z. J. Yang and M. R. Scheinfein, J. Appl. Phys. 74, 6810 (1993).
- <sup>9</sup>L. Néel, J. Phys. Radium 15, 225 (1959).
- <sup>10</sup>H. Fujiwara, H. Kadomatsu, and T. Tokaunaga, J. Magn. Magn. Mater. 31-34, 809 (1983).
- <sup>11</sup>D. S. Chuang, C. A. Ballentine, and R. C. O'Handley, Phys. Rev. B 49, 15084 (1994).
- <sup>12</sup>M. R. Scheinfein (LLG Micromagnetics Simulator, © 1997).
- <sup>13</sup>W. Wulfhekel, S. Knappmann, B. Gehring, and H. P. Oepen, Phys. Rev. B 50, 16074 (1994).
- <sup>14</sup>W. Weber, C. H. Back, A. Bischof, D. Pescia, and R. Allenspach, Nature (London) 374, 788 (1995).
- <sup>15</sup>M. Giesen, P. Schmitz, and H. Ibach, Surf. Sci. 336, 269 (1995).

Electron holography is a powerful technique used to determine magnetic microstructure at nanometer spatial resolution. It has been used to characterize domain structure in thin films, to examine internal and stray fields in and around small particles [9,10], to study magnetization states in single Co nanowires [11], to examine Aharonov-Bohm effect by using ferromagnetic rings fabricated by lithography and to analyze the magnetic coupling of nanofabricated ferromagnetic arrays [9]. In this paper, we present results of direct observation of the magnetic coupling in nanoscale wire arrays examined using the magneto-optic Kerr effect and electron holography. Results are compared with a full three-dimensional micromagnetics simulation.

## II. EXPERIMENT

Optical-grade (110) polished NaCl single crystals (miscut angle  $< 3^\circ$ ) were used as substrates. These substrates were etched in deionized water for several seconds to remove surface contamination prior to loading into an ultra-high vacuum growth chamber (base pressure  $\sim 3 \times 10^{-8}$  Pa) equipped with Fe electron-beam and SiO thermal evaporation sources. Annealing these substrates *in situ* produced ordered templates. The annealed (110) oriented substrates form long, straight in-plane macrosteps along [001]. The (100) and (010) terraces which result from the thermal annealing process are tilted by  $45^\circ$  with respect to the surface normal. Annealing the NaCl at  $440^\circ\text{C}$  for 10 minutes produces step separations of 90 nm. A 20 nm SiO passivation layer was deposited directly on stepped NaCl surfaces (normal incidence deposition) since the NaCl substrates must be removed prior to characterization using electron microscopy. This also prevents the Fe from establishing an epitaxial relationship with the substrates which is important in magnetic coupling (strength) studies.

Fe was deposited from an electron-beam evaporation source at a rate of 0.20 nm/min. We denote the thickness,  $t$ , to be that nominal thickness on an exposed terrace in the direction normal to that terrace, e.g.  $45^\circ$  off of the (macroscopic) template normal for annealed (110) substrates. After depositing up to 15 nm of Fe, a 10-15 nm SiO capping layer was overlayed to prevent oxidation upon removal from UHV. Thus, the magnetically active Fe layer was embedded in an insulating SiO matrix.

Hysteresis loops were recorded *ex-situ* using the longitudinal magneto-optical Kerr effect (MOKE). Since both SiO and NaCl are transparent at the He-Ne laser wavelength, and the Fe films were extremely thin, the Kerr intensity was very small. The 2F (first harmonic of the photo-elastic modulator) mode was employed in order to obtain as high a signal-to-noise ratio as possible. Both the sample and the magnet could be rotated with respect to the optical scattering plane to examine the magnetization components parallel and perpendicular to an external magnetic field [12].

The microstructure was examined using a conventional transmission electron microscope (TEM: Topcon EM-002B). Specimen were fixed to 200-mesh Cu grids by floating the films off of the NaCl substrates in deionized water. The sizes of individual particles and wires were quantitatively measured using image analysis software. The holograms were recorded by using a field-emission transmission electron microscope (Philips, CM-200FEG) equipped with a 1024x1024 slow scan CCD camera. The images were reconstructed using image processing software developed by our group.

## III. RESULTS AND DISCUSSION

Fig.1 shows a bright field TEM image of the SiO(10 nm)/Fe wire array(13 nm)/ SiO (20 nm). The wires seen in dark contrast are formed near the ridges of the grating. The average projected width is 30 nm, hence, the real wire width

is expected to be 42 nm on facets inclined by  $45^\circ$  from the film normal. The standard deviation of the wire width is 18 nm, approximately 40% of the nominal wire width. Some wires terminate where terraces are perpendicular to steps accompanied by a miscut from the exact crystal axis. Most of the wires run through the approximately 3 mm field of view shown in Fig.1a. The average wire length calculated from the termination density is about 10  $\mu\text{m}$ . Though the array looks like a network of straight segments of a few  $\mu\text{m}$  long, low joint density is considered not to affect the magnetic behavior of the array. Since the wire aspect ratio is at least 200, strong shape anisotropy is expected. The corresponding electron diffraction patterns showed typical random polycrystalline features. No specific orientation relationship was observed between neighboring crystal grains.

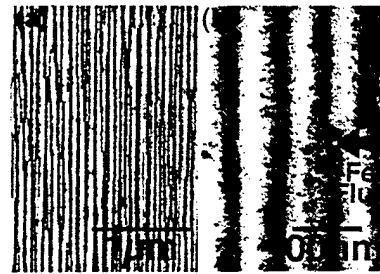


Fig.1 A bright field image of the SiO(10 nm)/Fe wire array(13 nm)/SiO(20 nm) deposited on the stepped NaCl(110). The wire width is 30 nm and the interwire spacing is 90 nm such that the gap between the wires is 60 nm.

Fig.2 shows longitudinal MOKE loops of the wire array recorded by applying an external field parallel (solid) and perpendicular (dotted) to the scattering plane, and rotating the specimens in the film plane by  $\theta^\circ$  with respect to the scattering plane. The angular dependence of the hysteresis loops is characteristic of uniaxial Stoner-Wohlfarth coherent rotation [13]. The specimen shows strong in-plane anisotropy when  $\theta=0^\circ$  and the coercivity is approximately 1.8 kOe. When the field is applied perpendicular to the wire, an external field of 3 kOe is not large enough to saturate the magnetization. When  $\theta=45^\circ$ , the switching field is minimum at half of the long-axis coercivity ( $H_c \sim 1.1$  kOe), and a peak is seen in the magnetization component perpendicular to the wires (indicated by the arrow in Fig. 2). The open-circle loop observed for perpendicular magnetization when  $\theta=80^\circ$  also indicates that the whole wire array switches simultaneously [14]. The long-axis coercivity is still lower than that expected for an infinitely long uniaxial Fe. The coercive field decreases with decreasing wire thickness (e.g.,  $H_c \sim 1.3$  kOe when  $t = 4$  nm). Domain wall motion is likely not occurring since significant transverse magnetization components are present during switching. Curling and buckling modes are known to effectively reduce the switching field in the case of uniaxial fine particle systems [15], but these processes are not accompanied by the perpendicular magnetization observed in the Kerr loops in Fig. 2.

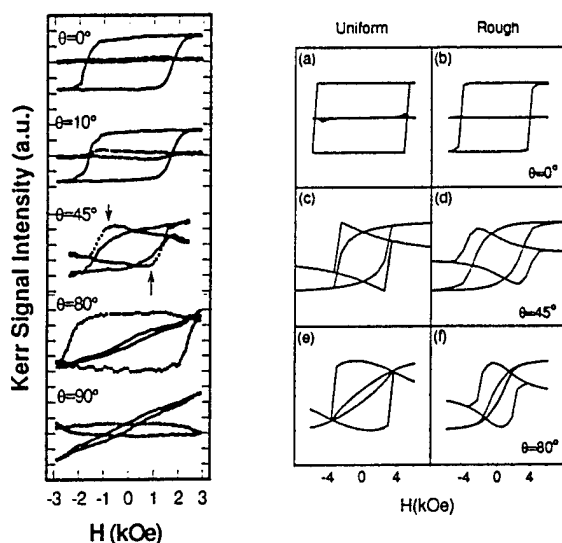


Fig. 2: (left) MOKE hysteresis loops acquired while rotating the specimen in the film plane.  $q$  denotes angle between the long-axis of the wire array and the scattering plane with the field applied in plane. Solid and dotted lines are magnetization components parallel and perpendicular to the field, respectively.

Fig. 3: (right) Hysteresis loops obtained from 3-D micromagnetics simulations for perfect (a,c,e) and rough (b,d,f) wire arrays oriented at  $0^\circ$ ,  $45^\circ$  and  $80^\circ$  to the field and scattering plane directions.

The magnitude of magnetic coupling in the wire array was extracted from 3-D micromagnetics calculations. The code [16] is capable of calculating three-dimensional magnetization distributions for arbitrary shaped systems composed of ferromagnets, antiferromagnets and metals. The computed hysteresis loops shown in Fig.3 use bulk magnetic properties for Fe ( $A = 2.1 \mu\text{erg/cm}$ ,  $M_s = 1714 \text{ emu/cm}^3$ ). No magnetocrystalline anisotropy was included since the orientation of the grains along the wires was random. Periodic boundary conditions were employed for a tiled array of 7 individual wires. Hysteresis loops for perfect (left) and rough (right) wires oriented at  $0^\circ$ ,  $45^\circ$  and  $80^\circ$  from the field and Kerr scattering planes (compare to Fig. 2) also indicate coherent rotation during switching. The broadened  $45^\circ$  (rough edge) loop is the result of pinning at edge defects due to the coarseness of the grid. The coercive field is larger in the computed loops as the result of assuming a rectangular cross section for each individual wire.

The magnetization distribution can be directly examined by electron holography. Fig. 4 shows a reconstructed phase image and accompanying line profile from the wire array at zero field. The Fe nanowire contrast is slightly asymmetric as evidenced by the electrostatic phase shifts arising from the mean inner potential and seen as white in the image. The magnetic contribution to the phase profile manifests itself as the consistent phase increase as each wire is crossed giving rise to the net positive slope. The phase shift expected from each wire is consistent with that expected from an Fe wire with  $390 \text{ nm}^2$  cross section, in agreement the dimensions of the wire. The sign of the magnetic phase shift is the same for

each wire indicating that the magnetization within each wire is aligned, i.e. the array is ferromagnetically coupled. This coupling is consistent with the coherent rotation features observed in Kerr measurements.

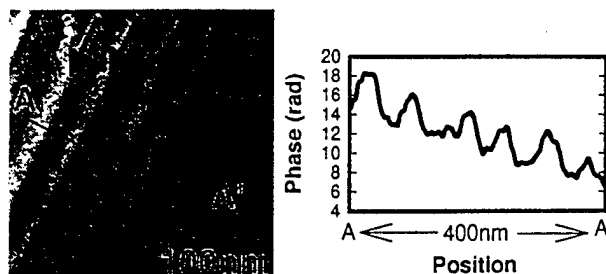


Fig.4: (left) An electron holographic phase image of the wire array reconstructed from an electron hologram, and (right) a line scan across A-A'. The phase is amplified by factor of 8, and wires are indicated by arrows in (a).

## REFERENCES

- [1] R.D. Gomez, M.C. Shih, R.M.H. New, R.F. Pease and R.L. White, J. Appl. Phys. **80**, 342 (1996); S.Gidar, J.Shi, P.F. Hopkins, K.L. Chapman, A.C.Gossard, D.D. Awschalon, A.D. Kent, and S. von Molnár, Appl. Phys. Lett., **69**, 3269 (1996).
- [2] S.Y. Chou, P.R. Krauss, L. Kong, J. Appl. Phys. **79**, 6101 (1996)
- [3] Akira Sugawara and M.R. Scheinfein, Phys. Rev. **B56** (1997) R8499
- [4] C. Mathieu, C. Hartmann, M. Bauer, O. Buettner, S. Riedling, B. Ross, S. O. Demokritov, B. Bartenlian, C. Chappert, D. Decanini, F. Rousseaux, E. Cambril, A. Müller, B. Hoffmann, and U. Hartmann, Appl. Phys. Lett., **70** (1997) 2912.
- [5] S. Morup, Phys. Rev. Lett. **72**, 3278 (1994); S. Morup, G. Christiansen, J. Appl. Phys. **73**, 6955 (1993); S. Morup, Hyperfine Int. **60**, 959 (1990); S. Morup, P.H. Christensen, B.S. Clausen, J. Mag. Mag. Mat. **68**, 160 (1987); S. Morup, M.B. Madsen, J. Franck, J. Villadsen, C.J.W. Koch, J. Mag. Mag. Mat. **40**, 163 (1983); W-N. Wang, Z-S. Jiang and Y-W. Du, J. Appl. Phys., **78**, 6679 (1995); S. Matsuo, T. Matsuura, I. Nishida and N. Tanaka, Jpn. J. Appl. Phys., **33**, 3907 (1994).
- [6] H. Takeshita, Y. Suzuki, H. Akinaga, W. Mizutani, K. Tanaka, T. Katayama, and A. Itoh, Appl. Phys. Lett. **68**, 3040 (1996); J. Shen, R. Skomski, M. Klaua, H. Jenniches, S. Sundar Manoharan, and J. Kirschner, Phys. Rev. **B56**, 2340 (1997).
- [7] A. Sugawara, S.T. Coyle, G.G. Hembree and M.R.Scheinfein, Appl. Phys. Lett., **70**, 1043 (1997).
- [8] A. Sugawara, G.G. Hembree and M.R.Scheinfein, J. Appl. Phys., (in print).
- [9] A. Tonomura, Rev. Mod. Phys., **59** (1987).
- [10] M. Mankos, M.R. Scheinfein, and J. M. Cowley, Phys. Stat. Sol. (a), **154**, 469 (1996).
- [11] C. Beeli, B. Doudin and P. Stadelmann, Phys.Rev. Lett., **75** (1995) 4630. And comments on it: M.R. Scheinfein, D. Streblechenko, and M. Mankos, Phys. Rev. Lett., **77**, 976 (1996); T. M. Hiller, P. A. Midgley, M. Saunders, Yi Ge, and W. Schwarzachar., **77**, 977 (1996).
- [12] Z.J. Yang, M.R. Scheinfein, J. Appl. Phys. **74**, 6810 (1993).
- [13] E.C.Stoner, E.P. Wohlfarth, Philos. Trans. Roy. Soc. London **A240**, 599 (1948).
- [14] M. Prutton, *Thin Ferromagnetic Films* (Butterworths, Washington, 1964).
- [15] D. Craik, *Magnetism, Principles and Applications*, (John Wiley and Sons, Chichester, 1995).
- [16] LLG Micromagnetics Simulator is a flexible, user friendly, three-dimensional micromagnetics tool commercially licensed by M.R. Scheinfein.

# Co on stepped Cu(100) surfaces: A comparison of experimental data with Monte Carlo growth simulations

S. T. Coyle and M. R. Scheinfein

Department of Physics and Astronomy, Arizona State University, Tempe, Arizona 85287

James L. Blue

National Institute of Standards and Technology, Gaithersburg, Maryland 20899

(Received 10 November 1997; accepted 24 November 1997)

Monte Carlo simulations of the growth of Co/Cu(100) in the presence of steps, terraces, and kinks were performed. The beginning stages of Co growth enhance the roughening of step edges. Interdiffusion increases with increasing temperature and decreasing growth rate. Varying the step orientation from  $\langle 100 \rangle$  to  $\langle 110 \rangle$  produced a steady decrease in interdiffusion. The lateral width of the interdiffused region in steps (10%–90% concentration) is  $\sim 0.7$ – $1.5$  nm. Decreasing the Co–Cu binding energy produced an increase in the frequency of double-height islands and step edge decoration. A value of  $\sim 0.21$  eV/nearest neighbor bond produced step edge decoration indicative of a Schwoebel barrier with very few double-height islands. Simulation results were compared to growth results obtained via nanometer resolution ultrahigh vacuum scanning electron microscopy. Island statistics compare favorably with growth results. Experimentally observed large etching features at steps were not well reproduced by the model, suggesting an exchange mechanism may be important. © 1998 American Vacuum Society. [S0734-2101(98)00703-9]

## I. INTRODUCTION

Co/Cu(100) has become an important system in the study of thin film magnetism. Face centered cubic (fcc) Co has a small lattice mismatch with fcc Cu(100) and will grow pseudomorphically. Cu surfaces vicinal to  $\langle 100 \rangle$  allow Co to be grown with a regularly spaced array of  $\langle 110 \rangle$  steps and  $\langle 100 \rangle$  terraces.<sup>1</sup> Bulk Co and Cu are considered immiscible below  $\sim 900$  K, however, Co and Cu have been reported to form an alloy<sup>2</sup> above  $\sim 450$  K, and interdiffusion during growth above  $0^\circ\text{C}$  has been suggested.<sup>3</sup> Co/Cu multilayers exhibit giant magnetoresistance, therefore understanding the Co/Cu interface is important. <sup>(GMR)</sup>

We have performed a study of the growth and magnetic properties of Co/Cu(100) at room temperature (RT)<sup>4</sup> in an attempt to understand how morphology and defects affect film growth and magnetic properties. We described two growth modes: island growth and exchange mediated growth, and reported a continuum of combinations of these two modes in different films. Island growth mode is characterized by the formation of islands on terraces and little interaction with steps, while exchange mediated growth is characterized by little island formation and a high degree of roughening of step edges. A Co adatom moves along a Cu step until it is pinned by a kink, thereby lowering the free energy. Because Co has a higher free energy<sup>5,6</sup> than Cu, the configurational energy may be lowered when Cu atoms move to surround the Co atom. This results in a restructuring of the step edge resulting in faceting along the lower energy  $\langle 110 \rangle$  directions. Incorporation into a  $\langle 110 \rangle$  step is much more energetically favorable than incorporation into a  $\langle 100 \rangle$  step,<sup>4</sup> and this difference may contribute to the difference between island and exchange growth.

We have performed growth simulations using Blue's ki-

netic Monte Carlo simulation program<sup>7</sup> in order to understand the various growth modes encountered during growth experiments. We are also interested in exploring the effects of growth parameters on interdiffusion. Interdiffusion and its affect on magnetic properties at the Co–Cu interface is of central importance in understanding GMR and other thin-film magnetic properties. We attempt to describe the sharpness and character of the interface, and its dependence on parameters such as growth temperature, growth rate, and terrace width. <sup>(leave as is)</sup>

## II. MONTE CARLO GROWTH SIMULATIONS

Kinetic Monte Carlo simulations of the growth of Co on Cu(100) in the presence of step edges were performed. Prior to deposition the Cu substrate was 100 by 100 atoms (square), 6 layers deep, and included one or two terraces with steps oriented along either  $\langle 100 \rangle$  or  $\langle 110 \rangle$ . Simulations were also performed at intermediate step orientations in  $5^\circ$  increments. Deposition of Co was simulated at rates of 0.15 ML/min (slow) and 1.5 ML/min (fast), and for coverages between 0.05 ML and 0.50 ML in increments of 0.05 ML. Initial kink densities of 0 and 0.15 kinks per site along the step edges were selected. Substrate temperature during growth was varied from 275 to 325 K to investigate the effect of temperature on morphology and interdiffusion for RT deposition. Five different simulations were performed with different random number seeds, and the quantitative measures were averaged.

The simulations assumed an Arrhenius-type barrier model, where the transition rate is  $r=R_0 \exp(-\epsilon/kT)$ . Activation energies ( $\epsilon$ ) were set proportional to beginning and ending bond energies according to  $\epsilon=A/(1+|\Delta E|/B)+H(\Delta E)$ . The constant A is the energy bar-



rier for hopping to a state of the same energy, and was set to approximate the experimental activation energy for Co adatom diffusion on Co(100).<sup>8</sup>  $H$  is the Heaviside function,  $T$  is the substrate temperature,  $k$  is Boltzmann's constant, and  $B$  is a constant which reduces the barrier somewhat when the final state is more tightly bound than the initial state.  $A$  and  $B$  were each set to 0.5 eV. Periodic boundary conditions were employed, with hops allowed along  $\langle 110 \rangle$  directions only. The difference in beginning and ending bond energies ( $\Delta E$ ) is found from the sum of all nearest neighbor (NN) and next nearest neighbor (NNN) bond energies before and after the hop. The Co-Co bond energy was 0.271 eV/NN and 0.004 eV/NNN.<sup>5</sup> The Cu-Cu bond energy was 0.190 eV/NN and 0.003 eV/NNN.<sup>5</sup> The Co-Cu bond energy was 0.2305 eV/NN and 0.0035 eV/NNN. To our knowledge, the Co-Cu bond energy has not been reported in the literature, we therefore chose a value that is the average of the Co-Co and the Cu-Cu bond energies. We also varied this as a parameter to see its effect on growth.

We have defined a set of measures in order to characterize the effect of various parameters on morphology. Mean island size ( $S_{av}$ ) is the mean of the distribution of island areas. Island density ( $N_{av}$ ) is the number of islands per unit area. Interface width ( $W_i$ ) is calculated as the standard deviation of the surface height distribution in units of  $a_0$  ( $a_0 = 0.361$  nm). This is a measure of the film-vacuum interface roughness. Step width ( $W_s$ ) is calculated as the standard deviation of the distance of each step edge atom from the center of the terrace. This is a measure of the roughness of the step, also in units of  $a_0$ . Interdiffusion width ( $W_d$ ) is a measure of the mean width of the interdiffused atoms for each row of atoms perpendicular to a step edge, in units of  $a_0$ . For example, the width is zero for the following arrangement of atoms perpendicular to a  $\langle 100 \rangle$  step: Co-Co-Co-Cu-Cu-Cu, while the width is two for: Co-Co-Cu-Co-Cu-Cu. This provides a measure of interdiffusion which is independent of the length and roughness of the step.

### III. RESULTS

#### A. General effects

The shape, size and density of the islands is essentially the same for simulations with the same deposition rate, independent of step orientation. The islands are approximately rectangular with edges along  $\langle 110 \rangle$  directions. Between 30% and 60% of the adatoms were captured by terraces, with more being captured during slower growth. Mean island area increases approximately linearly with increasing coverage until approximately 0.4 ML have been deposited, where island capture by steps and the agglomeration of very large islands becomes significant. Island density initially increased, then above 0.15 ML was fairly constant as a function of deposition. Both island density and mean island size were essentially unaffected by initial kink density. Interface width increases approximately linearly with coverage due to the deposition of adatoms and the nucleation of islands. Films grown at 1.5 ML/min have a slightly larger interface width than films grown at 0.15 ML/min due to their higher

nucleation density. Interface width is essentially unaffected by initial kink density. Step width of  $\langle 100 \rangle$  and  $\langle 110 \rangle$  steps are approximately the same and are unaffected by growth rate and initial kink density within the statistical uncertainty. The largest increase in step width occurs between 0 and 0.05 ML of Co deposit. A small amount of Co arriving at a step edge apparently induces a significant amount of restructuring, after which further Co deposition causes only incremental restructuring of the step edge. The addition of initial kinks to the steps did not affect the interdiffusion width. Slow growth produced significantly more interdiffusion than fast growth, with the effect being more pronounced on  $\langle 100 \rangle$  steps compared to  $\langle 110 \rangle$  steps.

Simulations were also performed on terraces without Co deposition.  $\langle 100 \rangle$  steps formed  $\langle 110 \rangle$  facets similar to those formed during the Co deposition simulations, however, the step width was approximately half as large for the equivalent amount of simulation time.  $\langle 110 \rangle$  steps formed rectangular inclusions only during simulations that included a nonzero initial kink density. These inclusions were much less deep and wider than those simulated during Co deposition. Co deposition is therefore enhancing the roughening of the step edges.

#### B. Temperature effects

Simulations of the initial stages of growth (0.05–0.20 ML) on substrates held at 275 K, 300 K, and 325 K were performed. We chose this temperature range because experiments suggest that in this region interdiffusion begins to become important.<sup>2,3</sup> Simulations were performed only for no initial kinks, since kink density was not a significant factor in the simulations described previously.

Mean island area increases linearly from 7 nm<sup>2</sup> at 275 K to 25 nm<sup>2</sup> at 325 K for slow growth on  $\langle 100 \rangle$  while the nucleation density decreases from 0.015 nm<sup>-2</sup> to 0.005 nm<sup>-2</sup>. For fast growth, the mean island area is about half as large as for slow growth accompanied by a corresponding increase in the island density by a factor of 2. This is consistent with increased adatom mobility at higher temperatures. Average island size for growth with  $\langle 110 \rangle$  steps does not reflect this trend because the terrace separation is smaller and at high temperatures all adatoms often migrated to the bottom of the steps. Thus the mean island size was about 5 nm<sup>2</sup> at all temperatures for both growth rates, while the nucleation density was comparable to that on  $\langle 100 \rangle$  at all temperatures.

Interface width decreases slightly with increasing temperature for fast and slow growth proximal to both  $\langle 100 \rangle$  and  $\langle 110 \rangle$  steps. This is related to the size distribution since islands of smaller size increase the interface width. Step width increased only slightly for increased temperature for  $\langle 100 \rangle$  steps. This is consistent with a greater mobility of step edge atoms. The steps are more free to restructure along  $\langle 110 \rangle$  directions in order to lower energy. For  $\langle 110 \rangle$  steps, the step edge is in fact becoming more smooth with increasing temperature.

Interdiffusion width increases markedly with increasing temperature (from  $<1a_0$  to  $>5a_0$ ). The effect is more pronounced for slow growth, which is again consistent with increased mobility. Interdiffusion is approximately the same for  $\langle 100 \rangle$  and  $\langle 110 \rangle$  steps at RT, however at higher temperature is larger for  $\langle 100 \rangle$ . Initial kink density appears to have no significant effect on interdiffusion. In the simulations for 0.15 ML/min at 325 K with steps along  $\langle 110 \rangle$  all of the Co has attached to step edges (no islands). The average width of the transition from pure Co to pure Cu (interdiffusion width) is  $5a_0$ , or  $\sim 1.8$  nm. The average width of the Co region along the step is  $\sim 3$  nm, therefore over half of the Co atoms in this simulation could be considered to be in a surface alloy phase. If we continued growth to 1.7 ML (the ferromagnetic transition), assuming no further interdiffusion, this would represent about 7% of the Co atoms. This number would decrease with increasing terrace width. It would, however, increase significantly with the inclusion of step bands, which have a high step density. We have simulated step bands by including a trough in the Cu substrate, and find that the level of interdiffusion in the troughs is even higher than that at steps. While the actual percentage of interdiffused atoms will depend on step and step band density, it is clear that an increase in temperature of 50 °C can produce a significant increase in interdiffusion and perhaps a significant surface alloy phase.

We have also simulated Co growth of 1 ML at RT near a trough followed by several seconds of annealing at 300 and 350 K. Annealing at 300 K did not have a significant effect, however annealing at 350 K for 10 s resulted in a single layer of Cu covering approximately 2/3 of the Co. The Cu migrated from areas of exposed Cu, leaving behind large vacant areas. This is consistent with experimental results.<sup>9,10</sup> The morphology obtained in these simulations resembles that obtained in our scanning electron microscopy (SEM) results which exhibit the exchange mediated growth mode.

### C. Co–Cu binding energy effects

Because the Co–Cu binding energy was not precisely known, it was varied as a parameter to see its effect on film growth morphology. Co–Cu binding energy was varied from 0.17 to 0.29 eV in increments of 0.02 eV. Representative samples are shown in Fig. 1, which include the atomic positions of the top three levels of atoms for Co deposition of 0.20 ML grown with Co–Cu binding energy for 0.17 (a), (b) 0.21 (c), (d) and 0.25 (e), (f) eV/NN bond for  $\langle 100 \rangle$  (a), (c), (e) and  $\langle 110 \rangle$  (b), (d), (f) terraces at 0.15 ML/min with no initial kinks. The most striking effect is the increasing frequency of double-height Co islands with decreasing Co–Cu binding energy, which, at 0.17 eV/NN bond, nearly all Co atoms including those decorating the step edge existing in this double-height state. This is reasonable since an atom on the top level of a double height island will be more tightly bound than an atom in a single height island with the same number of NNs.

Quantitative results of previously described measures as a function of Co–Cu binding energy have been compiled in

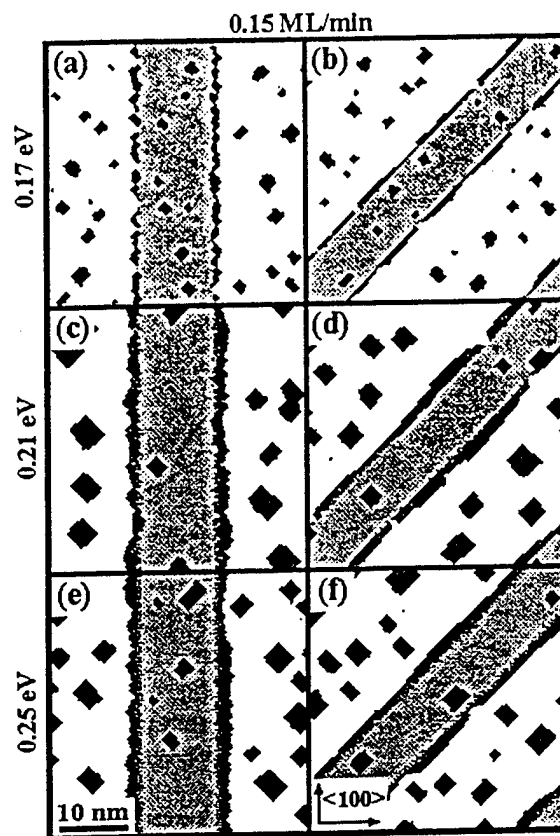


FIG. 1. Simulation results for Co deposition of 0.20 ML at 0.15 ML/min in the presence of  $\langle 100 \rangle$  (a), (c), (e) and  $\langle 110 \rangle$  (b), (d), (f) terraces for Co/Cu NN binding energies of 0.17, 0.21, and 0.25 eV/NN bond. Black squares are Co, gray squares are Cu, and white squares are the Cu substrate.

Fig. 2. The mean island size is larger and density smaller for slow growth than fast growth [Figs. 2(a), 2(b)]. The mean island size increases with increasing binding energy from 0.17 to 0.21 eV, above which it remains fairly constant. The island density [Figs. 2(c), 2(d)] decreases dramatically between 0.17 and 0.21 eV, then remains fairly constant thereafter. Both of these are consequences of the increase in double-height islands.

The interface and interdiffusion width as a function of Co–Cu binding energy is shown in Figs. 2(e)–2(h). Interface width is highest at low energies due to double-height islands. The dependence of the interdiffusion width on Co–Cu binding energy is quite different for  $\langle 100 \rangle$  and  $\langle 110 \rangle$  steps. The interdiffusion width for  $\langle 100 \rangle$  steps peaks at 0.21 eV. The interdiffusion width for  $\langle 110 \rangle$  steps increases steadily with increasing binding energy. The interdiffusion width for  $\langle 110 \rangle$  steps increases at a higher rate for slow growth than fast growth. No other measure reflects such a qualitative difference between the dependence of  $\langle 100 \rangle$  and  $\langle 110 \rangle$  steps on Co–Cu binding energy.

### D. Step orientation effects

The orientation of steps in our growth experiments often do not lie entirely along  $\langle 100 \rangle$  or  $\langle 110 \rangle$ , as steps often are pinned by defects. In order to investigate the general orientational dependence of steps, we have simulated the begin-

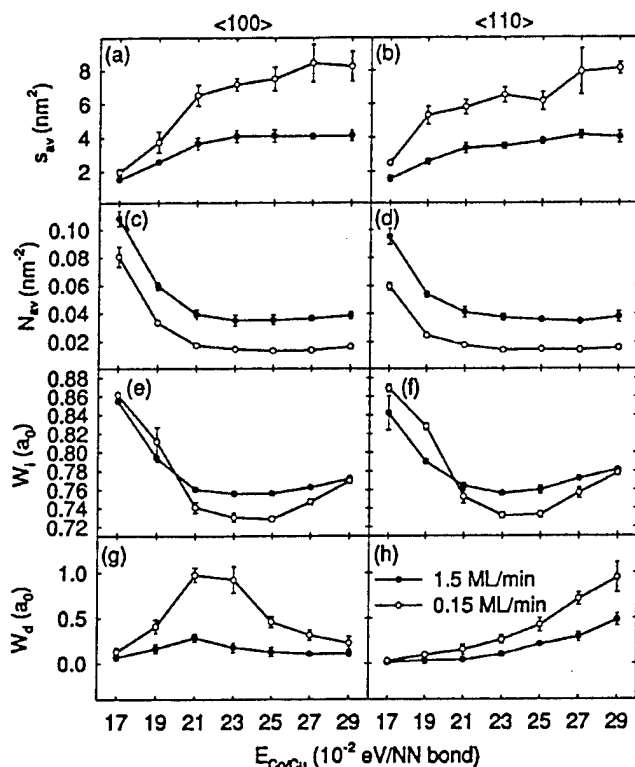


FIG. 2. Mean island size ( $s_{av}$ ) (a), (b), island density ( $N_{av}$ ) (c), (d), interface width ( $W_i$ ) (e), (f), and interdiffusion width ( $W_d$ ) (g), (h) as a function of Co/Cu binding energy for 0.20 ML of deposited Co for terraces with steps oriented along  $\langle 100 \rangle$  (a), (c), (e), (f) and  $\langle 110 \rangle$  (b), (d), (f), (h). Each graph includes plots of growth at 1.5 and 0.15 ML/min with initial kink densities of 0 kinks/site.

ning stages of growth for 1.5 ML/min and 0.15 ML/min for orientations between  $\langle 100 \rangle$  and  $\langle 110 \rangle$  in increments of 5°. The kink density will, by necessity, change with orientation with the maximum half way between  $\langle 100 \rangle$  and  $\langle 110 \rangle$ . The step width was equal for  $\langle 100 \rangle$  and  $\langle 110 \rangle$  steps, and was approximately 1/3 smaller for all other orientations. The step width was slightly larger for fast compared to slow growth. Interdiffusion decreases approximately linearly with orientation from a maximum at  $\langle 100 \rangle$  to a minimum at  $\langle 110 \rangle$ . Interdiffusion is larger for slow growth than fast growth. This is consistent with earlier interdiffusion width results. These results tend to rule out the possibility of dramatic morphological changes occurring for intermediate step orientations.

### E. Comparison with growth experiment

Monte Carlo growth simulations reproduced many features of the island growth mode observed during growth experiments. The faceting of step edges is reproduced, however the length scale of the facets is smaller in the simulations than in the growth experiments. During growth experiments step bands tend to form arcs between pinning sites, therefore perfecting  $\langle 100 \rangle$  or  $\langle 110 \rangle$  step edges is not the norm. We do find, however, many small lengths of step edges which are aligned nearly along crystallographic axes. These segments can be compared to simulation results in order to test the efficacy of the simulations. Figure 3 includes SEM micro-

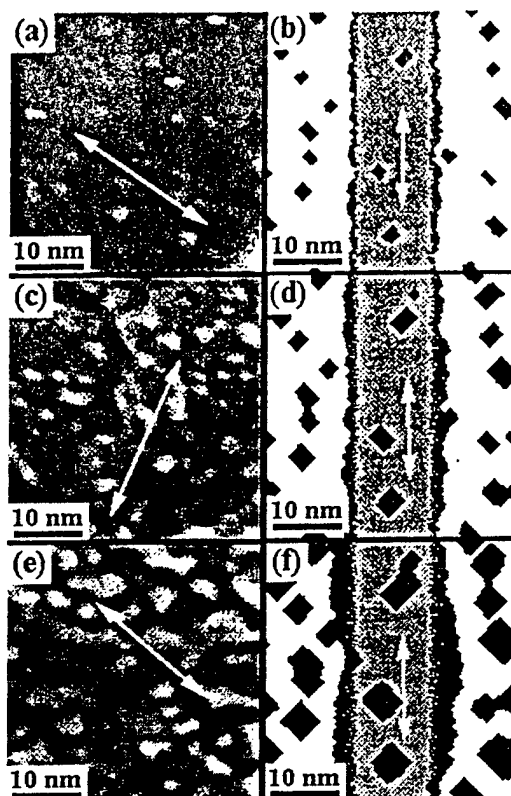


FIG. 3. Comparison of SEM micrographs with simulation results for 0.1 ML (a), (b), 0.2 ML (d), and 0.4 ML (e), (f) depositions with step edges aligned along  $\langle 100 \rangle$ . Arrows denote  $\langle 100 \rangle$  directions. Growth rate was 0.15 ML/min for all.

graphs (left) and simulation results (right) of RT growth near  $\langle 100 \rangle$  steps of 0.1, 0.2, and 0.4 ML all at 0.15 ML/min. White arrows in the micrographs denote the  $\langle 100 \rangle$  direction. The step edge parallel to the arrow in Fig. 3(a) shows large scale faceting, on the order of 5–7 nm. Faceting of the step edge in the 0.10 ML simulation [Fig. 3(b)] appears similar although the size of the facets is slightly smaller (2–3 nm). In Fig. 3(d), an island has grown into the step edge in the middle of the right step which produces a feature similar to the facets seen in Fig. 3(c). This could conceivably account for the larger scale faceting observed in the micrographs, however the islands do not appear to be large enough or rectangular enough to have caused the faceting in either Fig. 3(a) or 3(c). The irregular shape of the islands in the micrographs is not reproduced by the shape of the islands in the simulations. STM images<sup>9,11–13</sup> show islands with similar shapes to those in Figs. 3(a), 3(c), 3(e). Relaxation likely occurs at the edge of islands and at steps. This process is omitted in our simulation model. Addition of this process would change the kinetics and might account for the discrepancy in island shapes.

Figure 4 includes SEM micrographs (left) and simulation results (right) of growth near  $\langle 110 \rangle$  steps of 0.1, 0.2, and 0.35 ML, also at 0.15 ML/min. The step edges in the simulations have formed approximately rectangular inclusions, usually in a region with islands close to the step. Areas without these inclusions tend to have a region denuded of islands

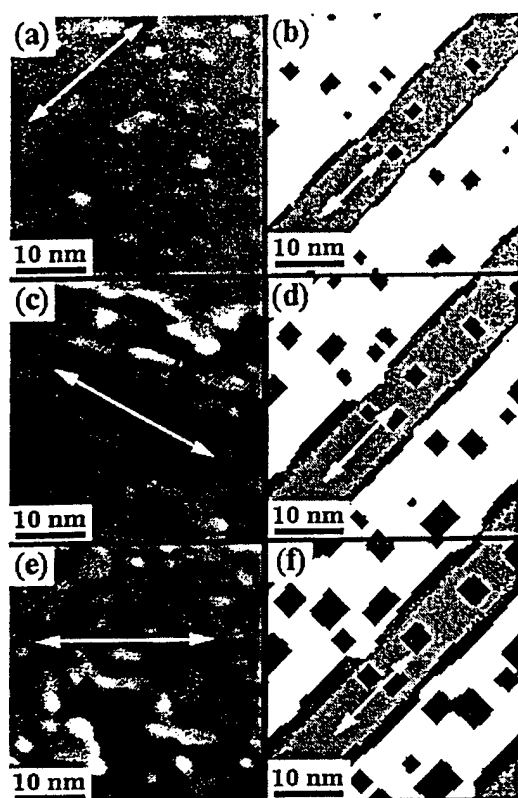


FIG. 4. Comparison of SEM micrographs with simulation results for 0.1 ML (a), (b), 0.2 ML (c), (d), and 0.35 ML (e), (f) depositions with step edges aligned along  $\langle 110 \rangle$ . Arrows denote  $\langle 110 \rangle$  directions. Growth rate was 0.15 ML/min for all.

near the terrace. The missing Co atoms are obviously in the islands near the inclusions. Such a region appears to exist in the vicinity of the arrow in Fig. 4(a), however the inclusions are much deeper than those in 4(b). This suggests that an exchange mechanism may be contributing to the restructuring of the step edges. As deposition increases [Figs. 4(c)–4(f)] the size of the inclusions increases in both growth and simulation experiments. The growth experiments, however, produce some striking step edge morphologies, as seen in Figs. 4(c) and 4(e). These features were not reproduced in the simulations, except perhaps for higher deposition where island capture by the terrace is evidenced. This observation suggests, again, that some exchange process is at work, or perhaps Cu has migrated from this area, thereby forming the inclusion. Clearly the kinetics at steps are more complicated than the barrier model in our simulation produces. The surface in Fig. 4(c) is an example of the exchange growth mode described previously.<sup>4</sup> Islands are quite rare and step edge restructuring tends to be more pronounced than in surfaces exhibiting the island growth mode. This morphology has not been reproduced in the corresponding simulations.

A comparison of island statistics for growth experiments exhibiting the island growth mode with simulation results is presented in Fig. 5. Mean island size (a), island density (b), and the percent of the surface covered by islands (c) is shown as a function of deposit. The smaller symbols represent simulation results and the larger symbols represent

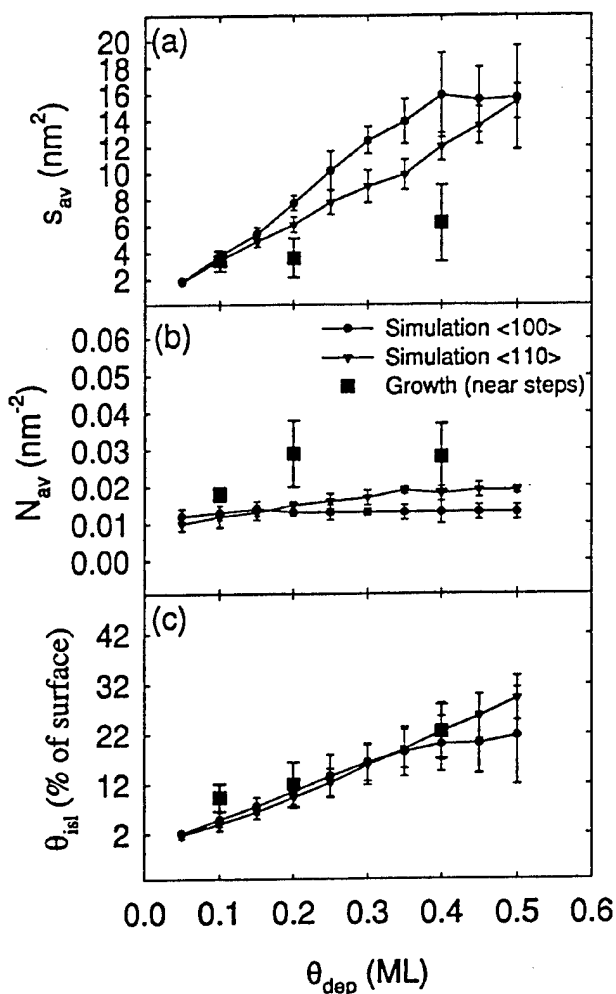


FIG. 5. Comparison of mean island size ( $s_{av}$ ) (a), island density ( $N_{av}$ ) (b), and the percent of the surface covered by islands ( $\theta_{isl}$ ) (c) as a function of Co deposit between simulation experiments and growth experiments. Growth experiment data was measured in regions with step densities similar to the simulations. Growth rate was 0.15 ML/min for all.

growth experiment results. Each growth data point represents the mean value obtained by analyzing several micrographs taken in different areas of the sample. The error bars represent one standard deviation. SEM micrographs selected for analysis included single height steps with a similar step length to surface area ratio as in the simulations. The simulation data represent 0.15 ML/min growth near  $\langle 100 \rangle$  and  $\langle 110 \rangle$  step edges with no initial kinks. The percent of the surface covered is reproduced well by the simulations, while island density is slightly higher and mean island area is lower in the simulation experiments than in the growth experiments.

In Figs. 4(c), 4(e) and in many micrographs not shown, bright regions are evident along some of the step edges, indicating that some step edge decoration has occurred. For Co–Cu binding energy near 0.21 eV there is a significant amount of step edge decoration with a small number of double height islands. The step edge decoration tends to be as deep as the Co adsorption region at the terrace level, since the lower Co–Cu binding energy favors Co–Co bonds.

While we cannot precisely determine the Co-Cu binding energy from these experiments, we can say that it is probably greater than 0.19 eV/NN bond based on the island density and lack of double-height islands. Another possible explanation for the step edge decoration is the existence of a Schwoebel barrier<sup>14</sup>—that is an additional barrier to hop down over a step edge. These simulation results indicate that for heteroepitaxial systems such a barrier may, in fact, be the result of a particular ratio of binding energies rather than a separate effect.

#### IV. CONCLUSION

We have performed Monte Carlo growth simulations of the growth of Co/Cu(100) in the presence of steps, terraces, and kinks. These simulations were not intended to study Co/Cu(100) growth from first principles, rather we were looking to answer specific questions relating to our experimental results. Simulation results for systems with and without Co growth have confirmed that the beginning stages of Co growth accelerate the faceting of  $\langle 100 \rangle$  steps along  $\langle 110 \rangle$  directions, and promote faceting of  $\langle 110 \rangle$  steps, also along  $\langle 110 \rangle$  directions. We believe this is driven by surface free energies: first by Cu moving to lower the number of dangling Co bonds, then by restructuring of the step edge to facets along the lowest energy face ( $\langle 110 \rangle$ ). The size of the faceted features observed in growth experiments was often significantly larger than those observed in simulation experiments. Larger scale facets were observed in simulations of annealed surfaces. This suggests that the model does not reproduce well the kinetics at steps, and could probably be improved upon with more realistic barrier heights.

Interdiffusion is essentially complete by 0.20 ML deposition. Interdiffusion increases with increasing temperature and decreasing growth rate, consistent with more time for atoms to rearrange positions between subsequent adatom arrival. Interdiffusion increased with increasing Co-Cu binding energy, presumably because these Co-Cu bonds are more difficult to break and thus the rate at which they break decreases. Varying the step orientation from  $\langle 100 \rangle$  to  $\langle 110 \rangle$  in small increments produced a steady decrease in interdiffusion. This result may be important for the magnetism of vicinal (100) surfaces which have regularly spaced  $\langle 110 \rangle$  steps only,<sup>1</sup> and thus would have a minimum amount of interdiffusion for a given step density. It is clear that the interface between Co and Cu is not sharp on an atomic scale: the width of the interdiffusion region (10%–90% concentration) is approximately 0.7–1.5 nm. For growth at 0.15 ML/min

there is approximately one interdiffused atom for every two unit cells ( $\sim 0.7$  nm) along the length of an average step. Interdiffusion, therefore, is highly dependent on step density (terrace width).

Island size and density compare favorably with growth results for the island growth mode, and the effects of deposition rate and temperature are consistent with accepted kinetic models. Island shapes are not well reproduced. Many of the features observed in the exchange mediated growth mode suggest an etching of the step rather than a simple restructuring along  $\langle 110 \rangle$  facets. This morphology was duplicated somewhat during annealing simulations. We believe the discrepancy between growth experiments and simulation experiments is due to kinetics. The barrier height model employed in our simulations works well for nucleation and growth of islands, however the kinetics at steps is more complicated. One or more processes at steps must occur at much different rates than predicted by our model. One possible example is adatom diffusion along a step, which as evidence suggests<sup>15</sup> may have a lower activation energy than adatom diffusion across a terrace. The most promising method to improve the simulation results would be to use a complete set of barrier height calculations. This may allow the determination of exactly which processes are responsible for the etching features we observed.

#### ACKNOWLEDGMENTS

The authors would like to thank Dr. G. G. Hembree for collaboration in the experimental work and a critical reading of this manuscript. This work is supported by ONR under Grant No. N00014-93-1-0099.

- <sup>1</sup> A. Berger, U. Linke, and H. P. Oepen, *Phys. Rev. Lett.* **68**, 839 (1992).
- <sup>2</sup> M. T. Kief, G. J. Mankey, and R. F. Willis, *J. Appl. Phys.* **10**, 5929 (1991). *J. M. Jenniches, S. Manoharan, and J. Kirschner*
- <sup>3</sup> J. Shen, R. Skomski, M. Klaua, *et al.*, *Phys. Rev. B* **56**, 2340 (1997).
- <sup>4</sup> S. T. Coyle, G. G. Hembree, and M. R. Scheinfeln, *J. Vac. Sci. Technol. A* **15**, 1785 (1997).
- <sup>5</sup> L. Z. Mezey and J. Giber, *Jpn. J. Appl. Phys., Part 1* **21**, 1569 (1982).
- <sup>6</sup> Y. W. Lee, K. C. Russell, and H. I. Aaronson, *Scr. Metall.* **15**, 723 (1981).
- <sup>7</sup> J. L. Blue (to be published).
- <sup>8</sup> M. T. Kief and W. F. Egelhoff Jr., *Phys. Rev. B* **47**, 10785 (1992).
- <sup>9</sup> A. K. Schmid, D. Atlan, and H. Itoh, *et al.*, *Phys. Rev. B* **48**, 2855 (1993).
- <sup>10</sup> M. Giesen, F. Schmitz, and H. Ibach, *Surf. Sci.* **336**, 269 (1995).
- <sup>11</sup> U. Ramsperger, A. Vaterlaus, and D. Pescia, *Phys. Rev. B* **53**, 8001 (1996).
- <sup>12</sup> A. K. Schmid and J. Kirschner, *Ultramicroscopy* **42**, 483 (1992).
- <sup>13</sup> R. Allenspach, A. Bischof, and U. Durig, *Surf. Sci. Lett.* **381**, L573 (1997).
- <sup>14</sup> R. L. Schwoebel, *J. Appl. Phys.* **40**, 614 (1969).
- <sup>15</sup> P. Stoltze, *J. Phys.: Condens. Matter* **6**, 9495 (1994).

J. B. Heinrich, T. Ichinokawa, and J. Kirschner

# Magnetic nanostructures produced by electron beam patterning of direct write transition metal fluoride resists

Dmitry Streblechenko<sup>a)</sup> and M. R. Scheinfein

Department of Physics and Astronomy, PSF-470 Box 871504, Arizona State University, Tempe, Arizona 85287-1504

(Received 26 September 1997; accepted 22 December 1997)

Transition metal (TM) fluoride electron beam sensitive resists suitable for the *in situ* fabrication of arbitrarily shaped nanometer scale magnetic structures have been developed. 20 nm thick TM fluoride films are prepared by thermal evaporation onto thin carbon films. Nanopatterns are written directly into the TM fluoride film in a scanning transmission electron microscope using a 0.5 nm diameter electron probe. Electron energy loss spectroscopy measurements indicate that as fluorine is released, the TM coalesces. Electron micrographs of exposed patterns show that the resist resolution is on the order of nanometers. Exposure of broad areas leads to coalescent TM layers which cap the remaining fluoride and decrease the rate of fluorine removal. The cross section for the removal of a fluorine atom and the cross section for the same process in the presence of an arbitrarily thick capping layer were measured. An electron dose of 1000 C/cm<sup>2</sup> at 100 keV will remove 90% of the fluorine from a 20 nm thick CoF<sub>2</sub> film. © 1998 American Vacuum Society. [S0734-2101(98)02303-3]

## I. INTRODUCTION

Recent progress in the experimental study of the growth and characterization of metals on insulators and semiconductors has been motivated by the need to develop smaller integrated semiconductor and magnetic devices. The majority of solid state devices are still fabricated using Si due to the existence of its native oxide, SiO<sub>2</sub>. Direct patterning of electron beam sensitive transition metal halides allows for the creation of nanometer scale magnetic structures at room temperature without chemical processing. This method may facilitate the fabrication of fully integrated electronic and magnetic devices on a single substrate without the deleterious effects of silicide formation. Magnetic sensors, high speed microwave guides, and non-volatile memory are just three of the many applications which may result from constructing solid state devices using transition metals on Si.

Nanometer scale magnetic structures are ideal canonical systems for studying fundamental processes in magnetism. *In situ* fabrication mediates the effects of oxide formation such that magnetic coupling studies can be performed between structures composed of different shapes over a wide range of length scales. The ability to vary the precise shapes and geometric order of arrays of nanometer size magnetic structures creates opportunities for studying magnetic stability as a function of temperature and externally applied magnetic field.

There are several methods that are employed in the manufacture of small magnetic structures. The most common, optical lithography,<sup>1</sup> is a well developed technology that has been widely used. Although optical lithography can provide very high throughput, the smallest size that can be created is limited by diffraction to about 0.2  $\mu$ m. The optical method involves exposure, processing, evaporation, lithography and

lift-off. Conventional x-ray and electron beam lithography<sup>2-6</sup> increases the resolution of the pattern transfer process to nm length scales, but still requires post processing to remove the resist. The creation of large arrays of small structures can be accomplished through self-organization.<sup>7,8</sup> This method allows for the fast manufacture of nm structures over large (macroscopic) areas. Although self-organization produces a very rich variety of structures, there is little control over individual particle shapes, ordering in arrays and length scales. Self developing resist x-ray and electron beam lithography<sup>9-12</sup> is a compromise among throughput, resolution and chemical reactivity during processing. The method is very flexible for the *in situ* manufacture of nano-structures yet the throughput is limited by resist sensitivity and serial processing. However, it is ideally suited for the generation of the small structures needed to examine fundamental magnetic properties at nanometer length scales.<sup>7,8</sup> Na, Li, Mg, and Al metal halides self-developing resists<sup>9-12</sup> have been used successfully to prepare nanometer metal structures in an electron microscope. However, there appears to have been no successful attempts at the manufacture of nanometer magnetic structures using direct writing in self-developing resists.

We have tested several transition metal halide compounds for suitability as self-developing resists for the manufacture of magnetic nanostructures. Of the eight transition metal halides tested (FeF<sub>2</sub>, FeF<sub>3</sub>, FeCl<sub>2</sub>, FeCl<sub>3</sub>, CoF<sub>2</sub>, CoF<sub>3</sub>, CoCl<sub>3</sub>, and NiF<sub>2</sub>) only FeF<sub>2</sub> and CoF<sub>2</sub> are sensitive enough to the electron beam. In this article we report on *in situ* experiments designed to produce controlled, nanometer sized magnetic structures using FeF<sub>2</sub> and CoF<sub>2</sub> electron beam sensitive resists. The resist properties are characterized using electron energy loss spectroscopy.

<sup>a)</sup>Electronic mail: Dmitrys@asu.edu; Michael.Scheinfein@asu.edu

## II. SPECIMEN PREPARATION

The preparation and properties of self-developing  $\text{FeF}_2$  and  $\text{CoF}_2$  films will ultimately define their utility as the electron beam resists. The thickness of the evaporated film affects both intrinsic properties such as grain size and uniformity as well as extrinsic properties such as the transparency of the resist to the electron beam during the exposure process. Extremely thick ( $\geq 100$  nm) resists are not sufficiently electron transparent to use electron holography<sup>13</sup> for characterization. Thick films degrade the resolution in the direct write process as they scatter the electron beam strongly.<sup>14</sup> The grain size which increases with increasing film thickness may also limit the ultimate resolution of the patterns transferred with the electron beam. While thin films are easy to write and can have extremely small grains, the coalesced metal structures may not be thick enough to be thermally stable.

Thin  $\text{FeF}_2$  and  $\text{CoF}_2$  (10–20 nm) films were prepared by thermal evaporation onto a 2–5 nm thick amorphous carbon films in a vacuum of  $10^{-8}$  mBar. Thermal evaporation of metal halides typically requires temperatures in excess of 1000 °C.<sup>15</sup> To ensure chemical uniformity of the resists, we use a molybdenum boat which does not form any stable compounds with the resist components. The residual pressure of oxygen and water in the evaporation chamber must be low enough to prevent the halides from decomposing and forming oxides and/or hydrates. The evaporated films have a polycrystalline structure with a crystal grain size ranging from 10 nm to 200 nm. The size of the polycrystals is a strong function of temperature, film thickness and growth rate, ranging from about 10 nm (1 nm/sec) to 100 nm (0.08 nm/sec) for 20 nm thick  $\text{FeF}_2$  films grown at room temperature. A growth rate of 1 nm/sec was a practical compromise. The thickness and composition of the films were analyzed using Rutherford back scattering.

Both  $\text{FeF}_2$  and  $\text{CoF}_2$  form anhydrous compounds.<sup>16</sup>  $\text{CoF}_2$  has three hydrates:  $\text{CoF}_2 \cdot 2\text{H}_2\text{O}$ ,  $\text{CoF}_2 \cdot 3\text{H}_2\text{O}$ , and  $\text{CoF}_2 \cdot 4\text{H}_2\text{O}$ .  $\text{CoF}_2 \cdot 4\text{H}_2\text{O}$  decomposes at a temperature of 200 °C. It is expected that the other two hydrates decompose at the same temperature range.  $\text{FeF}_2$  has two hydrates:  $\text{FeF}_2 \cdot 4\text{H}_2\text{O}$  and  $\text{FeF}_2 \cdot 8\text{H}_2\text{O}$ . These hydrates decompose at 100 °C. The presence of water in the halide films degrades both the sensitivity and resolution of the resist. Preheating the evaporant and boat to 200 °C in UHV decomposes the hydrates and removes the water. Evaporation was performed at a temperature between 1000–1100 °C. Although a higher temperature would increase the growth rate and decrease the polycrystallite size, it could decompose the bulk halide. After evaporation of the film, the specimen must be transferred immediately to the microscope since leaving the halide film exposed to air for ten minutes severely degrades the resist properties.

## III. EXPERIMENTAL INVESTIGATION OF THE METAL HALIDES PROPERTIES

Both the nanopatterning and nanocharacterization experiments were performed in a Vacuum Generators HB501

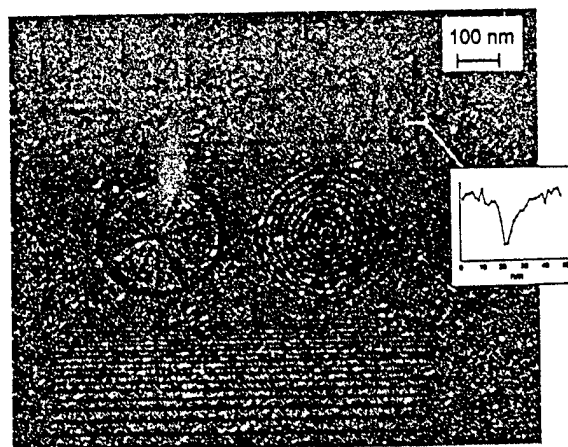


FIG. 1. High angle annular dark field image of a resolution test pattern transferred into  $\text{CoF}_2$  using 100 keV electrons in STEM. The gray areas are  $\text{CoF}_2$ , the black areas are metallic Co. The resolution here is limited by the scan rather than the resist to about 5 nm. Proximity resist effects can be observed.

Scanning Transmission Electron Microscope. This microscope is equipped with a Gatan® Parallel Electron Energy Loss Spectrometer (PEELS) and an EmiSpec Vision® computer controlled data acquisition system.<sup>17</sup> Ultimately, this microscope can focus 1 nA of 100 keV electrons into a beam  $\frac{1}{2}$  nm in diameter. Digitized patterns were transferred into the halide films by controlling the 100 keV electron beam with a computer while monitoring the electron dose. The computer controlled National Instruments® AT-MIO-16E-2 multichannel digital-to-analog converter can scan the electron beam at rates of up to 400 kHz. Our custom scanning software allows virtually any pattern to be transferred into the resist. Figure 1 shows a resolution test pattern that has been transferred into the  $\text{CoF}_2$  resist. This high-resolution annular dark field (ADF) image shows the  $\text{CoF}_2$  as gray, and the coalesced Co metal as black. A line scan taken across a single Co line at right has a width (FWHM) of approximately 5 nm. This is not the resolution limit of the resist but rather the linewidth selected for this exposure. There are some proximity effects in lines exposed close to one another. The boxes at the top of Fig. 1 have incomplete exposure of the lines that comprise the left side of each box. This is because the pattern was written from left to right. The exposed right side of the box immediately to the left of a given box decreased the resist sensitivity local to that exposed line. This proximity effect can be seen in the center of the exposed spoke pattern in the wheel at left in Fig. 1, and as roughness in the smallest lines written close together at the top of the array of lines at the bottom of Fig. 1. In all other cases, the lines are continuous, even and clearly resolved.

The self-development process was qualitatively characterized using bright and dark field imaging, and quantitatively characterized with electron energy loss spectroscopy (EELS). EELS spectra can provide valuable information in both low loss (0–100 eV) and high or core loss (100–1000 eV) energy loss ranges. The low loss EELS spectra can be used to investigate changes in the electronic properties dur-



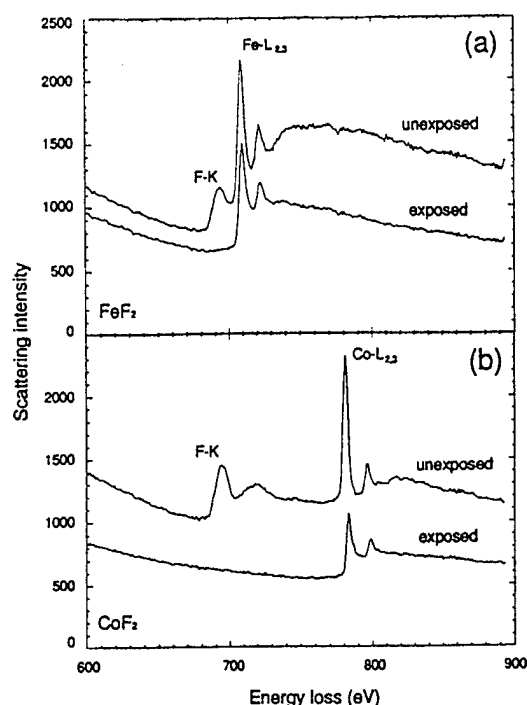


FIG. 2. Electron energy loss spectra in the energy region surrounding the fluorine *K*-edge (685 eV), the Co (779 eV) and Fe (708 eV)  $L_{2-3}$  excitations for (a)  $\text{FeF}_2$  and (b)  $\text{CoF}_2$  before and after electron beam irradiation.

ing irradiation. Changes in the composition of the compound during electron irradiation can be determined by monitoring the core loss excitation spectra (scattering cross section) during the electron exposure process. Figures 2(a) and 2(b) illustrate typical EELS spectra for  $\text{FeF}_2$  ( $\text{CoF}_2$ ) taken from both exposed and unexposed areas in the energy region surrounding the fluorine *K* (685 eV) excitation and the Co (779 eV) and Fe (708 eV)  $L_{2-3}$  excitations. It is clear from the spectra shown in Fig. 2 that in the exposed areas fluorine was completely removed, while little iron/cobalt mass loss is observed.

We separate the analysis of the self-development process in electron beam exposed regions of  $\text{FeF}_2$  and  $\text{CoF}_2$  into two categories: (a) An electron-beam/resist interaction occurs in exposed areas where F is liberated and the transition metal coalesces. This interaction governs the most basic properties of the resist such as its sensitivity and any thickness dependent effects. (b) In the vicinity of the exposed areas, diffusion of iron/cobalt, redistribution of the halide, and proximity effects due to high angle electron scattering and secondary electron creation reduce the sensitivity of the resist.

The sensitivity of  $\text{CoF}_2$  to electron exposure can be measured by monitoring the relative concentrations of Co and F during the irradiation process. Typically, a small region of the sample surface is scanned with the electron beam. The current is monitored as a function of time so that the total electron dose can be established. EELS spectra are accumulated frame by frame as a function of time (dose). One such time series acquired for a 20 nm thick  $\text{CoF}_2$  film is shown in

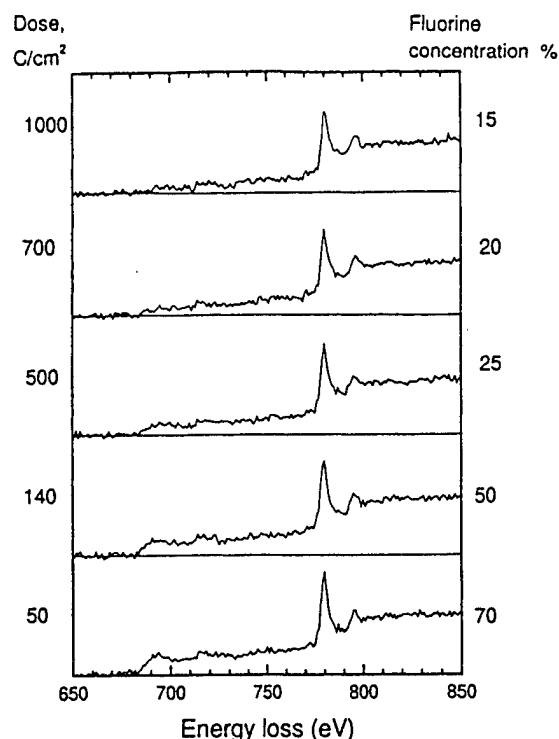


FIG. 3. Dose response EELS spectra in the core excitation region for  $\text{CoF}_2$ . The decrease in the F *K*-edge intensity near 690 eV energy loss is evident as a function of the dose indicated at left. The relative F concentration is shown at right.

Fig. 3. EELS spectra are shown near the F-*K* and Co- $L_{2,3}$  edges for the five electron doses shown at left. The relative concentration of F can be determined by fitting ( $I = AE^{-\gamma}$ ) the EELS spectra before the edge ( $E < 675$  eV), subtracting this background, and integrating for a fixed energy window under the excitation peak.<sup>18</sup> The relative concentration of F is shown in Fig. 3 at right.

A series of spectra like that shown in Fig. 3 illustrates how the dose response can be extracted from EELS spectra. Using EmiSpec Vision® image acquisition and processing software, such EELS spectra can be collected in real time, the background subtracted, and the suitable energy window integrated, yielding the elemental concentration as a function of dose. The four dose response curves in Figure 4 show both the Co and F concentrations as functions of time (dose) for four different exposed areas,  $48 \times 48 \text{ nm}^2$ ,  $70 \times 70 \text{ nm}^2$ ,  $140 \times 140 \text{ nm}^2$  and  $190 \times 190 \text{ nm}^2$  in Figs. 4(a)–4(d) respectively. The different size areas were selected in order to explore the dose rate dependence during the exposure process. Each experimental point in Fig. 4 indicated by a solid symbol is extracted from an EELS spectrum similar to those shown in Fig. 3. The time scale in Fig. 4 was normalized to give a constant current of 100 nA on the condenser aperture (corresponding to 140 pA at the specimen) using a series of current measurements, each taken simultaneously with the EELS spectral series. This procedure is required in order to correct for the beam current instabilities which can be as high as 70% over a period of several minutes. Variations in electron beam current (dose) were also monitored by mea-



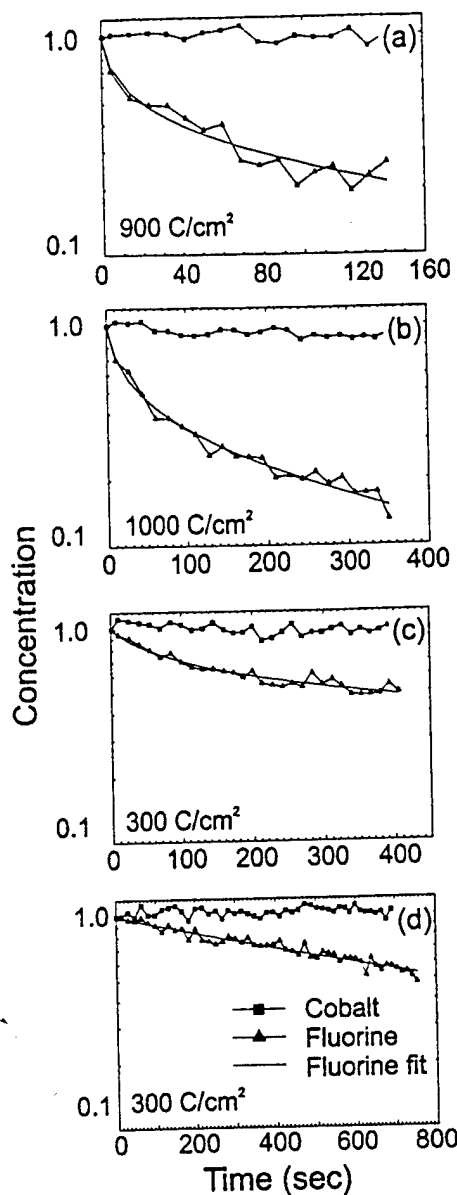


FIG. 4. Dose response curves for  $\text{CoF}_2$  show both the relative Co and F concentrations as the functions of time (dose) for four different exposed areas, (a)  $48 \times 48 \text{ nm}^2$ , (b)  $70 \times 70 \text{ nm}^2$ , (c)  $140 \times 140 \text{ nm}^2$ , and (d)  $190 \times 190 \text{ nm}^2$ . The different size areas were selected in order to explore the dose rate dependence in the exposure process.

During the area under the carbon  $K$ -edge excitation peak in each EELS spectrum. Since each transition metal halide film was deposited on a thin amorphous C substrate, this signal should remain constant in time unless carbon builds up on the specimen during exposure. Bright and dark field STEM images and EELS spectra were inspected both before and after each exposure to ensure that no appreciable carbon buildup occurred.

Expected trends are illustrated in Fig. 4. The Co concentration is approximately constant, while the F concentration decreases nearly exponentially. A very simple model of F liberation was developed in order to explain the observed

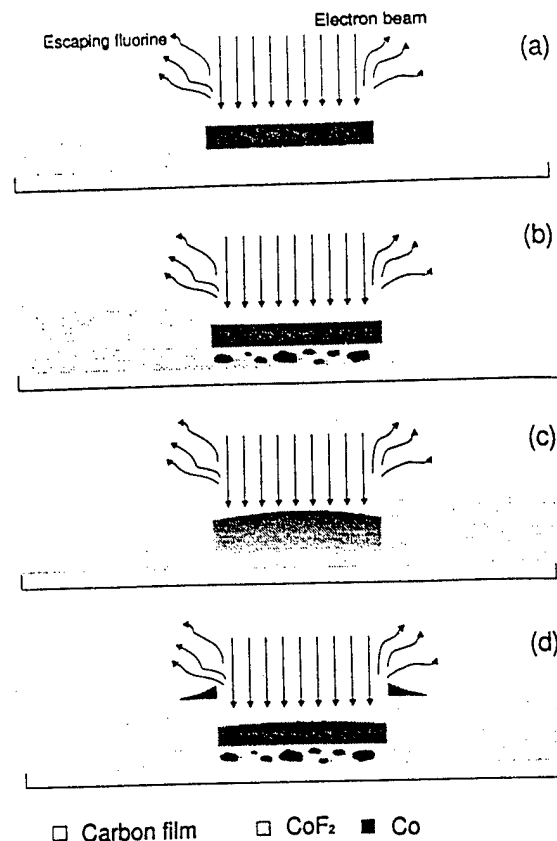


FIG. 5. Simple models for exposure include in order of increasing complexity (a) a simple capping layer; (b) simple capping layer with volume exposed regions; (c) continuous distribution of metallic Co; and (d) the addition of Co diffusing out of the exposed region.

behavior of the resist under electron beam irradiation as schematically illustrated in Fig. 5. The simplest model of the exposure process is shown in Fig. 5(a). Metallic cobalt coalesces only on the exposed region of the surface of the  $\text{CoF}_2$  film. A surface layer is expected when the probability of F escape to vacuum is higher close to the surface. It is possible that metallic cobalt forms a continuous surface layer with coalesced clusters with some unknown distribution underneath [Fig. 5(b)], or even some continuous depth distribution [Fig. 5(c)]. It is possible to measure the Co (metal) depth distribution performing dose response measurements for resist of different thickness. However, since the usable range of film thickness is limited in our application, this was not pursued. Co surface migration can play an important role in defining the resist resolution through proximity effects. The Co migrating along the surface out of an exposed region [Fig. 5(d)] can be minimized by exposing sufficiently large areas and monitoring Co concentration.

Since the nearly exponential initial decay in F concentration becomes much slower at later stages of exposure, we postulate that the reduced rate of F escape at higher dose can be explained by the newly coalesced Co metal trapping the F in the layer of  $\text{CoF}_2$  that is still unexposed underneath the capping layer [Fig. 5(a)]. This is the simplest model [Fig. 5(a)] to analyze the exposure process. The process

TABLE I. Dose response model parameters for CoF<sub>2</sub>.

Figure #	Area nm <sup>2</sup>	$\beta I_e$	$\gamma N_0$	$\sigma_F, 10^{-20} \text{ cm}^2$	$\sigma_{Co}, 10^{-20} \text{ cm}^2$
Fig. 4(a)	48×48	0.1±0.03	14±3	0.25±0.1	750±200
Fig. 4(b)	70×70	0.04±0.01	11±3	0.23±0.07	600±200
Fig. 4(c)	140×140	0.005±0.002	12±3	0.11±0.04	650±200
Fig. 4(d)	190×190	0.0007±0.0002	2±0.5	0.03±0.01	100±300

described by the following differential equation:

$$\frac{dN'_{F(t)}}{dt} = \beta I_e N_{CoF_2}(t) \exp[-\gamma N_{Co}(t)]. \quad (1)$$

$N'_{F(t)}$  is the areal density (atoms per cm<sup>2</sup>) of F escaping from the film,  $N_{Co}$  the areal density of the coalescent metallic Co, and  $N_{CoF_2}$  the areal density of CoF<sub>2</sub> molecules,  $\beta$  is the ionization cross section for removing one atom of fluorine from a CoF<sub>2</sub> molecule (if the 100 keV incident beam current density  $I_e$  is expressed in electrons/sec/cm<sup>2</sup>), and the exponential factor reflects the potential barrier which traps the F beneath the Co layer, with  $\gamma$  as a measure of the trapping strength, i.e.,  $\gamma$  is a cross section for one Co atom capping one F atom. The time dependent concentrations of CoF<sub>2</sub> and coalescent metallic Co are given by

$$N_{CoF_2}(t) = N_0 e^{-t/\tau(t)}, \quad N_{Co}(t) = \frac{N_0}{3} (1 - e^{-t/\tau(t)}), \quad (2)$$

where  $N_0$  is the initial number of atoms in CoF<sub>2</sub> molecules in the unexposed film. The number of atoms of the remaining F (bound in CoF<sub>2</sub>) is

$$N_F(t) = \frac{2}{3} N_0 - N'_{F(t)} = \frac{2}{3} N_{CoF_2}(t) = \frac{2}{3} N_0 e^{-t/\tau(t)}. \quad (3)$$

Note that Eqs. (2) and (3) are completely general since  $\tau = \tau(t)$  is an explicit function of time; the only model dependent equation is Eq. (1). Substitution of (2) and (3) into (1) gives the relative concentration of the remaining fluorine ~~exp~~  $\frac{N_F(t)}{N_0}$  as

$$\frac{d}{dt} e^{-t/\tau(t)} = -\frac{3}{2} \beta I_e \exp[-t/\tau(t)] \times \exp\left(-\gamma \frac{N_0}{3} \{1 - \exp[-t/\tau(t)]\}\right) \quad (4)$$

which cannot be solved in closed form for general  $\tau(t)$ ; solution in a series expansion of  $t$  for small  $t$  tends to be inaccurate.

The results of fitting Eq. (4) to the experimental data in Fig. 4 with  $\beta I_e$  and  $\gamma N_0$  as unknown parameters for a film of 22 nm nominal thickness, resist density of 4.46 g/cm<sup>3</sup> and electron beam current of 140 pA on the sample are shown in Table I.  $\sigma_F$  is the ionization cross section for removing one atom of F by with one 100 keV electron, and  $\sigma_{Co}$  is the capping cross section defined as probability of capturing one F atom by one Co atom. The decrease in the values of the cross sections with the increasing exposed area size can be attributed to specimen drift. Errors of such kind are hard to

correct since it is not possible to view the image on the microscope screen while the resist is being irradiated. The cross-sections shown in Table I indicate that a 100 keV electron has a  $3 \times 10^{-6}$  chance of ejecting one F atom out when passing through the CoF<sub>2</sub> elementary cell while one metallic Co atom has a  $5 \times 10^{-3}$  chance of trapping one F atom from the coalescent layer below. The Co trapping cross section ultimately defines the maximum practically useful thickness of the resist, e.g., for 500 layers of the coalescent cobalt ( $\approx 150$  nm) on top of CoF<sub>2</sub>, a F atom has only a 10% chance of escape according to the model used.

The image shown in Fig. 1 suggests that CoF<sub>2</sub> resist resolution is not limited by the polycrystallite size. Unlike some other self-developing electron sensitive resists (e.g., AlF<sub>3</sub>),<sup>9</sup> the coalescent metal in CoF<sub>2</sub> and FeF<sub>2</sub> resists does not seem to form clusters. Rather it is distributed uniformly across exposed areas. However, the proximity effect can limit the resist resolution. CoF<sub>2</sub> and FeF<sub>2</sub> may become less sensitive to the electron beam in the vicinity of exposed areas since some transition metal can diffuse out of the locally exposed areas, and cap the resist layers below. EELS spectrum taken from an exposed point (limited by the resist resolution rather than by the electron beam size) shows a somewhat lower concentration of the Fe/Co than a similar spectrum taken from an unexposed area. This loss of the transition metal in extremely small areas supports the explanation that some of the transition metal may spill over onto adjacent areas during exposure.

In order to try to quantify the length scales for Co migration during the exposure/capping process, we exposed a series of the rectangular regions with the same area but varying aspect ratio. It is intuitively clear that rectangles with a higher aspect ratio will have more Co diffusing out since the perimeter/area ratio is larger and hence there is a higher probability for a Co atom to escape the exposure region. In the crudest approximation, this process can be thought of as simple diffusion with a Gaussian distribution of the distance traveled by Co atoms and the diffusion distance independent on whether atom travels across an exposed or unexposed area. An expression for the Co concentration in the exposed region can be calculated by convoluting a Gaussian distribution with an initial concentration of the free Co, which is 1 for a point inside an exposed region and 0 otherwise. Fig. 6 shows a simulation of the relative Co concentration as a function of the aspect ratio for 5 different diffusion lengths (1, 2, 4, 8, and 16 nm) and an area of 5000 nm<sup>2</sup>.

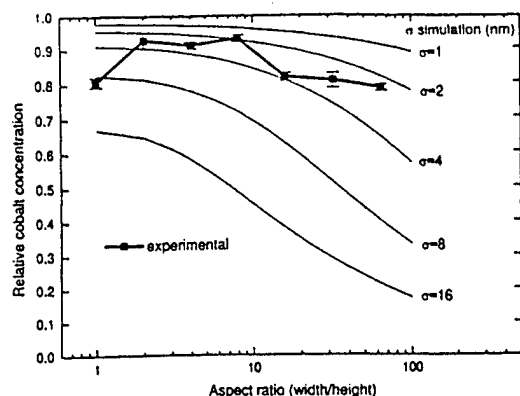


FIG. 6. Relative Co concentration as a function of the aspect ratio for 5 different diffusion distances (1, 2, 4, 8, and 16 nm) and an area of 5000 nm<sup>2</sup>. The experimental data are superimposed and indicated by solid symbols.

mental data for the rectangles with the aspect ratios of 1, 2, 4, 8, 16, 32, and 64 with the exposed area of 5000 nm<sup>2</sup> are superimposed on Fig. 6. Even though the experimental data can serve only as a qualitative measure, it allows us to estimate an upper limit for the diffusion distance as  $\sigma \leq 4$  nm, which is consistent with the proximity effect in the experimental image in Fig. 1.

#### IV. CONCLUSIONS

We have demonstrated that new high-resolution electron beam sensitive FeF<sub>2</sub> and CoF<sub>2</sub> resists can be vacuum sublimated and used for the *in situ* manufacture of small magnetic structures. Measured sensitivity, capping, and proximity effects show that it is feasible to use those resists for the manufacturing of the arbitrary shaped magnetic structures with the linear size of 10 nm and a thickness of 100 nm or less over the area on the order of several  $\mu\text{m}^2$ . The lower limit on the size of the manufactured magnetic structure is set by the resists resolution. While the resist sensitivity is lower than that for traditional electron beam resists, electron microscope images can still be obtained in a conventional electron microscope with the beam current on the order of 1 nA.

Currently experiments are under way to investigate magnetic properties of the nanostructures produced using FeF<sub>2</sub> and CoF<sub>2</sub> beam sensitive resists.

#### ACKNOWLEDGMENTS

The authors are indebted to Dr. G. Hembree for collaboration and assistance. They thank A. Higgs and J. Wheatley for providing electron microscope support. This work was supported by the ONR 00014-95-1-0891. The microscopy was performed in the Center for High-Resolution Microscopy at Arizona State University supported by NSF DMR93-14326.

<sup>1</sup>W. Van Roy, E. L. Carpi, M. Van Hove, A. Van Esch, R. Bogaerts, J. De Boeck, and G. Borghs, *J. Magn. Magn. Mater.* **121**, 197 (1993).

<sup>2</sup>P. R. Krauss and S. Y. Chou, *J. Vac. Sci. Technol. B* **13**, 2850 (1995).

<sup>3</sup>S. McVitie and J. N. Chapman, *IEEE Trans. Magn.* **MAG-24**, 1778 (1988).

<sup>4</sup>J. F. Smyth, S. Schultz, D. Kern, H. Schmid, and D. Yea, *J. Appl. Phys.* **63**, 4237 (1988).

<sup>5</sup>S. J. Hefferman, J. N. Chapman, and S. McVitie, *J. Magn. Magn. Mater.* **95**, 76 (1991).

<sup>6</sup>A. B. Johnston, J. N. Chapman, B. Khansehpour, and C. D. W. Wilkinson, *Phys. Rev. B* **54**, 1419 (1996).

<sup>7</sup>A. Sugawara, T. Coyle, G. G. Hembree, and M. R. Scheinfein, *Appl. Phys. Lett.* **70**, 1043 (1997).

<sup>8</sup>A. Sugawara and M. R. Scheinfein, *Phys. Rev. B* **56** (in press).

<sup>9</sup>A. Muray, M. Scheinfein, and M. Isaacson, *J. Vac. Sci. Technol. B* **3**, 367 (1985).

<sup>10</sup>Qun Dou and D. W. Lynch, *Surf. Sci.* **219**, 623 (1989).

<sup>11</sup>H. Watanabe, Jun-ichi Fujita, Y. Ochiai, S. Matsui, and M. Ichikawa, *Jpn. J. Appl. Phys., Part 1* **34**, 6950 (1995).

<sup>12</sup>I. G. Salisbury, R. S. Timsit, S. D. Berger, and C. J. Humphreys, *Appl. Phys. Lett.* **45**, 1289 (1984).

<sup>13</sup>A. Tonamura, *Electron Holography* (Springer, Berlin, 1993).

<sup>14</sup>L. Reimer, *Transmission Electron Microscopy* (Springer, Berlin, 1993).

<sup>15</sup>R. D. Mathis Company, *Thin Film Evaporation Source Reference* (Lebow Co, Goletta, 1987).

<sup>16</sup>*CRC Handbook of Chemistry and Physics*, edited by R. C. Weast (CRC, Boca Raton, FL, 1980).

<sup>17</sup>Thanks to scientists at EmiSpec Corporation for help with custom data acquisition and control software.

<sup>18</sup>R. F. Egerton, *Electron Energy Loss Spectroscopy in the Electron Microscope* (Plenum, New York, 1986).

# A reliable calibration method based on ion current measurement for an electron beam transition metal deposition source

E. T. Bullock, S. T. Coyle, G. G. Hembree, and M. R. Scheinfein<sup>a)</sup>  
*Dept. of Physics and Astronomy, Arizona State University, Tempe, Arizona 85287-1504*

(Received 9 February 1998; accepted for publication 29 April 1998)

A calibration scheme based on ion-current measurement has been implemented for an electron-beam transition metal deposition source. Repeatable and practical means of positioning the source (tip), measuring the ion current, and determining the flux rate are given. Intrinsic variations in the structural parameters of the source and thermal effects which can modify the observed deposition rate were examined and compensated for. A stable regime where ion-beam current is directly proportional ( $\pm 5\%$ ) to the growth rate has been determined. © 1998 American Institute of Physics. [S0034-6748(98)03407-8]

## I. INTRODUCTION

Electron beam deposition sources are used extensively in surface science and for monolayer growth experiments.<sup>1</sup> Typically a metal tip (source) held at high voltage is placed in the proximity of a tungsten wire thermionic electron source. The current emitted by the filament heats the tip, thermally activating atoms in the source which enter the gas phase, radiate outward, and create a flux of metal atoms. A thickness monitor is often placed next to the sample so that the growth rate can be monitored in real time. In other cases, Auger electron spectroscopy and/or reflection high energy electron diffraction are used to monitor the amount of material deposited. When these options are not available an independent real time method for determining the deposition rate must be found.<sup>2</sup>

The calibration method of Jones *et al.*<sup>2</sup> relies on the principal that a small fraction of the metal atoms are ionized as they pass through the bombarding electrons. These ions can be collected on an aperture (with negative potential) placed in the beam path. The magnitude of the ion current is related to the deposition parameters as

$$I \sim \int_V f(\mathbf{r}, z_f) j(\mathbf{r}, z_f) d^3r, \quad (1)$$

where  $I$  is the ion current,  $f$  is the flux density of metal atoms,  $j$  is the bombarding current density,  $z_f$  is the source-to-filament distance, and the volume of integration is over the region subtending all flux trajectories which will strike the collecting aperture. The  $z_f$  dependence is included only to indicate that  $f$  and  $j$  vary with tip position. In principle, the functions  $f$  and  $j$  are not known quantities. Instead, the variables  $F$  and  $J$ , referring to the total atomic flux measured at the sample (or thickness monitor) and the total bombarding current are used since these quantities can be measured directly.

If a range of source positions can be found where the ratio  $I/F$  is constant then the ion current,  $I$ , will be a direct measure of the flux rate. To successfully use this calibration

method such a linear region must be identified and a means of accurately relocating the tip in this linear region between subsequent depositions must be found. This task must be accomplished within the constraints that the tip length decreases with use and the physical structure of the evaporator prohibits direct viewing of the tip. We demonstrate here that these requirements can be met. We also show two methods for compensating for the thermal effects in the quartz-crystal thickness monitor (XTC) calibration measurements.

## II. EXPERIMENT

A schematic of our electron beam evaporator is shown in Fig. 1. The design is similar to that of Jonker<sup>1</sup> and Jones *et al.*<sup>2</sup> with the exception that the tip projects through a grounded cylindrical shroud orientated along the tip axis. A 1 mm diameter cobalt rod floats at 3 kV and is fastened to a linear motion feedthrough which can be positioned with an accuracy of .05 mm along the evaporator axis. A tungsten filament located about 6 mm from the tip of the rod is heated with approximately 4 A of current. The tungsten filament consists of one cylindrical winding 1 cm in diameter. Not shown are the electrical feedthroughs used for filament current and measurement of the ion current. Also not shown is the rotary motion feedthrough used for opening and closing the shutter.

Two apertures are shown in Fig. 1. The first is part of the heat shield. The second is electrically isolated, held at  $\sim -27$  V and is used to collect ion current. The first aperture (diameter=4 mm) has a slightly larger diameter than the second (diameter=3 mm) resulting in a reasonable ion current on the order of 0.1 nA. The size of the second aperture is chosen to ensure a deposition area that is somewhat larger than the sample area for a typical tip-to-sample distance. In our experiments, the tip-to-crystal thickness monitor was 4 in. The tip position,  $z$ , is measured on the linear motion feedthrough micrometer and  $z_f$  refers to the tip-to-filament distance. The tip voltage, filament current and voltage, emission current, and ion current were all measured directly during depositions.

<sup>a)</sup>Electronic mail: Michael.Scheinfein@asu.edu

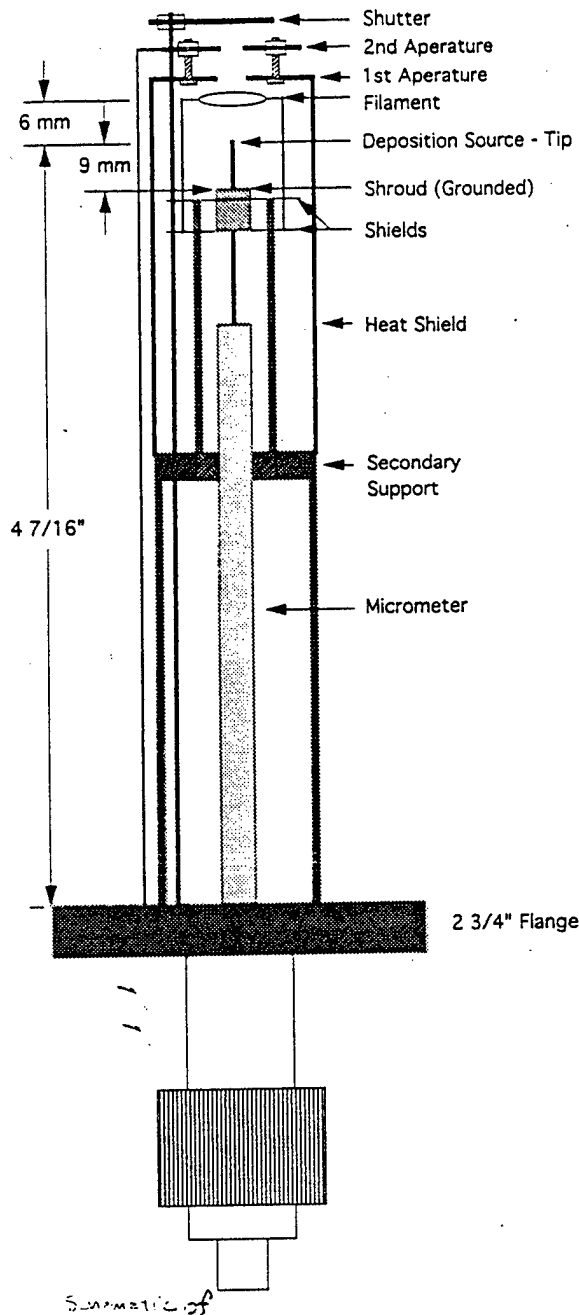


FIG. 1. CAD drawing electron beam deposition source. Note the grounded shroud containing the tip axis.

Flux rates were measured using a Leybold Inficon model XTC crystal thickness monitor. Though water cooled, the crystal thickness monitor is thermally sensitive. Thermal effects due to the electron beam source can yield false readings as high as a few tenths of ML/min. Data from a deposition where the shutter was not opened demonstrate this false growth rate in Fig. 2. Although the initial and final readings of the XTC coincide almost exactly, a resting time of greater than 200 min was required for thermal equilibrium to be achieved. The initial dip and final rise in the flux rate, where the power supplies were turned on and off, were due to a ground loop between the evaporator power supplies and the XTC.

The thermal effects associated with the XTC were cir-

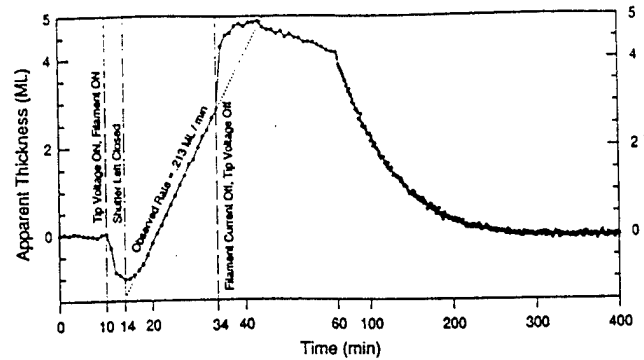


FIG. 2. Plot of flux rate vs time due to the thermal effects of a deposition as measured on the XTC. A deposition is conducted for 24 min with the shutter closed and then the system is allowed to return to thermal equilibrium.

cumvented in two ways. In the first method the XTC was turned on and allowed to run for 5–10 min in order to establish a stable zero value. The filament and tip power supplies were subsequently turned on and the tip was allowed to come into thermal equilibrium (about 10 min). The shutter was opened for a fixed period of time (5 or 10 min) and then closed. Once the shutter was closed, the filament and the tip voltages were turned off and the XTC was allowed to return to thermal equilibrium. The flux rate was computed by taking the difference between the initial and final readings on the XTC and dividing by the deposition time.

In the second method the filament current was set to its deposition value (tip voltage off) to allow the system to come into thermal equilibrium. The process took about 80–120 min as shown in Fig. 3. At this point, measurements from the XTC coincided with the amount of deposited material, assuming the filament current was held constant. Once thermal equilibrium was reached, the tip voltage was applied and the deposition rate would be measured by recording the film thickness for several minutes and then fitting a line to the data.

Finding a reproducible location of the tip is a fundamental requirement for using ion current as a measurement of

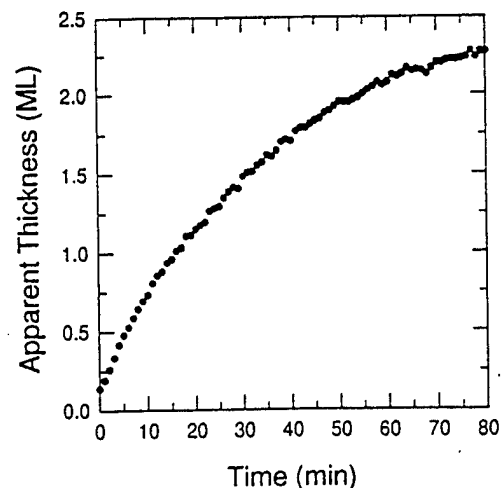


FIG. 3. Plot of flux rate vs time due to the thermal effects of the filament over an extended period of time as measured on the XTC.

flux rate. Repositioning the tip at the same position between depositions ensures that the bombarding electrons strike the tip in a geometrically repeatable way. This ensures a stable tip shape which in turn produces reproducible flux rates for equal incident electron power densities. The following discussion will outline a method of repositioning the tip with an accuracy of better than  $\pm 0.1$  mm.

Jones *et al.*<sup>2</sup> published a method of determining the tip position. In their method the tip was placed near the filament and operated at an emission current well below the deposition value. Without changing the filament current or the tip voltage, the tip was then slowly retracted and the emission current was recorded as a function of tip position. The resulting plots of  $J$  vs  $z$  were curves which decayed slowly and nonlinearly. They found by plotting the quantity  $d \ln(J)/dz$  vs  $z$  that all of the values, regardless of  $J$ , fell on a single curve with negative and decreasing slope. This procedure was performed prior to the first deposition when the exact location of the tip was still known. A plot of  $d \ln(J)/dz$  vs  $z$  was made and the slope of the curve at the desired position of  $z$  was noted. By repeating this procedure after each deposition and finding the previously recorded slope, the tip could be accurately repositioned.

Attempts to duplicate this method with our apparatus were not successful. The grounded shroud shown in Fig. 1 had a dramatic effect on the emission current, essentially acting as an electron lens. Starting with the tip near the filament,  $J$  fell off roughly linearly with  $z$ . However, as the tip neared the grounded shroud (diameter=5 mm),  $J$  fell off exponentially. As the tip was pulled back into the shroud the curvature of the current density,  $dJ/dz$ , changed sign (inflection point).  $J$  then leveled off and began to decline linearly again. Our data could be fit quite well with the function

$$J(z) = A / \{1 + \exp[(z-B)/C]\} + Dz + E. \quad (2)$$

Sample emission current measurements and their fits are shown in Fig. 4. The symbols are the data points and the lines are the fits. Positions of the shroud and the filament are shown above the graph. The values of the fit parameters,  $b$ , from Eq. (2) are the positions of the inflection points and are indicated above each curve.

The inflection points of  $J$  occur at different values of  $z$  for each curve in Fig. 4. Thus, to use the inflection point as a measure of tip position, it is necessary to relocate the same curve each time the tip length changes. For a fixed tip voltage, the emission current,  $J$ , is determined by the filament current and the tip position. That is,  $J = J(i_f, z_f)$  with  $i_f$  being the filament current. The curves shown in Fig. 4 show two distinct regions. In the first region, where the tip is close to the filament, the dependence of the emission current on  $z_f$  is small. If the tip were projected completely through the filament coil then the dependence of  $J$  on  $z_f$  would vanish entirely and  $J$  would only be a function of  $i_f$ . In the second region, inside the shroud, the emission current depends strongly upon  $z_f$  and only weakly on  $i_f$ . Thus, a method for repositioning the tip would be as follows. Project the tip completely through the filament and adjust  $i_f$  to generate a starting value of  $J$  equal to  $J_0$ , retract the tip and record  $J$  vs  $z$ , then fit the curve using Eq. (2). The fitting parameter  $b$

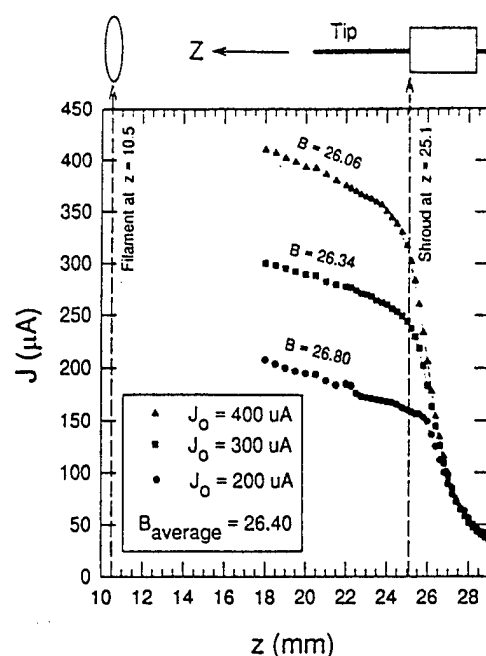


FIG. 4. Plots of  $J$  vs  $z$  for three initial values of  $J$ . The symbols represent the data points and the connecting lines are best fits using the fitting function described in the literature.

gives a reference position for the tip. After a deposition, the same curve is found again by projecting the tip completely through the filament coil and adjusting  $i_f$  to generate  $J_0$ . By again recording  $J$  vs  $z$  a new value of  $b$  can be found and the change in the tip length can be computed from the difference of the two  $b$  values.

The problem with the above method is that the tip length decreases with use. There would be a point when the filament would be out of the range of the linear motion feedthrough and a large amount of usable tip would be left. Thus, a compromise was made. Instead of starting the tip completely through the filament coil, it was started at the deposition position. This procedure introduces a small amount of error in relocating a given curve. To compensate for this error three different  $J_0$  curves were used and the  $b$  values from each curve were averaged, as shown in Fig. 4. This average was used as the reference position for the tip. This technique was used during a period of testing and calibration in which over 6 mm of tip was consumed. Upon venting and examining the tip the error in the expected tip position was found to be less than  $\pm 0.1$  mm.

New tips were presharpener for 1 h by depositing at a flux rate of 1 ML/min in the linear region of  $J$  vs  $z$  shown in Fig. 4. A stable tip shape was crucial to obtain repeatable results. In the linear region of  $J$  vs  $z$ , the bombarding current strikes the tip from the sides, forming a sharp tip. This process is self-stabilizing. That is, at some point in time evaporation causes the tip length to decrease without changing the tip shape. However, if the tip is pulled back into the nonlinear  $J(z)$  region during deposition, the bombarding current is focused onto the end of the tip causing it to blunt. No consistent results were obtained with the tip positioned in the nonlinear region. A stable tip shape is critical for repeatable results. Once a suitable tip position is found, the tip should

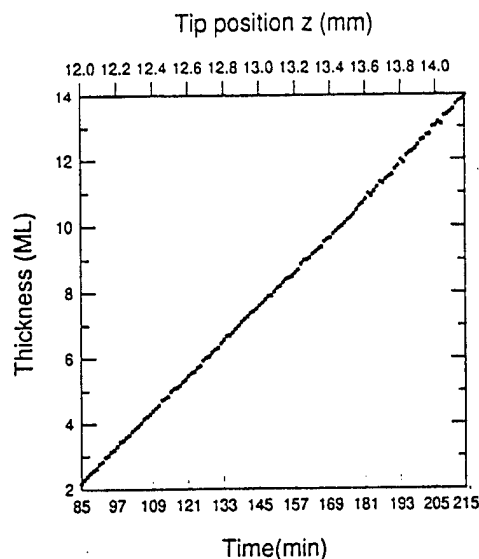


FIG. 5. Plot of film thickness vs time for various tip positions. The tip is left at each position for 12 min.

be conditioned at that position and subsequent depositions should be carried out at that position.

Figure 5 shows a plot of film thickness versus time. The tip position was started 4.5 mm from the filament (12 mm on the micrometer) and retracted by 0.2 mm every 12 min to a final position of  $z_f = 6.5$  mm ( $z = 14$  mm). The filament current of 3.65 A was not changed and  $J$  was allowed to fall off linearly with tip position starting at 1.358 mA and ending at 1.302 mA. The ion current was recorded for each tip position. As can be seen from the constant slope of the data in Fig. 5, the flux rate ( $F$ ) for this entire region was constant. In addition, the measured ion current ( $I$ ) was 0.065 nA with variations no greater than  $\pm 0.002$  nA over the entire deposition. The fact that  $J$  decreased with  $z_f$  by exactly the right amount to keep  $F$  constant is remarkable. Upon checking the tip position after this deposition it was found that a total of 0.6 mm of material was removed, meaning that the total range of tip positions was  $z_f = 4.5$ –7.1 mm.

A position of  $z_f = 6$  mm was selected and measurements of  $F$  vs  $I$  were made using two methods. First, the tip was started at 6 mm and not adjusted during the measurement process. The data points were obtained sequentially after using the 80–120 min preheat method described above. The filament current was increased in discrete steps in order to measure  $F$  for eight different ion currents in the range from 0.03 to 0.08 nA. A plot of  $F$  vs  $I$  with a best fit line is shown for three of the runs in Fig. 6. The tip position was readjusted between runs using the method described above. Approximately 0.3 mm of tip was consumed during each run. The results from the first run in Fig. 6 show that the tip shape was changing slightly during the deposition period. Prior to this deposition at  $z_f = 6$  mm the tip had been at  $z_f = 7.1$  mm. The best fits for the subsequent two runs have a slope of 1.66 ML/min/nA and 1.63 ML/min/nA, respectively. Each line has a y intercept less than zero but greater than  $-0.01$  ML/min.

Several individual measurements (single depositions) were made using the no-preheat, 200 min cool down method

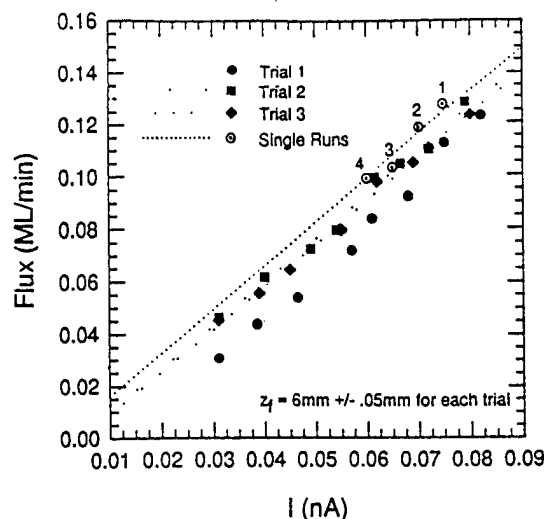


FIG. 6. Plots of flux rate vs ion current for sequential increases of filament current (trials) and for single depositions.

described above. These results are also shown in Fig. 6. For each measurement,  $I$  was started at  $\sim 0.02$  nA and slowly increased over a period of about 15–20 min. When this warm-up period was not employed, the flux rate was inconsistently high and for the subsequent deposition it was low, as heating the tip too rapidly affected the tip shape. Total deposition times of 10 min were used for each data point. As can be seen in Fig. 6, the flux rates for the single depositions agree quite well with those of runs 2 and 3. For each single measurement the flux rate was slightly higher than those of the linearly fitted trials. In computing the best fit line for the four single deposition measurements the data point (0,0) was included. The slope of the line was 1.67 ML/min/nA and the y intercept was in the same range as those of runs 2 and 3.

Ion current can be used as a measure of flux rate for transition metal e-beam deposition sources. For our evaporator design shown in Fig. 1, operating at  $V = 3$  kV and a tip-to-filament distance of 6 mm, the flux rate was given by the linear relationship

$$F = 1.67I - 0.005, \quad (3)$$

where  $F$  is in ML/min when  $I$ , the induced ion current, is measured in nA for our collection aperture and a source to crystal thickness monitor distance of 4 in. The reproducibility is found to be better than 5%. A method of accurately relocating the tip to the position  $z_f = 6$  mm between depositions has been found which is analogous to that of Jones *et al.*<sup>2</sup> The presence of a grounded shroud affected the  $J(z)$  plots in a way that aided in the location of the tip position. The tip could be relocated with an accuracy of better than  $\pm 0.1$  mm. Thermal effects on calibration measurements from a quartz crystal thickness monitor can be reduced by using proper measurement protocols.

#### ACKNOWLEDGMENT

This work was supported by the Office of Naval Research under Grant No. N00014-93-1-0099.

<sup>1</sup>B. T. Jonker, J. Vac. Sci. Technol. A 8, 3883 (1990).

<sup>2</sup>T. Jones, J. Sawler, and D. Venus, Rev. Sci. Instrum. 64, 2008 (1993).

# ARIZONA STATE UNIVERSITY

Department of Physics and Astronomy  
Tempe, Arizona 85287-1504  
(602) 965-3561

Michael R. Scheinfein  
Phone : (602) 965 - 9658  
FAX : (602) 965 - 7954  
Internet : shine@shine.la.asu.edu  
Internet : scheinfein@phyast.la.asu.edu

**Date:** 6 October 1997

**To:** Dr. Richard Brandt  
Office of Naval Research  
Electronics Division Code 312  
800 N. Quincy Street  
Arlington, VA 22217-5660

**Subject:** Year 5 Annual Report on ONR-N00014-93-0099 and ONR-00014-95-0891

Dr. Brandt,

Enclosed are some reprints and preprints that document our productivity during the last Grant Year. Our goals remain the same. Our research focus has not changed since our last annual report. In the interest of space in your files, I submit these publications as our annual report. You can expect a more expansive document later this autumn when I submit my renewal proposal to you.

The individual publications included in this report are:

A Comment of "Flux Quantization in Magnetic Nanowires Imaged by Electron Holography", M.R. Scheinfein, D. Streblechenko, M. Mankos, Phys. Rev. Lett. **77**(5), 976 (1996).

Quantitative Magnetometry Using Electron Holography: Field Profiles Near Magnetic Force Microscope Tips, D.G. Streblechenko, M. Mankos, M.R. Scheinfein, IEEE Trans. MAG **32**(5), 4124 (1996).

Growth of Nanometer-size Metallic Particles on  $\text{CaF}_2(111)$ , K.R. Heim, S.T. Coyle, G.G. Hembree, J.A. Venables, J. Appl. Phys. **80**(2), 1161 (1996).

Greatly Defocused Off-Axis STEM Electron Holography, J.M. Cowley, M.Mankos, M.R. Scheinfein, Ultramicrosc. **63**, 133 (1996).

Electron Holography and Lorentz Microscopy of Magnetic Materials, M.Mankos, M.R. Scheinfein, J.M. Cowley, Advances in Imaging and Electron Physics, P.W. Hawkes ed. vol. 98, 323-426 (1996) (\*\*not included since it is a 104 page article).



Growth, Morphology and Magnetic Properties of Ultrathin Epitaxial Co Films on Cu(100), S.T. Coyle, G.G. Hembree, M.R. Scheinfein, J. Vac. Sci. Technol. **A15**(3), (in press - 1997).

Self-Organized Fe Nanowire Arrays Prepared by Shadow Deposition on NaCl(110) Templates, A. Sugawara, S.T. Coyle, G.G. Hembree, M.R. Scheinfein, Appl. Phys. Lett. **70**(8), 1043 (1997).

Self Organized Mesoscopic Magnetic Structures, A. Sugawara, M.R. Scheinfein, J. Appl. Phys. (in press - 1997).

Room Temperature Dipole Ferromagnetism in Linear, Self-Assembling Mesoscopic Fe Particle Arrays, A. Sugawara, M.R. Scheinfein, Phys. Rev.B. (in press- 1997).

Co on Stepped Cu(100) Surfaces: A Comparison of Experimental Data With Monte Carlo Growth Simulations, S.T. Coyle, M.R. Scheinfein, J.L. Blue, J. Vac. Sci. Technol. (submitted - 1997).

Magnetic Nanostructures Produced By Electron Beam Patterning Of Direct Write Transition Metal Fluoride Resists, D. Streblechenko, M.R. Scheinfein, J. Vac. Sci. Technol. (submitted - 1997).

Defect Induced Lowering Of Activation Energies At Step Bands in Co/Cu(100), S.T. Coyle, M.R. Scheinfein, J.L. Blue, Appl. Phys. Lett. (submitted - 1997).

A Reliable Calibration Method For An Ion Current Controlled Electron Beam Transition Metal Deposition Source, E.T. Bullock, S.T. Coyle, G.G. Hembree, M.R. Scheinfein, Rev. Sci. Instrum. (submitted - 1997).

In addition to these publications that are out or in press, we have submitted many abstracts to AVS and MMM which will result in publications by Jan 98. These abstracts are included and listed below.

Self-Organized Mesoscopic Magnetic Structures, A. Sugawara, M.R. Scheinfein, MMM-98;

Quantitative Micromagnetics Using Electron Holography (INVITED), M.R. Scheinfein, D.G. Streblechenko, MMM-98.

Nanometer Resolution Quantitative Electron Holography (INVITED), M.R. Scheinfein, APS-97.

Co on Stepped Cu(100) Surfaces: A Comparison of Experimental Data With Monte Carlo Growth and Micromagnetics Simulations, S.T. Coyle, J.L. Blue, G.G. Hembree, M.R. Scheinfein, AVS-97.

Room Temperature Dipole Ferromagnetism in Linear-Self-Assembling Mesoscopic Fe Particle Arrays, A. Sugawara, M.R. Scheinfein, AVS-97.

Magnetic Nanostructures Produced by Electron Beam Patterning of Transition Metal Fluorides, D.G. Streblechenko, M.R. Scheinfein, AVS-97.

Our construction of the UHV SEM/STM/REELS system is on schedule. The SEM and STM have been tested and work according to design. The MBE chamber (evaporators, heating stage etc) are complete. We have done the standard Au/Mica experiments to be sure that we know what it going on. We are slated for Co/Au by summers end, and then on to STM of insulators using the electron beam for stabilization. Modification of the specimen stage in MIDAS is complete. We have L-N<sub>2</sub> capability. The new MIDAS stage purchased from Lesker came contaminated with Flobolin (sp?) and when baked contaminated our whole system. We spent a tough almost 5 months cleaning up the mess. This is all repaired and we are back on line.

I hope that this brief input is enough. Take care.

Sincerely,

Mike Scheinfein  
Professor

YEAR 4 ANNUAL (9-MONTH) REPORT  
ONR CONTRACT CONTINUATION OF #N00014-93-0099

Titled

**Correlations Between Micromagnetic, Microstructural and Microchemical  
Properties  
in Ultrathin Epitaxial Magnetic Structures**

and

YEAR 1 (15-MONTH) ANNUAL REPORT  
ONR AASERT CONTRACT #N00014-95-1-0891

Titled

**Magnetic Microstructure Observed With Electron Holography in STEM**

The Office Of Naval Research  
Directed to  
Dr. Richard G. Brandt, Electronics Division

by

M.R. Scheinfein and G.G. Hembree  
Department of Physics and Astronomy  
PSF-470 Box 871504  
Arizona State University  
Tempe, AZ 85287-1504

Submitted : 17 October 1996

## Contents

Title Page .....	1
Contents .....	2
Interface Magnetism and Film Growth : Co/Cu(100) .....	3
UHV SEM-STM .....	6
Electron Holography .....	8
Self-Organization of Magnetic Nanowires : Fe/SiO/NaCl(110) .....	11
Publication Summary : January 1996-October 1996 .....	14
Preprints .....	15

## Interface Magnetism and Film Growth : Co/Cu(100)

A great deal of theoretical and experimental work has been done on the fcc Co/Cu(100) system, and the results have been quite varied. Curie temperature increases with film thickness, and coercivity increases steeply just after the ferromagnetic transition. Anisotropy is in-plane along  $\langle 110 \rangle$ . The onset of ferromagnetism at RT has been found to be between 1 and 2 monolayer (ML) coverage ( $1\text{ML} = 1.53 \times 10^{15} \text{ atoms/cm}^2$ ). Both layer-by-layer and bilayer growth have been reported. A Cu capping layer and perpendicular anisotropy after annealing have been reported, as well as coercivity dependant on capping layer thickness, peaking at about 1 ML. Co grown on vicinal Cu substrates has a uniaxial in-plane anisotropy along  $\langle 110 \rangle$  step directions. Much of the variability of these results has been attributed to inconsistent film preparation conditions and contaminants. It is important, therefore, to understand how morphology and defects affect film growth and magnetic properties. We have studied how Co films grown under seemingly identical conditions on Cu(100) which resulted in very different film morphologies. Our goal is to find correlations between the evolution of film structure during growth and magnetic properties.

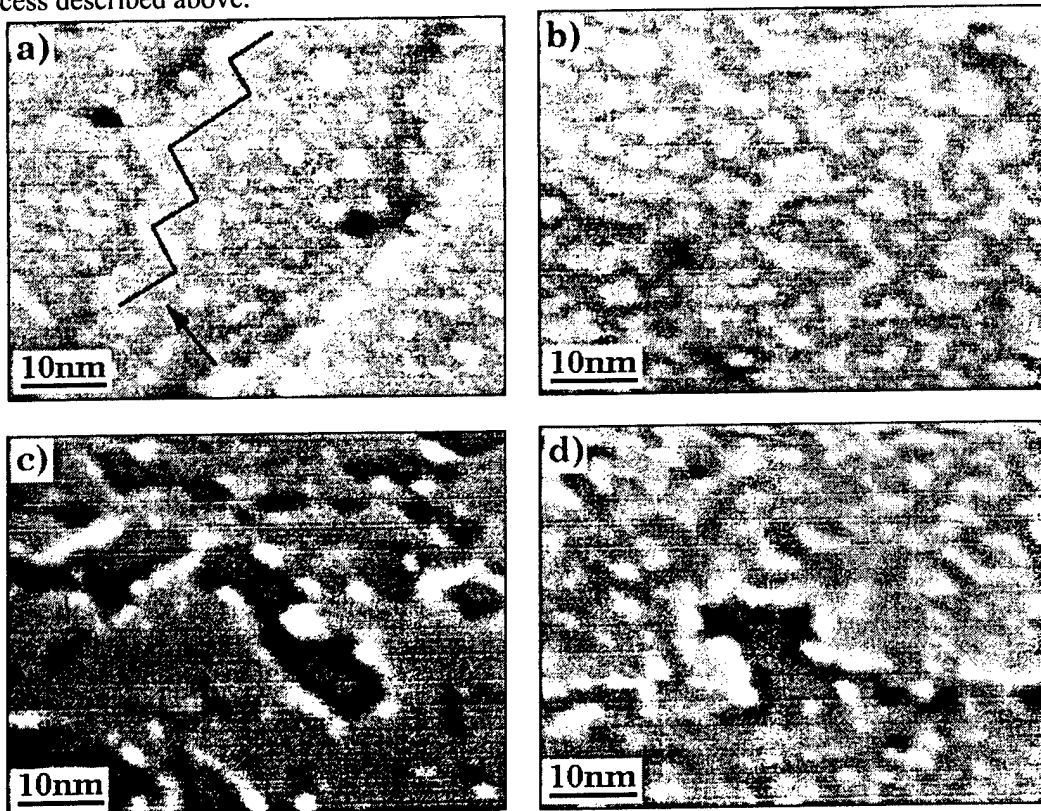
From the beginning stages of film growth, many different structures were observed. Some films grew via island nucleation on terraces with little interaction with steps while other films grew with very little island formation and a high degree of step roughening. In the figure below, representative SE micrographs from three different fcc Co/Cu(100) films, grown at room temperature (RT) at a rate of 0.15 ML/min. These images will be used to illustrate different growth processes on a typical Cu(100) surface as shown in Fig. 1 (prior to Co deposition). The bright lines are bunched step bands which are pinned by copper oxide islands (brightest spot). The dark spot in the top right corner is a vacancy island (inclusion) typical of these substrates. The density of the vacancy islands varied greatly between substrates (from  $<20/\mu\text{m}^2$  to  $10^3/\mu\text{m}^2$ ) and to a lesser degree between different areas of any particular sample. The vacancy islands do not appear to serve as nucleation sites during film growth, however, they may serve as sources for Cu migration onto the surface during later stages of growth since they often persist through several monolayers of growth.

In (a) and (b), sequential growths of 0.2 ML and 0.4 ML of Co are shown. Co islands are clearly visible on the terraces. A monatomic step is visible on the left side of (a), while a three-step step-band is visible on the right side of (a), running diagonally across the image. The two dark spots in (a) are vacancy islands in the substrate. By 0.4 ML coverage, (b), it can be seen that the Co islands are beginning to coalesce. By contrast, (c) shows a micrograph of a 0.3 ML film grown under identical conditions on a different substrate. There is very little island formation and a great deal of roughening of steps. There is also the formation of large meandering vacancy islands on the terraces. We will refer to this mode as step edge mediated growth. The top third of the micrograph shows a bunched step band. The roughened step edges align mostly along crystallographic axes  $\langle 110 \rangle$ . Islands have nucleated preferentially along the up side of step edges. This may be indicative of an Ehrlich-Schwoebel barrier. A 0.3 ML film on another substrate is shown in (d). This film exhibits both island growth and extensive reordering of step edges, i.e., is a combination of the island growth and step edge mediated growth modes.

The formation of rectangular pits from small pinholes in Co/Cu(100) after annealing has been reported by Schmid. They concluded that Cu migrated from these pits to form a capping layer. Similar pinholes were reported by Giesen for room temperature growth of Co/Cu(111). They found that the size of these pinholes increased and the density decreased upon annealing. They also found a dramatic roughening of step edges at the beginning stages of film growth. Terraces on their vicinal surfaces are aligned along  $\langle 110 \rangle$ , and roughening took the form of steps oriented perpendicular to the original step direction. Giesen et al calculated the change in surface

energy for the formation of a pit. Initially the surface energy increases significantly with the size of the pit, then decreases beyond a critical size. Because of this they question why the pits form at all. They then calculated the elastic energy stored in the film due to misfit strain and the change in energy due to strain relief by formation of a pit. For thicker films they find significantly more elastic energy than surface energy stored in the pits. They concluded that the relief of misfit strain is the driving force behind the enlargement of pits upon annealing.

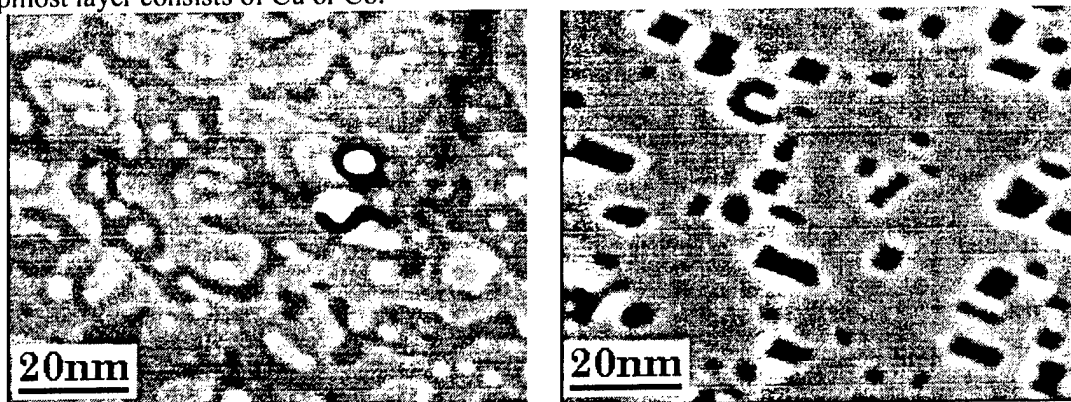
We find similar pits in our films without annealing, and they appear to form differently. Early stages of such pits can be seen in (c) and (d). After continued Co growth these pits will appear similar to those described separately by Schmid and Giesen. We believe that surface energy may be a significant component in pit formation along steps, at least in the early stages of growth. The pits along step bands in our experiments seem to form from the reorientation of randomly oriented steps along mainly  $\langle 110 \rangle$  directions rather than the spontaneous formation of rectangular pits. Step bands often follow curves between pinning sites, thus the step edges have a high density of kinks. When a Co adatom adheres to a step edge it is probably free to move along the step until it encounters another Co atom or adheres to a kink site. Once one or more Co atoms are trapped, the surface energy may be lowered if Cu atoms move to surround the Co atom. This produces a reordering of the step in the region surrounding the Co atoms. The new step faces will prefer to be  $\langle 110 \rangle$ , since this has the lowest surface energy (see below). If such sites are arranged randomly along a step one can imagine a step forming a jagged edge such as that indicated by the arrow and the jagged dark line inserted in (a). Pits on terraces where island growth occurs appear to form due to incomplete Co coverage, and their growth likely proceeds as described by Giesen. Pits on terraces where step edge mediated growth occurs seem to form due to the exchange process described above.



SE micrographs of Co/Cu(100) films grown at RT at  $\sim 0.15$  ML/min for the following coverages: (a) 0.1 ML, (b) 0.4 ML, (c) 0.3 ML, (d) 0.3 ML. The arrow and black line in (a) highlight a roughened step edge.

For higher coverages the island growth mode proceeds as simultaneous multilayer growth. By about 0.8 ML coverage, a second layer typically covers about 10% of the first layer. The first layer is almost completely filled in by about 2 ML coverage, except for the pits described earlier, which vary in size and density between different films. Three layers are easily distinguished for subsequent coverages, with the top layer oscillating between about 1% and about 50% coverage. An example is shown below in (a). In this 11.6 ML film, three layers are clearly seen. The top layer covers about 10% of the surface, the next layer about 50%, and the lower layer about 40%. The dark bands are believed to be misfit dislocations along  $\langle 110 \rangle$ .

When the step edge mediated growth mode is dominant, higher coverages of films grow somewhat differently. The etching features in the steps begin to form rectangular shapes, then eventually become separate rectangular pits. As growth continues, these pits slowly fill in. An example of such a film is shown below in (b), which is the film shown above in 2(c) after another 2 ML of Co has been deposited (2.3 ML total). Most of the pits in this film were probably formed at steps, some of which were in step bands and some of which were single height steps in the middle of terraces. The recorded intensity contrast in this micrograph can be separated into three levels: the brightest (top most) which occupies  $\sim 50\%$  of the surface area, the middle which occupies  $\sim 40\%$  of the surface area, and the pits which occupy  $\sim 10\%$ . Since the pits (bare substrate) occupy 10% of the surface area, two layers of coverage would require 1.8 ML of growth. Another 0.5 ML of growth would then cover  $\sim 50\%$  of the surface. This is consistent with 2.3 ML total coverage. We have analyzed many such micrographs with similar results, indicating that growth occurs by incomplete single layers rather than bilayers. The average pit size for this micrograph is  $9.8 \pm 6.9 \text{ nm}^2$ , and the pit density is  $7 \times 10^3 / \mu\text{m}^2$ . We cannot determine whether the topmost layer consists of Cu or Co.



(a) An 11.6 ML Co/Cu(100) film illustrating the island growth mode. (b) A 2.30 ML Co/Cu(100) film illustrating the step-edge mediated growth mode.

Co/Cu(100) films grown in this study became ferromagnetic at RT at about 1.7 ML, regardless of the growth mode. For films exhibiting nearly pure island growth, this corresponded to complete coverage of the first layer. Zero field susceptibility in the paramagnetic regime and remanence in the ferromagnetic regime generally increase with coverage. In many of our films we detected a second magnetic phase with out-of-plane remanence and a coercivity 5-10 times larger than the in-plane value. There appears to be a correlation between out-of-plane remanence and terrace width. We did not detect out-of-plane remanence in any films with  $>100 \text{ nm}$  terrace width, and out-of-plane remanence appeared to be more likely to occur for very narrow terraces ( $<50 \text{ nm}$ ).

We consider four possible causes for the out-of-plane remanence. One possibility is that  $\langle 111 \rangle$  surfaces are created by  $\langle 110 \rangle$  steps bunched completely together. This could happen in the walls of the pits, or along step bands.  $\langle 111 \rangle$  surface atoms have bi-axial in-plane anisotropy

oriented along  $\langle 110 \rangle$  directions, thus their easy axis could be aligned at  $45^\circ$  from the sample normal. For the sample in Fig. 4(b),  $\sim 5\%$  of the area could be composed of such surfaces. A second possible cause is due to the growth process described earlier. If a large number of Co atoms are surrounded by Cu atoms at steps, then an alloy could be formed. Evidence for perpendicular remanence has been reported for Co-Cu alloys, however, the authors did not report a larger polar coercivity. The third possibility is that of a Cu capping layer, which also has been shown to produce perpendicular remanence. Different coercivities could be the result of changes in Cu overlayer thickness. Other groups report Cu overlayers forming upon annealing, concurrent with the formation and growth of pits, through which they believe the Cu is migrating. Since pits form in our surfaces during growth at RT, it is possible that Cu is also migrating to the surface through these pits.

The fourth possibility is due to the uniaxial anisotropy of atoms along the bottom of a  $\langle 110 \rangle$  step (denoted "step corner" by Chuang et al). The easy axis is canted  $45^\circ$  from the sample normal and aligned along the step direction. The magnetization of these atoms may couple to neighboring atoms, creating an out-of-plane component in the affected atoms. We have performed 1-D micromagnetic calculations which indicate that this may be a significant effect for regions magnetized parallel to the step direction. Continued work in this area is in progress and will be published at a later date.

Work is ongoing on both the Co/Cu(100) and Co/CaF<sub>2</sub>(111) projects with more experiments and publications in progress.

## UHV SEM-STM

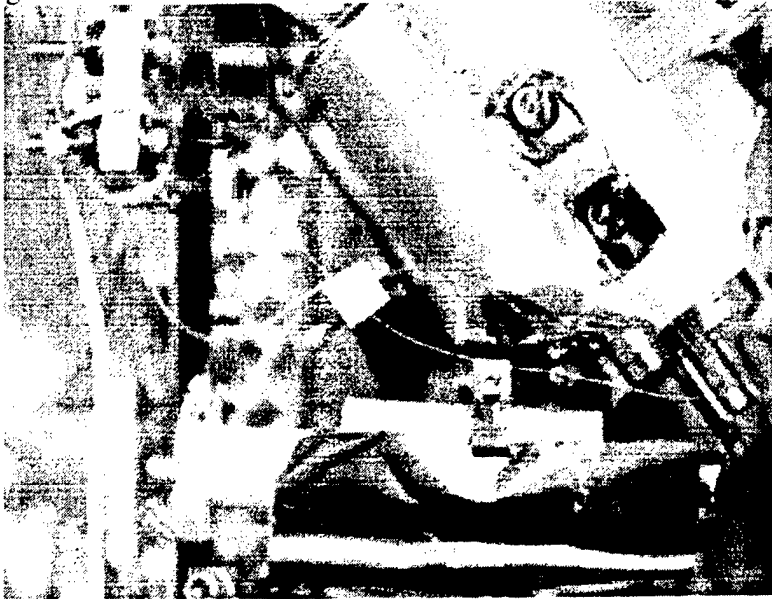
The primary goal is to design, build and ultimately utilize a system which will allow the operation of both a scanning tunneling microscope (STM) and a scanning electron microscope (SEM) for the purpose of thin film characterization. The constraints are; (1) The system must be UHV; (2) The STM and SEM must be able to run concurrently; (3) Sample preparation must be performed *in situ* and should include, annealing (up to  $700^\circ\text{C}$ ), sputtering, and deposition; (4) multiple samples must be stored in UHV without the necessity of venting the chamber. The system is subdivided into three separate chambers connected by UHV gate valves. The roles of the three chambers are as follows; analysis, preparation, storage/exchange.

The analysis chamber contains the STM, SEM, and all electron detection devices and is pumped by a 120 l/s ion pump. The current electron detection devices consist of a four quadrant channel plate analyzer and a Everhart-Thornley detector. Eventually a spin polarized detector will be added. The STM, SEM and sample stage have been positioned on a steel plate which can be suspended by springs during analysis for vibration isolation. The plate can be locked into a rigid position during sample exchange. The STM approaches the sample perpendicularly by necessity whereas the SEM projects the electron beam at an angle of  $\sim 37.5^\circ$  with respect to the sample plane (shown below). This allows for the simultaneous operation of the SEM and the STM.

The preparation chamber is positioned linearly between the analysis chamber and the storage chamber. The chamber consists of a 6" six way cross and is pumped by a 60 l/s ion pump. The prep chamber can be isolated from the analysis chamber via a 6" gate valve giving the ability to perform analysis and preparation concurrently. Two of the prep chamber flanges are used to connect to the other chambers and one is used for the ion pump. This leaves three flanges each of which can support three devices. Of these, one will support an ion gauge, one will be used as a view port and one will be used for electrical connections. This leaves access for six preparation sources.



The storage/exchange chamber is designed to store up to six samples. A 36" rotatable feed through is used to retrieve the samples and introduce them into the prep chamber and ultimately the analysis chamber. The storage chamber can be isolated from the other two chambers via a gate



A top view of the UHV SEM (top within magnetic shielding) and the STM (front). The amplifiers are in-situ and the SEM/STM/Stage assembly floats on an internal spring system with electromagnetic dampers.

valve. This allows samples to be removed from and introduced to the system without the necessity of breaking vacuum in the preparation and analysis chambers. In addition, the storage chamber is of modest dimensions allowing it to be brought down to near UHV conditions within a few hours using a turbo/rough pump combination. Thus, the turn over time for sample exchange will be quite fast.

The samples will be placed in cartridges which have been designed to accommodate the geometry of the three chambers. Each cartridge contains a small button heater allowing the samples to be heated at any point in the system provided the proper electrical connections are made available. The button heaters have an ultimate temperature of  $\sim 1200^{\circ}\text{C}$ . Presently, it is possible to heat the samples in the preparation chamber. The cartridges have been constructed entirely of tantalum, molybdenum and alumina so as to withstand large variations in temperature without degradation.

Initial testing of the apparatus has been completed. SEM images have been acquired from GaAs and Pt on Si surfaces with 1 - 2 keV beams without an operating stigmator. The STM and the STM controller have been found to be in proper working order. Repeatable images have been taken from both substrates. Atomic resolution imaging, which has not yet been attempted in STM, must wait for the preparation of clean surfaces. The SEM astigmatic focus requires an 8-pole octopole stigmator which was recently installed. While the STM has been used to image semiconductor surfaces, the SEM has monitored the region of the surface probed with STM.

Final testing will occur in November once the specimen preparation facilities have been completed and bonafide clean surfaces can be prepared. Implementation of the SEMPA detector shall occur in year 2 of the continuation period.

## Electron Holography

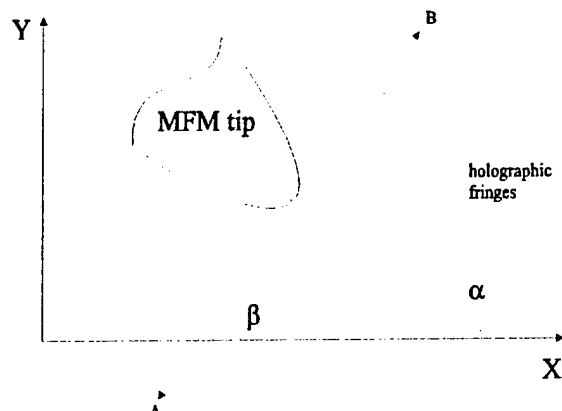
The attractiveness of electron holographic methods stems from the absolute measurement of phase shifts of the electron beam. The combination of high spatial resolution inherent in scanning electron microscopes and these absolute phase measurements extracted from electron holograms allows magnetometry to be performed on nanometer sized regions with high precision. Here, the far-out-of-focus implementation of electron holography in a scanning transmission electron microscope (STEM) is applied to the analysis of the fields emanating from sputter-deposited magnetic force microscope (MFM) tips. The challenge is an analysis of three-dimensional fields emanating from MFM tips. Since all transmission-based analysis techniques integrate along the direction of the beam path, any variations of the fields along this direction are averaged. Instead of using a rigorous three-dimensional tomographic method, the expected symmetries in the tip magnetization and resulting field profiles are exploited. In this case, the only assumption used is that fields emanating from the tips can be expanded in a multipole expansion. The expansion coefficients for the multipole moments are extracted from fits to the phase images of the reconstructed electron holograms.

Since MFM tips may strongly interact with soft ferromagnetic materials and perturb the magnetization distribution of the sample, it is important to characterize the field emanating from such structures. The MFM tip magnetic field is three dimensional. The holographic image is two dimensional since the phase has been integrated along the beam path. There is an inherent ambiguity in recovering the true three-dimensional magnetic field unless some *a priori* knowledge is used. One way of removing this ambiguity is to assume that the magnetic field from the tip is cylindrically symmetric, and therefore reduce the number of dimensions of the magnetic field to two, and represent expressions for the phase shift in the detector plane using this assumption. This approach would require application of the Fourier-Bessel transform on a non-rectangular region. Moreover, due to the limited beam current that can be focused into a nanometer diameter probe in STEM, counting statistics may limit the statistical validity of the recovered magnetic field. Rather than employing the Fourier-Bessel transform, we chose to approximate the magnetic field with a multipole expansion. Since there are no currents present, the field from the MFM tips can be derived from the negative gradient of a magnetic scalar potential whose sources are the (effective) magnetic charges which result from the divergence of the magnetization in bulk, and the discontinuity of the normal component of the magnetization at the surface. The multipole expansion for the magnetic scalar potential  $\Psi(x,y,z)$  includes monopole, dipole and quadrupole (tensor) terms, expanded about the center of the tip, but without any *a priori* assumption about the size and orientation of the tip dipole (quadrupole) moment.

$$\Psi(x, y, z) = \frac{q}{r} + \frac{1}{r^3} \sum_{k=1}^3 p_k r_k + \frac{1}{2r^5} \sum_{k=1}^3 \sum_{l=1}^3 Q_{kl} r_k r_l$$

Here,  $r = (x^2 + y^2 + z^2)^{1/2}$  is the distance to the origin,  $r_i$  are cartesian components of  $\mathbf{r}$  ( $r_1=x$ ,  $r_2=y$  and  $r_3=z$ ),  $q$  is the monopole charge,  $p_k$  are cartesian components of the dipole moment and  $Q_{kl}$  is a symmetric traceless quadrupole tensor. The magnetic field can be expressed as  $\vec{B} = -\vec{\nabla}\Psi$ . We want to express the phase shift given by (2) using the multipole expansion in (3). Consider the experimental geometry of the tip and the resulting electron interference fringes shown below. Here,  $\beta$  is the angle between the projection of the line connecting the electron sources (and perpendicular to the interference fringes) and the X-axis and  $\alpha$  is the angle between the MFM tip-axis and X-axis. The coordinate system of the phase image can be translated to the MFM tip center. The phase shift, becomes:

$$\Delta\phi(x, y) = \cos(\beta) \frac{e}{h} \int_{-x}^x \int_{-y}^y B_y dx dz - \sin(\beta) \frac{e}{h} \int_{-x}^x \int_{-y}^y B_x dy dz.$$



Experimental configuration of the MFM tip and interference fringes. Line A-B connects the electron sources.

After integration, the expression for  $\Delta\phi$  is

$$\Delta\phi(x,y) = -\frac{e}{h}[q \cdot F_1 + P_x \cdot F_2 + P_y \cdot F_3 + (Q_{xy} - Q_{yx}) \cdot F_4 + Q_{xx} \cdot F_5].$$

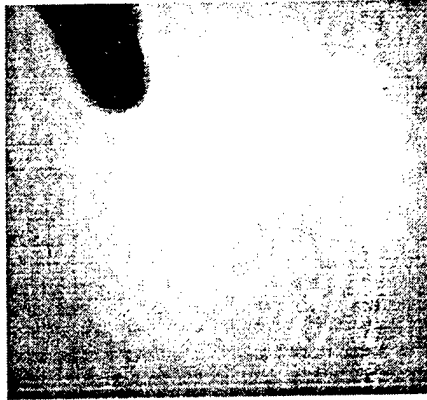
where the constant are multipole field coefficients and the functions are analytic integrals over the magnetic flux contained within the area defined by the probes.

The reconstruction process for electron holograms includes several steps. These are: Fourier transformation of the electron hologram; isolation and centering of a single sideband; defocus correction to remove Fresnel fringes around objects of interest; inverse Fourier transformation; extraction of the phase image from the resulting complex electron wavefunction; and phase unwrapping to remove unwanted periodicities of  $2\pi$  that result from principle values of the trigonometric functions. These two-dimensional phase images are the starting point for recovering the magnetic fields emanating from the MFM tips. The image resolution is limited to twice the fringe spacing referred to the specimen plane. We use the expression above to fit the experimental reconstructed phase image for the multipole-field coefficients  $q$ ,  $P_x$ ,  $P_y$ ,  $Q_{xy}$  and  $Q_{yx}$  using a linear least-squares method. The absolute-phase resolution is limited to about  $\pi/30$ . In the figure below, an electron hologram has been reconstructed from a sputter-coated MFM canilever tip. The nominal radius of the tip is 30 nm. The tip was initially magnetized along the axis. The full scale width of the images is 760 nm x 700 nm. Shown are an experimental amplitude image (a), an experimental phase image (b), an experimental phase image with the multipole expansion fit overlayed in the region in proximity to the tip (c), and a magnitude of the magnetic field in proximity to the tip (d). The phase images have been amplified (x4) such that phase contours span  $\pi/2$ .

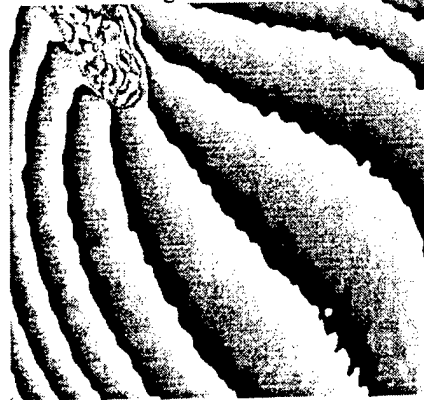
The phase fits of the multipole expansion fields were produced from fits to the multipole expansions, and the clear agreement of the fit is evident in the overlays superimposed over the phase data. The reconstructed magnetic fields use only the monopole and dipole terms since the contribution from quadrupole terms were negligible on the distances comparable to the MFM tip radius. The field for the MFM tip shown in the figure falls from about 620 Oe at (near) the tip surface to 310 Oe 10 nm in front of the tip along the tip axis. The linear terms in the background that are left after a proper centering of the sideband (in Fourier space) result from flux originating from the magnetic material sputtered onto the large conical base supporting the tip. In our implementation, where the sources are separated by about 2 microns at the sample, the upper limit on the residual stray field from the tip base is estimated to be approximately 10 Oe.

The magnetic dipole moment in the plane of the holographic phase image is oriented at  $\theta = 135^\circ$ . The tips axis is along  $\theta = 120^\circ$ . Thus, the dipole is oriented nearly along the tip ( $15^\circ$  off

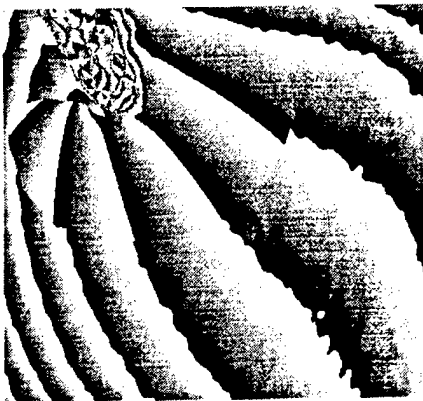
760 nm x 700 nm full scale on all images.



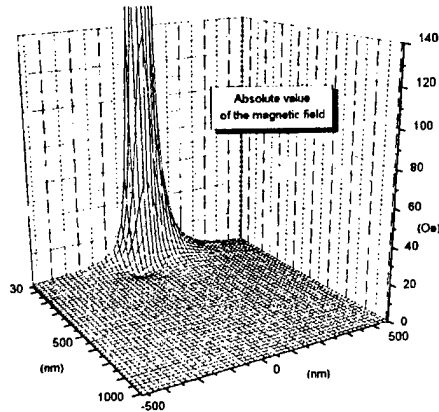
(a) Reconstructed amplitude -



(b). Amplified (x4) reconstructed phase.



(c) Phase with the fit superimposed.



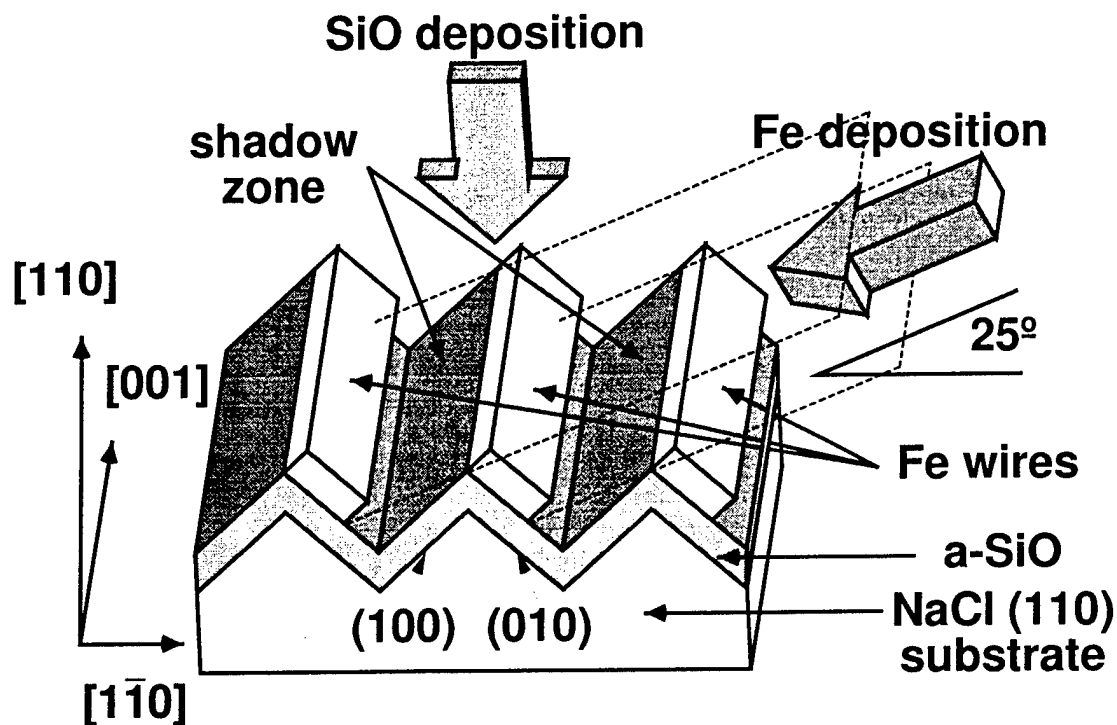
(d) Reconstructed magnetic field .

axis. This is consistent with the fact that during the magnetization process the tip axis is oriented about  $12^\circ$  away from the magnetic field axis. During magnetization, the physical tip axis is no longer aligned with the magnetic-field axis. Therefore, the measured dipole moment axis is actually quite close to that axis defined during the magnetization process.

## Self-Organization of Magnetic Nanowires : Fe/SiO/NaCl(110)

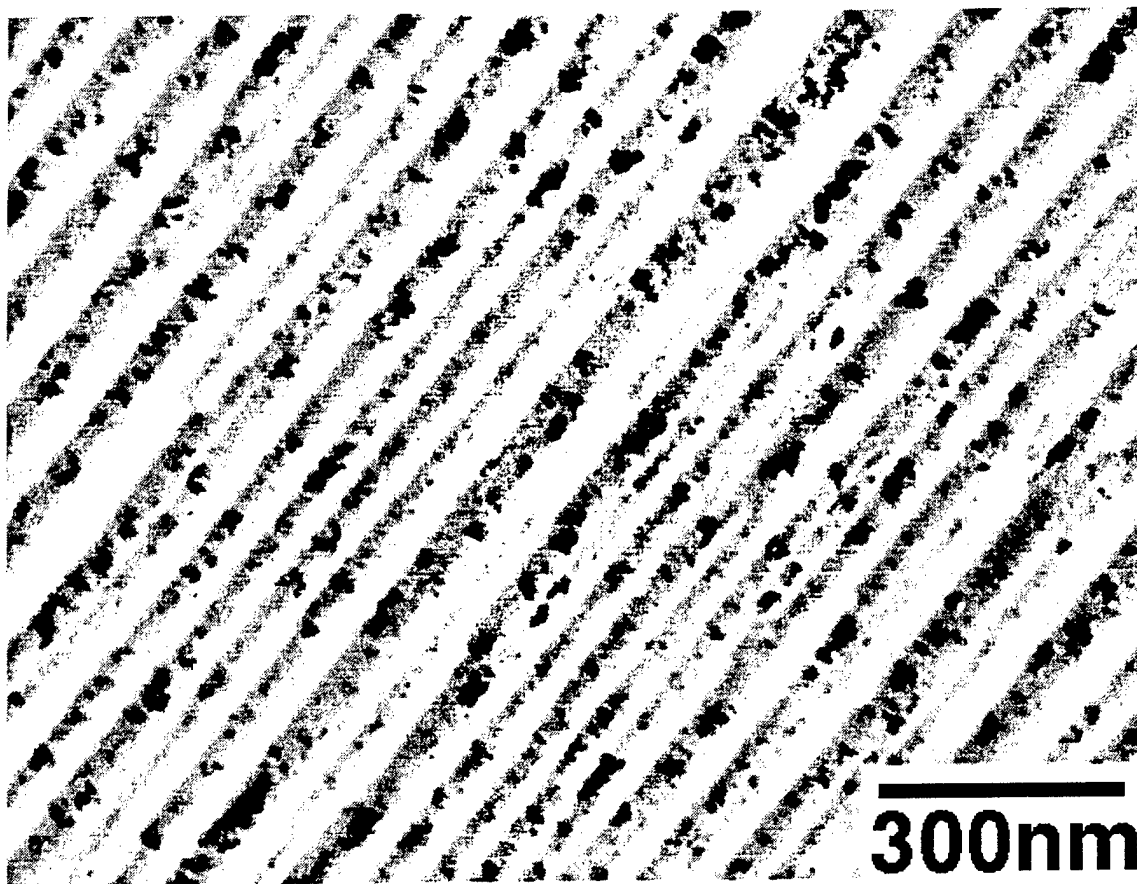
It has been of interest to control the shape, size and spatial arrangement of small magnetic particles from a viewpoint of high-density magnetic recording. Some interesting magnetic properties have been reported for dot and wire arrays fabricated by electron-beam lithography. However, the throughput of the method is so slow that it is quite difficult to obtain uniform microstructure over the large areas (cm) required for magnetic storage media. From this point of view, self-organization phenomena which has been applied to the nano-fabrication of semiconductors, may provide a mechanism for the fabrication of magnetic microstructures. A self-aligned 2-D array of dots, a few monolayers thick, has been grown through the preferential nucleation of magnetic particles on the surface at defects such as step edges and kinks. However, this kind of microstructure disappears with increasing film thickness due to coalescence. Further, signal outputs (SMOKE or some equivalent magnetization detection system) are limited by the small total magnetic volume isolated at the surface defects. We are interested in a thicker regime (1~10 nm) where we can obtain a higher output signal.

We have grown Fe nanowire arrays by shadow deposition on a graded template. Self-patterning of non-cleavage planes of ionic crystals that have highly anisotropic surface energy is important in this study. For example, when the NaCl (110) surface is heated in vacuum, the surface becomes faceted with (100) and (010) planes thereby minimizing the total surface energy. In this case, periodic macrosteps appear parallel to [001]. The macrostep periodicity can be varied from 5 to 100 nm, depending on the annealing temperature and annealing time. When Fe is deposited on such a graded template at a grazing angle (nominally about 65 degrees from the template normal), nanowires are formed only near the top of the edge, as schematically shown below.



Schematic drawing of shadow growth of nanowire arrays on a graded template formed by the annealing of NaCl(110).

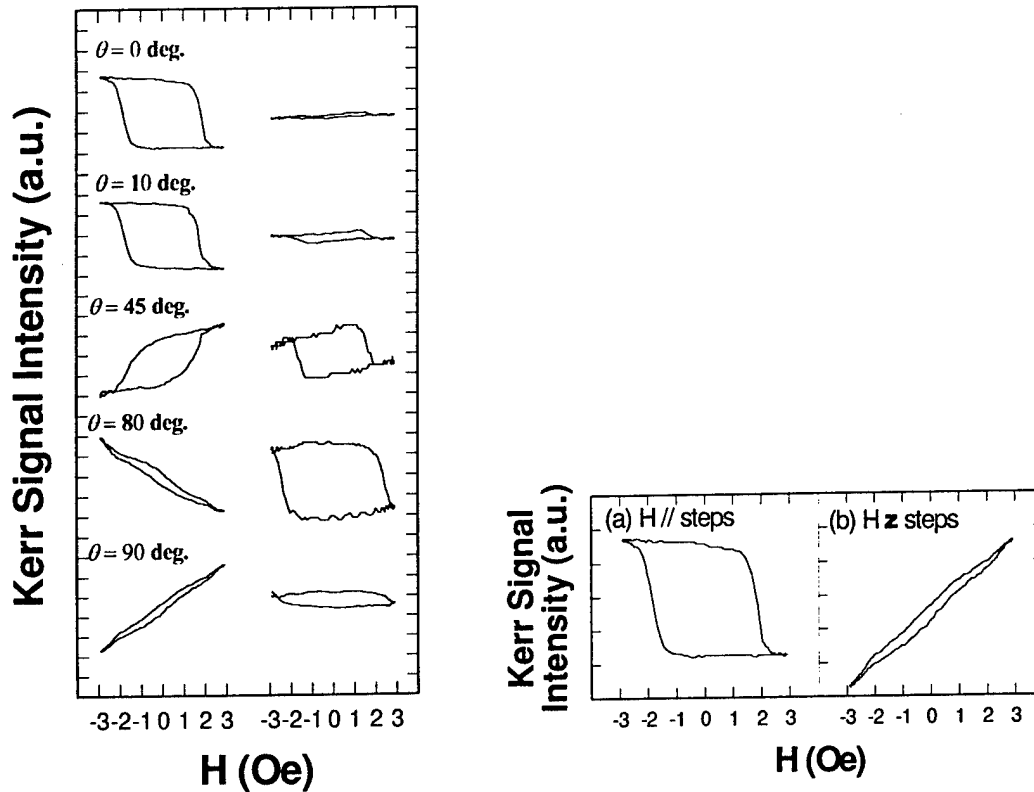
A bright field TEM image of one of the nanowire wire arrays is shown below. The Fe wires, seen in dark contrast, run along the macrosteps of the substrate. The typical width of the wires is about 20nm. Since these wires are thin slabs lying on slope tilted by 45 degrees from the normal, the actual width is around 30nm. The average length of the wires is about 10 $\mu$ m, so an aspect ratio larger than  $3 \times 10^2$  is achieved.



Fe nanowire array fabricated by shadow deposition on a graded template.

The film shown above (characteristic of the many examined in this study) had strong in-plane magnetic anisotropy, as expected from the observed microstructure. When the field is applied along the macrosteps, a longitudinal loop shows easy-axis behavior with high coercivity about 2 kOe (below). This large coercive field suggests that the magnetization process is either not dominated by domain wall motion, or that the domain walls are strongly pinned by defects within the nanowires. When the field is applied perpendicular to the steps, the loops show hard-axis behavior. The magnetization did not saturate for external fields of 3 kOe due to large demagnetization field along the short axis of the wire array. We should note that the real hard-axis is considered to be perpendicular to the thin Fe slabs, i.e., out of the film plane by 45 degrees. However, we could not measure this magnetization component by MOKE, because there was no strong reflection in that direction, indicating that the wires themselves are not planar, but rather cylindrical. This agrees with results of contrast analysis of Fig. 2b. The longitudinal loops measured with the applied field oriented between the easy- and hard-axes gives information on the magnetization rotation process. The two loops shown below are for the magnetization along (left) and perpendicular (right) to the steps for the field angle with the wire direction as specified. The large open-circle loop for perpendicular magnetization when  $\theta=80^\circ$  is characteristic of

coherent rotation. The collapsed loop for  $\theta=90^\circ$  results from the limited applied field strength. Even though we cannot ascertain that the switching proceeds through coherent rotation, it is clear that the whole wire array switches simultaneously. This result is interesting in that the magnetization switching process seems to be present across the film array even though individual lines are not coupled. Either each wire has nearly the same coercivity, and hence each wire individually switches coherently in unison with all others, or all the wires are magnetostatically linked, and hence switch as a single film. The presence of domain walls across the wire array is possible, the mechanism being magnetostatic, and of similar in strength to that required to coherently couple the wire array during switching.



Hysteresis loops measured by MOKE rotating the specimen in the film plane.  $\theta$  denotes angle between the macrostep direction and the scattering plane with the field applied in-plane.

Ongoing studies include controlling the periodicity and aspect ratio of the wires, and examining ordering in 2-dimensional arrays.

## Publication Summary : January 1996-October 1996

Magnetic Order in Tow-Dimensional Arrays of Nanometer-Sized Superparamagnets, M.R. Scheinfein, K.E. Schmidt, K.R. Heim, G.G. Hembree, Phys. Rev. Lett. **76**(9), 1541 (1996).

Long Range Order in 2-D Arrays of Nanometer-sized Islands on  $\text{CaF}_2/\text{Si}(111)$ , M.R. Scheinfein, K.E. Schmidt, K.R. Heim, G.G. Hembree, J. Appl. Phys. **79**(8), 5056 (1996).

Quantitative Micromagnetics At High Spatial Resolution Using Far-out-of-Focus STEM Electron Holography, M. Mankos, J.M. Cowley, M.R. Scheinfein, phys. stat. sol. (a) **154**, 469 (1996).

A Comment of "Flux Quantization in Magnetic Nanowires Imaged by Electron Holography", M.R. Scheinfein, D. Streblechenko, M. Mankos, Phys. Rev. Lett. **77**(5), 976 (1996).

Growth of Nanometer-size Metallic Particles on  $\text{CaF}_2(111)$ , K.R. Heim, S.T. Coyle, G.G. Hembree, J.A. Venables, J. Appl. Phys. **80**(2), 1161 (1996).

An Alternative Approach For Magneto-Optic Calculations Involving Layered Media, K.R. Heim, M.R. Scheinfein, J. Mag. Mag. Mat. **154**, 141 (1996).

Quantitative Micromagnetics: Electron Holography of Magnetic Thin Films and Multilayers, IEEE Trans. MAG-**32**(5), 4150 (1996).

Quantitative Magnetometry Using Electron Holography: Field Profiles Near Magnetic Force Microscope Tips, D.G. Streblechenko, M. Mankos, M.R. Scheinfein, IEEE Trans. MAG-**32**(5), 4124 (1996).

Electron Holography and the Scanning Transmission Microscope, M. Mankos, M.R. Scheinfein, J.M. Cowley, Proceedings of the Pfefferkorn Conference, Scanning Microscopy International (in press - 1996).

Growth, Morphology and Magnetic Properties of Ultrathin Epitaxial Co Films on  $\text{Cu}(100)$ , S.T. Coyle, G.G. Hembree, M.R. Scheinfein, J. Vac. Sci. Technol. (in press-1996).

Self-Organized Fe Nanowire Arrays Prepared by Shadow Deposition on  $\text{NaCl}(110)$  Templates, A. Sugawara, S.T. Coyle, G.G. Hembree, M.R. Scheinfein, Appl. Phys. Lett. (submitted-1996).



YEAR 3 ANNUAL REPORT AND 3-YEAR CUMMULATIVE REPORT

PRIOR TO THE CONTINUATION OF

ONR CONTRACT #N00014-93-0099

Titled

**Correlations Between Micromagnetic, Microstructural and Microchemical Properties  
in Ultrathin Epitaxial Magnetic Structures**

The Office Of Naval Research

Directed to

Dr. Richard G. Brandt, Electronics Division

by

M.R. Scheinfein and G.G. Hembree

Department of Physics and Astronomy

PSF-470 Box 871504

Arizona State University

Tempe, AZ 85287-1504

Submitted : 18 December 1995

Contents:

	Contents	2
0.0	Continuation Proposal Summary	3
1.0	Summary of Results From the First Grant Period	4
1.1	Magnetic Anisotropy, Thin-Film Growth and Metastable States in Epitaxial Fe/Cu(100)	4
1.2	Giant Magnetoresistance in Imperfect Superlattices: 90° Coupling in Co/Cu Multilayers	5
1.3	Selective Nucleation and Growth on Nanopatterned CaF <sub>2</sub> /Si(111) Substrates	8
1.4	Ordering Transitions and Coupling in Two-Dimensional Arrays of Fe Islands	11
1.5	Electron Holography of Thin Films, Superlattices and Small Particles	15
1.6	Magnetometry of Superlattices Using Surface Magneto-Optic Kerr Effect	16
1.7	Publication Summary From Prior Grant Period	17
1.8	Degrees Granted During the Prior Grant Period	19
2.0	Continuing Research Program	20
2.1	Effects on Anisotropy of Rough Interfaces Due to Site Exchange In Metal-Metal Epitaxy	20
2.2	Epitaxy on Electron Beam Sensitive Inorganic Halide Resists on Si Substrates	22
2.3	Self-Organization: Anisotropy at Step Edges and Two-Dimensional Magnetoresistance	24
2.4	UHV STM-SEM with Reflection Electron Energy Loss Spectroscopy	25
3.0	Publications/Reprints/Preprints	27

YEAR 3 ANNUAL REPORT AND 3-YEAR CUMMULATIVE REPORT  
PRIOR TO THE CONTINUATION OF  
ONR CONTRACT #N00014-93-0099

Correlations Between Micromagnetic, Microstructural and Microchemical Properties  
in Ultrathin Epitaxial Magnetic Structures

M.R. Scheinfein and G.G. Hembree  
Department of Physics and Astronomy  
PSF-470 Box 871504  
Arizona State University  
Tempe, AZ 85287-1504

0.0 Continuation Proposal Summary

Quantitative measurements of the microstructural, microchemical and micromagnetic properties of surfaces and interfaces of ultrathin films composed of magnetic materials deposited on non-magnetic, and insulating substrates will be continued. Our surface microanalytic methods are based on a unique ultrahigh-vacuum scanning transmission electron microscope/scanning electron microscope (UHV-STEM/SEM) equipped with in-situ thin film preparation and characterization tools. This instrument was successfully used during the previous funding period for: the study of anisotropy in Fe/Cu(100); characterization of magnetic, nucleation and growth properties of Fe/CaF<sub>2</sub>/Si(111); and characterization of Co/Cu superlattices with imperfect interfaces. The new funding period will see the commissioning of a new combined scanning tunneling microscope/scanning electron microscope (STM-SEM) with reflection electron energy loss spectroscopy. This instrument will be used to access atomic level physical structure. As in the prior grant period, magnetic characterization will be made in-situ using the surface magneto-optical Kerr effect (SMOKE). In the second year of this grant period, an electron-spin polarimeter will be interfaced to the UHV STM-SEM for analysis of surface magnetic microstructure using polarized electrons. Additional ex-situ measurements of interface properties will continue to be made with high resolution transmission electron microscopy (HREM) and low angle x-ray scattering. Ex-situ calibrated static magnetization measurements will be made with SQUID magnetometry and far out of focus STEM electron holography. Magnetoconductance measurements of heterogeneous two-dimensional giant magnetoresistance samples will be conducted ex situ. Dynamic magnetic properties will be investigated with SQUID magnetometry.

Systems for study include Ag/Fe, Ag/Co, Co/Cu, Fe/CaF<sub>2</sub>, Co/CaF<sub>2</sub>, Co/CaF<sub>2</sub>/Si(111), and Fe/CaF<sub>2</sub>/Si(111). Alternative insulating substrates including MgO, NaCl and other inorganic halides will also be considered. Our measurements will clarify the relationship between the observed real-space microstructure of interfaces, ultrathin magnetic films and superlattices with magnetic properties, such as surface anisotropy, ferromagnetic/antiferromagnetic coupling between ferromagnetic layers in superlattices, the transition from the superferromagnetic to the ferromagnetic state, and the role of proximity in the coupling of ultrasmall islands spaced by less than a nanometer. The dependence of magnetic properties on film morphology, which may be controlled by varying deposition parameters during the initial stages of growth, and on structural properties such as strain, interface roughness, and the formation of misfit dislocations will be emphasized. Utilization of electron beam modification of CaF<sub>2</sub> (substrate) and other inorganic halide electron-beam resists, and selective nucleation and growth will continue to be studied as a means of defining nanometer sized epitaxial magnetic devices.

## 1.0 Summary of Results From the First Grant Period

The first grant period extended from 1 January 1993 to 31 December 1995. By all measures, we accomplished all of the goals set out in the first proposal. A summary of selected highlights of the first grant period is given below.

### 1.1 Magnetic Anisotropy, Thin-Film Growth and Metastable States in Epitaxial Fe/Cu(100)

(Refer to Publications Listed in Section 1.7 : References 1-7)

Ferromagnetic ultrathin epitaxial films grown on single crystal metal substrates display unusual properties characteristic of two-dimensional ferromagnetism stabilized by magnetic (surface) anisotropy<sup>1</sup>. The exchange coupling and crystalline anisotropy depend very sensitively on the lattice. Ultrathin films, grown epitaxially on templates which distort the bulk lattice are often highly strained enabling metastable film properties to be explored at room temperature. The most studied, and perhaps the most complex metal/metal epitaxial system is fcc Fe/Cu(100). The fcc phase of Fe, stable in bulk above 911 °C<sup>2</sup>, can be grown epitaxially on Cu(100) with 0.83% lattice mismatch. For fcc (fcc) Fe, a non-magnetic, high and low spin, or an antiferromagnetic phase can be stable depending upon the lattice constant<sup>3</sup>. The magnetic properties of fcc Fe/Cu(100) have been investigated using the surface magneto-optical Kerr effect (SMOKE)<sup>4,5</sup>, spin-polarized photoemission<sup>6</sup>, spin-polarized secondary electron spectroscopy<sup>7,8</sup>, conversion-Mössbauer spectroscopy<sup>9</sup>, inverse photoemission<sup>10</sup> and spin-polarized scanning electron microscopy (SEMPA)<sup>11</sup>. The energy balance between surface anisotropy and shape anisotropy, both strong functions of film thickness, growth and measurement temperature<sup>4,11-13</sup>, determine the easy axis of magnetization. Interest in this system is stimulated by rich structural properties present during various phases of film growth<sup>12-18</sup>, including bilayer growth during initial phases of epitaxy<sup>15-18</sup>, strain-relief at intermediate thicknesses, weak surface reconstructions<sup>12</sup>, and fcc to bcc transitions<sup>13</sup>. Extensive work has been devoted to correlating film microstructure with magnetic properties<sup>12,13,19</sup> with emphasis on the non-magnetic-to-magnetic transition at 1-2 ML (ML denotes a monolayer, 0.18 nm for fcc Fe(100)) coverages and the polar-to-longitudinal transition in the easy axis of magnetization at 4-8 ML.

In the previous grant period, we identified for the first time, a field induced, reversible, metastable transition for magnetization measured perpendicular to the film plane (polar direction). Room-temperature grown, fcc Fe/Cu(100) films in the 2.5-3.5 ML regime possess both in-plane and perpendicular remanence. After application of a 9.0 kOe polar field, the out-of-plane response was dramatically reduced, and polar remanence was lost. This magnetic state was stable until the film was either heated or subjected to a large in-plane magnetic field. We interpreted these results in terms of magneto-elastic distortions in the strain stabilized fcc Fe lattice induced by large applied magnetic fields. Induced film distortions can lead to anisotropic behavior within, and out-of the film plane. Calculated changes in magnetic (ordering) properties as a result of small lattice distortions were predicted for stable non-magnetic and magnetic phases of fcc Fe<sup>3</sup>.

---

<sup>1</sup>N.D. Mermin, H. Wagner, Phys. Rev. Lett. 17, 1133 (1966).

<sup>2</sup>L.J. Schwartzendrubber, **Binary Phase Diagrams** : vol. 2, ( Publisher, 1990).

<sup>3</sup>O.N. Mryasov, A.I. Liechtenstein, L.M. Sandratskii, V.A. Gubanov, J. Phys.: Condens. Matter 3, 7683 (1991); G.L. Krasko, G.B. Olson, Phys. Rev. B40, 11536 (1989); T. Kraft, M. Methfessel, M. van Schilfgaarde, M. Scheffler, Phys. Rev. B47, 9862 (1993); V.L. Moruzzi, P.M. Marcus, K. Schwarz, P. Mohn, Phys. B34, 1784 (1986).

<sup>4</sup>C. Liu, E.R. Moog, S.D. Bader, Phys. Rev. Lett. 60, 2422 (1988); C. Liu, E.R. Moog, S.D. Bader, J. Appl. Phys. 64, 5325 (1988); C. Liu, S.D. Bader, J. Vac. Sci. Technol. A8, 2727 (1990); S.D. Bader, Proc. IEEE 78, 909 (1990).

<sup>5</sup>W.R. Bennett, W. Schwarzacher, W.F. Egelhoff Jr., Phys. Rev. Lett. 65, 3169 (1990).

<sup>6</sup>D. Pescia, M. Stampanoni, G.L. Bona, A. Vaterlaus, R.F. Willis, F. Meier, Phys. Rev. Lett. 58, 2126 (1987).

<sup>7</sup>D.P. Pappas, K.-P. Kamper, H. Hopster, Phys. Rev. Lett. 64, 3179 (1990).

<sup>8</sup>D.P. Pappas, K.-P. Kamper, B.P. Miller, H. Hopster, D.E. Fowler, A.C. Luntz, C.R. Brundle, Z.-X. Shen, J. Appl. Phys. 69, 5209 (1991).

- <sup>9</sup> W.A.A. Macedo, W. Keune, Phys. Rev. Lett. **61**, 475 (1988).  
<sup>10</sup> F.J. Himpsel, Phys. Rev. Lett. **67**, 2363 (1991).  
<sup>11</sup> R. Allenspach, A. Bishof, Phys. Rev. Lett. **69**, 3385 (1992).  
<sup>12</sup> P. Xhonneux, E. Courtens, Phys. Rev. **B46**, 5561 (1992).  
<sup>13</sup> J. Thomassen, F. May, B. Feldmann, M. Wuttig, H. Ibach, Phys. Rev. Lett. **69**, 3831 (1992).  
<sup>14</sup> W.A. Jesser, J.W. Mathews, Phil. Mag. **15**, 1097 (1967); Phil. Mag. **17**, 461 (1968).  
<sup>15</sup> S.A. Chambers, T.J. Wagener, J.H. Weaver, Phys. Rev. **B36**, 8982 (1987).  
<sup>16</sup> D.A. Steigerwald, W.F. Egelhoff Jr, Surf. Sci. **192**, L887 (1987); D.A. Steigerwald, F. Jacob, W.F. Egelhoff Jr., Surf. Sci. **202**, 472 (1988).  
<sup>17</sup> H. Glatzel, Th. Farster, B.M.U. Scherzer, V. Dose, Surf. Sci. **254**, 58 (1991).  
<sup>18</sup> A. Brodde, H. Neddermeyer, Ultramicro. **42-44**, 556 (1991).  
<sup>19</sup> H. Magnan, D. Chandesris, B. Vilette, D. Heckmann, J. Lecante, Phys. Rev. Lett. **67**, 859 (1991).

## 1.2 Giant Magnetoresistance Effects in Imperfect Superlattices: 90° Coupling in Co/Cu Multilayers

(Refer to Publications Listed in Section 1.7 : References 4,11,12,13,16,17,19,20 and Conference Proceedings 4,6,7,9,10)

The strength and sign of the interlayer coupling coefficient in superlattices composed of ferromagnetic transition metals and non-magnetic spacer layers has been correlated with magneto-transport measurements for a wide class of systems<sup>1</sup>. Experiments have been focused on the bcc Fe/Cr<sup>2</sup> and the fcc Co/Cu systems<sup>3-5</sup> in an effort to confirm quantitative predictions on the orientation dependence of the interlayer coupling<sup>6</sup>. Models based on an RKKY-like treatment which couple spanning vectors normal to the superlattice layers that join extremal points of the bulk Fermi surface have successfully predicted the oscillation periods of interlayer coupling. Magnetotransport models which rely on antiferromagnetic alignment of adjacent ferromagnetic layers have been used to interpret experimental data<sup>7</sup>. Interlayer coupling can be complicated by surface and interface roughness, primarily due to conditions during growth<sup>8,9</sup>. In addition to antiferromagnetic (or 180 degree) interlayer coupling, 90 degree interlayer coupling has been observed in epitaxial systems with wedge-shaped interlayers, including Fe/Cr/Fe(100) and Fe/Au/Fe(100)<sup>10-12</sup>. Theoretical treatments attribute intrinsic 90 degree, or biquadratic coupling (which is to be contrasted to 90 degree domain orientation) between layers to spatial nanoscopic variations in the interlayer coupling arising from thickness variations<sup>13,14</sup>. Intrinsic bilinear (180 degree) coupling in general coexists with the higher order biquadratic (90 degree) coupling<sup>15</sup>. Evidence for 90 degree domains in the coupling in Co/Cu(001) superlattices has been recently observed in the non-symmetric spin states from Kerr hysteresis loops at the second antiferromagnetic maximum<sup>16</sup> due to the competing effects of anisotropy and exchange coupling. Elemental specific magnetic hysteresis loops extracted from magnetic circular dichroism experiments from Fe/Cu/Co trilayers indicates the presence of significant misalignment between the orientation of the magnetization in adjacent ferromagnetic layers<sup>17</sup>. We have demonstrated the strong correlation between giant magnetoresistance and 90 degree domain formation between adjacent layers in electron beam evaporated Co/Cu superlattices as a function of the Cu interlayer spacing when the interfaces are imperfect.

Magnetic measurements were made with the combined three-axis Magneto-Optical Kerr Effect<sup>18</sup> (MOKE) on 6mm diameter circular samples. Longitudinal Kerr effect hysteresis loops were obtained by orienting the superlattice's in-plane easy axis along the applied magnetic field direction in the scattering plane. The longitudinal in-plane magnetization is  $M_x$ . In order to obtain the transverse in-plane component of the magnetization,  $M_y$ , both the sample and the magnetic field were rotated until both the easy-axis and the applied field direction were perpendicular to the scattering plane. In this orientation, when the field was applied along the in-plane easy-axis, the detector records magnetization in the scattering plane,  $M_y$ <sup>19</sup>. Without modifying the position of any optical elements, calibrated  $M_x$  and  $M_y$  components of the magnetization could be recorded during the switching process. The components can be added together in quadrature as a measure of the total magnetization,  $M_s$ . When the normalized total magnetization differed from one, there were regions where the magnetization was misaligned. This misalignment could have been due to domain formation within a given layer(s) of the superlattice, or to

small regions of anti-alignment between adjacent layers. As the light is attenuated during its traversal of the superlattice, the topmost layers will contribute more strongly to the detected Kerr signal<sup>20</sup>. In order to assess effects due to cumulative roughness in layered structures, Kerr effect hysteresis loops were measured from both sides of samples grown on glass substrates. No obvious difference was observed in hysteresis loops measured from the top or the bottom of the superlattice stack. The variation in the absolute value of the Kerr signal as samples are changed and the magnet and sample are rotated is less than 5%.

The correlation between 90 degree coupling and MR in superlattices with rough interfaces is illustrated in Fig. 1.2.1 below. Here, two in-plane components of the magnetization extracted from longitudinal and 'transverse'<sup>21</sup> Kerr hysteresis loops, the total magnetization  $M_s$ , and the magnetoresistance are shown for characteristic superlattices of thickness  $t_{Cu}$ . The longitudinal Kerr hysteresis loops detect the component of the in-plane magnetization along the easy axis,  $M_x$ , while the transverse Kerr hysteresis loops measure the component  $M_y$ , perpendicular to  $M_x$ <sup>19</sup>. For films which show substantial giant magnetoresistance (the peaks of the GMR vs. interlayer thickness curves are shown in Fig. 1.2.2), during the switching process, the magnetization reorients itself along a direction 90 degrees from the easy axis and the field direction. This is clear evidence that there is 90 degree domain formation in the superlattice which appears as 90 degree coupling. The MR can also be fit with the transverse magnetization curve, leaving a small residual (1%).

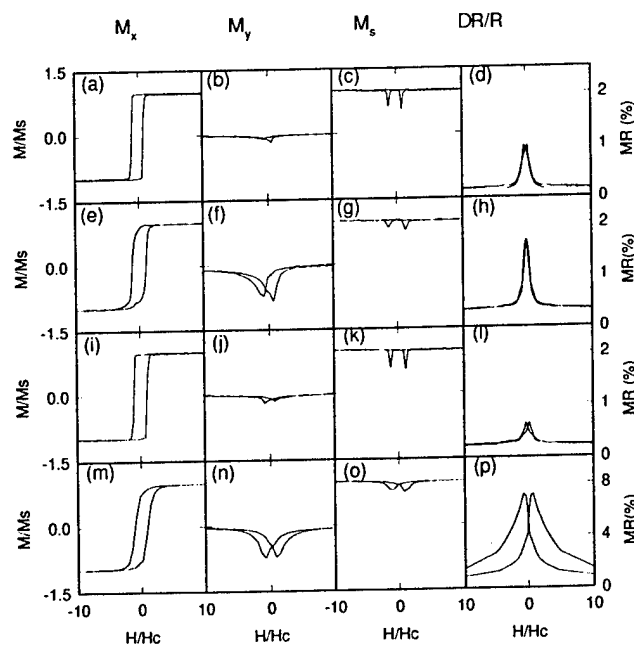


Fig. 1.2.1 : Components of the magnetization along the easy axis,  $M_x$ , and along the hard axis,  $M_y$ , are recorded during the switching process for fields applied along the easy axis. The normalized in-plane magnetization,  $M_s$ , results from adding the two in-plane components together in quadrature. The MR data are shown in the far right hand column. The Cu interlayer thickness is (a)-(d) 0.7 nm, (e)-(h) 0.8 nm, (i)-(l) 1.0 nm, and (m)-(p) 2.0 nm.  $H_e$  is 35 Oe, such that the maximum range on all plots is 350 Oe.

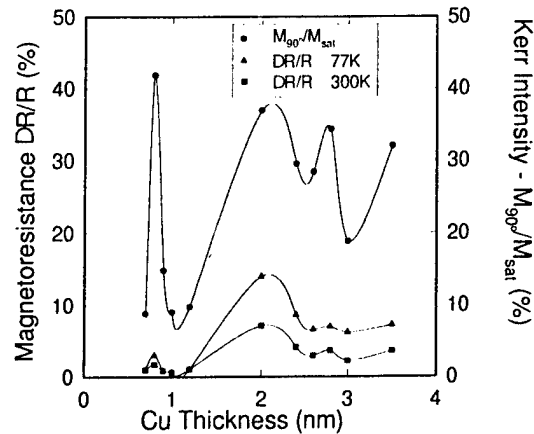


Fig. 1.2.2 : MR at room temperature (squares) and at 77 K (triangles) are plotted as a function of the Cu interlayer thickness. The maximum normalized magnetization (circles) oriented at 90° with respect to the field direction is also shown.

- <sup>1</sup>M.N. Baibich, J.M. Broto, A. Fert, F. Nguyen Van Dau, F. Petroff, P. Etienne, G. Creuzet, A. Friederich, J. Chazelas, *Phys. Rev. Lett.* **61**, 2472 (1988); S.S.P. Parkin, N. More, K.P. Roche, *Phys. Rev. Lett.* **64**, 2304 (1990); P. Grunberg, J. Barnas, F. Saurenbach, J.A. Fub, A. Wolf, M. Vohl, *J. Mag. Mag. Mat.* **93**, 58 (1991); S.S.P. Parkin, *Phys. Rev. Lett.* **67**, 3598 (1991).
- <sup>2</sup>E.E. Fullerton, M.J. Conover, J.E. Mattson, C.H. Sowers, S.D. Bader, *Phys. Rev.* **B48**, 15755 (1993); E.E. Fullerton, M.J. Conover, J.E. Mattson, C.H. Sowers, S.D. Bader, *J. Appl. Phys.* **75**, 6461 (1994); C.D. Potter, R. Schad, P. Belien, G. Verbanck, V.V. Moshchalkov, Y. Bruynseraede, M. Schafer, R. Schafer, P. Grunberg, *Phys. Rev.* **B49**, 16055 (1994).
- <sup>3</sup>S.S.P. Parkin, R. Bhadra, K.P. Roche, *Phys. Rev. Lett.* **66**, 2152 (1991).
- <sup>4</sup>A. Fert, A. Barthelemy, P. Etienne, S. Lequien, R. Loloe, D.K. Lottis, D.H. Mosca, F. Petroff, W.P. Pratt, P.A. Schroeder, *J. Mag. Mag. Mat.* **104-107**, 1712 (1992); D.H. Mosca, F. Petroff, A. Fert, P.A. Schroeder, W.P. Pratt Jr. R. Laloe, *J. Mag. Mag. Mat.* **94**, L1 (1991); Y. Chen, J.M. Florczak, E.D. Dahlberg, *J. Mag. Mag. Mat.* **104-107**, 1907 (1992).
- <sup>5</sup>M.T. Johnson, P.J.H. Bloemen, R. Coehoorn, J.J. deVries, N.W.E. McGee, R. Jungblut, A. Reinders, J. aan de Stegge, *Mat. Res. Soc. Symp. Proc. Vol.* **313**, 212 (1993); P.H.J. Bloemen, R. van Dalen, W.J.M. Jonge, M.T. Johnson, J. aan Stegge, *J. Appl. Phys.* **73**, 5972 (1993).
- <sup>6</sup>P.M. Levy, K. Ounadjela, S. Zhang, Y. Wang, C.B. Sommers, A. Fert, *J. Appl. Phys.* **67**, 5914 (1990); J. Mathon, D.M. Edwards, R.B. Muniz, M.S. Phan, *J. Mag. Mag. Mat.* **104-107**, 1721 (1992); K.B. Hathaway, J.R. Cullen, *J. Mag. Mag. Mat.* **104-107**, 1840 (1992); P. Bruno, C. Chappert, *Phys. Rev.* **B46**, 261 (1992); J. Mathon, M. Villeret, D.M. Edwards, R.B. Muniz, *J. Mag. Mag. Mat.* **121**, 2423 (1993).
- <sup>7</sup>P.M. Levy, S. Zhang, A. Fert, *Phys. Rev. Lett.* **65**, 1643 (1990); S. Zhang, P.M. Levy, *Phys. Rev.* **B47**, 6776, (1993); P.M. Levy, H.E. Camblong, S. Zhang, *J. Appl. Phys.* **75**, 7076 (1994); J.L. Duvail, A. Fert, L.G. Pereira, D.K. Lottis, *J. Appl. Phys.* **75**, 7070 (1994).
- <sup>8</sup>F. Giron, P. Boher, Ph. Houdy, F. Pierre, P. Beauvillain, C. Chappert, K. Le Dang, P. Vieillet, *J. Mag. Mag. Mat.* **104-107**, 1887 (1992); F. Giron, P. Boher, Ph. Houdy, P. Beauvillain, K. Le Dang, P. Vieillet, *J. Mag. Mag. Mat.* **121**, 318 (1993); P.P. Freitas, I.G. Trindade, L.V. Melo, J.L. Leal, N. Barradas, and J.C. Soares, *J. Appl. Phys.* **73**, 5527 (1993).
- <sup>9</sup>J.J. de Miguel, A. Cebollada, J.M. Gallego, R. Miranda, C.M. Schneider, P. Schuster, J. Kirschner, *J. Mag. Mag. Mat.* **93**, 1 (1991).
- <sup>10</sup>M. Ruhrig, R. Schafer, A. Hubert, R. Mosler, J. A. Wolf, S. Demokritov, P. Grunberg, *Phys. Stat. Sol. (A)* **125**, 635 (1991).
- <sup>11</sup>J. Unguris, R. J. Celotta, D. T. Pierce, *J. Appl. Phys.* **75**, 6437 (1994).
- <sup>12</sup>M. E. Filipkowski, C. J. Gutierrez, J. J. Krebs, G. A. Prinz, *J. Appl. Phys.* **73**, 5963 (1993); Z. Celinski, B. Heinrich, J. F. Cochran, *J. Appl. Phys.* **73**, 5966 (1993).
- <sup>13</sup>J.C. Slonczewski, *Phys. Rev. Lett.* **67**, 3172 (1991).
- <sup>14</sup>R. Ribas, B. Dieny, *J. Mag. Mag. Mat.* **121**, 313 (1993).
- <sup>15</sup>M.E. Filipkowski, C.J. Gutierrez, J.J. Krebs, G.A. Prinz, *J. Appl. Phys.* **73**, 5963 (1993).
- <sup>16</sup>K. Brohl, S. DiNunzio, F. Schreiber, Th. Zeidler, H. Zabel, *J. Appl. Phys.* **75**, 6184 (1994).
- <sup>17</sup>Y. U. Idzerda, C. -T. Chen, S. F. Cheng, W. Vavra, G. A. Prinz, G. Meigs, H. -J. Lin, and G. H. Ho, to be published.
- <sup>18</sup>J.-F. Bobo, B. Baylac, L. Henet, O. Lenoble, M. Piecuch, B. Raquet, J.-C. Oussett, *J. Mag. Mag. Mat.* **121**, 291 (1993); M.J. Pechan, J.F. Aukner, C.F. Majkrzak, D.M. Kelley, I.K. Schuller, *J. Appl. Phys.* **75**, 6178 (1994).
- <sup>19</sup>Z.J. Yang, M.R. Scheinfein, *J. Appl. Phys.* **74**, 6810 (1993); Z.J. Yang, S.D. Healy, K.R. Heim, J.S. Drucker, G.G. Hembree, M.R. Scheinfein, *J. Appl. Phys.* **75**, 5589 (1994).
- <sup>20</sup>E.R. Moog, C. Lui, S.D. Bader, *J. Zak. Phys. Rev.* **B39**, 6949 (1989).
- <sup>21</sup>We use the notation transverse here to indicate that the field direction and easy axis are oriented in-plane and perpendicular to the polarization detection axis. We are not measuring the transverse Kerr effect which would require an additional rotation of 90° of the detection axis.

### 1.3 Selective Nucleation and Growth on Nanopatterned $\text{CaF}_2/\text{Si}(111)$ Substrates

(Refer to Publications Listed in Section 1.7 : References 8,21)

Recent progress in the experimental study of the growth and characterization of metals on insulators has been motivated by expectations that these materials will improve upon our current solid state device technology. Components such as quantum-interference high-speed electron devices<sup>1</sup>, triple-barrier resonant tunneling diodes<sup>2</sup>, hot electron transistors<sup>3</sup>, and metal-epitaxial insulator-semiconductor field-effect transistors<sup>4</sup> have been fabricated or proposed using metals, insulators, and semiconductors. Presently, the majority of solid state devices are fabricated using Si as the semiconducting material due to the existence of its native oxide,  $\text{SiO}_2$ . The lack of an atomically smooth  $\text{SiO}_2$ -Si interface does, however, impede the production of three dimensional Si-based devices. Rough interfaces not only decrease the mobility of carriers in devices, but can also destroy the three dimensional epitaxial ordering of subsequent depositions.  $\text{CaF}_2$  has been considered as a suitable replacement for  $\text{SiO}_2$  since it can be grown epitaxially and atomically smooth on  $\text{Si}(111)$  substrates<sup>5</sup>. A small lattice mismatch (0.6% at 298 K) between  $\text{CaF}_2$  and Si, a relatively large band gap (12.1 eV) for electronic isolation, and a larger dielectric constant (6.8) than  $\text{SiO}_2$  (3.9) for an increased electric field at the insulator-semiconductor device interface are but a few of the many reasons for considering  $\text{CaF}_2$  as an obvious replacement for the native  $\text{SiO}_2$ <sup>5</sup>. In addition,  $\text{CaF}_2$  layers may be used as a buffer region such that devices utilizing highly reactive metals such as Fe are not able to form compounds with the Si substrate. The patterned deposition of Fe on  $\text{CaF}_2/\text{Si}(111)$  would enable the fabrication of fully integrated electronic and magnetic devices on a single substrate. Magnetic sensors, high speed microwave wave guides, and non-volatile memories<sup>6</sup> are just three of the many applications which may result from constructing solid state devices using Fe,  $\text{CaF}_2$ , and Si.

The effects on film morphology due to electron-beam exposure of  $\text{CaF}_2$  before and after Fe deposition were explored. Unrelaxed 10 nm thick  $\text{CaF}_2$  films were selectively irradiated with 8.2-140 pA, 100 keV electrons. The intent was to preferentially grow nanoscale structures by changing the surface energy of the substrate through the conversion of  $\text{CaF}_2$  into a metallic, higher surface energy, Ca-rich surface. As a result, the growth mode of the Fe would be modified in the irradiated regions.

Fig. 1.3.1a displays the decreased secondary electron yield for eleven regions which were methodically dosed with 100 keV, 140 pA electrons. From left to right, the charge per unit area impinged upon the sample was; 1.44, 5.78, 2.89, 4.81, 7.22, 14.4, 14.4, 28.9, 57.8, 144, and 217  $\text{C}/\text{cm}^2$ . The two right-most irradiated regions best reveal the proximity effects of electronic charge dissipation. Proximity effects adjacent to exposed regions obfuscate the comparison between unexposed and exposed film morphology. As depicted in Fig. 1.3.1b, a  $\Theta = 21.4$  ML deposition of Fe greatly diminishes image contrast. Although Figs. 1.3.1a and 1.3.1b were acquired at the same location, surface imperfections which were visible on the clean  $\text{CaF}_2$  surface became imperceptible after the Fe was deposited. The Fe did not, however, mask the presence of the pre-growth irradiated areas. Fig. 1.3.1c illustrates the results of a pre-growth electron dose of 5.78  $\text{C}/\text{cm}^2$  on the Fe film morphology. The surface structure shown in the lower portion of the image (below the dashed line), which was not exposed to irradiation, appears more distinct and separated than the upper region.

As a second example, a  $\Theta = 7.1$  ML film of Fe grown on a room temperature  $\text{CaF}_2/\text{Si}(111)$  substrate, which had been patterned with an electron-beam, produced a uniform distribution of Fe islands over most of the  $\text{CaF}_2$  surface. This film also displayed an expected change in morphology for those regions which had been irradiated with more than 1.14  $\text{C}/\text{cm}^2$  before the Fe deposition. Fig. 1.3.2a portrays the effects of pre-growth and post-growth electron irradiation effects on the Fe film's morphology. The lower left portion of Fig. 1.3.2a (enclosed by the dotted white line) is a region which had been subjected to 4.56  $\text{C}/\text{cm}^2$  before the Fe growth. The Fe on the pre-growth exposed region is much more continuous than on the region which was not exposed. The contrast observed for this region may be due to island formation atop a continuous ultra thin film of Fe. If, for example, the pre-growth



exposed region consisted of islands on a finer scale it would be expected that the film would suffer similarly to the effects of post-growth electron irradiation, as is evident near the center of Fig. 1.3.2a. The area within the dashed white line of Fig. 1.3.2a was subjected to  $355 \text{ C/cm}^2$  of electron irradiation *following* the Fe deposition. By comparing the intersection of the two highlighted regions (A) with that of the remaining area within the dashed white line (B), qualitative arguments of Fe island position stability can be set. The pre-growth irradiated area (A) is more stable to post-growth electron irradiation. In fact, very little morphological change is observed for the pre-growth irradiated area except near the border of the dosed/undosed region. The occurrence of more damage near the edges is simply due to an insufficiently distinct separation of the two regions during exposure. Electronic charge dissipation and mechanical instabilities (over the course of several tens of minutes) allowed slightly more area to be affected by the electron beam than intended. Fig. 1.3.2b is a lower magnification SE image obtained immediately after Fig. 1.3.2a. Two complete regions of pre-growth irradiation are visible along with part of a third area. Since insulators generally have higher secondary electron yields than metals, the regions of pre-growth irradiation which are now more metallic (due to the Fluorine desorption) appear darker than the surrounding areas. The brighter region in the center of Fig. 1.3.2b is due to post-growth electron irradiation and was formed when the image shown in Fig. 1.3.2a was obtained. This bright contrast, though not always observed, probably results from a redistribution of  $\text{CaF}_2$  under specific post-growth electron exposures. Only for greater coverages, such as a  $\Theta = 21.4 \text{ ML}$  film, does post-growth electron-beam-induced damage remain negligible. For instance, both the pre-growth exposed region and the unexposed region of the  $\Theta = 21.4 \text{ ML}$  Fe film shown in Fig. 1c were able to withstand  $343 \text{ C/cm}^2$  of post-growth electron irradiation with no obvious morphological change, unlike what was observed for the  $\Theta = 7.1 \text{ ML}$  ( $355 \text{ C/cm}^2$ ) regime shown in Fig. 1.3.2a.

---

<sup>1</sup>T. Sakaguchi, M. Watanabe, and M. Asada, IEICE Trans. E 74, 3326 (1991).

<sup>2</sup>M. Watanabe, T. Suemasu, S. Muratake, and M. Asada, Appl. Phys. Lett. 62, 300 (1993).

<sup>3</sup>S. Muratake, M. Watanabe, T. Suemasu, and M. Asada, Electronics Letters 28, 1002 (1992). T. Suemasu, M. Watanabe, M. Asada, and N. Suzuki, Electronics Letters 28, 1432 (1992).

<sup>4</sup>T. P. Smith, J. M. Phillips, W. M. Augustyniak, and P. J. Stiles, Appl. Phys. Lett. 45, 907 (1984).

<sup>5</sup>L. J. Schowalter and R. W. Fathauer, CRC Critical Reviews in Solid State and Materials Sciences 15, 367 (1989).

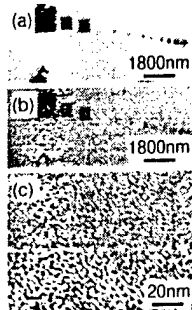


Fig. 1.3.1: Pre-growth electron-beam irradiated regions were observed at lower magnification (a) before and (b) after  $\Theta = 21.4$  ML of Fe had been deposited. These equivalent regions of the same crystal display large differences in secondary electron contrast. Surface imperfections located at the lower left of (a) were no longer visible after the Fe deposition (b). In contrast, electron-beam exposed regions remain apparent before and after the Fe deposition. The two right-most irradiated regions in (a) best reveal the proximity effects of electronic charge dissipation. A pre-growth electron dose of  $5.78 \text{ C/cm}^2$  changes the Fe film's morphology, as depicted in (c). The much more distinct and separated region of (c) below the dashed, white line was not exposed to irradiation prior to the Fe growth, as had the upper region. The top-most area of (c) is slightly more continuous and less distinct because of the morphological changes that resulted from the 100 keV, 140 pA pre-growth electron irradiation.

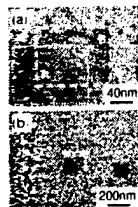


Fig. 1.3.2: Secondary electron images depict the pre-growth and post-growth electron-beam induced effects on Fe film morphology. A  $\text{CaF}_2/\text{Si}(111)$  film was selectively exposed to  $4.56 \text{ C/cm}^2$  of electron irradiation prior to the Fe growth. This region is enclosed by the dotted white line in (a). After a  $\Theta = 7.1$  ML room temperature deposition of Fe, most of the substrate surface is covered with 2 nm diameter Fe islands. The region which had been irradiated before the Fe growth, however, is much more continuous than the surrounding area. A post-growth electron dose of  $355 \text{ C/cm}^2$  (enclosed by the dashed, white line) greatly affected the Fe film morphology for regions that had not been irradiated before growth (B). Conversely, post-growth irradiation did not effect the Fe film morphology for areas which had been exposed to electron irradiation prior to the Fe growth (A). A lower magnification secondary electron image of (a) is shown in (b). Two complete regions of pre-growth irradiation are visible in (b). A step edge which runs nearly vertical can be seen to the left of the center-most irradiated region in (b).

## 1.4 Ordering Transitions and Coupling in Two-Dimensional Arrays of Fe Islands

(Refer to Publications Listed in Section 1.7: References 21-23)

Magnetic systems are ideal for studying interactions and phase transitions<sup>1</sup>. Clusters of ferromagnetic metal atoms transform from molecular states with atomic magnetic moments to bulk-like states with bulk moments as the number of atoms within a cluster increases<sup>2</sup>. Super-paramagnetic relaxation is exhibited when the individual exchange-coupled magnetic moments form a single fluctuating super-moment<sup>3</sup>. The local fields and relaxation times can be altered when moments are positioned in close proximity<sup>4</sup>. Ordered arrays of sub-micron ferromagnetic structures can be fabricated by electron-beam<sup>5</sup> and scanning tunneling microscope<sup>6</sup> based lithographies. We examined the magnetic properties<sup>7</sup> of ultrathin Fe films grown on  $\text{CaF}_2/\text{Si}(111)$ . This system is unique since the Fe nucleates into islands with a high density<sup>8</sup> ( $8 \times 10^{12}/\text{cm}^2$ ), and narrow size distribution, providing closely spaced two-dimensional arrays of nanometer sized particles.  $\text{CaF}_2$ , with its 11 eV bandgap has no electronic states that are likely to couple to the Fermi-level spin-split states in the Fe. The radius and density of the Fe islands can be controlled experimentally; by varying these parameters we can see the onset of interparticle exchange coupling as well as transitions in magnetic ordering. The magnetic phases included two-dimensional ferromagnetism, weakly interacting superparamagnetism with two and three degrees of (magnetic) freedom, and spin-glass like (and antiferromagnetic) phases. This single physical system provided, as a function of island radius, a random long-range coupled Ising spin regime, a long-range coupled in-plane XY rotator regime, and a superferromagnetically ordered phase.

Mean-field and Monte Carlo models were used to evaluate the magnetic properties as a function of particle radius and density. Although mean-field methods over estimate the transition temperature, and ignore fluctuations<sup>1</sup>, trends can be examined straightforwardly. The Monte Carlo method, which rigorously accounts for fluctuations, uses the Metropolis et al.<sup>9</sup> algorithm to determine the equilibrium magnetization distribution using the Hamiltonian defined below. Simulations were done with periodic boundary conditions, and 100 or 400 islands. Both models incorporate the experimental size distribution of Fe islands. The irregular actual island shape is approximated by a cylinder. This allows in-plane vs. out-of-plane shape anisotropies to be considered self-consistently.

The mean-field self-energy written in terms of the island's radius  $a$ , and height  $L$ , is

$$E_{\text{self}} = (2\pi M_s^2)(\pi a^2 L) \left[ m_z^2 + (m_x^2 + m_y^2 - 2m_z^2) \frac{2}{\pi} \int_0^\infty \frac{dx}{x^2} \sin^2 x K_1\left(\frac{2a}{L}x\right) I_1\left(\frac{2a}{L}x\right) \right].$$

$K_1$  and  $I_1$  are modified Bessel functions. When the value of the integral exceeds  $\pi/6$ , the easy direction changes from in-plane to out-of-plane, i.e. when  $2a/L < 1.3$ , or at experimental coverages of 3.3 and 6.7 ML. When  $2a/L < 1.3$ , the system behaves as a random, two-dimensional Ising array with long range interactions. This regime is like a long-range interaction Sherrington-Kirkpatrick<sup>10</sup> (spin-glass) model. When  $2a/L > 1.3$ , the moments are confined to lie in-plane, and the system is similar to a long-range interaction X-Y rotator model<sup>11,14</sup>. The coupling energy is found from integrating the field due to the average magnetization  $\langle m_i \rangle$  of all the surface islands (density  $\sigma \text{ cm}^{-2}$ ) from the nearest neighbor radius,  $a_{nn}$ , to infinity.

$$E_{\text{coupling}} = (4\pi M_s^2)(2aa_{nn}\sigma)(\pi a^2 L) \left( 2m_z \langle m_z \rangle - m_x \langle m_x \rangle - m_y \langle m_y \rangle \right) \int_0^\infty \frac{dx}{x} \sin x K_1\left(\frac{2a_{nn}}{L}x\right) I_1\left(\frac{2a}{L}x\right)$$

The order parameter determined from numerical integration<sup>12</sup> of the partition-function is a function of temperature and the externally applied field. In the absence of fluctuations, in-plane dipolar ferromagnetism<sup>13</sup> is possible at room temperature when  $a=3.3 \text{ nm}$ . A transition temperature of about 300 K exists when  $a=2.2 \text{ nm}$ . When Monte Carlo methods are employed, the transition temperature is reduced by a factor of two, and the ordering is local<sup>14</sup>, rather than global<sup>1,15</sup> with non-zero magnetization correlated over length scales on the order of 100 nm. These high transition temperatures result from the

altered length scales of this system over that of one whose moments are individual Fe moments. Each superparamagnetic moment is spatially extended<sup>16</sup> (rather than a point dipole), composed of approximately  $10^3 \mu_B$ , and spaced by nm. A two-dimensional ordered lattice of Fe point dipoles ( $2.2 \mu_B$ ) experiencing equivalent nearest-neighbor fields would need to be spaced by several hundredths of a nm.

The Monte Carlo method includes fluctuations. The dipolar coupling energy is summed over all pairs of islands on the surface. Dipolar coupled random arrays which have high enough transition temperatures to support room temperature dipolar ferromagnetism possess fluctuations which destroy long range order. The order parameter for local structure resulting from the Monte-Carlo calculation is shown in Fig. 1.4.1. To explain the observed room temperature ferromagnetism<sup>8</sup> either exchange or anisotropy is required. Since there is no easy axis<sup>4</sup>, exchange must be responsible for the long range order. When nearest neighbor exchange,

$$\sum_{\text{Neighbors}} J(\mathbf{M}_i \cdot \mathbf{M}_j) = \sum_{i \neq j} J(\mathbf{M}_i \cdot \mathbf{M}_j) = \sum_{i \neq j} J(\mathbf{M}_i \cdot \mathbf{M}_j) \cdot \mathbf{H}_j$$

is included in the hamiltonian, exchange fields on the order of 100-250 Oe are sufficient to order the  $a=3.3$  nm islands ferromagnetically. This coupling field is insufficient to ferromagnetically order the  $a=2.2$  nm islands. These fields correspond to interisland exchange coefficients of  $J/J_{\text{Fe-bulk}}=0.013-0.033$ . A superferromagnetic exchange coupling between the supermoments is a plausible source for the observed ferromagnetic ordering in two dimensions<sup>4</sup> as a function of particle size

Superparamagnetism<sup>17,18</sup> is distinguished from paramagnetism by the magnitude of the magnetic moment. When superparamagnetic moments are brought close together, exchange interactions can couple neighboring moments; this interaction leads to long range order, hence the nomenclature of superferromagnetism.<sup>19</sup> Superparamagnetism and superferromagnetism were observed in high density two-dimensional arrays of nanometer-sized Fe islands on  $\text{CaF}_2/\text{Si}(111)$ .<sup>20</sup> We reported on enhanced two-dimensional superparamagnetism for  $\text{Ag}/\text{Fe}/\text{CaF}_2/\text{Si}(111)$ . The magnetic signature of this system is mediated through long-range exchange between individual superparamagnetic Fe islands within larger, several nanometer-diameter Ag islands.

The  $\text{Fe}(3.3 \text{ ML})/\text{CaF}_2/\text{Si}(111)$  ( $1 \text{ ML} = 1.73 \times 10^{15} \text{ atom/cm}^2$ )<sup>21</sup> system is unusual since the Fe atoms nucleate and form a high-density ( $8 \times 10^{12} \text{ islands/cm}^2$ ), two-dimensional array of nanometer-sized islands characterized by an extremely narrow size distribution (0.95 nm in radius, and 85% of the islands fall within  $\pm 0.48$  nm of this radius).<sup>20</sup>

Monte Carlo models were used to compute the in-plane normalized magnetization at  $H = 1 \text{ kOe}$  for this two dimensional array.  $M/M_s = 0.084 \pm 0.002$ . The normalized magnetization at  $H = 1 \text{ kOe}$ , evaluated with the Langevin function for the average size Fe island, is 0.074. This illustrates the effects of interactions in this closely-spaced array. For example, when the density of Fe particles is reduced by a factor of 10, the calculated normalized magnetization at  $H = 1 \text{ kOe}$  is  $0.074 \pm 0.003$ , in agreement with predictions based upon the (uncoupled) Langevin function.

When Kerr signals were obtained from  $\text{Ag}/\text{Fe}(3.3\text{ML})/\text{CaF}_2/\text{Si}(111)$  surfaces, the measured magnetic signal contained contributions from both Ag-covered and uncovered Fe islands. In order to recover the magnitude of the superparamagnetic response of Ag-covered Fe islands, the background from the uncovered Fe islands were subtracted from the total Kerr signal. In this fashion, the low-field susceptibility ( $\chi = N m^2 / 3 k_B T$ ) was used to compare the effective normalized moment ( $\mu_{\text{Covered}} / \mu_{\text{Single}} = (\chi_{\text{Covered}} N_{\text{Single}} / \chi_{\text{Single}} N_{\text{Covered}})^{1/2}$ ) for each surface. A plot of the normalized moment in Fig. 1.4.2 displays an increasing in-plane effective moment as a function of the average number of Fe islands per average Ag island, including corrections for the changing optical scattering coefficients<sup>22</sup>. Such corrections were necessary since the Kerr signal diminishes with increasing Ag coverage due to increased reflectivity at the top Ag surface.

If the Ag did not mediate the magnetic exchange between Fe islands enclosed within a Ag island, the low-field susceptibility would have been identical for all surfaces (once the background subtraction and optical scattering corrections are made). Only the longitudinal Kerr intensity increased with the

number of Fe islands covered by Ag, while the polar Kerr intensity remained virtually unchanged. This signifies that the Ag atoms *do* help correlate the in-plane magnetic moments between individual Fe islands contained within a single Ag island. The lack of an increasing out-of-plane signal suggests that the Ag atoms induce an in-plane (surface) anisotropy which favors in-plane magnetic alignment.<sup>23</sup>

Our Monte Carlo model was used to assess the strength of the Fe inter-island coupling within each Ag island. The susceptibility was computed for a given applied field and a variable phenomenological inter-island exchange field. The response of the uncovered islands was subtracted, and the ratio of the moment of a cluster of Fe islands covered by Ag to that of a single Fe island moment was computed. Each (initial) configuration contributed to a family of curves whose asymptotic value of the normalized moment plotted vs the interisland coupling constant approached the number of islands covered by a single Ag island when  $J/J(\text{Fe})$  is large. The coupling of the individual Fe islands through the Ag overlayer was detected unambiguously through the enhancement in the low-field susceptibility. The size of the coupling field required to produce the observed change in susceptibility is estimated to be on the order of 5000 Oe ( $J/J_{\text{Fe}}=0.25$ ) using Monte Carlo simulations.

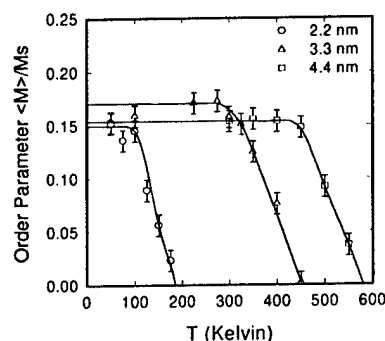


Fig. 1.4.1 : Local order derived from Monte Carlo calculations indicate that the transition temperature is a function of particle radius.

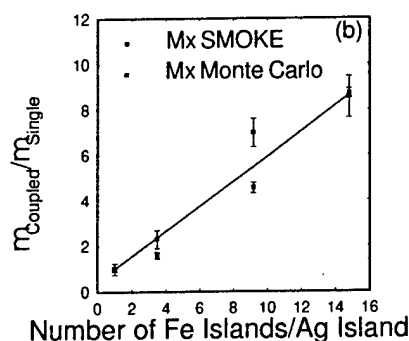


Fig. 1.4.2 : Normalized effective moment of Fe islands covered by a single Ag island as a function of the number of islands covered within that single Ag island. The abscissa of one corresponds to the uncovered (Ag) surface.

<sup>1</sup>H.E. Stanley, *Introduction to Phase Transitions and Critical Phenomena*, (Oxford University Press, London, 1971); D.C. Mattis, *The Theory of Magnetism II*, (Springer-Verlag, Berlin, 1985); J.J. Binney N.J. Dowrick, A.J. Fisher, M.E.J. Newman, *The*

- Theory of Critical Phenomena*, (Oxford Science Publications, London, 1993); K.H. Fischer, J.A. Hertz, *Spin Glasses*, (Cambridge University Press, Cambridge, 1991).
- <sup>2</sup>I.M.L. Billas, A. Chatelain, W.A. de Heer, *Science*, **265**, 1682 (1994); D. Gatteschi, A. Caneschi, L. Pardi, R. Sessoli, *Science*, **265**, 1054 (1994); S. Linderoth, S.N. Khanna, *J. Mag. Mag. Mat.* **104-107**, 1574 (1992).
- <sup>3</sup>L. Neel, *Ann. Geophys.* **5**, 99 (1949).
- <sup>4</sup>S. Morup, *Phys. Rev. Lett.* **72**(20), 3278 (1994); S. Morup, G. Christiansen, *J. Appl. Phys.* **73**(10), 6955 (1993); S. Morup, *Hyperfine Int.* **60**, 959 (1990); S. Morup, P.H. Christensen, B.S. Clausen, *J. Mag. Mag. Mat.* **68**, 160 (1987); S. Morup, M.B. Madsen, J. Franck, J. Villadsen, C.J.W. Koch, *J. Mag. Mag. Mat.* **40**, 163 (1983).
- <sup>5</sup>S.Y. Chou, M.S. Wei, P.R. Krauss, P.B. Fischer, *J. Appl. Phys.* **76**(10), 6673 (1994); A. Maeda, M. Kume, T. Ogura, K. Kuroki, *J. Appl. Phys.* **76**(10), 6667 (1994).
- <sup>6</sup>A.D. Kent, T.M. Shaw, S. von Molnar, D.D. Awschalom, *Science*, **262**, 1249 (1993); A.D. Kent, S. von Molnar, S. Gider, D.D. Awschalom, *J. Appl. Phys.* **76**(10), 6656 (1994).
- <sup>7</sup>H.-B. Braun, *J. Appl. Phys.* **76**(10), 6310 (1994); H.-B. Braun, *Phys. Rev. Lett.* **71**(21), 3557 (1993); R.W. Chantrell, A. Lyberatos, M.El-Hilo, K. O'Grady, *J. Appl. Phys.* **76**(10), 6407 (1994). A. Lyberatos, R.W. Chantrell, *J. Appl. Phys.* **73**(10), 6501 (1993).
- <sup>8</sup>K.R. Heim, G.G. Hembree, M.R. Scheinfein, *J. Appl. Phys.* **76**(12), 8105 (1994); K.R. Heim, G.G. Hembree, M.R. Scheinfein, *J. Mag. Mag. Mat.* (submitted).
- <sup>9</sup>N. Metropolis, A.W. Rosenbluth, M.N. Rosenbluth, A.H. Teller, E. Teller, *J. Chem. Phys.* **21**, 1087 (1953).
- <sup>10</sup>D. Sherrington, S. Kirkpatrick, *Phys. Rev. Lett.* **35**, 1972 (1975).
- <sup>11</sup>J. Villain, *J. Phys.* **C10**, 1717 (1977); J. Villain, *J. Phys.* **C10**, 4793 (1977);
- <sup>12</sup>V.I. Lebedev, *Zh. Vychisl. Mat. Fiz.* **15**, 48 (1975); V.I. Lebedev, *Zh. Vychisl. Mat. Fiz.* **16**, 293 (1976).
- <sup>13</sup>M.H. Cohen, F. Keffer, *Phys. Rev.* **99**(4), 1128 (1955); M.H. Cohen, *Phys. Rev.* **99**(4), 1135 (1955).
- <sup>14</sup>J.M. Kosterlitz, D.J. Thouless, *J. Phys.* **C6**, 1181 (1973); J. M. Kosterlitz, *J. Phys.* **C7**, 1046 (1974).
- <sup>15</sup>N.D. Mermin, H. Wagner, *Phys. Rev. Lett.* **17**, 1133 (1966).
- <sup>16</sup>M.E. Fisher, D. Ruelle, *P. Math. Phys.* **7**(2), 260 (1966).
- <sup>17</sup>D.C. Mattis, *The Theory of Magnetism II*, (Springer-Verlag, Berlin, 1985).
- <sup>18</sup>L. Neel, *Ann. Geophys.* **5**, 99 (1949).
- <sup>19</sup>S. Mørup, *Phys. Rev. Lett.* **72**(20), 3278 (1994); S. Mørup, G. Christiansen, *J. Appl. Phys.* **73**(10), 6955 (1993); S. Mørup, *Hyperfine Int.* **60**, 959 (1990); S. Mørup, P.H. Christensen, B.S. Clausen, *J. Mag. Mag. Mat.* **68**, 160 (1987); S. Mørup, M.B. Madsen, J. Franck, J. Villadsen, C.J.W. Koch, *J. Mag. Mag. Mat.* **40**, 163 (1983).
- <sup>20</sup>K.R. Heim, G.G. Hembree, M.R. Scheinfein, *J. Appl. Phys.* **76**(12), 8105 (1994); K.R. Heim, G.G. Hembree, M.R. Scheinfein, *J. Mag. Mag. Mat.* (submitted-1995); M.R. Scheinfein, K.E. Schmidt, K.R. Heim, G.G. Hembree, *Phys. Rev. Lett.* (in press-1995).
- <sup>21</sup>Since the atomic ordering of the Fe adatoms is unknown, we have adopted the convention that 1 ML is equivalent to the surface atom density for the close-packed direction of bcc Fe, i.e., Fe(110). This was defined as such so that the total number of magnetic moments on these CaF<sub>2</sub> surfaces (there is a very large lattice mismatch between Fe and CaF<sub>2</sub>), could be more readily compared to other magnetic systems. This convention was also used for the Ag.
- <sup>22</sup>K.R. Heim, M.R. Scheinfein, *J. Mag. Mag. Mat.* (in press-1995).

## 1.5 Electron Holography of Thin Films, Superlattices and Small Particles

(Refer to Publications Listed in Section 1.7 : References 1,9,10,11,14,15,17,18 and Conference Proceedings 1-6,8-10)

Various modes of Lorentz microscopy, reveal the in-plane component of magnetization as well as the local (microcrystalline) microstructure. However, electron holography, where both the amplitude and phase of the transmitted electron waves are recorded is the method of choice for analysis of magnetic structure at nanometer length scales since the phase shift in the specimen contains valuable **quantitative** micromagnetic information that can be straightforwardly retrieved from the electron hologram. Electron holography with its absolutely calibrated electron interference fringe spacing and high spatial resolution is an absolute means of measuring in-plane magnetization in thin magnetic films, with a sensitivity that surpasses the most sensitive SQUID magnetometer by many orders of magnitude. This feature significantly expands the abilities of STEM as a tool for investigating magnetic materials.

We have implemented two important modes of STEM holography. In the absolute mode, well-known from TEM holography, one of the waves passes through vacuum and the other through the specimen and the phase difference is measured with respect to vacuum. In a domain with uniform magnetization located at a sharply defined edge, the phase will change linearly with increasing distance from the edge as the enclosed flux increases. The gradient of the phase will absolutely determine the magnitude and direction of the magnetization in the domain if the thickness is known. The differential point projection (DPP) mode of electron holography is particularly well-suited for the STEM configuration. Both of the split electron waves pass through the specimen. These two virtual sources are separated by a very small distance when projected onto the sample, typically several tens of nm. This separation can be varied not only by changing the voltage applied to the biprism, but also by simply changing the excitation of the condensor and/or objective lenses. The size of the illuminated area which contributes to the phase difference (through the magnetic flux), is approximately constant for every point in the detector plane (illumination is almost parallel). The sensitivity to local changes in the phase is limited in this mode by the separation of the virtual sources. Our method uses a biprism near the gun which splits the STEM probe into two stationary probes. As in Young's pin-hole experiment, (since these probes are coherent) the two sources interfere to produce the required carrier fringes for holography. The probe is not scanned, so a shadow image is seen on the detector, crossed by the carrier fringes. The fringes are locally shifted by an amount proportional to the magnetic flux enclosed by the two independent beam paths. Using standard methods of Fourier image processing, a holographic reconstruction can be made to give a map of magnetic field  $B$  (projected in the beam direction).

We explored the micromagnetic structure of giant magnetoresistance superlattice structures to clarify the role of intralayer and interlayer electron scattering processes in the giant magnetoresistance effect in superlattices with interfaces of varying degree of perfection. We used electron holographic methods to quantitatively determine the orientation of domains in a superlattice, with an eye towards identifying whether or not domains penetrate through the ferromagnetic layers. Measurements on  $[\text{Co}(t_{\text{Co}})/\text{Cu}(t_{\text{Cu}})]_n$  multilayers prepared by molecular beam epitaxy indicate that the giant magnetoresistance effect is correlated with the formation of domains oriented at 90 degrees with respect to the field direction in systems with rough interfaces.) as shown in section 1.2. We were able to determine with electron holography that most of the domains 'structures' penetrate the sandwich. Since the magnetization was measured with an accuracy of 1% and spatially mapped, it was straightforward to observe that most of the domains penetrated the superlattice were uniformly (ferromagnetically) aligned. However, some domains had a reduced magnetization (10% less) when compared with the uniformly magnetized domain value. This indicated that the magnetization in one of the layers (10% of the active thickness) had rotated by 90 degrees with respect to the magnetization in the other layers. This information is not obtainable by any other technique. Other measurements of this type include quantitative micromagnetic structure of domains and domain walls in thin films, and the magnetic structure in small particles and MFM tips.

## 1.6 Magnetometry of Superlattices Using Surface Magneto-Optic Kerr Effect

(Refer to Publications Listed in Section 1.7 : References 4,19)

As ultrathin film systems become more sophisticated through the production of complex multilayered specimens, it becomes increasingly important to be able to predict and analyze the magneto-optical properties for these systems. A computational technique useful in performing this task must not only handle the phase changes upon scattering from well-defined boundaries, but also account for the mode coupling which occurs between interfaces of anisotropic media. When an optical technique, such as SMOKE, is used to probe the magnetic properties of a surface, the anisotropy of the magnetic film manifests itself as a change in the polarization state of the reflected light relative to that of the incident polarization. Calculations to determine the polarization rotation for a simple magnetic metal on non-magnetic metal system are tractable enough that a computer is not typically necessary. However, for systems which arbitrarily combine one or more metals (magnetic and/or non-magnetic) with dielectric multilayers, the utility of a more complete optical description is obvious.

Several approaches have been outlined to compute the Fresnel reflection and transmission coefficients for layered media. In the simplest theoretical formalism multiple reflections are not taken into consideration and, hence, such a method is not reliable for multilayered thin-film systems.<sup>1</sup> Other techniques have accounted for multiple reflections at the layered interfaces, however, versatility was lacking for arbitrary incidence angles, the type of layered material which could be modeled, or the order in which the material could be arranged (i.e., some models require bounding by dielectrics only).<sup>2,3</sup>

We developed an alternative approach to calculating the effects of magneto-optic scattering for even the most general of optical systems. The parameters necessary to facilitate the computations are; (1) the angle of incidence, (2) the frequency of the probing laser, (3) the thickness of each film, (4) the complex indices of refraction for each material at the desired laser wavelength, and (5) the Voight coefficient for the magneto-optic media. The maximum number of individual layers is limited only by the precision of the machine arithmetic. Magneto-optic effects can be determined as a function of the incidence angle, laser frequency, individual film thickness, as well as film composition.

This 4x4 matrix method is based upon a general theory of electromagnetic propagation in periodic stratified media set forth by Yeh et. al.<sup>4</sup> The logical extension was to incorporate magnetic media so that the complex Fresnel reflection and transmission coefficients could be calculated for an arbitrary arrangement and number of magnetic, non-magnetic, and dielectric layers.<sup>5</sup> The reflection (or transmission) coefficients can then be inserted into an intensity equation which describes the optical components of the desired system. Relative sensitivities are easily obtainable which interrelate the three Kerr geometries (polar, longitudinal, and transverse) as well as the two most common modulated intensity measurement modes. The intensity equation is relevant to magneto-optic Kerr effect measurements using (1) a polarized laser, (2) a photo-elastic modulator, (3) a reflective specimen, (4) an analyzing polarizer, and (5) a photo-diode connected to a lock-in amplifier (such as used in our laboratory), but may be suitably adjusted to incorporate a myriad of possible optical configurations.

A computer code based on Yeh's method has been implemented and tested. The theory serves as an integral component in the computation of coupling between nanometer diameter islands, the analysis of switching in magnetic multilayers, and it has been used in collaboration with researchers at Stanford to compute the reflectivities of x-ray mirrors.

<sup>1</sup> G. Metzger, P. Pluvinage, and R. Torguet, *Ann. Phys. (Leipzig)* **10** (1965) 5.

<sup>2</sup> C. C. Robinson, *J. Opt. Soc. Am.* **53** (1963) 681; C. C. Robinson, *ibid.* **54** (1964) 1220; D. O. Smith, *Optica Acta* **12** (1965) 13; R. P. Hunt, *J. Appl. Phys.* **38** (1967) 1652; C. C. Robinson, *J. Opt. Soc. Am.* **58** (1968) 1342

<sup>3</sup> J. Zak, E. R. Moog, C. Liu and S. D. Bader, *J. Magn. Magn. Mater.* **89** (1990) 107.

<sup>4</sup> P. Yeh, A. Yariv, and C-S. Hong, *J. Opt. Soc. Am.* **67** (1977) 423; A. Yariv and P. Yeh, *J. Opt. Soc. Am.* **67**, (1977) 438; P. Yeh, *J. Opt. Soc. Am.* **69** (1979) 742; P. Yeh, *Surface Science* **96** (1980) 41.

<sup>5</sup> K. R. Heim, Ph. D. Thesis, Arizona State University, United States (1994).



1.7 Publications During The Previous Grant Period: ONR CONTRACT #N00014-93-0099

Refereed Publications

- 23 Two-Dimensional Long-Range Coupling : Enhanced Superparamagnetism in Two-Dimensional Arrays of Nanometer Sized Fe Islands, M.R. Scheinfein, K.E. Schmidt, K.R. Heim, G.G. Hembree, Appl. Phys. Lett. 67(19), 2878 (1995).
- 22 Long Range Order and Coupling in Two-Dimensional Arrays of Nanometer Size Superparamagnets, M.R. Scheinfein, K.E. Schmidt, K.R. Heim, G.G. Hembree, Phys. Rev. Lett. (in press-1995).
- 21 Magnetic and Structural Characterization of Ultrathin Fe Films on  $\text{CaF}_2/\text{Si}(111)$ : Superparamagnetic and Ferromagnetic Behavior of Nanometer Sized Particles, K.R. Heim, G.G. Hembree and M.R. Scheinfein, J. Mag. Mag. Mat. (submitted - 1995).
- 20 Interfacial Roughness Effects on Giant Magnetoresistance and Interlayer Coupling in Co/Cu Superlattices, Z.J. Yang and M.R. Scheinfein, Phys. Rev. B52(6), 4263 (1995).
- 19 An Alternative Approach For Magneto-Optic Calculations Involving Layered Media, K.R. Heim, M.R. Scheinfein, J. Mag. Mag. Mat. (in press - 1995).
- 18 Absolute Magnetometry Using Electron Holography: Magnetic Superlattices and Small Particles, Marian Mankos, J.M. Cowley, M.R. Scheinfein, Material Research Society Bulletin, (in press-1995).
- 17 Quantitative Micromagnetics: Electron Holography of Magnetic Thin Films and Multilayers, Marian Mankos, M.R. Scheinfein, J.M. Cowley, IEEE Trans. MAG (in press-1995).
- 16  $90^\circ$  Domains and Coupling in Co/Cu Giant Magnetoresistance Superlattices, Z.J. Yang, M.R. Scheinfein, IEEE Trans. MAG-31(6), 3921 (1995).
- 15 Nanomagnetometry: Electron Holography of Small Particles, M. Mankos, J.M. Cowley, M.R. Scheinfein, IEEE Trans. MAG-31(6), 3796 (1995).
- 14 Quantitative Micromagnetics at High Spatial Resolution Using Electron Holography, M. Mankos, J.M. Cowley, M.R. Scheinfein, phys. stat. sol.(a), (submitted-1995).
- 13 STEM Holography of Magnetic Materials, M. Mankos, P. de Haan, V. Kambersky, G. Matteucci, M.R. McCartney, Z.J. Yang, M.R. Scheinfein, J.M. Cowley, in Electron Holography, Delta Series, eds. A. Tonomura, L. Allanrd, G. Pozzi, D. Joy, Y. Ono, Elsevier Science BV, 329-341, (1995).
- 12  $90^\circ$  Domains in Co/Cu Giant Magnetoresistance Superlattice, Z.J. Yang, M.R. Scheinfein, Appl. Phys. Lett. 66(2), 236 (1995).
- 11 Absolute Magnetometry of Thin Cobalt Films and Co/Cu Multilayer Structures at Nanometer Spatial Resolution, Marian. Mankos, Z.J. Yang, M.R. Scheinfein, J.M. Cowley, IEEE-Trans. MAG 30(6), 4497 (1994).

- 10 Far Out-of-Focus Electron Holography in a Dedicated FEG STEM, M. Mankos, A.A. Higgs, M.R. Scheinfein, J.M. Cowley, *Ultramicrosc.* 58, 87 (1995).
- 9 Absolute Magnetometry At Nanometer Spatial Resolution : STEM Holography Of Thin Cobalt Films, M. Mankos, M.R. Scheinfein, J.M. Cowley, *J. Appl. Phys.* 75(11) 7418 (1994).
- 8 Ultra High Vacuum Scanning Electron Microscopy Characterization of the Growth of Fe on  $\text{CaF}_2/\text{Si}(111)$ : Selective Nucleation on Electron-Beam Modified Surfaces, K.R. Heim, G.G. Hembree, M.R. Scheinfein, *J. Appl. Phys.* 76(12), 8105 (1994).
- 7 Structural and Magnetic Properties of Epitaxially Grown fcc Fe/Cu(100) and Fe/ $\text{CaF}_2/\text{Si}(111)$ , M.R. Scheinfein, S.D. Healy, K.R. Heim, Z.J. Yang, J.S. Drucker, G.G. Hembree, *Proc. Mat. Res. Soc.* vol. 332, *Determining Nanoscale Properties of Materials by Microscopy and Spectroscopy*, eds. M. Isaacson, M. Sarikaya, K. Wickramasinghe, 473 (1994).
- 6 Surface Magnetization Processes Investigated by the Combined Surface Magneto-Optical Kerr Effects in fcc Fe/Cu(100) Thin Films, Z.J. Yang, S.D. Healy, K.R. Heim, J.S. Drucker, G.G. Hembree, M.R. Scheinfein, *J. Appl. Phys.* 75(10), 5589 (1994).
- 5 The Initial Phases of Epitaxy of fcc Fe/Cu(100): Supersurface and Subsurface Island Formation, S.D. Healy, K.R. Heim, Z.J. Yang, J.S. Drucker, G.G. Hembree, M.R. Scheinfein, *J. Appl. Phys.* 75(10), 5592 (1994).
- 4 Combined Three-Axis Surface Magneto-Optical Kerr Effects in the Study of Surface and Ultrathin Film Magnetism, Z.J. Yang, M.R. Scheinfein, *J. Appl. Phys.* 74(11) 6810 (1993).
- 3 Correlations Between Ultrathin Film Microstructure and Magnetic Properties in Epitaxial Films of fcc Fe/Cu(100), K.R. Heim, S.D. Healy, Z.J. Yang, J.S. Drucker, G.G. Hembree, M.R. Scheinfein, *J. Appl. Phys.* 74(12), 7422 (1993).
- 2 Field Induced Metastable States in Ultrathin Films of fcc Fe/Cu(100), G.G. Hembree, J.S. Drucker, S. Healy, K. Heim, Z. Yang, M.R. Scheinfein, *Appl. Phys. Lett.* 64(8), 1036 (1993).
- 1 Scanning Transmission Electron Microscopy of Thin Magnetic Films, M. Mankos, J.M. Cowley, R.V. Chamberlin, M.R. Scheinfein, M.B. Stearns, *IEEE Trans. MAG*-30(2), 720 (1994).

#### Conference Prodeedings and Extended Abstracts

- 10 Part of the article (39-40 and Fig. 6) in "Micromagnetic Microscopy and Modeling," E. Dan Dahlberg, J-G. Zhu, *Physics Today*, April, 34-40 (1995).
- 9 Quantitative Micromagnetics: Electron Holography of Magnetic Thin Films and Multilayers, Marian Mankos, M.R. Scheinfein, J.M. Cowley *Intermag-95 Digest*, San Antonio, Texas, 19 April 1995.
- 8 Nanomagnetometry: Electron Holography of Small Particles, M. Mankos, J.M. Cowley, M.R. Scheinfein, *IEEE Intermag-95 Digest*, Intermag-95, 18-21 April, 1995, San Antonio, TX.
- 7  $90^\circ$  Coupling in Co/Cu Giant Magnetoresistance Superlattices, Z.J. Yang, M.R. Scheinfein, *IEEE Intermag-95 Digest*, Intermag-95, 18-21 April, 1995, San Antonio, TX.

- 6 STEM Holography: Quantitative Characterization of Magnetic Microstructure at Nanometer Spatial Resolution, M. Mankos, M.R. Scheinfein, J.M. Cowley, Proc. of the International Workshop on Electron Holography, Oak Ridge National Laboratory, 28-31 August 1994, p. 8.3 (1994).
- 5 STEM Holography of Small Metal Particles, M. Mankos, G. Matteucci, M.R. Scheinfein, J.M. Cowley, Proceedings of ICEM-13, Paris, France, 17-22 July 1994, p. 1179.
- 4 Quantitative Investigations of Magnetic Microstructure: Electron Holography in a Scanning Transmission Electron Microscope, M. Mankos, Z.J. Yang, M.R. Scheinfein, J.M. Cowley, Proceedings of ICEM-13, Paris, France, 17-22 July 1994, p. 317.
- 3 Characterization of Magnetic Microstructure at High Spatial Resolution, M.R. Scheinfein, Proceedings of the 51<sup>st</sup> Annual Microscopy Society Of America (MSA), G. W. Bailey, Ed., (San Francisco Press, San Francisco, CA 1993) p. 5.
- 2 The Origins of High Spatial Resolution Secondary Electron Microscopy, M.R. Scheinfein, J.S. Drucker, J.K. Weiss, Proceedings of the 51<sup>st</sup> Annual Microscopy Society Of America (MSA), G. W. Bailey, Ed., (San Francisco Press, San Francisco, CA 1993) p. 766.
- 1 STEM of Order and Dynamics in Novel Magnetic Materials, M. Mankos, J.M. Cowley, R.V. Chamberlin, M.R. Scheinfein, J.D. Ayers, Proceedings of the 1<sup>st</sup> Annual Microscopy Society Of America (MSA), G. W. Bailey, Ed., (San Francisco Press, San Francisco, CA 1993) p. 1026.

#### 1.8 Degrees Granted During the Prior Grant Period

<u>Deg.</u>	<u>Student's Name</u>	<u>Graduation Date</u>	<u>Current Employment</u>
Ph.D.	Kevin Heim	December 1994	Jet Propulsion Laboratory, California Institute of Technology, Staff Scientist
Ph.D.	Marian Mankos	December 1994	IBM Thomas J. Watson Research Center, Post Doctoral Associate
Ph.D.	Zhijun Yang	December 1994	Seagate Magnetics, Minneapolis, MN, Senior Development Engineer
M.S.	Sean Healy	May 1994	M.S. Program, Computer Science and Engineering, Arizona State University

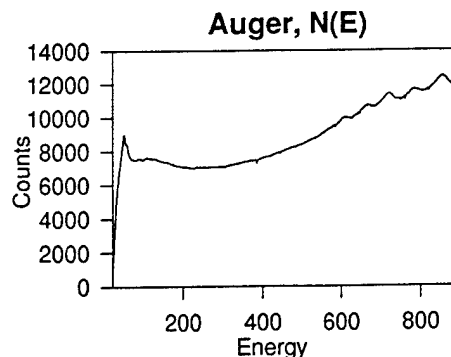
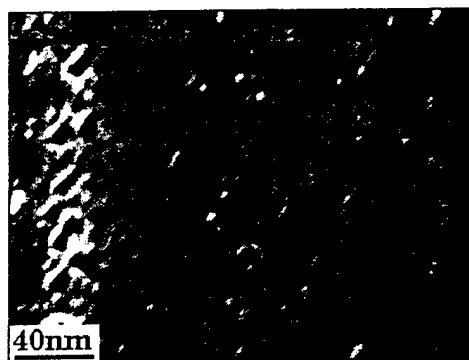
## 2.0 Continuing Research Program

Continuation of the current effort will be oriented along the same lines of inquiry established during the previous grant period. We outline below, and in the next section, specific projects to be carried out during the continuation of the grant period. We note that the original proposal provided resources for two students and one third of a post doctoral associate, or three students. This continuation proposal will support two students (we have separate support for a third student under the AASERT program, see section 6.0). The scope of this renewal proposal's continuing research goals reflects the fact that there will only be two students associated with the grant.

### 2.1 Effects on Anisotropy of Rough Interfaces Due to Site Exchange In Metal-Metal Epitaxy

Interface roughness in Co/Cu giant magnetoresistance superlattices plays an important role in determining the equilibrium magnetization orientation, the orientation during switching, and the magneto-resistance. As in many metal-metal epitaxy systems, the mobility of the evaporant and surface substrate atoms during the growth process greatly affects the magnetic and magnetoconductance properties. Although no complete theory for giant magnetoresistance exists<sup>1</sup>, it is generally accepted that electron scattering at the interfaces of the Co/Cu and in the bulk Co have some spin dependent character. Evidence for the importance of the non-magnetic-ferromagnetic interface exists<sup>2,3</sup>. It is generally thought that increased roughness decreases the GMR<sup>4,5</sup>, with the length scale of the roughness playing a more minor role. Complicated domain structure has been observed for fcc Co/Cu(100)<sup>6</sup> and hcp Co/Au(111)<sup>7</sup> using scanning electron microscopy with polarization analysis (SEMPA) with easy axes seen in Co/Cu(100) along  $\langle 110 \rangle$  directions. Susceptibility measurements<sup>8</sup> on vicinal surfaces, and anisotropy measurements<sup>9</sup> as a function of miscut angle and temperature all indicate magnetic orientation effects arising from structure, as well as roughness<sup>10</sup>.

We will complete our studies of Co/Cu(100) single bulk crystals in our UHV-STEM. This system is ideally equipped to evaluate whether: the Co grows initially as islands; the Co grows initially in bilayers; the Cu acts as a surfactant during the growth process, and how this affects the interface morphology and the resulting magnetic properties. Our initial magnetic studies of room temperature grown fcc Co/Cu(100) indicate unusual magnetic behavior near the onset of ferromagnetism near 1.5 ML. In Figs. 2.2.2 and 2.2.2, two examples of Co films on Cu(100) near the ferromagnetic transition are shown. Both films show rectangular vacancy islands<sup>11</sup> which follow crystallographic axes. These are possible sources for Cu migration. The difference in polar coercive field appears to be related to film roughness and/or sample history. The 1.5 ML film is much rougher due to incomplete Co removal or intermixing during previous sputter/anneal cycles. Further studies will be oriented towards clarifying these issues.



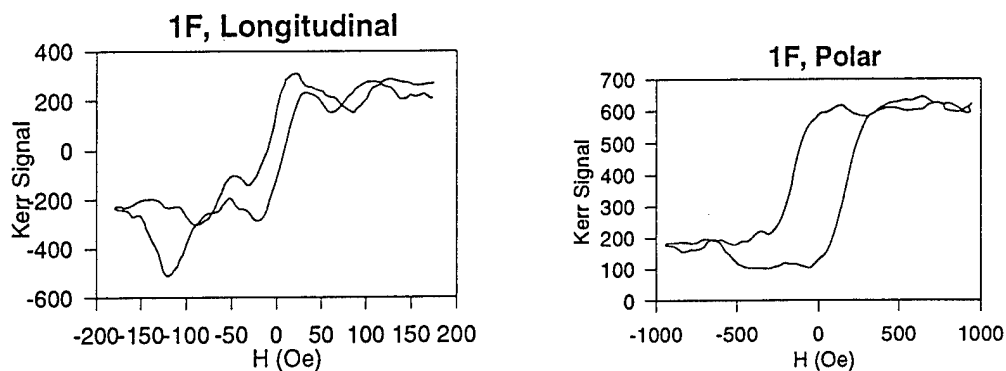


Fig. 2.1.1 : 1.5 ML of room temperature grown Co/Cu(100) show the surface morphology, the Auger electron spectrum, and the longitudinal and polar Kerr signals.

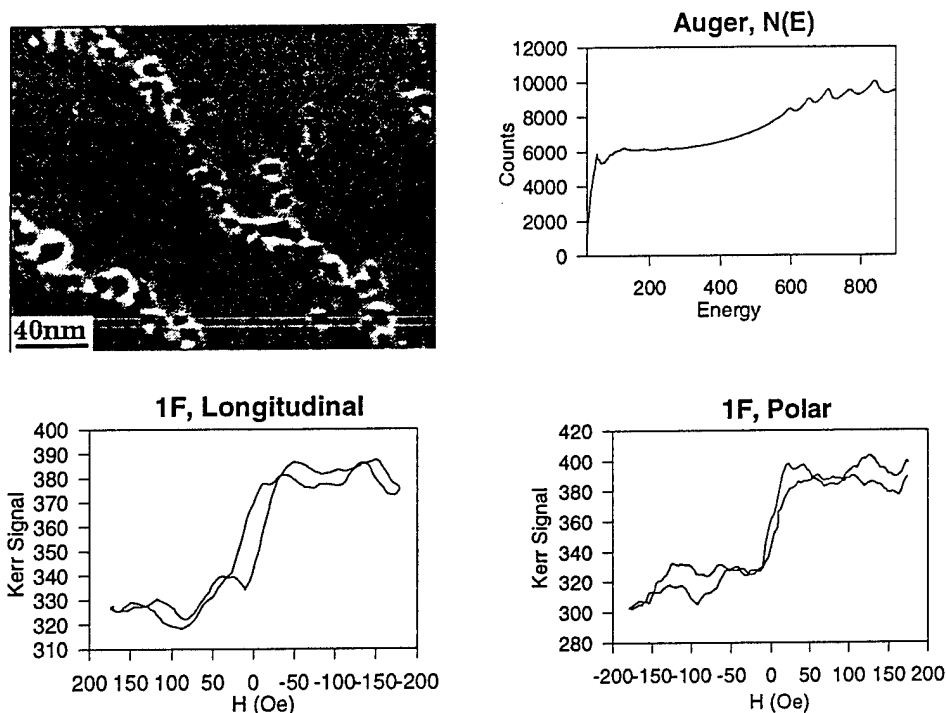


Fig. 2.1.2 : 1.8 ML of room temperature grown Co/Cu(100) show the surface morphology, the Auger electron spectrum, and the longitudinal and polar Kerr signals.

<sup>1</sup> P.M. Levy, J. Mag. Mag. Mat. **14-144**, 485 (1995).

<sup>2</sup> S.S.P. Parkin, Phys. Rev. Lett. **71**, 1641 (1993).

<sup>3</sup> K.P. Willock et. al, J. Mag. Mag. Mat. **140-144**, 585 (1995).

<sup>4</sup> G.R. Harp et. al, Phys. Rev. **B47**, 8721 (1993).

<sup>5</sup> T. Thomson, P.C. Riedl, D. Greig, Phys. Rev. **B50**, 10319 (1994).

<sup>6</sup> H.P. Oepen, M. Benning, H. Ibach, C.M. Schneider, J. Kirschner, J. Mag. Mag. Mat. **86**, L137 (1990).

<sup>7</sup> M. Speckmeann, H.P. Oepen, H. Ibach, Phys. Rev. Lett. **75**(10), 2035 (1995).

<sup>8</sup> W. Wulfhekkel, S. Knappmann, B. Gehring, H.P. Oepen, Phys. Rev. **B50**(21), 16074 (1994); A. Berger, S. Knappmann, H.P. Oepen, J. Appl. Phys. **75**(10), 5598 (1994); H.P. Oepen, S. Knappmann, W. Wulfhekkel, J. Mag. Mag. Mat. **148**, 90 (1995).

<sup>9</sup> A. Berger, U. Linke, H.P. Oepen, Phys. Rev. Lett. **68**(6), 839 (1992); H.P. Oepen, A. Berger, C.M. Schneider, T. Reul, J. Kirschner, J. Mag. Mag. Mat. **121**, 490 (1993); P. Krams, F. Laukas, R.L. Stamps, B. Hillebrands, G. Guntherot, Phys. Rev. Lett. **69**(25), 3674 (1992);

<sup>10</sup> M.T. Kief, G.J. Mankey, R.F. Willis, J. Appl. Phys. **69**(8), 5000 (1991).

<sup>11</sup> A.K. Schmid et al, Phys. Rev. **B48**, 2855 (1993).

## 2.2 Epitaxy on Electron Beam Sensitive Inorganic Halide Resists on Si Substrates

The epitaxial growth of nanopatterned ferromagnets on an insulating substrate will provide an ideal test structure to examine coupling interactions at mesoscopic length scales. Our preliminary work on this topic was briefly summarized in sections 1.3 and 1.4 above. In those studies we observed unusual coupling between closely spaced, mesoscopic sized ferromagnets, coupling between superparamagnetic moments through noble metal overlayers, evidence for long range dipolar interactions between arrays of closely spaced particles, selective nucleation and growth on electron beam damaged regions, and unusually short diffusion lengths on surfaces of inorganic halides.

The success of nanopattern definition through electron beam irradiation and selective epitaxy relies on increasing the diffusion length on the surface to a length scale on the order of the pattern spacing. The nucleation density of Fe/CaF<sub>2</sub>/Si(111) was about  $8 \times 10^{12}/\text{cm}^2$ , unusually high. This indicates that there is a nucleation event for a single adatom on roughly one of every 100 atomic surface sites, and a spacing of nucleation sites on the surface on the order of 2 nm. Our efforts at pattern definition were initially aimed at fabricating structures on the order of 10 nm since thermal effects destabilize the magnetization in the 2 nm regime. Although the unique cause of the extremely high, temperature independent nucleation density is not known, we postulate that either site defects, or chemical reactivity is responsible. We are currently

Fig. 2.2.1 : (LEFT COLUMN OF FIGURES) 3 ML Co on CaF<sub>2</sub>/Si(111) showing the initial island density and the superferromagnetic regime. Hysteresis loops were taken using the Surface Magneto Optic Kerr Effect (SMOKE).

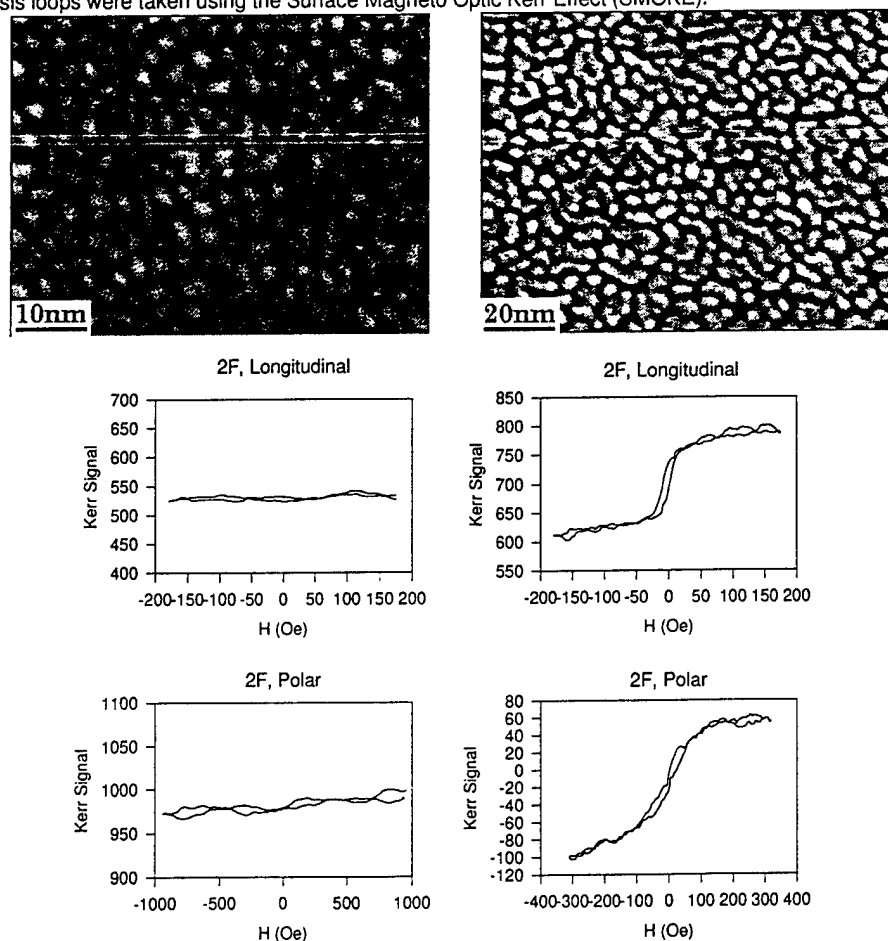


Fig. 2.2.2 : (RIGHT COLUMN OF FIGURES) 15 ML Co on CaF<sub>2</sub>/Si(111) showing the initial island density and the transition to the ferromagnetic regime. Hysteresis loops were taken using the Surface Magneto Optic Kerr Effect (SMOKE).

exploring nucleation and growth models to further analyze our data. If chemical reactivity (chemical compound formation with fluorine) is responsible, we should be able to increase the diffusion lengths by moving rightward on the period table, or selecting a chlorine based halide insulator. We have made initial studies on the deposition of Co/CaF<sub>2</sub>/Si(111) in order to test this line of inquiry which are shown in Figs. 2.2.1 and 2.2.2 (previous page) for 3 ML and 15 ML of Co deposited on CaF<sub>2</sub>/Si(111). The magnetic properties are similar to the Fe/CaF<sub>2</sub>/Si(111) system with subtle differences arising from the increased (as expected) island spacing in this system. We summarize the differences between the island density, coverage and island size for Co/CaF<sub>2</sub>/Si(111) and Fe/CaF<sub>2</sub>/Si(111) in Fig. 2.2.3 below. The trends indicate that we are moving in the right direction.

We plan to continue to increase the diffusion lengths in the transition metal on CaF<sub>2</sub>/Si(111) system. Additional studies will utilize other inorganic halide insulators as substrates. Although we have not stressed the magnetoconductance properties of heterogeneous GMR structure, all of these systems are excellent candidates for 2-D GMR. Our initial efforts at passivation with Ag were unsuccessful. The next grant period will see other alternatives explored for (conducting) passivation layers including Cu, or perhaps Au. The GMR measurements will be conducted *ex situ* in a high field EPR magnet.

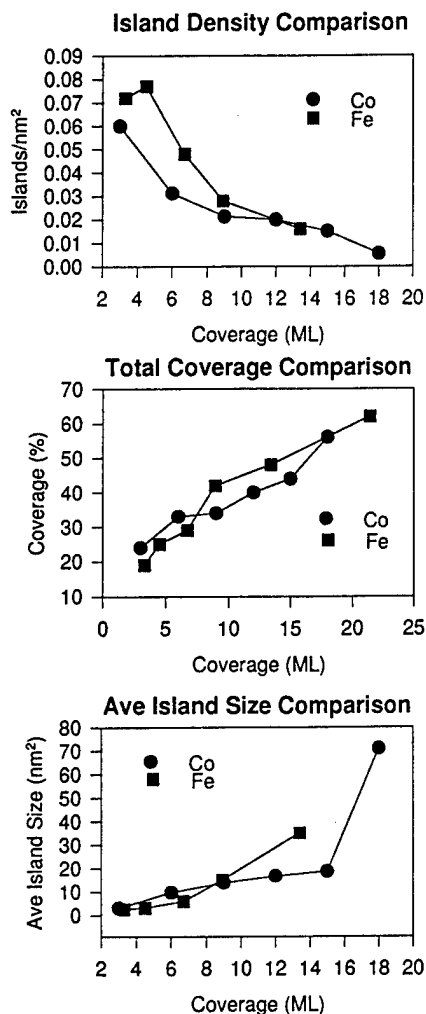


Fig. 2.2.3: Comparison of island statistics of Co/CaF<sub>2</sub>/Si(111) with previous work done on Fe/CaF<sub>2</sub>/Si(111). The transition to the ferromagnetic regime occurs at about the same coverage for both systems (~14ML). At low coverage, Co forms islands that are more widely separated. This may be due to higher mobility, less reactivity, or fewer pinning sites.

### 2.3 Self-Organization: Anisotropy at Step Edges and Two-Dimensional Magnetoresistance

Our experience with two dimensional arrays of closely spaced ferromagnetic particles (section 1.3 and 1.4 above) indicates that long range order can be achieved with uniaxial anisotropy or superferromagnetic coupling. This makes such arrays ideal candidates for 2-D heterogeneous GMR structures. The usually high GMR values obtainable with heterogeneous 3-D systems may be greatly enhanced in ordered 2-D systems, especially if the magnetic order can be arranged antiferromagnetically rather than superparamagnetically. The high saturation fields typical in heterogeneous alloy GMR devices prevents taking full advantage of the unusually high GMR values for applications in sensors, heads and memory elements. However, with suitably small anisotropy, long range anti-ferromagnetic ordering between lines of particles is possible. In order to exploit such a system as a 2-D GMR device, the lines (or linear array of particles) must be spaced by several nm along well oriented directions, have small enough anisotropy such that switching fields are low, yet large enough anisotropy to stabilize a particle array against thermal fluctuations. We propose to explore several different systems in an attempt to realize such an arrangement.

The simplest way to achieve such structures is through self-organization (or smart materials) since no overhead need be paid in time for 'creating' the structures (at such high island densities, the overhead for repeatedly and accurately writing macroscopic arrays of structures can become daunting in a research environment). Our earlier work on Fe/CaF<sub>2</sub>/Si(111) indicated some preferential nucleation at step edges. However, since the nucleation density was so high, little, if any line formation occurred. Initial experiments will involve epitaxy on highly miscut insulating surfaces in the ferro-magnetic/insulating inorganic halide system with suitably long surface diffusion lengths (see section 2.2).

A second approach will utilize directional evaporation on highly misoriented and miscut surfaces. The preliminary work on this system will be done by Dr. Akira Sugarawa, a self-supporting, visiting Post Doctoral Fellow from Tokyo Institute of Technology. We will utilize step band terraces on NaCl (110) surfaces as the template and perform shadow evaporation to form lines. The spacing between, and depth of the troughs can be modified through high temperature annealing. In this way, the aspect ratio of the structures can be manipulated. In this experiment, we want the evaporant to stick where it lands, hence the extremely short diffusion length for transition metals on CaF<sub>2</sub> is now a salient feature. Since CaF<sub>2</sub> grows readily on NaCl, a pre-evaporation of CaF<sub>2</sub> may be necessary to define the desired structures. Initial experiments will occur off-line (not in the UHV STEM/SEM). Transmission electron microscope replicas will be fabricated for initial assessment of the epitaxial relationship between evaporant and substrate. Surface analysis will initially be performed *ex situ* in a commercial SEM.

Once a satisfactory approach has been established off line, *in situ* experiments will be performed to closely characterize the physical, morphological, chemical and magnetic properties of the surfaces. Structures will be passivated with overcoats of CaF<sub>2</sub>, removed from the UHV ambient, and their magnetic properties examined with SQUID and magnetoresistance measurements.



## 2.4 UHV STM-SEM with Reflection Electron Energy Loss Spectroscopy

In order to access atomic and intermediate length scales simultaneously for the studies cited above, we have designed and built a UHV STM-SEM system. This instrument has been built with cost share funds allocated by Arizona State University. The chamber was furnished through a grant from the Division of Materials Research at the National Science Foundation for the production and testing of point source electron emitters. One student will be completely dedicated to studies in this instrument.

The performance of the *in situ* UHV-SEM has been optimized for low-voltage (surface sensitivity) and high current (spectroscopy and polarimetry). The predicted operating characteristics of the SEM are shown below in Fig. 2.4.1, with a schematic shown in Fig. 2.4.2. Three electron optical columns were built out of Ti in our mechanical instrument shop. Note that the working distance of the gun is extremely long. This is a requirement in order for the SEM and STM to have simultaneous access to the surface. In this regime, chromatic aberrations dominate for all but the smallest apertures.

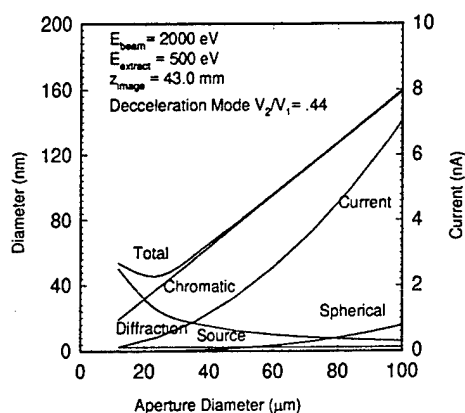


Fig. 2.4.1 : Electron optical properties of the *in situ* mini SEM for simultaneous STM-SEM-EELS operation, and later SEMPA.

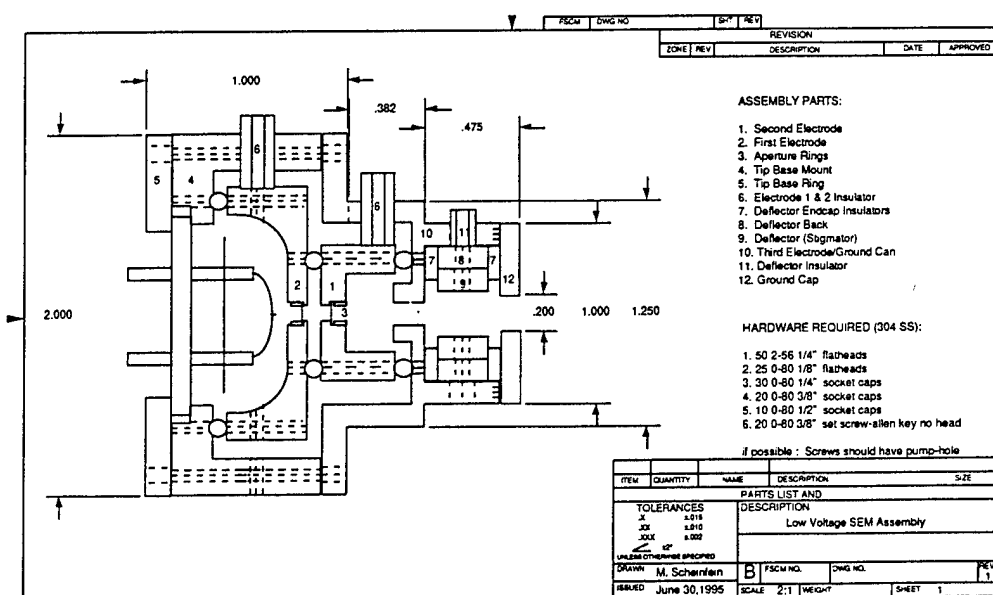


Fig. 2.4.2 : Schematic of the high performance, long focal length, *in situ* SEM. It is only two inches long and two inches across.

The layout configuration has been optimized for simultaneous scanning electron microscopy, scanning tunneling microscopy and reflection electron energy loss spectroscopy. The SEM detection is performed with a four quadrant anode coupled to a dual thin profile channel plate assembly. This will allow us to evaluate low voltage magnetic type II contrast as well as perform pure SEM. The channel plate has a hole in its center to allow the reflected beam to enter an electrostatic analyzer. Reflection electron energy loss spectroscopy of core edges is characterized by EXELS oscillations. These oscillations contained reflected partial waves from neighboring atoms and allow, with some data analysis, for the nearest neighbor distances between atomic sites to be determined. This is very important when looking at surfaces since surface relaxation can greatly effect the magnetic properties. In addition, the characteristic loss peak gives chemical specificity to the structural determination such interface mixing can be examined on the length scale of the incident probe diameter. The layout of the system from the vantage point of the sample is shown in Fig. 2.4.3 below. We expect the instrument to be operational by the beginning of the continuation grant period.

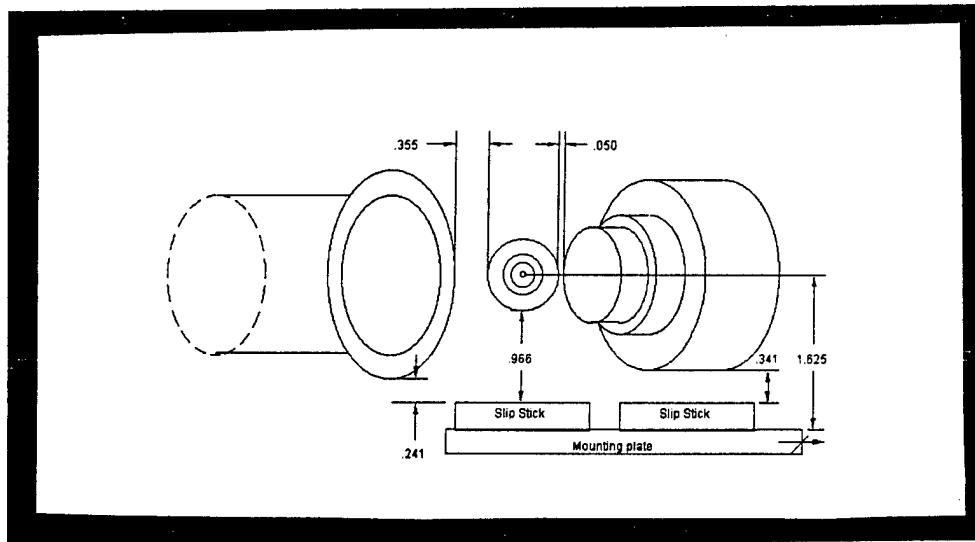


Fig. 2.4.3: The SEM is shown at right as seen from the vantage point behind the sample. The STM is in the center, and the EELS spectrometer is located at the far left. On the front of the EELS spectrometer extraction optics snout is the quadrant channel plate.

### 3.0 Spin Polarization Analysis in the UHV STM-SEM

The principle of scanning electron microscopy with polarization is well known and shown schematically in Fig. 3.1. A beam of unpolarized electrons is scanned across a sample's surface. The polarized electrons excited from the surface of a ferromagnet can be collected by some collection electron optical column, and focused onto a spin polarimeter, which is usually a high Z target, such as Au, where a left-right asymmetry scattering gives the polarization. This technique, pioneered by the electron physics group at NIST is well known and documented.

Both principal investigators on this grant worked with the electron physics group on SEMPA at NIST and are well suited to implement SEMPA at ASU. We intend to add a low-energy diffuse scattering electron-spin polarimeter to the UHV SEM-STM apparatus in year two of the continuation grant period. The complications in extraction electron optics, shown in Fig. 3.2 for our apparatus while at NIST can be greatly simplified with placement of the detector within the vacuum chamber. Our implementation will place the detector within the chamber necessitating only a single zoom lens for electron focusing, and a single deflection electrode pair for descanning. The technology for building the detector will mirror that implemented in the Brookhaven experiment, the schematic of which is shown in Fig. 3.3.

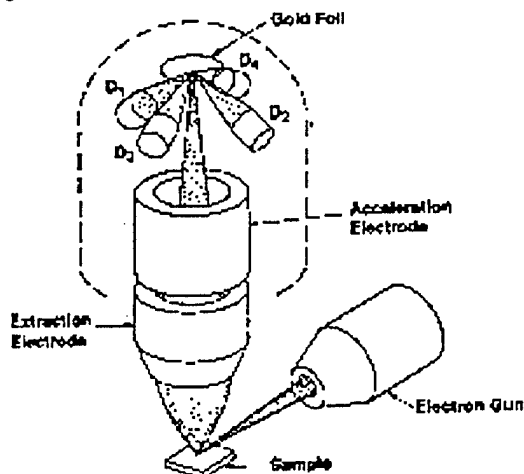


Fig. 3.1 A generic scanning electron microscopy with polarization analysis configuration requires an electron gun, extraction electron optics, and a spin-dependent scattering target, indicated here as a gold foil. (Extracted from Secheinfein et. al in Rev. Sci. Instrum. 61(10), 2501 (1990).)

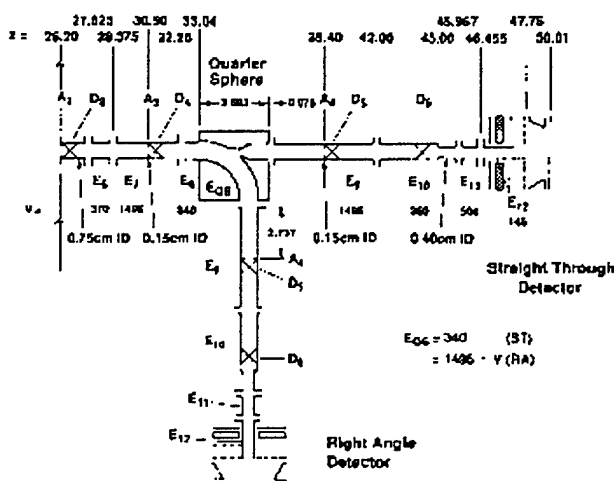


Fig. 3.2 Transport optics required in a SEMPA system which houses the detector outside of the vacuum chamber are necessarily complicated in order to transport the low energy beam. This example is taken from the system that we implemented at NIST for the transport optics. Our system, will be *in situ*, and will be comprised of the detector and electrodes  $E_{10}$  and  $E_{11}$  only. (Extracted from Secheinfein et. al in Rev. Sci. Instrum. 61(10), 2501 (1990).)

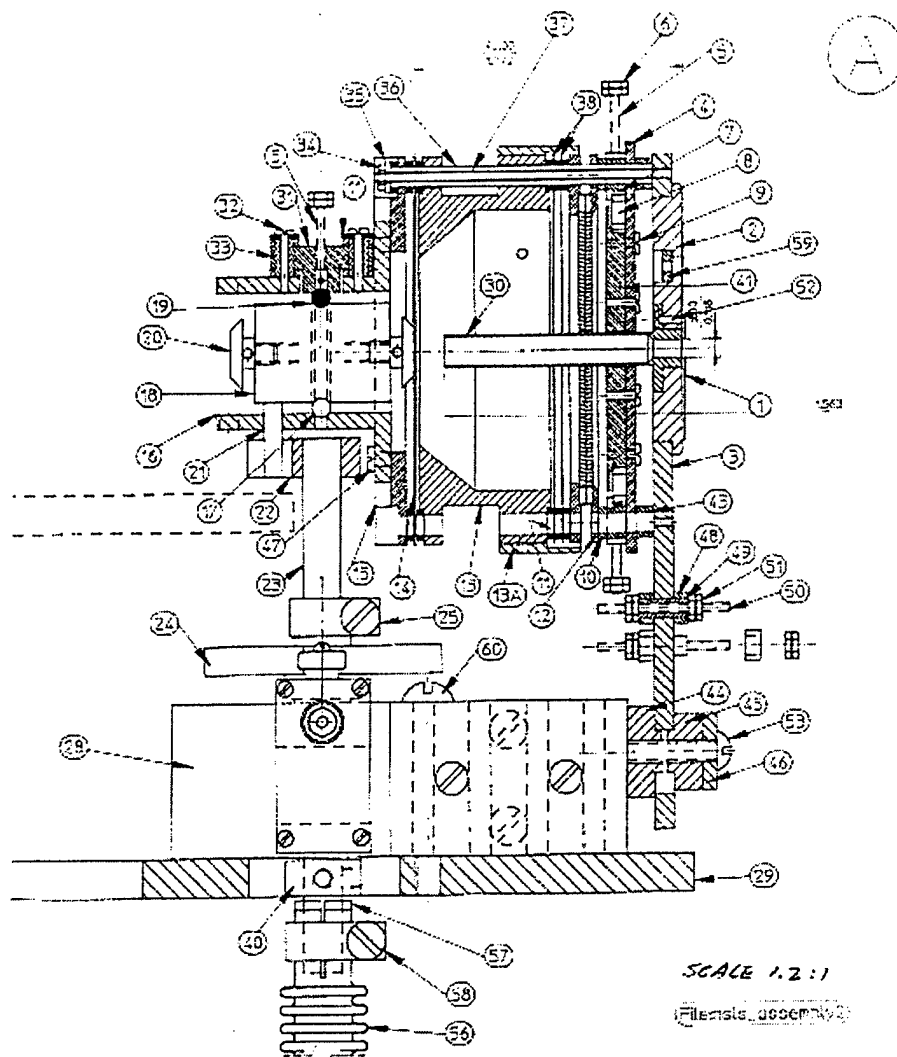


Fig. 3.3 Machine drawing of the spin-polarimeter that we will implement in our system. It is the same design that we built for the beamline at Brookhaven National Labs. ( Drawing from Bernie Wacklewski, formerly of the Electron Physics Group at NIST). See Johnson et. al. Rev. Sci. Instrum. **63**(3), 1902 (1992).

Our experiments using SEMPA will be undertaken on the systems described in sections 2.1-2.3 with an eye towards utilizing the simultaneous magnetic-SEMPA, STM and SEM results to correlate physical microstructure with magnetic microstructure.

#### 4.0 Biographies

### BIOGRAPHY OF MICHAEL R. SCHEINFELD

**Citizenship:** United States

**Birth Date:** March 24, 1958

**Education:**

- Ph. D. (1985) Applied and Engineering Physics, Cornell University, Ithaca, NY.
- M.S. (1982) Applied and Engineering Physics, Cornell University, Ithaca, NY.
- B.S. (1980) Electrical Engineering and Computer Science, MIT, Cambridge, MA.

**Professional Activities:**

American Physical Society, Materials Research Society, Microscopy Society of America.

**Experience:**

- 07/91 - Present Associate Professor, Department of Physics and Astronomy, Arizona State University, Tempe, AZ. Tenure granted April 1995.
- 10/90 - 07/91 Associate Research Scientist, Center for Solid State Science, Arizona State University, Tempe, AZ.
- 08/87 - 09/90 Staff Physicist, Electron Physics Group, National Institute of Standards and Technology, Gaithersburg, MD.

#### SCIENTIFIC PUBLICATIONS (1993-present)

- Two-Dimensional Long-Range Coupling : Enhanced Superparamagnetism in Two-Dimensional Arrays of Nanometer Sized Fe Islands, M.R. Scheinfein, K.E. Schmidt, K.R. Heim, G.G. Hembree, Appl. Phys. Lett. (in press-1995).
- Long Range Order and Coupling in Two-Dimensional Arrays of Nanometer Size Superparamagnets, M.R. Scheinfein, K.E. Schmidt, K.R. Heim, G.G. Hembree, Phys. Rev. Lett. (submitted-1995).
- Magnetic and Structural Characterization of Ultrathin Fe Films on  $\text{CaF}_2/\text{Si}(111)$ : Superparamagnetic and Ferromagnetic Behavior of Nanometer Sized Particles, K.R. Heim, G.G. Hembree and M.R. Scheinfein, J. Mag. Mag. Mat. (submitted - 1995).
- Interfacial Roughness Effects on Giant Magnetoresistance and Interlayer Coupling in Co/Cu Superlattices, Z.J. Yang and M.R. Scheinfein, Phys. Rev. **B52**(6), 4263 (1995).
- An Alternative Approach For Magneto-Optic Calculations Involving Layered Media, K.R. Heim, M.R. Scheinfein, J. Mag. Mag. Mat. (in press - 1995).
- Scanning Electron Microscopy With Polarization Analysis (SEMPA), J. Unguris, M.R. Scheinfein, M.H. Kelley, A. Gavrin, R.J. Celotta, D.T. Pierce, in *Handbook of Electron Microscopy*, edited by S. Amelinckx, D. Van Dyck, J.F. Van Landuyt, G. Van Tendeloo, (VCH Verlagsgesellschaft mbH, Weinheim, 1995).
- Absolute Magnetometry Using Electron Holography: Magnetic Superlattices and Small Particles, Marian Mankos, J.M. Cowley, M.R. Scheinfein, Material Research Society Bulletin, (in press-1995).
- Quantitative Micromagnetics: Electron Holography of Magnetic Thin Films and Multilayers, Marian Mankos, M.R. Scheinfein, J.M. Cowley, IEEE Trans. **MAG** (in press-1995).
- 90° Domains and Coupling in Co/Cu Giant Magnetoresistance Superlattices, Z.J. Yang, M.R. Scheinfein, IEEE Trans. **MAG** (in press-1995).
- Nanomagnetometry: Electron Holography of Small Particles, M. Mankos, J.M. Cowley, M.R. Scheinfein, IEEE Trans. **MAG** (in press-1995).
- Quantitative Micromagnetics at High Spatial Resolution Using Electron Holography, M. Mankos, J.M. Cowley, M.R. Scheinfein, phys. stat. sol.(a), (submitted-1995).
- Electron Holography of P-N Junctions, M.R. McCartney, B. Frost, R. Hull, M.R. Scheinfein, D.J. Smith, E. Voelkl, in *Electron Holography*, Delta Series, eds. A. Tonomura, L. Allanrd, G. Pozzi, D. Joy, Y. Ono, Elsevier Science BV, 189-198, (1995).
- STEM Holography of Magnetic Materials, M. Mankos, P. de Haan, V. Kambersky, G. Matteucci, M.R. McCartney, Z.J. Yang, M.R. Scheinfein, J.M. Cowley, in *Electron Holography*, Delta Series, eds. A. Tonomura, L. Allanrd, G. Pozzi, D. Joy, Y. Ono, Elsevier Science BV, 329-341, (1995).
- Magnetoresistance, M.R. Scheinfein, in *Macmillan Encyclopedia of Physics*, Macmillan Press, (1995).
- 90° Domains in Co/Cu Giant Magnetoresistance Superlattice, Z.J. Yang, M.R. Scheinfein, Appl. Phys. Lett. **66**(2), 236 (1995).

- A Low Cost Preamplifier for Fast Pulses from Microchannel Plates, S.T. Coyle, G.G. Hembree, M.R. Scheinfein, Rev. Sci. Instrum. **66**(7), 4000 (1995).
- Absolute Magnetometry of Thin Cobalt Films and Co/Cu Multilayer Structures at Nanometer Spatial Resolution, Marian. Mankos, Z.J. Yang, M.R. Scheinfein, J.M. Cowley, IEEE-Trans. MAG **30**(6), 4497 (1994).
- Far Out-of-Focus Electron Holography in a Dedicated FEG STEM, M. Mankos, A.A. Higgs, M.R. Scheinfein, J.M. Cowley, Ultramicrosc. **58**, 87 (1995).
- A Picosecond Electron Gun For Surface Analysis, M. Aeschlimann, E. Hull, C.A. Schmuttenmaer, J. Cao, L.G. Jahn, Y. Gao, H.E. Elsayed-Ali, D.A. Mantell, M.R. Scheinfein, Rev. Sci. Instrum. **66**(2), 1000 (1995).
- Evaluation of CoCrTaPt Alloy For Longitudinal Magnetic Recording, Y. Cheng, M. Sedighi, I. Lam, R. Gardener, Z.J. Yang, M.R. Scheinfein, J. Appl. Phys. **75**(10), 6138 (1994).
- Absolute Magnetometry At Nanometer Spatial Resolution : STEM Holography Of Thin Cobalt Films, M. Mankos, M.R. Scheinfein, J.M. Cowley, J. Appl. Phys. **75**(11) 7418 (1994).
- Ultra High Vacuum Scanning Electron Microscopy Characterization of the Growth of Fe on  $\text{CaF}_2/\text{Si}(111)$ : Selective Nucleation on Electron-Beam Modified Surfaces, K.R. Heim, G.G. Hembree, M.R. Scheinfein, J. Appl. Phys. **76**(12), 8105 (1994).
- Structural and Magnetic Properties of Epitaxially Grown fcc Fe/Cu(100) and Fe/ $\text{CaF}_2/\text{Si}(111)$ , M.R. Scheinfein, S.D. Healy, K.R. Heim, Z.J. Yang, J.S. Drucker, G.G. Hembree, Proc. Mat. Res. Soc. vol. **332**, *Determining Nanoscale Properties of Materials by Microscopy and Spectroscopy*, eds. M. Isaacson, M. Sarikaya, K. Wickramasinghe, 473 (1994).
- Surface Magnetization Processes Investigated by the Combined Surface Magneto-Optical Kerr Effects in fcc Fe/Cu(100) Thin Films, Z.J. Yang, S.D. Healy, K.R. Heim, J.S. Drucker, G.G. Hembree, M.R. Scheinfein, J. Appl. Phys. **75**(10), 5589 (1994).
- The Initial Phases of Epitaxy of fcc Fe/Cu(100): Supersurface and Subsurface Island Formation, S.D. Healy, K.R. Heim, Z.J. Yang, J.S. Drucker, G.G. Hembree, M.R. Scheinfein, J. Appl. Phys. **75**(10), 5592 (1994).
- Combined Three-Axis Surface Magneto-Optical Kerr Effects in the Study of Surface and Ultrathin Film Magnetism, Z.J. Yang, M.R. Scheinfein, J. Appl. Phys. **74**(11) 6810 (1993).
- Correlations Between Ultrathin Film Microstructure and Magnetic Properties in Epitaxial Films of fcc Fe/Cu(100), K.R. Heim, S.D. Healy, Z.J. Yang, J.S. Drucker, G.G. Hembree, M.R. Scheinfein, J. Appl. Phys. **74**(12), 7422 (1993).
- Field Induced Metastable States in Ultrathin Films of fcc Fe/Cu(100), G.G. Hembree, J.S. Drucker, S. Healy, K. Heim, Z. Yang, M.R. Scheinfein, Appl. Phys. Lett. **64**(8), 1036 (1993).
- Time Aberrations of Uniform Fields: An Improved Reflectron Mass Spectrometer for an Atom Probe Field Ion Microscope, M.R. Scheinfein, D.N. Seidman, Rev. Sci. Instrum., **64**(11), 3126 (1993).
- Scanning Transmission Electron Microscopy of Thin Magnetic Films, M. Mankos, J.M. Cowley, R.V. Chamberlin, M.R. Scheinfein, M.B. Stearns, IEEE Trans. MAG-**30**(2), 720 (1994).
- Micromagnetic Structure of Domains in Co/Pt Multilayers - Part A: Investigations of Wall Structure, R. Ploessl, J.N. Chapman, M.R. Scheinfein, J.L. Blue, M. Mansuripur, H. Hoffman, J. Appl. Phys. **74**(12), 7431 (1993).
- Electron Coincidence Spectroscopy Study of Secondary and Auger Electron Generation Mechanisms, J.S. Drucker, M.R. Scheinfein, J.Y. Liu, J.K. Weiss, J. Appl. Phys. **74**(12), 7329 (1993).
- Brightness Measurements of nanometer Sized Field Emission Electron Sources, W. Qian, M.R. Scheinfein, J.C.H. Spence, J. Appl. Phys. **73**(11), 7041 (1993).
- The Origins Of High Spatial Resolution Secondary Electron Microscopy, M.R. Scheinfein, J.S. Drucker, J.K. Weiss, J. Lui, G.G. Hembree, J.M. Cowley, Materials Research Society Symposium, Materials Research Society, **295**, 253 (1993).
- Secondary Electron Generation Studied by Momentum Resolved Electron Coincidence Spectroscopy, J.S. Drucker, M.R. Scheinfein, Phys. Rev. **B47**(23), 15973 (1993).
- Electron Optical Properties of Nanometer Field Emission Electron Sources, W. Qian, M.R. Scheinfein, J.C.H. Spence, Appl. Phys. Lett. **62**(3), 315 (1993).

Aberrations of Subnanometer Field Emission Electron Sources, M.R. Scheinfein, W. Qian, J.C.H. Spence, J. Appl. Phys. **73**(5), 2057 (1993).

Secondary Electron Production Pathways By Fast Incident Electrons, M.R. Scheinfein, J.S. Drucker, Phys. Rev. **B47**(7), 4068 (1993).

Correlations of Modulation Noise with Magnetic Microstructure, Transition Parameter and RMS Transition Variation For CoCrTa and CoNi Thin Film Media, M.R. Kahn, B. Marchon, D. Spiliotis, M. Scheinfein, J. Mag. Mag. Mat. **120**, 310 (1993).

Slow Magnetic Relaxation in Iron, R.V. Chamberlin, M.R. Scheinfein, Science **260**, 1098 (1993).

#### **CONFERENCE PROCEEDINGS AND EXTENDED ABSTRACTS : SCIENTIFIC PUBLICATIONS (1993-present)**

Part of the article (39-40 and Fig. 6) in "Micromagnetic Microscopy and Modeling," E. Dan Dahlberg, J-G. Zhu, Physics Today, April, 34-40 (1995).

Differential Phase Contrast in TEM For Magnetic Microstructure Observation, P. Kruit, A.H. Buist, M.R. McCartney, M.R. Scheinfein, Proceedings of the 53<sup>rd</sup> Annual Microscopy Society Of America (MSA), G. W. Bailey, Ed., (San Francisco Press, San Francisco, CA 1995).

Quantitative Micromagnetics: Electron Holography of Magnetic Thin Films and Multilayers, Marian Mankos, M.R. Scheinfein, J.M. Cowley Intermag-95 Digest, San Antonio, Texas, 19 April 1995.

Nanomagnetometry: Electron Holography of Small Particles, M. Mankos, J.M. Cowley, M.R. Scheinfein, IEEE Intermag-95 Digest, Intermag-95, 18-21 April, 1995, San Antonio, TX.

90° Coupling in Co/Cu Giant Magnetoresistance Superlattices, Z.J. Yang, M.R. Scheinfein, IEEE Intermag-95 Digest, Intermag-95, 18-21 April, 1995, San Antonio, TX.

Holography of P-N Junction, M.R. McCartney, R. Hull, J.C. Bean, E. Voelkl, B. Frost, M.R. Scheinfein, D.J. Smith, Proc. of the International Workshop on Electron Holography, Oak Ridge National Laboratory, 28-31 August 1994, p. 9.3 (1994).

STEM Holography: Quantitative Characterization of Magnetic Microstructure at Nanometer Spatial Resolution, M. Mankos, M.R. Scheinfein, J.M. Cowley, Proc. of the International Workshop on Electron Holography, Oak Ridge National Laboratory, 28-31 August 1994, p. 8.3 (1994).

Low-Voltage Nanometer-Size Field Emission Sources, W. Qian, M.R. Scheinfein, J.C.H. Spence, Proceedings of the Microbeam Analysis Society (MAS), Ed. John Friel, New Orleans, LA July 31-August 5, 1994, p. 129-130 (1994).

STEM Holography of Small Metal Particles, M. Mankos, G. Matteucci, M.R. Scheinfein, J.M. Cowley, Proceedings of ICEM-13, Paris, France, 17-22 July 1994, p. 1179.

Quantitative Investigations of Magnetic Microstructure: Electron Holography in a Scanning Transmission Electron Microscope, M. Mankos, Z.J. Yang, M.R. Scheinfein, J.M. Cowley, Proceedings of ICEM-13, Paris, France, 17-22 July 1994, p. 317.

SIMS Input Lens, R.L. Gerlach, M.R. Scheinfein, G.A. Crow, M. Utlaut, C. Bickford, Proceedings of the International Journal of Optical Engineering, **SPIE** vol. 2024, 149 (1993).

Characterization of Magnetic Microstructure at High Spatial Resolution, M.R. Scheinfein, Proceedings of the 51<sup>st</sup> Annual Microscopy Society Of America (MSA), G. W. Bailey, Ed., (San Francisco Press, San Francisco, CA 1993) p. 5.

Brightness Measurements of Nanometer Sized Field Emission Tips, M.R. Scheinfein, W. Qian, J.C.H. Spence, Proceedings of the 51<sup>st</sup> Annual Microscopy Society Of America (MSA), G. W. Bailey, Ed., (San Francisco Press, San Francisco, CA 1993) p. 632.

The Origins of High Spatial Resolution Secondary Electron Microscopy, M.R. Scheinfein, J.S. Drucker, J.K. Weiss, Proceedings of the 51<sup>st</sup> Annual Microscopy Society Of America (MSA), G. W. Bailey, Ed., (San Francisco Press, San Francisco, CA 1993) p. 766.

STEM of Order and Dynamics in Novel Magnetic Materials, M. Mankos, J.M. Cowley, R.V. Chamberlin, M.R. Scheinfein, J.D. Ayers, Proceedings of the 1<sup>st</sup> Annual Microscopy Society Of America (MSA), G. W. Bailey, Ed., (San Francisco Press, San Francisco, CA 1993) p. 1026.

Magnetic Force and Force Gradient Microscopy Utilizing An Ultra-Sensitive Vertical Cantilever Geometry, A. DiCarlo, M.R. Scheinfein, R.V. Chamberlin, Scanning Probe Microscopies II, ed. C. Williams, Proceedings SPIE-1855, 187 (1993).

#### **GRADUATE STUDENT SUPERVISION**

Degrees :	Ph.D.	Kevin Heim	December 1994
		Marian Mankos	December 1994
		Zhijun Yang	December 1994
	M.S.	Sean Healy	May 1994
Supervision:		Doug Bradley	June 1994 -
		Steve Coyle	June 1993 -
		Dan Waters	June 1995 -
		Eugene Bullock	June 1995 -
		Dmitri Streblencko	June 1995-
Post-Docs:		Zhijun Yang	January 1995-June 1995
		Akira Sugarawa	March 1995- (Jointly with J. Venables and G. Hembree)



## BIOGRAPHY OF GARY G. HEMBREE

<u>Education:</u>	1971 B.A.	Applied Physics, University of California San Diego, California
	1979 Ph.D.	Physics, Arizona State University Tempe, Arizona
<u>Positions Held:</u>	1979-1981	NRC Postdoctoral Fellow
	1981-1986	Physicist Center for Manufacturing Engineering National Bureau of Standards Gaithersburg, Maryland
	1986-1990	Research Specialist
	1990-1994	Associate Research Scientist
	1995-Present	Senior Research Scientist Department of Physics and Astronomy Arizona State University Tempe, Arizona
<u>Honors:</u>	1979-1981	NRC Postdoctoral Fellow
	1986	IR 100 Award Co-recipient
<u>Society Memberships:</u>		Microscopy Society of America Microbeam Analysis Society American Vacuum Society Sigma Xi

### Previous Research Areas:

Electron microscopy and diffraction applied to surface studies (experimental). Ph.D. dissertation: "An Investigation of Crystal Surface Structure by Reflection Electron Diffraction". J. M. Cowley, Graduate Advisor.

Length metrology by electron microscopy (experimental). Instrumentation and techniques for accurate sub-micrometer length metrology. D. A. Swyt, Post-doctoral Advisor.

Secondary electron microscopy of magnetic materials (experimental). Spin polarization analysis of secondary electrons, high resolution imaging of domain walls on solid surfaces.

### Synopsis of Recent Research:

Development and application of a low energy electron spectrometer system on an ultra-high vacuum scanning transmission electron microscope. Nucleation and growth of thin films studied by surface analytic techniques. Relationship of magnetic and structural properties of thin films. Diffraction enhanced low energy electron spectroscopy as a site-selective surface analysis technique

### 1994 - 1995 Publications

G. G. Hembree, Jeff Drucker, S. D. Healy, K. R. Heim, Z. J. Yang, and M. R. Scheinfein, "Field-induced metastable states in ultrathin films of fcc Fe/Cu(100)", Appl. Phys. Lett. **64**, 1994, 1036.

Z. J. Yang, S. D. Healy, K. R. Heim, J. S. Drucker, G. G. Hembree and M. R. Scheinfein, "Surface Magnetization Processes Investigated by the Combined Surface Magneto-Optical Kerr Effects in Fe/Cu(100) Thin Films", J. Appl. Phys. **75**, 1994, 5589.

S. D. Healy, K. R. Heim, Z. J. Yang, G. G. Hembree, J. S. Drucker and M. R. Scheinfein, "The Initial Phases of Epitaxy of fcc Fe/Cu(100): Supersurface and Subsurface Island Formation", J. Appl. Phys. **75**, 1994, 5592.

K. R. Heim, G. G. Hembree and M. R. Scheinfein, "Ultra High Vacuum Scanning Electron Microscopy Characterization of the Growth of Fe on  $\text{CaF}_2/\text{Si}(111)$ : Selective Nucleation on Electron-Beam Modified Surfaces", J. Appl. Phys. **76**, 1994, 8105.

### 1994 - 1995 Contributed Papers

M. R. Scheinfein, S. D. Healy, K. R. Heim, Z. J. Yang, J. S. Drucker, G. G. Hembree, "Structural and Magnetic Properties of Epitaxially Grown FCC Fe/Cu(100) and Fe/ $\text{CaF}_2/\text{Si}(111)$ ", in Materials Research Society Symposium Proceedings, Vol.

332, *Determining Nanoscale Properties of Materials by Microscopy and Spectroscopy*, eds. M. Isaacson, M. Sarikaya, K. Wickramasinghe, 1994, 473 (Invited paper).

J. A. Venables, G. G. Hembree, J. Liu, C. J. Harland and M. Huang, "Advances in Auger Electron Spectroscopy and Imaging", in *Proc. 13th Intl. Cong. on Electron Microscopy (Paris)*, 1994, 759 (Invited paper).

Li Yun, G. G. Hembree and J. A. Venables, "Quantitative Auger Analysis of Ge Surface Segregation in Si/Ge/Si(100) Heterostructures", *Materials Research Society, Symposium D*, Boston, December 1, 1994.

#### Selected Related Publications

K. R. Heim, S. D. Healy, Z. J. Yang, J. S. Drucker, G. G. Hembree and M. R. Scheinfein, "Correlations between ultrathin film microstructure and magnetic properties for room temperature epitaxial films of fcc Fe/Cu(100)", *J. Appl. Phys.* **74**, 1993, 7422.

G. G. Hembree and J. A. Venables, "Nanometer Resolution Scanning Auger Electron Microscopy", *Ultramicroscopy* **47**, 1992, 109 (Invited paper).

J. Liu, G. G. Hembree, G. E. Spinnler and J. A. Venables, "High Resolution Auger Electron Spectroscopy and Microscopy of a Supported Metal Catalyst", *Surface Science Letters* **262**, 1992, L111.

Jeff Drucker, Mohan Krishnamurthy and Gary Hembree, "Biassed secondary electron imaging of monatomic surface steps on vicinal Si(100) in a UHV STEM", *Ultramicroscopy* **35**, 1991, 323.

G. G. Hembree, J. S. Drucker, F. C. H. Luo, M. Krishnamurthy and J. A. Venables, "Auger Electron Spectroscopy and Microscopy With Probe-size Limited Resolution", *Applied Physics Letters* **58**, 1991, 1890.

G. G. Hembree, P. A. Crozier, J. S. Drucker, M. Krishnamurthy, J. A. Venables and J. M. Cowley, "Biassed Secondary Electron Imaging in a UHV-STEM", *Ultramicroscopy* **31**, 1989, 111.

G. G. Hembree, J. Unguris, R. J. Celotta, and D. T. Pierce, "Scanning Electron Microscopy with Polarization Analysis: High Resolution Images of Magnetic Microstructure", *Scanning Microscopy Supplement* **1**, 1987, 229.

## 5.0 Budget and Budget Explanation

### BUDGET SUMMARY CONTINUATION OF ONR CONTRACT #N00014-93-0099

Category	Year 1 1/1/96-9/30/96	Year 2 10/1/96-9/30/97	Year 3 10/1/97-9/30/98	Total 1/1/96-9/30/98
Summer Salary <sup>1</sup>	13,566	14,245	14,957	42,768
Students Salary <sup>2</sup>	21,248	34,498	36,222	91,968
Fringes 3 % <sup>3</sup>	4,028	4,596	4,826	13,450
<b>Salary plus fringes</b>	<b>38,842</b>	<b>53,339</b>	<b>56,005</b>	<b>148,186</b>
Travel	4,500	4,500	4,500	13,500
Materials-Supplies <sup>4</sup>	16,000	16,000	16,000	48,000
Publications	3,000	3,000	3,000	9,000
<b>Direct (No Capital)</b>	<b>62,342</b>	<b>76,839</b>	<b>79,505</b>	<b>218,686</b>
Capital Equipment <sup>5</sup>	58,600	12,500	0	71,100
Total Direct Costs	120,942	89,339	79,505	289,786
Indirect Costs 52.5%	32,730	40,340	41,740	114,810
<b>Total Cost</b>	<b>153,672</b>	<b>129,679</b>	<b>121,245</b>	<b>404,596</b>
Carry Over <sup>6</sup>	<29,059>			
<b>Total Funding Request</b>	<b>124,613</b>	<b>129,679</b>	<b>121,245</b>	<b>375,537</b>

<sup>1</sup>Summer salary for Prof. M. Scheinfein. Computation based on receiving promotion 4/1/96 (applied in summer 95). Monthly salary \$6783. First year salary inflated at the annual rate of 5%.

<sup>2</sup>Salary computation : Two students, 50 % Academic year @ \$11608 + 50% 3 mos.Summer @ \$3870 + In-State Tuition @ \$1950. First year salary inflated at the annual rate of 5%. 3 Students Total.

<sup>3</sup>Fringes: Faculty @ 25%. Students @ 3%.

<sup>4</sup>Materials and supplies includes \$8,000/yr operating expense of the UHV-STEM micromagnetics facility. During the last grant period support for the operation of this instrument became our responsibility, and instead of paying \$120.00/day for microscope use, we support the instrument. This support includes pump rebuilds, new field emission tips, electron multipliers and all services associated with the instrument. Other materials and supplies include \$4,000/yr machine shop charges for microscope repair, \$3,000/yr UHV components (replacement) and \$1,000/yr for phone and xerox charges.

<sup>5</sup>Capital equipment includes : yr. 1 \$58,600; yr. 2 \$12,500

(1) Lesker/VG UHV surface science stage which will allow extended heating and cooling ranges required to pursue experiments for *in-situ* installation in MIDAS (UHV-STEM). \$24000

(2) Kerr light scattering apparatus for bench-top measurements. This system includes an intensity stabilized He-Ne laser (\$4200), two Glan-Thompson crystal polarizers (\$1400), photo-elastic modulator (\$5100), photoconductive diode detector and amplifier (\$1400), phase sensitive lock-in amplifier (\$4500), bipolar regulated current supply (\$3000), data-I/O card (\$1500) and PC computer (\$4000). \$25100

(3) UHV components to build 2-inorganic halide evaporator Knudsen cells of our design (\$6000).

(4) Cryoshield for evaporators in MIDAS (\$3500).

(5) Resources for building electron spin-polarimeter in year two (\$12,500)

<sup>6</sup>Carry Over from previous grant period : \$29,059 Personnel

\$18,500	
Fringes (3%)	\$ 555
Overhead(52.5%)	\$10,004

6.0 Current and Pending Support

**GRANT ACTIVITY MICHAEL R. SCHEINFELD**

Current :

"Correlations Between Micromagnetic, Microstructural and Microchemical Properties in Ultrathin Epitaxial Magnetic Structures," M.R. Scheinfein, J.S. Drucker, G.G. Hembree. Office of Naval Research, Physics Division. \$510,280. Duration 36 months. Start date, January 1, 1993. N00014-93-1-0099.

"A Proposal to Develop the Nanodetector: A High Resolution Photo-Electron Electron Microscope", M.R. Scheinfein, R. Watts, T. Lucatorto, F. Pollack, Collaborative Research Grants of the National Institute of Standards and Technology, US Department of Commerce. \$85,242. Duration 12 months. Start date, October 1, 1993. NIST-70NANB4H1532.

"Magnetic Microstructure Observed With Electron Holography in STEM," M.R. Scheinfein. The Tri-Services AASERT Program. Requested \$115,440. Duration 36 months. Start Date 1 June 1995.

Recently Completed :

"A Low Energy Electron Microscope," J.D. Dow, E. Bauer, G.G. Hembree, W.E. Packard, M.R. Scheinfein, O.F. Sankey, D.J. Smith, J.C.H. Spence, I.S.T. Tsong, J.A. Venables. Instrumentation for Materials Research Division of the National Science Foundation. \$577,500. Duration 24 months. Start date, July 1, 1991. DMR-91-12021.

"Development of New Point Sources for Ions and Electrons," J.C.H. Spence and M.R. Scheinfein. Instrumentation for Materials Research Division of the National Science Foundation. \$210,599. Duration 18 months. Start date, October 1, 1991. DMR-91-12550.

Pending:

"Dynamics of Mesoscopic Structures in Magnetic Materials," R.V. Chamberlin, M.R. Scheinfein, Division of Materials Research, National Science Foundation. Total grant request \$288,600. Duration 3 years. Start Date, June 1, 1996.

"Magnetic Memory Elements: Magnetic Simulations of Giant Magnetoresistance Structures," Advanced Research Defense Agency, (Through IBM Almaden), S.S.P. Parkin, J. Slonczewski, M.R. Scheinfein, P. Levy, D.J. Smith, M. Salamon, J. Moodera, S. Conradson, W. Gallagher, M. Bhushan, G. Xiao, R. Scheuerlein, S.X. Wang, J. Kaufman, B.A. Jones. Total grant request \$6,900,000. My part, \$231,771. Duration 5 years. Start date 1 January 1996.

"A Nanoscale Magnetometer/Magnetoresistive Sensor," G.G. Hembree, M.R. Scheinfein, The Jet Propulsion Laboratory. Total grant request \$27,100. Duration 1 year. Start date 1 January 1996.

### GRANT ACTIVITY GARY G. HEMBREE

Current :

"Correlations Between Micromagnetic, Microstructural and Microchemical Properties in Ultrathin Epitaxial Magnetic Structures," M.R. Scheinfein, J.S. Drucker, G.G. Hembree. Office of Naval Research, Physics Division. \$510,280. Duration 36 months. Start date, January 1, 1993. N00014-93-1-0099.

Recently Completed :

"A Low Energy Electron Microscope," J.D. Dow, E. Bauer, G.G. Hembree, W.E. Packard, M.R. Scheinfein, O.F. Sankey, D.J. Smith, J.C.H. Spence, I.S.T. Tsong, J.A. Venables. Instrumentation for Materials Research Division of the National Science Foundation. \$577,500. Duration 24 months. Start date, July 1, 1991. DMR-91-12021.

Pending:

"A Nanoscale Magnetometer/Magnetoresistive Sensor," G.G. Hembree, M.R. Scheinfein, The Jet Propulsion Laboratory. Total grant request \$27,100. Duration 1 year. Start date 1 January 1996.

# ARIZONA STATE UNIVERSITY

Department of Physics and Astronomy  
Tempe, Arizona 85287-1504  
(602) 965-3561

Michael R. Scheinfein  
Phone : (602) 965 - 9658  
FAX : (602) 965 - 7954  
Internet : Michael.Scheinfein@asu.edu

**Date:** 10 June 1998

**To:** Dr. Larry Cooper  
Office of Naval Research  
Electronics Division Code 312  
800 N. Quincy Street  
Arlington, VA 22217-5660  
Phone (703) 696-4215

**Subject:** ONR # N00014-93-0099 / ONR/AASERT # N00014-95-0891

**From:** Michael R. Scheinfein  
Department of Physics and Astronomy  
Arizona State University  
PSF-470 Box-871504  
Tempe, AZ 85287-1504  
Phone (602) 965-9658  
FAX (602) 965-7954  
email Michael.Scheinfein@asu.edu

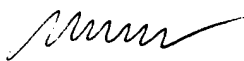
Dear Dr. Cooper:

I have enclosed a summary of my research supported by ONR and ONR/AASERT funds. This summary is meant to bring you up to date on where we are, and where we would like to be heading. I have also enclosed a short white paper as I would like you to consider my grant for continuation for another 3 year period.

Dick and I had already discussed the continuation grant but I assume those discussions are irrelevant now that Dick has retired. I have two student who are essentially in the middle of their PhD dissertation research supported by ONR. I would very much like to keep them active on their current projects. My personal schedule is complicated by my plans to be on sabbatical this coming academic year. If it is at all possible, I would like to solidify plans for the continuation by the beginning of July. If I cannot secure ONR funds for the students, I may cancel my sabbatical and stay on site in order to secure new funds to support the students. If you need to contact an ASU sponsored project representative while I am away, let me refer you to Teresa Robinette at (602) 965-4935. She handles all of my research awards.

I look forward to hearing back from you at your earliest convenience. Thanks and take care.

Sincerely,



Michael R. Scheinfein  
Professor